UNIVERSITY OF SOUTHAMPTON

Faculty of Environmental and Life Sciences
School of Ocean and Earth Science

# An Investigation of Diatom Physiology and its Effect on Silicon Trapping using Biogeochemical Models

*by*

**Jacob Thomas Harper**

MSci

ORCiD: 0000-0001-6118-7428

*A thesis for the degree of*
*Doctor of Philosophy*

October 2023

University of Southampton

Abstract

Faculty of Environmental and Life Sciences
School of Ocean and Earth Science

Doctor of Philosophy

**An Investigation of Diatom Physiology and its Effect on Silicon Trapping using Biogeochemical Models**

by Jacob Thomas Harper

Silicon (Si) distribution in the world's oceans is biologically controlled by silica-shelled phytoplankton called diatoms, which contribute 20% of global primary productivity. Diatoms decouple Si from other macronutrients that are upwelled in the Southern Ocean (SO), trapping Si and limiting the growth of siliceous algae elsewhere. This is caused by high diatom Si:N uptake ratios under Fe deficiency in combination with low attenuation through the water column and deep circulation back to the SO. The way diatom physiology is parameterised in biogeochemical models can lead to contrary responses to Fe fertilisation that occurred in past glaciations. It is important to understand the effect of diatom physiology on Si trapping to ensure models can address past climates and future changing oceans. This study firstly investigates the core mechanisms of SO Si trapping by using a simple 3-box model to represent the overturning circulation between the deep ocean SO and subtropical ocean. The model reproduced expected nutrient concentrations for P, Fe and Si as well as distributions of diatoms and non-diatoms. However, the addition of an Fe-dependent or Fe and Si-dependent diatom Si:N ratio led to near complete Si trapping and sensitivity testing showed that parameters and initial conditions required dramatic alteration to allow Si to escape to the subtropics. A simulation of Fe fertilisation produced no increase in Si leakage as the decrease in Si:N was overtaken by the growth of diatom productivity. In the second part of this study, two models with different representations of diatom physiology were tested against the observations of a series of SO nutrient addition experiments. A quota model which allowed for luxury uptake of Si and emergent Si:N stoichiometry outperformed a simple model using direct parameterisations of Si:N. The winning model was adapted to include an additional Chl state variable and then optimised using a genetic algorithm to fit the parameters. The algorithm was able to dramatically reduce the deviation between the model and the experiments. However, a sensitivity test that performed 120 optimisations found that many parameters were unconstrained by the data. This led to the adoption of a hybrid approach where only well-constrained parameters were fitted by the algorithm. The hybrid approach resulted in only a small

reduction in the fit of the model to the observations while hopefully avoiding over-tuning and retaining a higher performance at broader scales. When used to fit the initial proportion of diatoms in the model, the algorithm correlated with the results of pigment data implying the importance of community structure in addition to Fe and Si concentrations. Overall, this study suggests that raised Si:N ratios in SO diatoms can drastically reduce Si leakage even in the presence of Fe fertilisation and also presents a quota model approach to simulating diatom physiology, tuned to a powerful set of observations, which can be applied to other model frameworks.

# Contents

# List of Figures

# List of Tables

# Declaration

I, Jacob Thomas Harper, declare that this thesis and the work presented in it are my own and has been generated by me as the result of my own original research.

**An Investigation of Diatom Physiology and its Effect on Silicon Trapping using Biogeochemcial Models**

I confirm that:

1. This work was done wholly or mainly while in candidature for a research degree at this University;
2. Where any part of this thesis has previously been submitted for a degree or any other qualification at this University or any other institution, this has been clearly stated;
3. Where I have consulted the published work of others, this is always clearly attributed;
4. Where I have quoted from the work of others, the source is always given. With the exception of such quotations, this thesis is entirely my own work;
5. I have acknowledged all main sources of help;
6. Where the thesis is based on work done by myself jointly with others, I have made clear exactly what was done by others and what I have contributed myself;
7. None of this work was published prior to submission.

**October 2023**

# Acknowledgements

Firstly, I would like to thank and acknowledge the contributions of my supervisors Mark, Adrian and Toby. Thank you, Toby, for your thoughts on the modelling and help debugging, Adrian, for your provision of the genetic algorithm and advice on optimisation, and Mark, for providing the starting points for the models developed here, helping me conceptualise this thesis, helping me debug code and reviewing my writing. Thank you to Mark, Neil and everyone from CUSTARD cruise DY111 for the use of the experimental data collected there.

I also want to thank Mark for his generosity and kindness during the length of this PhD without which I would not have made it here. Your patience, guidance and compassion has helped see me though dark times and ill health. I feel extremely fortunate to have had you as my supervisor, thank you for the opportunities you have provided me to cultivate my interest in research, especially going to sea on DY149.

I would like to give a huge thank you to all of my friends during the PhD at the National Oceanography Centre in Southampton. Whether getting together to laugh, cry or celebrate each other's success I feel so grateful to have met you all. I have collected fond memories of Christmas balls, PG coffee, volleyball, meals together and the most uniquely themed cakes this world has to offer. This PhD has given me opportunity to make friends from all across the world who have broadened my horizons and I hope these friendships last a long time. I also want to thank my fellowship of three friends who have been with me since my school days, Ollie, Rufus and Luke. Knowing you always have my back no matter how much distance separates us brings me great comfort and I love celebrating our milestones together.

For all the support they have given me throughout my education, I want to give all my thanks and love to my Mum and Dad. They never ceased to believe in me, always celebrated my achievements and always offered a helping hand. Ever since I was little they have allowed me to explore and foster my interests and constantly reassured me of their pride. All of my best qualities I owe to them. They showed me beautiful places and passed on their love of the natural world including the ocean. My grandmother Miriam would always act fascinated by the shells I found as a child or

the pictures from my fieldtrips as a student and I know she would have celebrated my accomplishment now as if I had just been knighted.

Last but not least, I give my unending gratitude to my partner Africa, whom I love dearly. By far the greatest treasure of this PhD has been meeting you. You believe in me when I don't believe in myself, pick me up when I fall and a life spent next to you is a life worth living. Thank you for your unconditional support, I can't wait to see where this adventure leads us next.

Thanks be to God.

# Definitions and Abbreviations

| | |
|---|---|
| AABW | Antarctic Bottom Water |
| AABW | Antarctic Bottom Water |
| AAIW | Antarctic Intermediate Water |
| ACC | Antarctic Circumpolar Current |
| AZ | Antarctic Zone |
| BCP | Biological carbon pump |
| BSi | Biologic Silica |
| C | Carbon |
| $CaCO_3$ | Calcium Carbonate |
| $C_{cr}$ | Critical algal concentration for coagulation |
| CDW | Circumpolar Deep Water |
| Chl | Chlorophyll |
| CMIP6 | Coupled Model Intercomparison Project Phase 6 |
| $CO_2$ | Carbon dioxide |
| CUSTARD | Carbon Uptake and Seasonal Traits in Antarctic Remineralisation Depth |
| DIC | Dissolved organic carbon |
| DIN | Dissolved inorganic nitrogen |
| DNA | Deoxyribonucleic acid |
| EPS | Extracellular polymeric substances |
| ESM | Earth System Model |
| EXP1 | Exponential parametrisation 1 |
| EXP2 | Exponential parametrisation 2 |
| Fe | Iron |
| Fv/Fm | PSII photochemical efficiency |
| G1 | Growth phase 1 |
| G2 | Growth phase 2 |
| GA | Genetic algorithm |
| GE | Gradient experiments |
| GCM | General circulation model |
| $HCO_3^-$ | Bicarbonate |

| | |
|---|---|
| HNLC | High Nitrate, Low Chlorophyll |
| HPLC | High-performance liquid chromatography |
| HYP | Hyperbolic parametrisation |
| IDW | Indian Deep Water |
| LCDW | Lower Circumpolar Deep Water |
| LGM | Last Glacial Maximum |
| LTE | Large-type experiments |
| M phase | Mitosis |
| Mn | Manganese |
| MOC | Meridional overturning circulation |
| N | Nitrogen and nitrate |
| NADW | North Atlantic Deep Water |
| NPZD | Nutrient–phytoplankton–zooplankton–detritus ecosystem model |
| OOI | Ocean Observative Initiative |
| P | Phosphorus and phosphate |
| PDW | Pacific Deep Water |
| PF | Polar Front |
| PFT | Plankton functional type |
| PFZ | Polar Frontal Zone |
| POC | Particulate organic carbon |
| PON | Particulate organic nitrate |
| PSII | Photosystem II |
| RRS Discovery | Royal Research Ship Discovery |
| S phase | DNA replication |
| S/V | Surface area to volume ratio |
| SAF | Subantarctic Front |
| SALH | Silicic Acid Leakage Hypothesis |
| SAMW | Subantarctic Mode Water |
| SAVH | Silicic Acid Ventilation Hypothesis |
| SAZ | Subantarctic Zone |
| SDV | Silica deposition vesicle |
| Si | Silicon and silicic acid |
| SO | Southern Ocean |
| SOIREE | The Southern Ocean Iron RElease Experiment |
| SPZ | Subpolar Zone |
| SRs | Surface dissolution fraction of silicic acid |
| ST | Subtropical Ocean |
| STF | Subtropical Front |
| TEP | Transparent exopolymer particles |
| TN | Transect North |

| | |
|---|---|
| TS | Transect South |
| UCDW | Upper Circumpolar Deep Water |

# Chapter 1

# Introduction

The ocean is the largest reservoir of inorganic carbon holding around 38,000 gigatons (Sarmiento and Gruber, 2002), and has played a huge role in mitigating climate change having sequestered about a third of anthropogenically released $CO_2$ (Khatiwala et al., 2009; Sabine et al., 2004). Two main mechanisms contribute to the oceanic storage of carbon, the so-called solubility pump and biological carbon pump (BCP) (Volk and Hoffert, 1985).

The BCP results from the sinking flux of organic and calcium carbonate detritus from the surface to the deep ocean where it can be trapped for hundreds to thousands of years (Volk and Hoffert, 1985). It is estimated that, without the BCP, atmospheric $CO_2$ levels would be $\sim$200 ppmv higher than in the present day (Parekh et al., 2006; Boyd, 2015). This pump helps maintain a gradient of surface dissolved organic carbon (DIC) 15% lower than in the deep which is crucial as, if carbon was vertically homogeneous, atmospheric $CO_2$ would be $\sim$50% higher (Gruber and Sarmiento, 2002). The BCP begins with the fixation of inorganic carbon in the surface by unicellular autotrophs known as phytoplankton, which are collectively responsible for nearly half of the carbon fixation associated with global net primary production (Longhurst et al., 1995; Field et al., 1998). A fraction of this organic matter is exported to the deeper ocean, mainly through gravitationally settling particles (Boyd et al., 2019) whereupon it is remineralised. This results in the net transfer of inorganic carbon to depth, removed from contact with the atmosphere.

Phytoplankton use light to fix carbon and so must remain in the uppermost well-lit layer of the ocean known as the euphotic zone, which has a maximum extent of around 200 m deep. The essential elements, or nutrients, required by phytoplankton include nitrogen, phosphorus and in some cases silicon although multiple micronutrients such as iron are also required and have been shown to limit production in certain regions (Moore, Mills, Arrigo, Berman-Frank, Bopp, Boyd, Galbraith, Geider, Guieu, Jaccard, Jickells, La Roche, Lenton, Mahowald, Marañón, Marinov,

Moore, Nakatsuka, Oschlies, Saito, Thingstad, Tsuda and Ulloa, 2013). Redfield (1934) discovered that the ratio of C:N:P is an average of 106:16:1 throughout the world's oceans, both in the composition of phytoplankton biomass and in dissolved nutrient pools. Although, important deviations from this ratio exist regionally due to species composition, nitrogen fixation and nutrient limitation (Weber and Deutsch, 2010; Singh et al., 2013; Guildford and Hecky, 2000).

If not for the BCP, nutrients in the ocean would be as uniformly distributed as salinity in the oceans (Sarmiento and Gruber, 2006). However, as well as sequestering carbon, the BCP acts to strip these nutrients from the surface layer and transport them to depth. As organic matter sinks, nitrate and phosphate undergo bacterial remineralisation while biogenic opal (hydrated, polymerized silica) dissolution is primarily temperature dependent (De La Rocha, 2006). Through successive utilisation of nutrients by phytoplankton, the surface seasonally becomes depleted while deep waters are continually enriched. Physical processes such as mixing and upwelling act to re-homogenise the distribution of nutrients.

The surface and the deep are locally connected through diffusive vertical mixing and entrainment during winter deepening of the mixed layer; and globally connected through the meridional overturning circulation (MOC). This large-scale ocean circulation system, also commonly known as the "ocean conveyor belt", connects the Arctic, Atlantic, Indian, and Pacific Oceans via the Southern Ocean (SO). It is driven by a combination of mechanical and density forcing, involving the surface winds, exchanges of heat, fresh water and salt, as well as tidal activity (Munk, 1966; Broeker, 1991; Toggweiler and Samuels, 1998; Talley, 2013). Deep water formation caused by decreased temperature and increased salinity occur in the high-latitude North Atlantic and the Weddell and Ross seas surrounding Antarctica resulting in the North Atlantic Deep Water (NADW) and the Antarctic Bottom Water (AABW) (Talley, 2013). These are mainly balanced by the gradual upward return flow of the Pacific Deep Water (PDW), Indian Deep Water (IDW) and the NADW to the surface of the SO driven by the circumpolar westerly winds (Toggweiler and Samuels, 1995). Deep water formation removes carbon from contact with the atmosphere while upwelling exposes it. As deep water masses continue along their meridional pathways they become enriched in carbon and nutrients thanks to the organic matter constantly raining from above (Sarmiento and Gruber, 2006).

It is clear that the SO has a particularly key role in regulating the Earth system as a whole; being responsible for approximately 40% of the global ocean uptake of anthropogenic $CO_2$ , predominantly through the solubility pump (Devries, 2014) and for around 75% of the excess heat generated in the Earth system (Frölicher et al., 2015), as well as being a key component region for the BCP. The powerful meridional circulation responsible for this also upwells abundant quantities of nutrients to the surface, which do not illicit the level of phytoplankton production we might expect

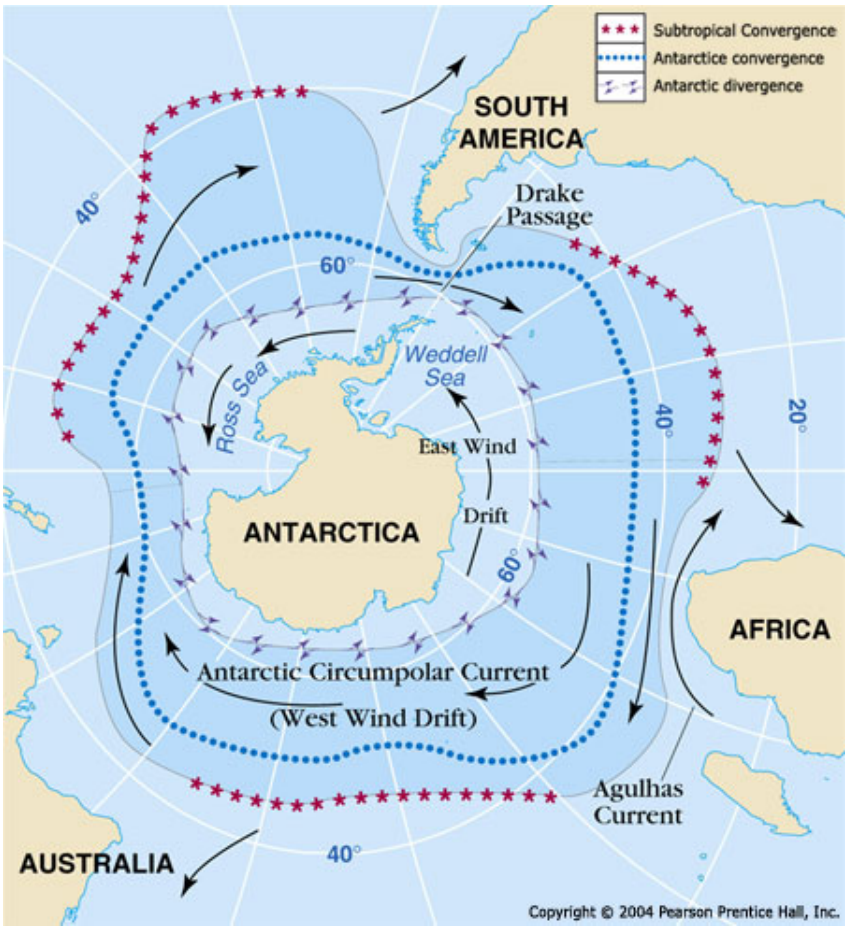


FIGURE 1.1: A map of the Southern Ocean depicting the latitudes of different oceanographic features and how their position varies longitudinally. Reproduced from *'Dive and Discover: Antarctica: Circulation'* 2005

due to the low deposition of iron-rich continental dust that makes it so far south (Jickells et al., 2005).

## 1.1 The Southern Ocean

### 1.1.1 Physical Structure

The SO is most commonly defined as the circumpolar waters south of the subtropical front, which is located around an average latitude of ~40°S (Figure 1.1). This vast water mass, which covers 20% of the world's ocean's surface, encircles Antarctic unimpeded by continental barriers, but remains under-sampled relative to the rest of the world's oceans. Strong westerly winds drive these waters in an eastward flow known as the Antarctic Circumpolar Current (ACC) (Nowlin and Klinck, 1986) which connects the major ocean basins.

The SO exists between the southern boundary of the Antarctic continent and the northern boundary of the Sub-tropical front which marks the divide between Sub-tropical and Subantarctic waters (Figure 1.1). It plays a key role in the global thermohaline circulation as the lack of continental boundaries allows it to connect the three major ocean basins and the exchange of properties between them. Between the Polar and Subantarctic fronts lies the Antarctic Circumpolar Current (ACC) which is the most powerful current on Earth because of strong westerly winds and a latitudinal density gradient (Post et al., 2014). Further south exists a counter-current flowing in the opposite direction to the ACC, fed by easterly winds though in places it is impeded by the Antarctic coastline.

While Ekman transport in the ACC draws surface waters north, this southern 'East Wind Drift' draws surface waters to the south leading to upwelling at what is known as the Antarctic Divergence. Here, nutrient rich Circumpolar Deep Water comes to the surface and enters two pathways (Figure 1.2). Water that moves south loses its buoyancy through atmospheric cooling and salt enrichment due to sea ice formation. It sinks and becomes dense Antarctic Bottom Water. Water moving north becomes more buoyant due to precipitation and warming, with the biogeochemical properties also being modified by the actions of biology in the surface. Upon exiting the north of the ACC the northward flowing waters are subducted during deep winter mixing to form Subantarctic Mode Water (SAMW) which continues to carry its properties northwards (Hanawa and Talley, 2001). The SO acts to both downwell and upwell large water masses and distributes them across the oceans, making it a central driver to the upper and lower limbs of the Meridional Overturning Circulation (Toggweiler and Samuels, 1998; Sloyan and Rintoul, 2001; Marshall and Speer, 2012).

### 1.1.2 Biological characteristics

Upwelling in the SO draws up aged water masses from around 2000-3000 m that have accumulated large nutrient inventories over time from the remineralisation of sinking matter (Morrison et al., 2015). The result is that surface waters of the SO have the highest nutrient concentrations in the world's oceans with nitrate, phosphate and silicic acid concentrations exceeding 24 µM, 1.6 µM and 50 µM respectively (Levitus et al., 1993). In other upwelling regions phytoplankton would have stripped the surface of these nutrients if they were so abundant. Holm-Hansen (1985) estimated that after upwelled water had travelled roughly 200 days to reach the Polar Front, the nutrients should have been completely removed.

The SO has been classified as one of the High Nitrate, Low Chlorophyll (HNLC) zones due to the low phytoplankton activity in the region that defies what is expected from the normal correlation between macronutrient availability and phytoplankton production (de Baar et al., 1995). This phenomenon was initially spotted by Ruud

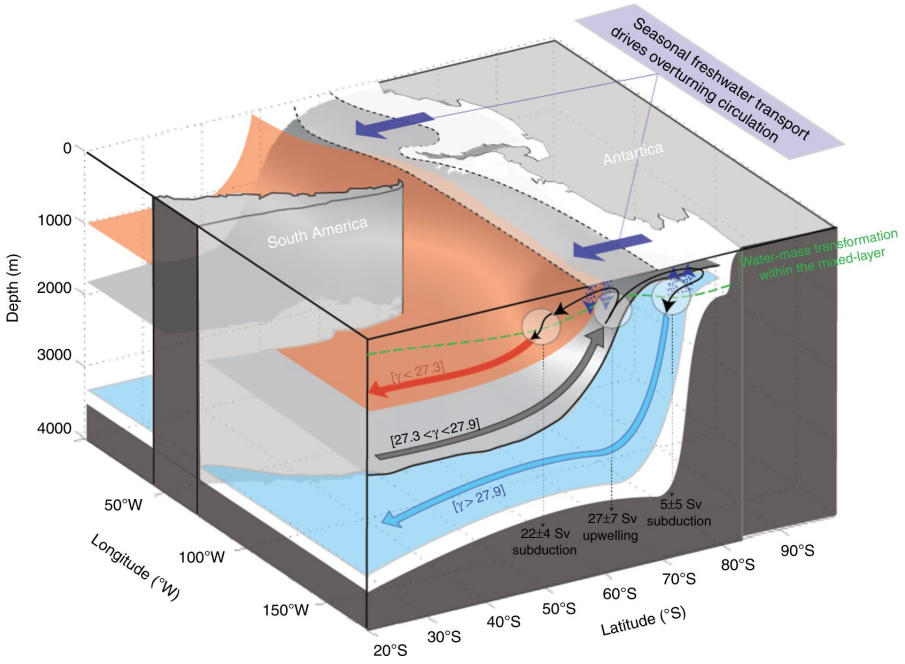


FIGURE 1.2: The components of Southern Ocean circulation: upwelling of the Circumpolar Deep Water in grey; sinking of the Antarctic Bottom Water in blue; and subduction and northwards transport of the Subantarctic Mode Water in red. Each is traced by its signature density profile ($\gamma$). Reproduced from Pellichero et al. (2018)

(1930) and was dubbed the "Antarctic Paradox" with Gran (1931) first postulating a possible connection to iron limitation, a trace element required by phytoplankton for key components of photosynthesis; this was later supported by more observations and iron enrichment experiments that led to enhanced growth (Martin et al., 1989, 1990, 1991). Martin (1990) further postulated that if iron were to be provided to this region, such as in past glacial periods, phytoplankton productivity would increase and subsequently sequester more carbon to depth, famously joking "Give me a half tanker of iron, and I will give you an ice age" (Weier, 2001). These findings drove decades of research and, despite alternative suggestions that light limitation and grazing pressure were more dominant contributors (Frost, 1991; Fasham, 1995), many iron fertilisation experiments have witnessed the clear response of SO phytoplankton to the relief of iron stress (Boyd et al., 2007).

River discharge and glacial inputs of iron are generally trapped in coastal regimes (Poulton and Raiswell, 2002) while hydrothermal vent iron may help buffer short term iron fluctuations despite forming particulates at depth (Tagliabue et al., 2010). However, in the oxygenated modern ocean where iron remains very insoluble (Kraemer, 2004), the main external source of iron to the world's oceans is aeolian dust transport from the world's deserts (Jickells et al., 2005). The surface of the SO is iron depleted due to its distance from the northern hemisphere dust sources from which 90% of total dust emissions originate (Li et al., 2008), the prevailing westerly winds that form a barrier to southward dust transport (Li et al., 2008), and the limited

resupply from deep winter mixing (Tagliabue et al., 2014). Ice cores suggest that, during glacial times, iron deposition to the world's oceans was approximately an order of magnitude higher than during interglacial periods; Martin (1990) hypothesised that this extra iron fertilisation led to the lower atmospheric $CO_2$ in these periods.

Under iron limited conditions, small phytoplankton groups in the pico- to nanophytoplankton range succeed, as iron uptake efficiency is dependent on cell surface area (Sunda and Huntsman, 1997). Abundant haptophytes such as *Phaeocystis* may be favoured under these conditions as they form colonies which may aid in grazer defence and help trap iron in the community's mucilage (Hamm, 2000; Schoemann et al., 2001); are more resilient to fluctuating light conditions (Arrigo et al., 1999); and have superior uptake of reduced forms of nitrogen when access to nitrate is limited (Tungaraza et al., 2003). This group and other small phytoplankton that dominate under iron deficiency (Cullen, 1991; Smetacek et al., 2004) are kept in check by small microzooplankton grazers that can respond quickly to population growth due to their quick generation times (Coale et al., 2004). However, during episodic inputs of iron or when a combination of abundant nutrients and the end of light limitation makes bloom conditions tenable, large diatoms take over, using their opal cell wall grazer defence (Hamm et al., 2003) and fast growth rate to escape grazer control before larger zooplankton with longer generation times are able to respond (Banse, 1995; Gall et al., 2001; Timmermans et al., 2001; Gervais et al., 2002; Timmermans et al., 2004). This leads diatoms to dominate blooms in the SO (Brzezinski et al., 2001; Petrou et al., 2016; Deppeler and Davidson, 2017).

Diatoms have an obligate requirement for silicon in order to build their strong cell wall, for which silica content has been demonstrated to be approximately inversely proportional to grazing by adult copepods and nauplii (Pančić et al., 2019). These blooms quickly use up available iron, or in some places silicon and then decline. Arrigo et al. (1999) observed that in some regions *Phaeocystis* and diatoms were separated based on mixed layer depth, with *Phaeocystis* likely out-competing in weakly stratified waters due to its adaptation to low light.

## 1.2 The Silicon Trap

Silicic acid distribution in the world's oceans bears broad similarity to that of nitrate, with high concentrations in the SO and the North Pacific (Figure 1.3), while concentrations are heavily depleted in the subtropical gyres (World Ocean Atlas, Garcia et al., 2018). Additionally, diatoms growing without restraints from light or nutrient availability exhibit a Si:N ration of 1:1 (Brzezinski, 1985). On the other hand, in contrast to nitrate and phosphate which are required by all phytoplankton, silicic

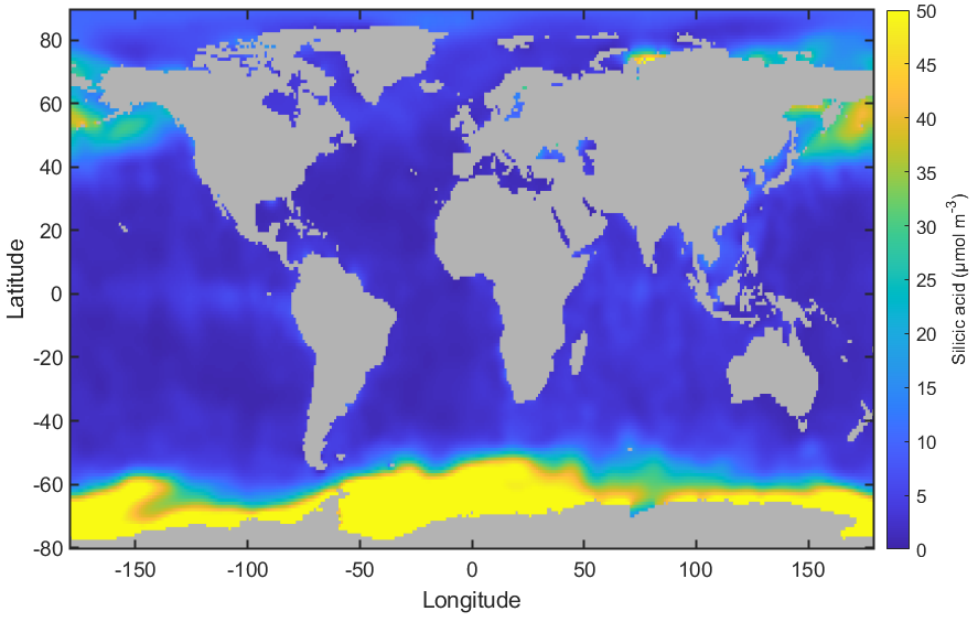


FIGURE 1.3: Mean annual surface silicic acid from the World Ocean Atlas (Garcia et al., 2018).

acid is used almost solely by diatoms and while the remineralisation of N and P is biologically mediated, dissolution of opal back to silicic acid is a temperature dependent chemical process (Lerman and Lal, 1977; Dugdale and Wilkerson, 2001). Sinking opal is further protected from dissolution by an organic matrix that covers the frustule exterior (Bidle and Azam, 1999).

However, when comparing distributions of silicic acid and nitrate in the SO, there is a clear discrepancy in the circumpolar region between 40°S and 60°S, where nitrate carried northwards from the nutrient-rich upwelling of the CDW remains high but silicic acid is suddenly absent (Smith et al., 2000; Dafner and Mordasova, 1994). What process decouples Si from N in this region and creates such a meridional gradient of silicic acid across the surface of the SO?

### 1.2.1 Causes of Silicon Trapping

Diatoms are the dominant force in the modern biological silicon pump, as the main contributor to the gross production of 240 Tmol Si $yr^{-1}$ biogenic silica in the ocean (Tréguer and De La Rocha, 2013). The stripping of Si from surface waters by diatoms is thought to be particularly strong in this band of the SO because of the tendency of many species to increase their Si to N uptake ratios under Fe stress (Brzezinski, 1985; Takeda, 1998; De La Rocha et al., 2000; Brzezinski et al., 2003; Timmermans et al., 2004; Hoffmann et al., 2007). Reasons suggested for this phenomena include an increase in surface area to cell volume ratio associated with reduced cell size (Martin-Jézéquel et al., 2000; Marchetti and Harrison, 2007); increased formation of heavily silicified

resting spores among some species (Sugie et al., 2010); and an interplay of reduced N uptake and increased Si uptake (M. Franck et al., 2000; Timmermans et al., 2004).

As discussed, the regeneration of Si is different to that of N and P and this leads to separate fates for these elements after being utilised in the surface. On average, 50% of opal produced in the euphotic zone is preserved to sink out and this rises to 84% in the cold waters of the SO which inhibit the process of dissolution (Sarmiento and Gruber, 2006). Comparatively, for ∼25% of the Si utilised during spring growth in the HNLC Gulf of Alaska, only ∼4% of the N was exported past 200 m (Whitney et al., 2005). Holzer et al. (2014) estimated that the mean depth of Si regeneration in the SO reached 2300 m, as opposed to 600 m for phosphate remineralisation.

Through the increased Si:N ratio of diatom uptake and the enhanced export of opal to deeper depths relative to organic material, silicon is decoupled from other macronutrients in both the surface and sub-surface of the lower latitude SO. But why does this decoupling in one location radically effect the distribution of silicon in the ocean as a whole? As discussed in Section 1.1.1, the SO is an exceptionally important hub in the global overturning circulation. A large part of the material that sinks out of the euphotic zone is regenerated in the CDW which subsequently returns these nutrients to the surface creating a loop of utilisation, export and upwelling (Sarmiento and Gruber, 2006). Modelling by Holzer et al. (2014) found that about half of the global Si inventory is successively involved in paths to subsequent SO utilisations, with Si last utilised in the SO having only a 5% chance of being next utilised outside the SO compared with a 44% chance for phosphate. Furthermore, the northwards decline in silicic acid occurs in the region of mode water formation; crucially the SAMW, which is the main source of nutrients for the thermocline and supplies the entire Southern Hemisphere and the North Atlantic Ocean (Hanawa and Talley, 2001). In fact, the decoupling silicic acid and nitrate created here has been used to observe the reach of the SAMW pycnostad (a layer of relatively uniform density)through the ocean using the tracer $Si^* = [Si(OH)_4] - [NO_3{}^-]$ (Sarmiento et al., 2004).

The result of exacerbated removal of silicon by diatoms combined with the return pathway of the CDW in a region that supplies nutrients responsible for about 75% of the biological production north of 30°S (Sarmiento et al., 2004) is extreme trapping of silicon within the SO. This trapping limits the production of diatoms over a large part of the world's oceans (Ragueneau et al., 2000; Hauck et al., 2018).

It should be said that simulations by Demuynck et al. (2020) suggest that physical processes are predominantly responsible for the creation of the gradient in Si across surface of the SO over the timescale of years to decades. They find these processes connecting the deep Si gradient to the surface play a greater role than local biology but leave the door open for biological control of those deep concentrations, for example via diatom stoichiometry.

### 1.2.2 Silicic Acid Leakage Hypothesis

Investigations of silicon trapping in the modern ocean may be a key to unlocking drivers of aspects of paleoclimatology. Antarctic ice cores show that past glacial maxima recorded $CO_2$ values 80-100 ppm lower than the interglacial period between them (Barnola et al., 1987; Petit et al., 1999; Lüthi et al., 2008). Hypotheses to explain this fluctuation have focused on the ocean due to its large carbon reservoir (Sigman and Boyle, 2000).

One hypothesis, named the 'Silicic Acid Leakage Hypothesis' (SALH) has sought to answer this question with the observation that supply of iron by atmospheric dust was higher during glacial intervals due to a drier climate and a more turbulent atmospheric circulation in high southern latitudes (Petit et al., 1999). Initially, these observations led to the idea that the relief of iron stress in iron-limited regions of the ocean would simply enhance production and therefore drawdown $CO_2$ (Martin, 1990), however, this was hampered by most data in fact showing a lower export production in glacial periods (Kumar et al., 1995; François et al., 1997). The SALH proposes that the addition of dust-borne iron in the Antarctic reduces the Si:N uptake ratios of diatoms and therefore alleviates silicon trapping in the SO and makes silicic acid available in the wide portion of the ocean supplied by the SAMW. The increased availability of silicic acid in the rest of the ocean then lead to a floristic shift away from coccolithophores, which lowered export of calcium carbonate. The reduction in carbonate burial increased the alkalinity of the oceans and allowed greater $CO_2$ drawdown by the oceans (Brzezinski et al., 2002; Matsumoto et al., 2002; Matsumoto and Sarmiento, 2008). An alternate "silica hypothesis" also exists which states that it was an increased dust flux of Si that lead to the floristic shift toward diatoms and subsequent $CO_2$ drawdown (Harrison, 2000).

However, evidence that leakage of Si from the SO occurred mainly during deglaciations rather than glacial maxima has lead to a new Silicic Acid Ventilation Hypothesis (SAVH) (Hendry and Brzezinski, 2014). This hypothesis puts forth that, although iron fertilisation increased the Si:N of mode waters during the Last Glacial Maximum (LGM), stratification and weakened upwelling and mixing reduced the Si concentration escaping in these waters. During the initiation of deglaciation, sea ice retreat and southward westerly wind migration is thought to have induced greater overturning in the SO resulting in both high Si:N and high Si concentration in mode waters.

### 1.2.3 Future Implications

As evidenced above by paleoceanography, stoichiometry and circulation centred in the SO have the power to drive changes in global climate. As humanity brings forth its

own climate change, how will this influential region of the ocean react? Earth system modelling by Moore et al. (2018) under a future climate scenario (RCP 8.5, a high baseline emission scenario) predicts that subsurface Fe concentrations south of 60°S will increase 34% by 2300 and that this, combined with warming waters and increased stratification resulting from the poleward shift of westerly winds encircling the SO, will lead to intense nutrient trapping and subsequent declines in primary production (24%) and carbon export (41%). Meanwhile, analysis of chlorofluorocarbons has suggested that these shifting westerlies have also decreased the age of subtropical subantarctic mode waters and increased the age of circumpolar deep waters (Waugh et al., 2013). Moreover, calcifying plankton may have to live in a SO undersaturated in aragonite as soon as 2030 if atmospheric $CO_2$ reaches 450 ppm by this time (McNeil and Matear, 2008). In summation, anthropogenic climate change has the potential to dramatically alter the physical, chemical and biological characteristics of the SO and therefore, understanding this region's role has never been more important.

## 1.3 Diatom Physiology

### 1.3.1 Cellular Silicon Cycle

The distinct, defining feature of the diatom cell is its silica frustule consisting of two intersecting valves: the smaller hypotheca fitting within the larger epitheca like the base and lid of a petri dish. Indeed, the name diatom comes from the greek diatomos meaning "cut in two". A silica band, called the girdle band, wraps around the equator of the diatom and holds the valves together (Round et al., 1990). Evolutionary advantages of a non-organic skeleton may have included being energetically "cheaper" to construct and offering enhanced protection from grazers (Martin-Jézéquel et al., 2000; Hamm et al., 2003). Deposition of silicic acid into a cell wall is calculated to require only 8% of the energy required for organic carbon (Raven, 1983). Experimentation by Hamm et al. (2003) has shown that frustules are mechanically strong, able to resist pressures ranging from 1 to 7 $N\,mm^{-2}$ perhaps leading to copepods and euphausiids co-evolving silica-edged mandibles. Furthermore, feeding experiments have found that diatom silica content was inversely proportional to grazing by adult copepods and nauplii (Pančić et al., 2019) and that weakly silicified diatoms with fast growth rates were more susceptible to grazers than those with more complex frustules (Friedrichs et al., 2013). Other advantages may include the action of frustule opal as a pH buffer for converting more readily available $HCO_3^-$ to $CO_2$ (Milligan and Morel, 2002).

Diatoms reproduce asexually by binary fission to produce two daughter cells which inherit one of the frustule halves from the parent as their epitheca and then generate a

new smaller hypotheca. This results in one same-sized and one smaller-sized daughter cell, thus decreasing the average size of the diatom population over cycles of mitosis. This continues until a critical size threshold is reached whereupon sexual reproduction occurs restoring cell size via a specialised cell called an auxospore (Chepurnov et al., 2004). Diatoms appear to divide at any point of the diel cycle, unlike many other algae (Martin-Jézéquel et al., 2000).

Because silicon is structurally integral to the diatom cell it is closely coupled to the cell cycle rather than directly to photosynthesis. Diatoms, like other eukaryotic cells, separate mitosis (M) and cell division (cytokinesis) from the phase of DNA replication (S) with two gap phases where growth occurs (G1 and G2) (Huysman et al., 2014). Starving diatoms of silicon arrests the cell cycle near the point of frustule formation in G2 or M and just prior to DNA synthesis near the G1/S boundary (Brzezinski et al., 1990). Some studies suggest that, at low growth rates induced by nutrient and light limitation, the length of the G2+M phase leads to an increase in cell silicification as deposition continues in these conditions (Martin-Jézéquel et al., 2000; Claquin et al., 2002). Claquin et al. (2002) suggest while Si metabolism is energetically cheaper and controlled by the cell cycle, N and C are linked by the energetic provision from photosynthesis and the processes of amino acid and protein synthesis.

Surface waters are highly undersaturated with respect to opal, requiring diatoms to actively transport silicic acid across the cell wall in order to maintain cellular concentrations high enough to precipitate opal (Paasche, 1973*b*,*a*; Azam et al., 1974). Silicon is used within organelles called silica deposition vesicles (SDV's) to construct new inner valves and girdle bands during asexual reproduction, after which they're exocytosed to the cell exterior (Zurzolo and Bowler, 2001). Soluble intracellular silicon brought into the cell but not yet incorporated into the insoluble silica phase are termed silicon pools (Azam et al., 1974). How much silicon is in these pools, where it is stored and in which chemical forms is still under debate.

A review by Martin-Jézéquel et al. (2000) compiled a range of 19 to 340 mM (assuming the form of monosilicic acid) across several species, representing up to 50% of the total cellular biosilica. Recent three-dimensional cryo–electron spectroscopy by (Kumar et al., 2020) landed in this range with ∼150 mM for *T. pseudonana*, three orders of magnitude higher than the external environment. These values strongly exceed saturation for silica solubility, which is around 2 mM below pH 9 (Iler, 1979) making the internal silicon pool supersaturated. The question therefore changes from how diatoms are able to precipitate silica to how they are able to stop the precipitation of silica in their supersaturated cellular environment.

The prevailing theory as to how diatoms are able to maintain these concentrations is that silicon is bound in organic molecules within the cell (Azam et al., 1974; Sullivan, 1977; Chisholm et al., 1978). The most common method for examining intracellular Si

pools, the molybdate method (Martin-Jézéquel et al., 2000), will not detect silicon bound to organic matter and therefore many measurements may be underestimating the total storage pool (Gröger et al., 2008). Brzezinski and Conley (1994) found that in Si-starved *T. weissflogii* deposition of an entire frustule was provided by the internal Si pool but that this pool was not sustained having been substantially acquired during G2. This is in keeping with the 'dynamic' view of the intracellular pool: which describes the level of intracellular silicon as transitory, coupled to the relative timing of silicic acid uptake and silica deposition (Martin-Jézéquel et al., 2000, and references therein). Kumar et al. (2020) instead find evidence for almost constant intracellular silicon levels within *T. pseudonana* and this was also found in *C. fusiformis* (Martin-Jézéquel et al., 2000), suggesting a degree of homeostasis. Hildebrand (2000) proposed that levels were determined by the capacity of intracellular silicon-binding components, with a greater availability of organic binding component allowing greater storage of Si leading uptake to fill the maximum pool. Furthermore, Hildebrand (2008) summarises the idea that because silica deposition draws Si from the cellular pool, silicic acid uptake acts as a feedback to sustain that pool in three modes. Surge uptake occurs when an Si-starved cell has depleted its intracellular pool and upon access to silicic acid achieves maximum uptake rates. Internally controlled uptake exists when the intracellular pool acts as a buffer to maintain equilibrium between deposition and uptake. Finally, externally controlled uptake arises when uptake is limited by the extracellular concentration of silicic acid where pool levels have minimal influence.

### 1.3.2 Iron response

Diatoms contribute about 40% of the annual fixation of organic carbon in the ocean (Nelson et al., 1995) and are chiefly responsible for the two-thirds of total ocean silica burial that presently occurs under the ACC (Tréguer and De La Rocha, 2013). For some time, scientists were perplexed by high accumulation of opal in SO sediments contrary to the iron deficient, low productivity, HNLC waters above (Pondaven et al., 2000). More recently this has been understood as an influence of ambient iron concentration on diatom overall chemical ratios, or stoichiometry. Specifically, the ratio of silicon to nitrate (Si:N) at a cellular level increases under conditions of iron limitation, utilising a greater proportion of the silicon available in the SO's surface per cell (Table 1.1). This enlarged silicon removal in the SO, a hub of global circulation responsible for nutrient supply to much of the world's oceans (Sarmiento et al., 2004), limits the growth potential of diatom communities further north fed by Subantarctic Mode Water.

Recently, growing concern over elevating atmospheric $CO_2$ has made the SO, high in macro-nutrients, a ripe candidate for geoengineering. It was controversially suggested that iron fertilisation could boost growth and result in more organic carbon sinking

into deep waters or deep-sea sediments where it would be trapped for a long time (Martin and Fitzwater, 1988). However, the elevated silicification of diatoms found in iron-limited waters has been suggested to act as a dense opal ballast for cell sinking and flux of silicon from the surface has been correlated to deep carbon fluxes (Armstrong et al., 2002; Honda and Watanabe, 2010; Brzezinski et al., 2015). This next section aims to establish whether alleviating iron stress and thus decreasing Si:N ratios therefore counteract or at least limit supplementary carbon export from fertilisation via less favourable sinking dynamics. Parameters that might be used in models to shed light on the interaction of iron and deep carbon storage in the SO are also evaluated.

Multiple studies (Table 1.1) have established that iron deficiency can lead to elevated S:N ratios in diatom cells; often in the region of 2 to 3-fold from the normal, iron-replete value of $\sim$1 (Brzezinski, 1985), but occasionally up to 4.1 (Timmermans et al., 2004) and 6.5 (Brzezinski et al., 2003) in extreme cases. This departure from normal stoichiometry creates a preferential depletion of Si in areas of mode water formation in the Antarctic Circumpolar Current, decoupling silicon from the abundant nutrients the SO otherwise feeds northwards (Sarmiento et al., 2004). Various theories have been put forward to explain this phenomenon. Firstly, because reduced iron leads to slowing of growth rate, the duration of the cell wall synthesis phase in cell development may be extended, leading to a thicker frustule (Claquin et al., 2002). Secondly, while nitrate uptake rate will decrease under iron limitation, silicic acid uptake by the cell may decrease to a lesser extent or not at all leading to a Si:N differential (Hutchins and Bruland, 1998; Takeda, 1998). Finally, at the community level, species composition and succession can change with iron availability resulting in a greater proportion of thinner or thicker-shelled species (Assmy et al., 2013).

Taking a closer look at how uptake rates affect Si:N, Marchetti and Harrison's 2007 study of stoichiometry in the pennate diatom *Pseudo-nitzschia* showed declines in both Si and N consumption but an increase in Si:N ratio suggesting that the more severe effect of iron limitation on nitrate uptake over silicic acid uptake was responsible. However, Marchetti and Cassar's 2009 paper includes a compendium of Si:N responses to iron deficiency from different studies which features a variety of cases: decreasing Si, increasing Si, or no change with declining N. Cell uptake kinetics conform to the Michaelis-Menten model, characterised by an initially steep increase in uptake rate with nutrient availability followed by the reaching a saturation point. Table 1.1 shows two parameters that describe the shape of this model: the maximum specific uptake rate $V_{max}$, and the half saturation constant $K_s$ which determines uptake efficiency at low nutrient concentrations. In oligotrophic conditions $K_s$ is expected to decrease, conferring a greater advantage at low nutrient concentrations and $V_{max}$, or technically apparent $V_{max}$ as iron limitation has been introduced, is expected to do the same. The studies in Table 1.1 agreed that maximum Si uptake rate $V_{Si-max}$ decreases

TABLE 1.1: Changes in diatom physiological parameters under iron deficiency.

| Parameter | Under iron deficiency | Reference |
|---|---|---|
| $K_{Si}$ (Si uptake half-saturation constant) | 3.2-fold decrease | (Leynaert et al., 2004) |
| | No effect | (De La Rocha et al., 2000) |
| | No effect in 3 experiments, 3-fold increase in one | (Franck et al., 2003) |
| $V_{Si-max}$ (maximum Si uptake rate) | 7-fold decrease (no additional influence of iron above 0.120 nmol Fe $L^{-1}$) | (Leynaert et al., 2004) |
| | 3-fold decrease | (De La Rocha et al., 2000) |
| | 2-fold decrease | (Hutchins et al., 1999) |
| | 2.7-fold decrease | (M. Franck et al., 2000) |
| | 2 to 3-fold decrease | (Franck et al., 2003) |
| Cell Size | 3-fold decrease (increased S/V) | (Leynaert et al., 2004) |
| | Reduction in length-normalized width resulting in 1.4-fold increase in S/V | (Marchetti and Cassar, 2009) |
| $V_{N-max}$ (maximum N uptake rate) | 2 to 3-fold decrease | (Franck et al., 2003) |
| | 2.2-fold decrease | (Hutchins et al., 1999) |
| Diatom Si:N ratio | 2-fold increase | (Takeda, 1998) |
| | 2 to 3-fold increase | (Hutchins and Bruland, 1998) |
| | 0, 1.6, 2.3, 6.5- fold increase | (Timmermans et al., 2004) |
| | 2-fold increase | (Hoffmann et al., 2007) |
| | 1.1 to 2.4-fold increase | (Marchetti and Harrison, 2007) |
| | No change | (De La Rocha et al., 2000) |
| | Net uptake increased 4.1-fold relative to normal iron-replete value ($\sim$1) | (Brzezinski et al., 2003); (Brzezinski, 1985) |
| Sinking | 5-fold increase in sinking rate | (Muggli et al., 1996) |
| | 4-fold decrease in sinking rate under iron fertilisation linked to 2-fold decrease in Si:C ratio | (Watson et al., 2000) (Waite and Nodder, 2001) |
| | 2.3-fold decrease in sinking rate 11 days after iron enrichment | (Boyd et al., 2000) |
| | 100 m $BSiO_2$ and POC export increase 37-fold and 2-fold respectively | (Brzezinski et al., 2015) |
| Cell Silicification | 4-fold increase in BSi content per unit of cell volume | (Leynaert et al., 2004) |
| | 1.7-fold increase in BSi content per unit of cell volume for two species | (Takeda, 1998) |
| | 1.4-fold increase in BSi per cell | (De La Rocha et al., 2000) |
| | 2.9-fold increase in BSi per cell | (Hutchins and Bruland, 1998) |
| | 2-fold increase in silicic acid cell quotas | (Coale et al., 2004) |

under iron limitation while the Si half saturation constant $K_{Si}$ has mixed responses. Leynaert et al. (2004) carried out a detailed study of the silicic acid uptake kinetics of the pennate diatom *Cylindrotheca fusiformis*, monitoring $V_{max}$ and $K_s$ over a gradient of iron concentrations. In both cases, these parameters decreased in the shape of a Michaelis-Menten type curve with decreasing iron. As no other study has reported over such a gradient, this is the best available picture of how Si uptake declines under iron limitation and may be a good model for this effect. Although a more severe reaction to iron deficiency is expected in nitrate maximum specific uptake rate $V_{N-max}$, the limited studies available (Table 1.1) show a similar decrease to that of Si. A similarily thorough study of nitrate uptake with rising iron is needed to make a better comparison.

### 1.3.3 Silicification

The suggestion that a thicker diatom frustule is concomitant to increased Si:N is supported by studies that specifically note an increase in biogenic silicification of the cell (Table 1.1, and refs. therein). This has been found both in single species experiments (Takeda, 1998) and in-situ additions to whole communities (Hutchins and Bruland, 1998), and also, normalised to cell volume (Leynaert et al., 2004) and not normalised (De La Rocha et al., 2000). At least in some cases, regardless of possible reductions in cell size under nutrient limitation, cell silicification has increased suggesting a mix of individual physiological response and community composition is at play (Takeda, 1998; Leynaert et al., 2004).

Increased silicification of a cell resulting in increased cell density may have a ballasting effect, weighing the cell down so it sinks faster (Brzezinski et al., 2015). Though this has not been shown directly, Muggli et al. (1996) have shown that iron deficiency increased the sinking rate of the diatom *Actinocyclus sp.* 5-fold while a coccolithophore underwent no change and Brzezinski et al. (2015) suggest that higher export efficiency under low Si:N waters, likely depleted in Si by high Si:N diatoms, was due to this ballasting effect. The studies of the SO Iron RElease Experiment (SOIREE), involving an iron fertilised bloom, also noted declines in sinking rates following alleviation of iron deficiency (Boyd et al., 2000; Watson et al., 2000; Waite and Nodder, 2001). Higher sinking rates would give dead cells less time to be remineralised in the surface and, furthermore, a thicker frustule offers protection from grazers during that time.

However, silicification is not the only way that iron deficiency could lead to increased sinking rate. While sinking phytoplankton generally adhere to Stokes Law (larger cells sink faster), large diatoms use energy in processes to bolster their buoyancy. This energy mainly comes from respiration in which electron transport processes can become iron-limited (Waite et al., 1992; Muggli et al., 1996).

Shifting from an individual cell focus to assess the community level, aggregation and repackaging of cells is the other major contributor to sinking efficiency. Repackaging can be instituted biologically by grazing and subsequent repackaging into dense faecal pellets. Diatom species grown under iron deficiency had mechanically stronger frustules which were more resistant to zooplankton grazing and therefore negatively affecting faecal repackaging (Wilken et al., 2011). However, some mesozooplankton can enhance remineralisation by processing faecal pellets within the upper mixed layer, reducing export into deep waters (Wassmann, 1997). Physical processes dominate aggregate formation when grazers can't keep up with sudden large blooms (Thornton, 2002). Of these physical factors the primary driver is concentration, or in fact the reaching of a critical concentration $(C_{cr})$ (Jackson, 1990). Another important factor is the presence of sticky extracellular polymeric substances (EPS) released by phytoplankton and, in the case of diatoms, especially a form of EPS called transparent exopolymer particles (TEP). TEP production by diatom *C. calcitrans* was greater under nitrate limitation than in nutrient-replete cultures (Corzo et al., 2000) and nutrient limitation has been suggested to increase the stickiness of diatoms in culture (Drapeau et al., 1994), although this likely involves additional factors such as spiny morphology.

As seen above, surface studies have suggested that increased Si:N could potentially lead to cells sinking faster and further, but is there research that connects changes in Si:N to deep-sea carbon export? Traditionally, flux of particulate organic carbon to the deep has been simulated using a power-law curve from Martin et al. (1987). Based on some near-surface organic carbon flux, the power-law models increasing removal of organic matter by remineralisation as it sinks to the deep, allowing for the estimation of how long carbon may be sequestered in the deep ocean based on the water flow of the water masses in the region.

However, more recently, Armstrong et al. (2002) have proposed that fluxes of ballast minerals (silicate and carbonate biominerals, and lithogenic material) determine deep-water POC fluxes instead. Working on evidence that flux of organic matter at depths sub-1800m were directly proportionate to the fluxes of ballast minerals, they have put forward that sinking organic matter can be divided into matter that is associated to ballast minerals that are dense and protect from remineralisation and residual matter that is not mineral-associated (Figure 1.4).

This new model has been supported by Honda and Watanabe (2010) who found deep sea POC flux was highly correlated with mineral ballast flux, accounting for almost 100% in the Western Pacific Subarctic Gyre, and also found that mineral associated flux increased proportionally with depth while residual flux declined. Furthermore, they found that opal was responsible for 70% of deep POC flux, outlining the importance of silicon-integrating organisms in deep carbon export and contradicting previous sediment trap data analysis downplaying the role of opal vs $CaCO_3$ (Klaas

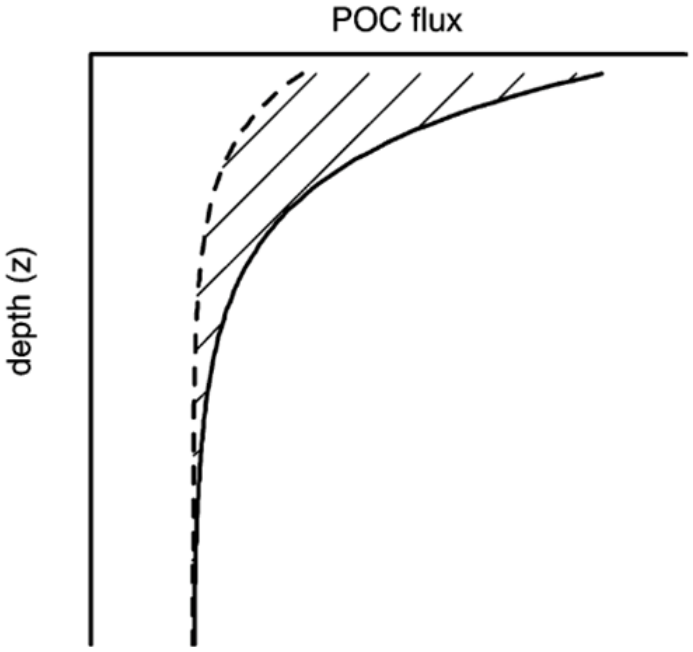


FIGURE 1.4: Reproduction of Armstrong et al.'s 2002 model hypothesis of organic carbon fluxes. Total flux of particulate organic carbon (POC) is denoted by the solid line while POC flux quantitatively associated with ballast minerals shown by the dashed line. Residual POC flux is shown by the crosshatched area.

and Archer, 2002) which may not have taken into account varying Si:C ratios (Passow and De La Rocha, 2006).

So, presence of silicified cells has been connected to deep export, but does the degree of silicification make a difference? Nelson et al. (1995) found that while heavily-silicified *F. kerguelensis* and moderately-silicified *F. curta* can both dominate diatom blooms in the SO; *F. curta* and other moderately silicified species are much less common in abyssal sediments; although, selective removal of species from the sediment and interspecific differences in diagenesis, the conversion of sediment into sedimentary rock, are not taken into account (Shemesh et al., 1989). However, Assmy et al. (2013) presented evidence that thick-shelled species like *F. kerguelensis* represent "silicon-sinkers" that, despite their persistence in low-iron environments release mainly empty or solitary low-carbon frustules from the surface; while, on the other hand, thin-shelled species such as *Chaetoceros dichaeta* are "carbon-sinkers" that employ a boom-and-bust strategy, undergoing mass mortality which is responsible for large high-carbon aggregates.

Literature regarding the relationship between iron and stoichiometry in diatom cells contains repeated references and links to cell size. When iron becomes deficient, cell volume scales down while surface area to volume ratio (S/V) scales up (Muggli et al., 1996; Leynaert et al., 2004; Sarthou et al., 2005; Marchetti and Cassar, 2009); therefore, while some cell processes are directly affected by iron, some are influenced indirectly

via these physical changes. For instance, when Leynaert et al. (2004) recorded changing $K_{Si}$ and $V_{Si-max}$ across decreasing iron concentration (Figure 1.5), they were able to reliably calculate the response of these parameters in *C. fusiformis* from the increasing S/V of the cells. Similarly, S/V has been used to determine power-law relationships for nitrate and iron half-saturation constants across species (Hein et al., 1995; Sarthou et al., 2005). There is also some suggestion that as the amount of silica in a cell wall is proportional to the surface area, this is to some extent responsible for increasing cell biogenic silica content (Takeda, 1998; Leynaert et al., 2004). However, other parameters, such as growth rate, have a more complex relationship with cell size. Maximum growth rate ($\mu_{max}$), achieved by the cell in light and nutrient replete conditions, scales inversely with cell size across diatom species due to a combination of surface area and diffusion boundary thickness effects on nutrient uptake and the decrease in effectiveness of increased pigmentation in light harvesting at greater cell size known as the 'package effect' (Sarthou et al., 2005). On the other hand, under iron stress at the species level, cell's specific growth rate ($\mu$) decreased proportionally with decreasing cell size and decreasing iron concentration (Sunda and Huntsman, 1995; Leynaert et al., 2004).

There is evidence for increased silicification resulting in higher sinking speed and likely protecting diatoms from remineralisation (Muggli et al., 1996; Boyd et al., 2000; Watson et al., 2000; Waite and Nodder, 2001; Brzezinski et al., 2015). Separately, there is evidence that the silicon flux from the surface is correlated to deep carbon flux (Armstrong et al., 2002; Honda and Watanabe, 2010; Brzezinski et al., 2015). However, the key gap in understanding is whether one is linked to the other; does Si:N play a significant role in determining silicon supported export? Or, are community composition and diatom success over non-silicified phytoplankton the dominant factors in regulating deep carbon flux?

While the Armstrong model should be tested against real SO surface and deep-water fluxes, it might also be integrated into models that factor in iron reliant Si:N ratios in order to test it's sensitivity to this dynamic. To better realise changing stoichiometry, a greater understanding of nitrate uptake kinetics in a gradient of iron conditions would be useful for combination with the detailed experiments with silicic acid already carried out. Si:N could further be functional in models as a negative impact on zooplankton grazing rates. Finally, cell size has already been used to reduce multiple parameters into one in more complex models (e.g. Ward et al., 2018) and this review finds that many of the factors correlated with cell size are relevant to the effects of changing iron.

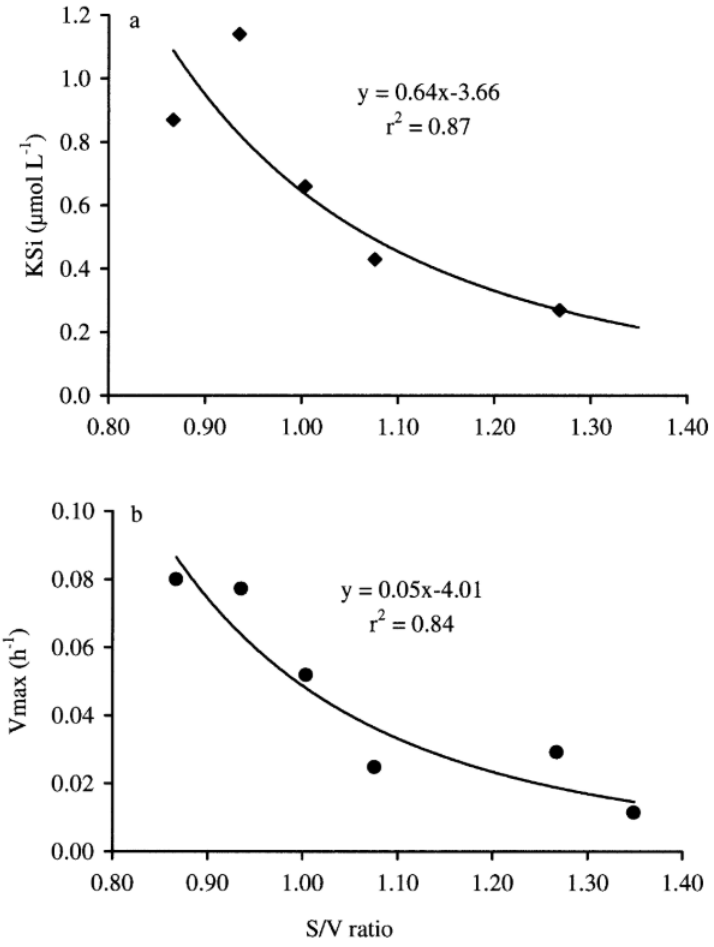


FIGURE 1.5: A reproduction from Leynaert et al. (2004) illustrating the relationship between surface to volume ratio and (a) apparent maximum uptake rate $(Vmax)$ and (b) the half-saturation constant for silicic acid $(KSi)$. These measurements of *Cylindrotheca fusiformis* were taken across a gradient of iron limitation.

## 1.4 Modelling Approaches

As access to computing power has become more readily available over the past few decades, numerical marine biogeochemical models have become an ever more important tool in addition to and complementing field and laboratory approaches. Numerical biogeochemical models have been used to estimate concentrations and fluxes; to elucidate the processes behind past and present data; and to make predictions about future conditions (Gentleman, 2002). Models are typically separated into the biochemical component and the physical component which are coupled together to provide global or regional products.

The most common structure of the biochemical component is the nutrient–phytoplankton–zooplankton–detritus (NPZD) ecosystem model which represents the flow of elements through a highly idealised ecosystem (Steele, 1958; Fasham et al., 1990). More complex models have been developed that represent a

more extensive trophic structure by grouping organisms as plankton functional types (PFTs) for example: diatoms, coccolithophores, nitrogen fixers, meso and microzooplankton (Le Quéré et al., 2005; Stock et al., 2020; Long et al., 2021).

The most basic formulations of phytoplankton growth need only include a nutrient limitation term but often also use terms for light limitation and temperature dependence (Haney and Jackson, 1996; Ilyina et al., 2013; Yool et al., 2013; Stock et al., 2020; Long et al., 2021). Nutrient limitation is generally formulated through Liebig's Law of the Minimum (1840) which was developed as an agricultural principle and has since been applied to phytoplankton ecology through the idea that the least available nutrient governs phytoplankton biomass accumulation or growth rate (de Baar, 1994). Models with multiple limitation terms have traditionally calculated fractional growth rates for each term and then found the minimum or threshold rate in accordance with Blackman's Law 1905 while others have used a multiplicative approach (O'Neill et al., 1989; Haney and Jackson, 1996). Nutrient uptake by phytoplankton has mainly followed the parameterisation set out by Caperon (1967) and Dugdale (1967) who used Michaelis-Menten kinetics to describe a saturating, hyperbolic relationship between external nutrient concentration and specific growth rate. However, Droop (1973) argued that there was a step between these factors, which was the internal nutrient pool or cell quota, defined as a ratio of the nutrient to cellular carbon, and this was what directly drove growth rate. These models are analogous under steady-state conditions (Burmaster, 1979).

Complexity in the physical component of biogeochemical models is mainly the result of resolution, both of depth and of latitude and longitude. At their simplest, a 2-box or 'slab' model may simply be used to resolve a mixed layer and a deep layer (Steele, 1958; Evans and Parslow, 1985; Anderson et al., 2015). Meanwhile, global scale biogeochemical models, which may also be paired with atmospheric and terrestrial models to produce whole Earth System Models (ESMs), contain many vertical layers, commonly increasing in thickness with depth. These large-scale models represent the ocean's horizontal plane in a grid structure, often with a $\sim 1^{\circ}$ resolution to balance complexity with simulation time (Collins et al., 2011; Seland et al., 2020; Gurvan and The NEMO Team, 2022). However, the most recent generation of ESMs from the Coupled Model Intercomparison Project Phase 6 (CMIP6) use a minimum resolution of 100 km up to 25 km which enables the representation of finer-scale ocean physical processes such as mesoscale eddies (Séférian et al., 2020).

Complexity in biogeochemical models comes at a cost. Firstly, the computational power required to run them and the difficulty of accessing those sometimes expensive, shared resources. Secondly, the increased time taken per run, which can limit the length of the simulation or the number of ensembles or sensitivity tests that can be accomplished. Finally, a greater number of parameters are required to tune more complex models, some of which may not be based on observations. Furthermore, the

increased number of variables and parameters can make it harder to ascribe a model result to a particular cause.

Among the models that have chosen to resolve diatoms and silicon, most choose to take into account the stochiometric variability in diatom silicon content/uptake relative to other major nutrients and have parameterised this in a myriad of ways Yool and Tyrrell (2003); Yool et al. (2013); Aumont et al. (2015); Stock et al. (2020); Long et al. (2021). A 2019 study by Holzer et al. used a data constrained model to investigate how different parameterisations of diatom Si stoichiometry respond to iron fertilisation. They found that depending on the parameterisation, iron fertilisation could result in strengthened trapping of silicic acid in the SO or enhanced leakage instead. This divergence suggests that how variable diatom stoichiometry is formulated could pace a large bias on future predictions of SO silicon trapping and therefore global biogeochemistry (Sarmiento et al., 2004).

## 1.5 Research Aims

The overall aim of this study is to understand how diatom physiology influences the trapping of Si in the SO and to investigate the best approaches to successfully modelling the important aspects of that physiology. The first main area of research focuses on the broader scale of SO Si trapping, investigating how phytoplankton production, nutrient availability and regeneration, dust deposition and the circulation of water masses affects the fate of Si upwelled in the SO. To investigate this topic in Chapter 2 I aim to:

- Build a 3-box model (3BOX-SIMPLE) of the key regions and processes involved in trapping Si in the SO using a simple setup of 2 phytoplankton groups and 3 nutrients.
- Observe the effect of different parameterisations of diatom Si:N ratios in response to Fe within the 3-box model.
- Perform sensitivity testing of the effect of relevant model parameters and starting conditions on the leakage of Si from the SO.
- Evaluate the model's response to Fe fertilisation that occurred during past glaciations.

The second main area of research focuses on the smaller scale detail of diatom uptake stoichiometry in response to Fe availability. This research revolves around nutrient addition experiments that were separately conducted in the SO as part of a research cruise. To investigate this topic in Chapters 3 and 4 I aim to:

- Establish the relationship of community Si:N uptake ratios to Fe deficiency at the research site.
- Build and compare two different models, a simple model and a more complex quota model, against the cruise dataset.
- Observe the ratio of chlorophyll to carbon in the nutrient addition experiments and incorporate an additional state variable to the quota model to represent a dynamic cellular chlorophyll pool.
- Optimise the variable chlorophyll quota model by using a genetic algorithm to select parameters.
- Perform a sensitivity optimisation using the genetic algorithm to observe the parameters that are most well constrained by the dataset.
- Compare the community structure picked by the genetic algorithm with HPLC data from the cruise.

## 1.6 Thesis Overview

- **Chapter 1** presents an introduction to the physical and biological characteristics of the SO, an overview of the causes and implications of Si trapping in the region and a review of diatom physiology especially targeting their use of Si and response to Fe availability. This chapter also provides an outline of the thesis and its aims.
- **Chapter 2** presents a simple 3-box model (3BOX-SIMPLE) representation of the core components of Si trapping in the SO. These components include the upwelling of nutrients in the SO, the attenuation of Si dissolution and the parameterisation of diatom Si:N stoichiometry by different methods. Sensitivity testing is conducted to compare how each factor mediates the leakage of Si from the SO.
- **Chapter 3** presents the modelling of a set of multifactorial nutrient addition experiments conducted on an SO cruise. The outputs of a simple model and a more complex quota model are compared against the dataset to evaluate their performance with particular focus on their replication of Si:N uptake ratios.
- **Chapter 4** presents an optimisation of the quota model to improve its simulation of the nutrient addition experiments. Firstly, an additional state variable is incorporated to represent a dynamic cellular chlorophyll pool. Secondly, a genetic algorithm is used to explore model parameters and to investigate community structure between the different experiment sites.

- **Chapter 5** summarises the scientific findings of Chapters 2-4, discusses the links between them and their context within the literature. The potential for future avenues of research within the topics outlined in this thesis are also discussed.

# Chapter 2

# Investigating the effect of diatom physiology on silicon trapping in the Southern Ocean with a 3-box model

## 2.1 Introduction

The structure and movement of water masses in the Southern Ocean (SO) is of major importance as a closure term in the global overturning circulation (Toggweiler and Samuels, 1993; Marshall and Speer, 2012; Talley, 2013) and key to the distribution of global nutrients (Sarmiento et al., 2004). A deep well of nutrients is upwelled in the Circumpolar deep water (CDW) to the surface of the Southern Ocean south of the Polar Front (Figure 2.1). Upon reaching the surface, the upper limb of the CDW is transported northwards undergoing transformation by biological processes as well as atmospheric forcing (Sigman et al., 2010). Crucially, these waters are then subducted into mode waters that supply the nutrients for the majority of the ocean's surface productivity and, therefore, alterations in the subantarctic have a far reaching influence (Sarmiento et al., 2004). While the lack of iron in this high nutrient low chlorophyll (HNLC) zone prevents phytoplankton from stripping most nutrients from the surface (Landry et al., 2000; Boyd and Law, 2001; Coale et al., 2004), a gradient of decreasing Si relative to N and P emerges as the upwelled waters move north (M. Franck et al., 2000). This creates mode water depleted in Si relative to other nutrients with knock-on effects for diatom productivity in the rest of the world's oceans (Sarmiento et al., 2004). Si removed by phytoplankton is exported by the

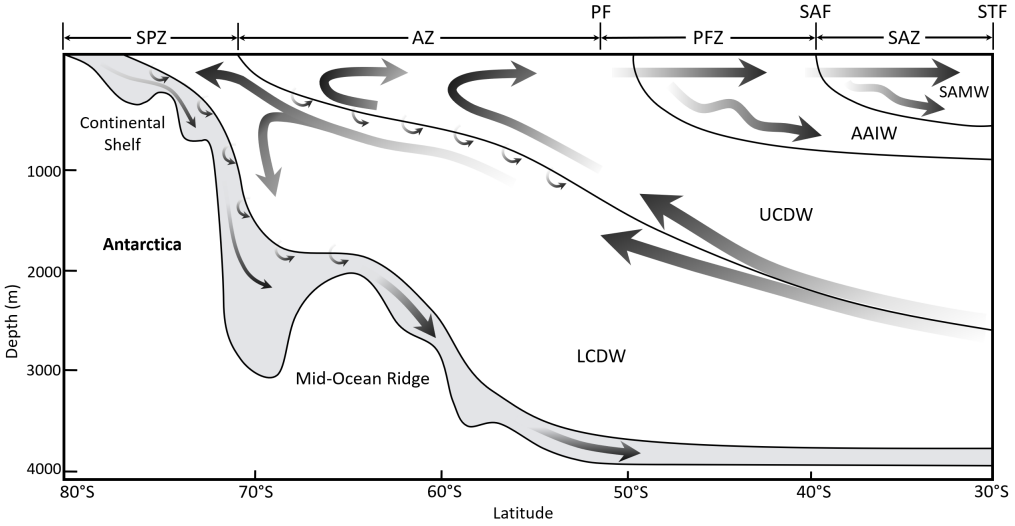


FIGURE 2.1: Diagram of the meridional overturning circulation in the Southern Ocean adapted from Post et al. (2014) and Speer et al. (2000). STF, Subtropical Front; SAF, Subantarctic Front; PF, Polar Front; SAMW, Subantarctic Mode Water; AAIW, Antarctic Intermediate Water; UCDW, Upper Circumpolar Deep Water; LCDW, Lower Circumpolar Deep Water; AABW, Antarctic Bottom Water; SAZ, Sub-Antarctic Zone; PFZ, Polar Frontal Zone; AZ, Antarctic Zone; SPZ, Subpolar Zone. Arrows indicate the mean direction of flow

biological pump and may re-enter the CDW to create a loop known as the Southern Ocean silicon trap (Primeau et al., 2013).

The main theory as to why Si becomes so depleted relative to other macronutrients is founded on the stoichiometry of the diatoms which dominate SO blooms. Under the iron stress phytoplankton experience in this region, diatoms can increase their Si:N ratios from 1:1 to as much as 6.5 (Timmermans et al., 2004). This decoupling is enhanced by the increased likelihood of N recycling in the surface compared to the remineralisation of biogenic opal which occurs at greater depths (Nodder and Waite, 2001; Salter et al., 2007). The silicon trap is an interplay of upwelling nutrients; diatom growth and stoichiometry; and silicon remineralisation which may balance differently in the future SO. Anthropogenic forcing may lead to variation in the supply of iron to the SO via aeolian dust transport (Mahowald et al., 2005); enhanced diatom growth due to temperature increases (Boyd et al., 2015); and decreased nutrient supply to the surface (Moore, Lindsay, Doney, Long and Misumi, 2013). Therefore, it is important to understand the balance of the factors that create silicon trapping to predict the outcomes if they may change in the future.

Simple box models have a long history of use in biogeochemical modelling and are still utilised despite the high resolution models available today (Tyrrell, 1999; Martin et al., 2002; Matsumoto et al., 2002). Box models have the advantage of being quick to run and are therefore useful for sensitivity testing. In addition, by removing complexity from the model and only considering the system's most important

components, it becomes easier to diagnose the effect of changing parameters. In this chapter a 3-box model designated as 3BOX-SIMPLE is developed and used to undertake an idealised examination of silicon trapping in the SO through its core components: the upwelling of nutrients to the SO surface; the biology that modifies nutrient stoichiometry in the euphotic zone; and the export of SO surface waters to the subtropical ocean. The aim of this chapter is to parameterise this model to approximate the modern silicon trap and the environment that causes it and then to observe how key parameters effect its strength.

## 2.2 Methods

The SO silicon trap is represented in an idealised 3-box model based on the models of Tyrrell (1999), Yool and Tyrrell (2003) and Weber and Deutsch (2012) (Figure 2.2). The physical structure is comprised of a deep box from 500 to 3720 m and two surface boxes of 0 to 500 m representing the southern and subtropical oceans (Weber and Deutsch, 2012) and represents a generalised vertical-horizontal slice of any segment beginning from Antarctica. . Constant mixing occurs vertically between the surface and deep boxes and an overturning circulation transports nutrients between boxes. The circulation upwells nutrients from the deep box to the SO box, transports them north into the subtropical box and then downwells them back into the deep box. This represents the upwelling of the CDW, northward transport out of the subantarctic and the eventual return paths (North Atlantic, Pacific and Indian Deep Waters; Talley, 2013) from all basins to the deep southern ocean and subsequently into the CDW. For simplification, this scheme ignores the proportion of CDW that is transported south upon reaching the surface and forms the Antarctic bottom water.

The biogeochemical component of this model includes three nutrients and two phytoplankton groups. The nutrients include phosphate and iron which are utilised by all phytoplankton in the model and silicic acid which is only consumed by the siliceous algae. Iron, which is a trace nutrient, is included due to its relative scarcity in the Southern Ocean and subsequent limitation of phytoplankton growth there. Furthermore, iron deficiency can cause increased silicic acid uptake relative to N in the diatoms that reside there (Hutchins and Bruland, 1998; Takeda, 1998; Timmermans et al., 2004; Hoffmann et al., 2007; Marchetti and Harrison, 2007). Phytoplankton in the model are divided into diatoms and other algae where diatoms use all three nutrients and the other algae do not require Si. While other silicifiers exist and a broad range of diversity in both diatoms and other algae, this is considered unnecessary to resolve in a coarse exploration of the silicon trap. The two groups compete for resources in the two surface boxes corresponding to the SO and subtropical ocean (ST) respectively but do not enter the deep box.

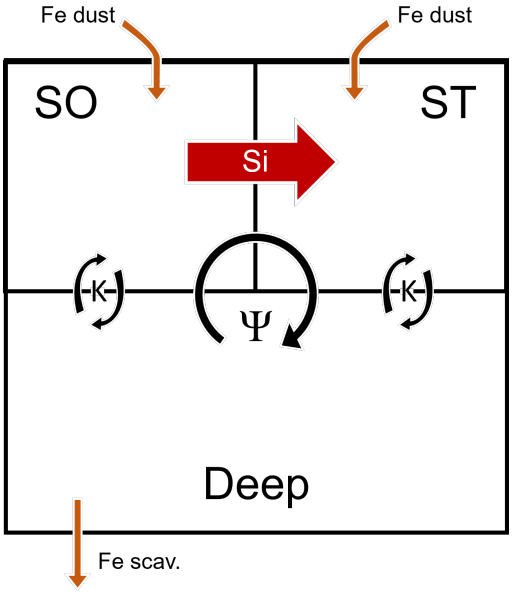


FIGURE 2.2: A diagram of 3BOX-SIMPLE containing three limiting nutrients (phosphate, iron and silicic acid) and two classes of phytoplankton (ordinary, non-silicified algae and diatoms). Boxes SO and ST represent the Southern Ocean and the 'Sub-Tropical' Ocean which are connected by the overturning circulation ($\Psi$) and mixing denoted by $K$. The red arrow represents the key purpose of the model: to understand what effects how much silicon can escape the Southern Ocean.

### 2.2.1 Model Equations

Each nutrient in the model is divided into three separate state variables corresponding to boxes SO and ST, which are labelled $a$ and $b$ in their respective equations, and the deep box while each phytoplankton group has two state variables limited to boxes SO and ST. Although not explicitly present in this version of the model, nitrate in mol $m^{-3}$ remains the currency of the model to facilitate introduction of Si:N uptake ratios, using an assumed constant N:P stoichiometry of 16:1 (Redfield, 1934).

$$\begin{aligned}\frac{\delta P_a}{\delta t} = &- \left[\mu_O \cdot min\left(\frac{P_a}{P_a + K_P}, \frac{Fe_a}{Fe_a + K_{Fe}}\right) \cdot O\right] \\ &- \left[\mu_D \cdot min\left(\frac{P_a}{P_a + K_P}, \frac{Fe_a}{Fe_a + K_{Fe}}, \frac{Si_a}{Si_a + K_{Si}}\right) \cdot D\right] \\ &+ [SR_P \cdot M_O \cdot O] + [SR_P \cdot M_D \cdot D] + \left[K \cdot \frac{P_d - P_a}{SD}\right] + \left[\Psi \cdot \frac{P_d - P_a}{SD}\right]\end{aligned} \tag{2.1}$$

$$\frac{\delta P_b}{\delta t} = -\left[\mu_O \cdot min\left(\frac{P_b}{P_b + K_P}, \frac{Fe_b}{Fe_b + K_{Fe}}\right) \cdot O\right] - \left[\mu_D \cdot min\left(\frac{P_b}{P_b + K_P}, \frac{Fe_b}{Fe_b + K_{Fe}}, \frac{Si_b}{Si_b + K_{Si}}\right) \cdot D\right] + [SR_P \cdot M_O \cdot O] + [SR_P \cdot M_D \cdot D] + \left[K \cdot \frac{P_d - P_b}{SD}\right] + \left[\Psi \cdot \frac{P_a - P_b}{SD}\right] \tag{2.2}$$

$$\frac{\delta Fe_a}{\delta t} = -\left[\mu_O \cdot min\left(\frac{P_a}{P_a + K_P}, \frac{Fe_a}{Fe_a + K_{Fe}}\right) \cdot O\right] - \left[\mu_D \cdot min\left(\frac{P_a}{P_a + K_P}, \frac{Fe_a}{Fe_a + K_{Fe}}, \frac{Si_a}{Si_a + K_{Si}}\right) \cdot D\right] + [SR_{Fe} \cdot M_O \cdot O] + [SR_{Fe} \cdot M_D \cdot D] + \left[K \cdot \frac{Fe_d - Fe_a}{SD}\right] + \left[\Psi \cdot \frac{Fe_d - Fe_a}{SD}\right] + Ex^a_{Fe} \tag{2.3}$$

$$\frac{\delta Fe_b}{\delta t} = -\left[\mu_O \cdot min\left(\frac{P_b}{P_b + K_P}, \frac{Fe_b}{Fe_b + K_{Fe}}\right) \cdot O\right] - \left[\mu_D \cdot min\left(\frac{P_b}{P_b + K_P}, \frac{Fe_b}{Fe_b + K_{Fe}}, \frac{Si_b}{Si_b + K_{Si}}\right) \cdot D\right] + [SR_{Fe} \cdot M_O \cdot O] + [SR_{Fe} \cdot M_D \cdot D] + \left[K \cdot \frac{Fe_d - Fe_b}{SD}\right] + \left[\Psi \cdot \frac{Fe_a - Fe_b}{SD}\right] + Ex^b_{Fe} \tag{2.4}$$

$$\frac{\delta Si_a}{\delta t} = -\left[\mu_D \cdot min\left(\frac{P_a}{P_a + K_P}, \frac{Fe_a}{Fe_a + K_{Fe}}, \frac{Si_a}{Si_a + K_{Si}}\right) \cdot D \cdot R^a_{Si:N}\right] + [SR_{Si} \cdot M_D \cdot D \cdot R^a_{Si:N}] + \left[K \cdot \frac{Si_d - Si_a}{SD}\right] + \left[\Psi \cdot \frac{Si_d - Si_a}{SD}\right] \tag{2.5}$$

$$\frac{\delta Si_b}{\delta t} = -\left[\mu_D \cdot min\left(\frac{P_b}{P_b + K_P}, \frac{Fe_b}{Fe_b + K_{Fe}}, \frac{Si_b}{Si_b + K_{Si}}\right) \cdot D \cdot R^b_{Si:N}\right] + \left[SR_{Si} \cdot M_D \cdot D \cdot R^b_{Si:N}\right] + \left[K \cdot \frac{Si_d - Si_b}{SD}\right] + \left[\Psi \cdot \frac{Si_a - Si_b}{SD}\right] \tag{2.6}$$

$$\frac{\delta P_d}{\delta t} = +\left[DR_P \cdot M_O \cdot O\frac{SD}{DD}\right] + \left[DR_P \cdot M_D \cdot D \cdot \frac{SD}{DD}\right] - \left[K \cdot \frac{P_d - P_s}{DD}\right] + \left[\Psi \cdot \frac{f_b \cdot P_b - f_a \cdot P_d}{DD}\right] \tag{2.7}$$

$$\frac{\delta Fe_d}{\delta t} = + \left[ DR_{Fe} \cdot M_O \cdot O \frac{SD}{DD} \right] + \left[ DR_{Fe} \cdot M_D \cdot D \cdot \frac{SD}{DD} \right] - \left[ K \cdot \frac{Fe_d - Fe_s}{DD} \right] + \left[ \Psi \cdot \frac{f_b \cdot Fe_b - f_a \cdot Fe_d}{DD} \right] - [K_{sc} \cdot Fe_d] \tag{2.8}$$

$$\frac{\delta Si_d}{\delta t} = + \left[ DR_{Si} \cdot M_O \cdot O \frac{SD}{DD} \right] + \left[ DR_{Si} \cdot M_D \cdot D \cdot \frac{SD}{DD} \right] - \left[ K \cdot \frac{Si_d - Si_s}{DD} \right] + \left[ \Psi \cdot \frac{f_b \cdot Si_b - f_a \cdot Si_d}{DD} \right] \tag{2.9}$$

Nutrients in the surface boxes SO and ST ($P_a, P_b, Fe_a, Fe_b, Si_a, Si_b$) are used up by phytoplankton growth, replenished by phytoplankton mortality and redistributed by mixing and overturning circulation (Equations 2.1-2.6). In the growth terms both phytoplankton groups, diatoms and 'ordinary' phytoplankton, are given a separate maximum growth rate ($\mu_O$ and $\mu_D$) which is factored by a Michaelis-Menten term for nutrient limitation. Following Liebig's law 1840, the minimum term limits growth; although for diatoms this includes Si in addition to P and Fe. All possible return pathways of nutrients from algal matter to the bioavailable pool are simplified to a single loss term in order to remove the complexity of multiple zooplankton and detrital variables. This includes independent mortality parameters for each group ($M_O$, $M_D$) and the fraction of each nutrient remineralised in the surface ($SR_P, SR_{Fe}, SR_{Si}$). The equations for Si only require diatom growth and loss terms. Mixing is simply determined by the concentration gradient between the surface and deep boxes and a constant (K). Similarly, the overturning constant ($\Psi$) is factored by the concentration difference between the current box and the preceding box in the circulation (Figure 2.5) to represent influx and efflux. In the case of iron, additional dust terms are included (Equations 2.3 and 2.4) to represent aeolian supply from land which are necessary to maintain surface concentrations. Finally, variable Si:N ratio (Equation 2.12) is applied to the growth and loss terms for Si to represent the changing stoichiometry of diatoms.

The equations for deep nutrients (Equations 2.7-2.9) share all but the phytoplankton growth terms from the surface nutrient equations. However, in the deep box, separate remineralisation parameters ($DR_P, DR_{Fe}, DR_{Si}$) are described as the remainder of the surface remineralisation fraction; meaning that anything not recycled in the surface is returned to the nutrient pool at depth. In addition, deep Fe has a scavenging term which occurs at a constant rate ($K_{sc}$) (Parekh et al., 2004). This scavenging term represents all processes which convert soluble iron into colloidal or particulate forms and has been included due to its important impact on deep Fe concentrations (Boyd and Ellwood, 2010).

$$\frac{\delta O}{\delta t} = + \left[ \mu_O \cdot min \left( \frac{P}{P + K_P}, \frac{Fe}{Fe + K_{Fe}} \right) \cdot O \right] - [M_O \cdot O] \tag{2.10}$$

$$\frac{\delta D}{\delta t} = + \left[ \mu_D \cdot min \left( \frac{P}{P + K_P}, \frac{Fe}{Fe + K_{Fe}}, \frac{Si}{Si + K_{Si}} \right) \cdot D \right] - [M_D \cdot D] \tag{2.11}$$

The equations for phytoplankton biomass in this model (Equations 2.10 and 2.11) simply contain a growth and loss term parameterised in the same manner as those in the nutrient equations. Diatoms and other algae are the only biological components of the model acting on nutrient concentrations. The Liebig's minimum term within the phytoplankton's growth ensures that once they have used up a nutrient there is a feedback to limit their growth, which over the course of the model integration leads to a steady state.

A key theory behind the gradient of Si across the surface of the SO is the increased drawdown of Si by diatoms under iron stress. Given that the removal of Si by surface biology is assumed to be key to silicon trapping in this region, this model must include a parameterisation of this effect on diatom stoichiometry. The ratio $R^{Si:N}$ represents the Si:N uptake ratio of diatoms and in this case is formulated by a direct parameterisation shown in Equation 2.12.

$$R^{Si:N} = \frac{\left(R^{Si:N}_{max} - R^{Si:N}_{min}\right) \cdot Fe}{Fe + K^{Fe}_{Si:N}} + R^{Si:N}_{max} \tag{2.12}$$

The model using this equation, which will be referred to as "Fe-dependent", is based on available Si:N data shown in (Chapter 1), producing a specific Si:N ratio between $R^{Si:N}_{min}$ and $R^{Si:N}_{max}$ for a given iron concentration. The steepness of the rise in Si:N at low iron is governed by the parameter $K_{Si:N}$. This parameterisation is also compared in this chapter to formulations used by Holzer et al. (2019) to examine the effect of modelled diatom stoichiometry on the silicon trap. These include a hyperbolic form (HYP: Equation 2.13) and an exponential form (EXP1 and EXP2: Equation 2.14):

$$R^{Si:N} = R^{Si}_{min} + \left(R^{Si}_{max} - R^{Si}_{min}\right) \left( \frac{Si}{Si + K^{Si}_{Si:N}} \right) \left( \frac{K^{Fe}_{Si:N}}{Fe + K^{Fe}_{Si:N}} \right) \tag{2.13}$$

$$R^{Si:N} = max \left( R^{Si}_{max} \cdot \frac{Si}{Si + K^{Si}_{Si:N}} \cdot exp \left( -\frac{Fe}{X_0} \right), R^{Si}_{min} \right) \tag{2.14}$$

The model is run for 6000 years to attain a steady state with a timestep of 0.005 years or 1.83 days.

TABLE 2.1: Parameters for Si:N formulations including those from Holzer et al. (2019).

| Parameter | Fe-dependent | EXP1 | EXP2 | HYPR | Units |
|---|---|---|---|---|---|
| $X_0$ | — | 0.1 | 0.2 | — | µmol Fe $m^{-3}$ |
| $K^{Fe}_{Si:N}$ | 0.022 | — | — | 0.077 | µmol Fe $m^{-3}$ |
| $R^{Si}_{min}$ | 1 | 1.4 | 1.4 | 1.2 | (mol Si)/(mol N) |
| $R^{Si}_{max}$ | 4 | 37 | 18 | 19 | (mol Si)/(mol N) |
| $K^{Si}_{Si:N}$ | — | 3.5 | 3.3 | 4.0 | mmol Si $m^{-3}$ |

### 2.2.2 Model Parameters and Initial Conditions

Base parameters in Table 2.2 are taken from the work of Yool and Tyrrell (2003). The diatom class is differentiated not only by their reliance on silicic acid but also a higher maximum growth rate matching what was seen in the literature (Timmermans et al., 2004) and a reduced mortality due to their silica grazer protection (Pančić et al., 2019). They are given a less competitive half-saturation constant for iron representing the dominance of small non-silicified phytoplankton during non-bloom periods. The Fe scavenging rate is chosen in the range of rates that best reproduced observations in Parekh et al. (2004) and this is balanced with the half saturation for iron uptake. The parameters for the Si:N parameterisations used in these experiments are compiled in Table 2.1 while initial conditions are provided in Table 2.3.

The model was tuned by varying the aeolian iron input to the surface boxes until nutrient distribution more closely approximated that of the real system. This meant high P and Si in the SO; low iron in the SO; and highest nutrient concentrations the deep boxes.

### 2.2.3 Experiments

In this chapter, the 3BOX-SIMPLE model will be run with and without variable Si:N parameterisations and sensitivity analysis will be conducted on the parameters most relevant to silicon trapping. In order to make these comparisons and analyses a metric of silicon escape efficiency will be used. This was calculated as:

$$\frac{Overturning\ Si\ export\ from\ A}{Overturning\ input\ to\ A + Si\ mixing\ between\ A\ and\ Deep} \tag{2.15}$$

As a base run, the model will firstly be utilised with a constant 1:1 Si:N ratio to observe the Si escape efficiency and nutrient and phytoplankton distributions without the effects of a variable Si:N ratio. Two different Si:N parameterisations will then be

TABLE 2.2: Model parameters and their values.

| Symbol | Parameter | Value |
|---|---|---|
| $SD$ | depth of surface layer | 500 m |
| $DD$ | depth of deep layer | 3230 m |
| $K$ | ocean mixing coefficient | 3.5 m $yr^{-1}$ |
| $\Psi$ | overturning strength | 0.5 |
| $SR_P$ | fraction of P remineralised in surface | 95% |
| $DR_P$ | fraction of P remineralised in deep | 5% |
| $SR_S$ | fraction of Si dissolution in surface | 50% |
| $DR_S$ | fraction of Si dissolution in deep | 50% |
| $R_{org}$ | minimum Si:P ratio in organic matter | 16 |
| $\mu_O$ | maximum O growth rate | 91.25 $yr^{-1}$ |
| $\mu_D$ | maximum D growth rate | 94.9 $yr^{-1}$ |
| $K_P$ | P uptake half-saturation constant | 0.03 nmol P $m^{-3}$ |
| $K_{Fe-O}$ | Fe uptake half-saturation constant for O | 0.01 nmol Fe $m^{-3}$ |
| $K_{Fe-D}$ | Fe uptake half-saturation constant for D | 0.012 nmol Fe $m^{-3}$ |
| $K_{Si}$ | Si uptake half-saturation constant | 0.5 mmol Si $m^{-3}$ |
| $M_O$ | O mortality rate | 73 $yr^{-1}$ |
| $M_D$ | D mortality rate | 70 $yr^{-1}$ |
| $Ex_{Fe-A}$ | external Fe input into box a | 0.002 mmol $yr^{-1}$ |
| $Ex_{Fe-B}$ | external Fe input into box b | 0.0086 mmol $yr^{-1}$ |
| $K_{SC}$ | scavenging rate for Fe | 0.005 $yr^{-1}$ |
| $K_{Si:N}$ | half-saturation constant for Si:N ratio to iron curve | 0.022 µmol Fe $m^{-3}$ |

TABLE 2.3: Initial conditions for the 3BOX-SIMPLE model.

| State Variable | SO | ST | Deep | Units |
|---|---|---|---|---|
| O | 20 | 20 | ∼ | µmol N $m^{-3}$ |
| Di | 20 | 20 | ∼ | µmol N $m^{-3}$ |
| P | 0.15 | 0.15 | 1.75 | mmol $m^{-3}$ |
| Si | 2.4 | 2.4 | 112 | mmol $m^{-3}$ |
| Fe | 0.1 | 0.1 | 0.7 | µmol $m^{-3}$ |

introduced to the model: an Fe-dependent formula (Equation 2.12) and three Fe and Si-dependent parameterisations taken from Holzer et al. (2019) (Equation 2.13 and 2.14). This will enable comparison of the results of different Si:N modelling methodologies, particularly in regard to Si trapping. The effect of raising and lowering parameter values on silicon escape efficiency will then be observed for a set of important parameters under the Fe-dependent formula. These parameters include: surface dissolution fraction of silicon; initial deep silicic acid concentration; aeolian iron input; iron scavenging; maximum diatom growth rate; diatom and non-diatom iron uptake half-saturation constant; diatom mortality rate; half-saturation constant of

the silicon to nitrate ratio curve; strength of the overturning circulation; and silicic acid uptake half-saturation constant. Finally, based on the results of sensitivity testing on aeolian iron input, a further investigation was carried out on the effects of enhanced Fe fertilisation to the model equipped with different Si:N parameterisations. This included increasing aeolian input to the model and additionally limiting diatom growth in order to separate the effects of Fe-enhanced Si:N uptake ratios and Fe-enhanced diatom growth.

## 2.3 Results

The base run of the model is shown in Figure 2.3, where Si:N ratios are kept at a constant 1:1 ratio. Although this means that diatoms will uptake Si and P in the same proportion, their inventories are still differentiated by the lack of Si requirement in the other algae and separate remineralisation fractions. Model outputs for nutrients in each box are displayed in Table 2.4 in comparison to values from the literature. The base model exhibits plausible nutrient concentrations when compared to ocean data with the main exception being lower SO Si than might be expected. Most importantly, the dynamics needed to answer the questions of this chapter are present. P and Si are both high in the SO box relative to the ST box, while iron is the reverse. The deep nutrient pools have the highest concentrations except iron which is affected by scavenging. Phytoplankton production is highest in the ST box where non-diatoms contribute more, while in the SO box diatoms dominate completely (Table 2.5). The Si escape efficiency of this constant Si:N model was 0.25.

TABLE 2.4: Comparison of 3BOX-SIMPLE's steady state outputs with observations.

| State Variable | Units | 1:1 | Fe-Dependent | EXP2 | Literature | |
|---|---|---|---|---|---|---|
| SO P | mmol P $m^{-3}$ | 1.22 | 1.22 | 1.22 | 1.57 | World Ocean Atlas (Garcia et al., 2018) |
| ST P | mmol P $m^{-3}$ | 0.12 | 0.12 | 0.12 | 0.73 | |
| Deep P | mmol P $m^{-3}$ | 1.67 | 1.67 | 1.67 | 2.18 | |
| SO Si | mmol Si $m^{-3}$ | 36.8 | 1.41 | 1.41 | 34.3 | |
| ST Si | mmol Si $m^{-3}$ | 1.41 | 1.41 | 1.41 | 6.90 | |
| Deep Si | mmol Si $m^{-3}$ | 110 | 112 | 112 | 85.4 | |
| SO Fe | µmol Fe $m^{-3}$ | 0.034 | 0.040 | 0.040 | 0.05-0.2 | (Tagliabue et al., 2012) |
| ST Fe | µmol Fe $m^{-3}$ | 0.51 | 0.51 | 0.51 | 0.42 | (Schlitzer et al., 2018) |
| Deep Fe | µmol Fe $m^{-3}$ | 0.30 | 0.30 | 0.30 | 0.3-0.7 | (Tagliabue et al., 2012) |

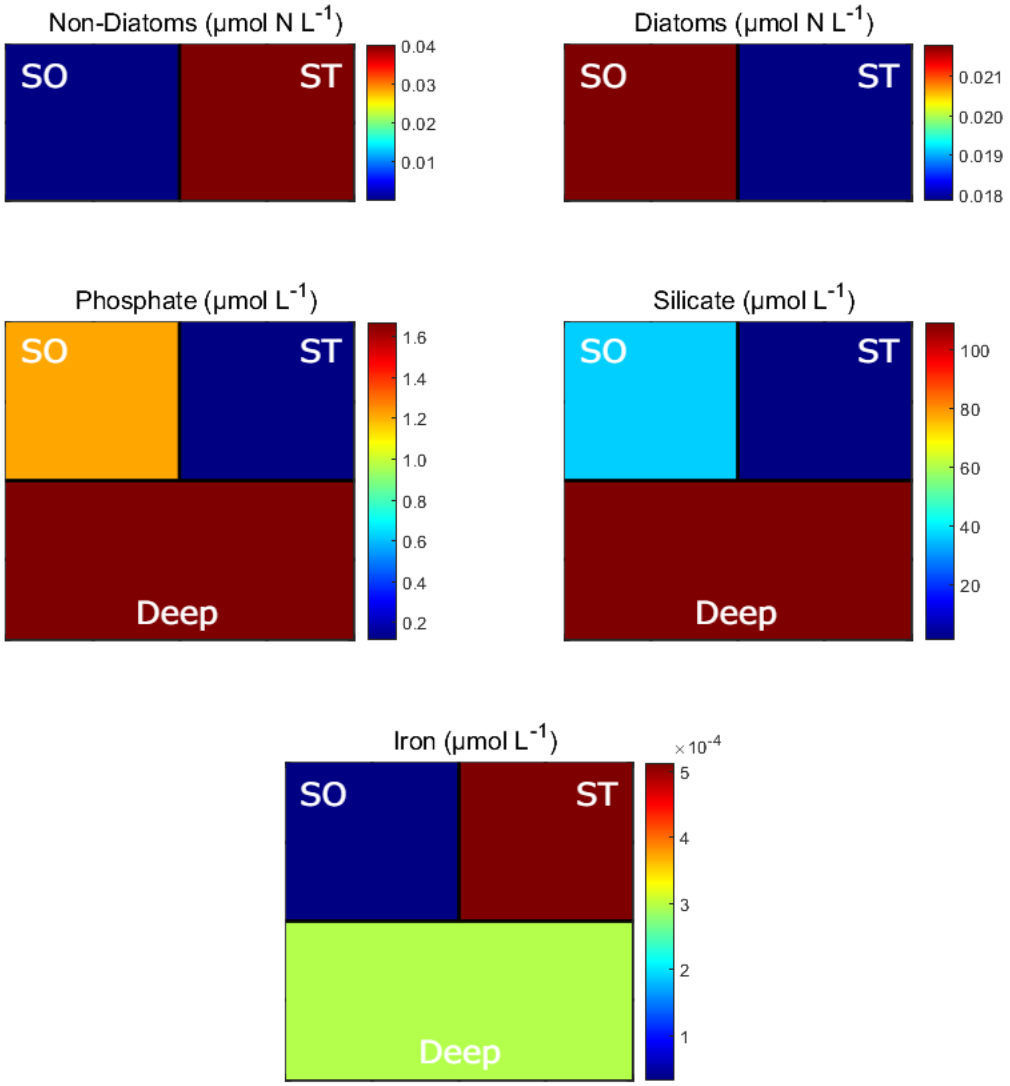


FIGURE 2.3: Distribution of state variables at steady state after the 3BOX-SIMPLE model is run with a constant 1:1 Si:N ratio. Phytoplankton are depicted solely for the surface boxes they are limited to, SO and ST, while nutrients are present in all 3 boxes. These diagrams do not represent the depth of the boxes to scale.

The model results for the addition of a variable Si:N ratio are shown in Figure 2.4. The parameterisation from Equation 2.12 allows the diatoms to vary their Si:N uptake ratio between 1:1 when iron is in abundance and 4:1 when iron is deficient. Table 2.4 shows that concentrations of P and Fe remain similarly distributed throughout the model while Si in the SO box has been diminished. In this model, phytoplankton are balanced equally between the SO and ST boxes with a decrease in diatoms in both surface boxes while non-diatoms increase by the same amount. The Si escape efficiency is reduced to 0.0084 with the inclusion of a variable Si:N parameterisation.

The sensitivity analysis presented in Figure 2.5 examines the response of Si escape efficiency to different model parameters and initial conditions. The fraction of Si remineralised in the surface boxes is set to 0.5 in the default configuration, however

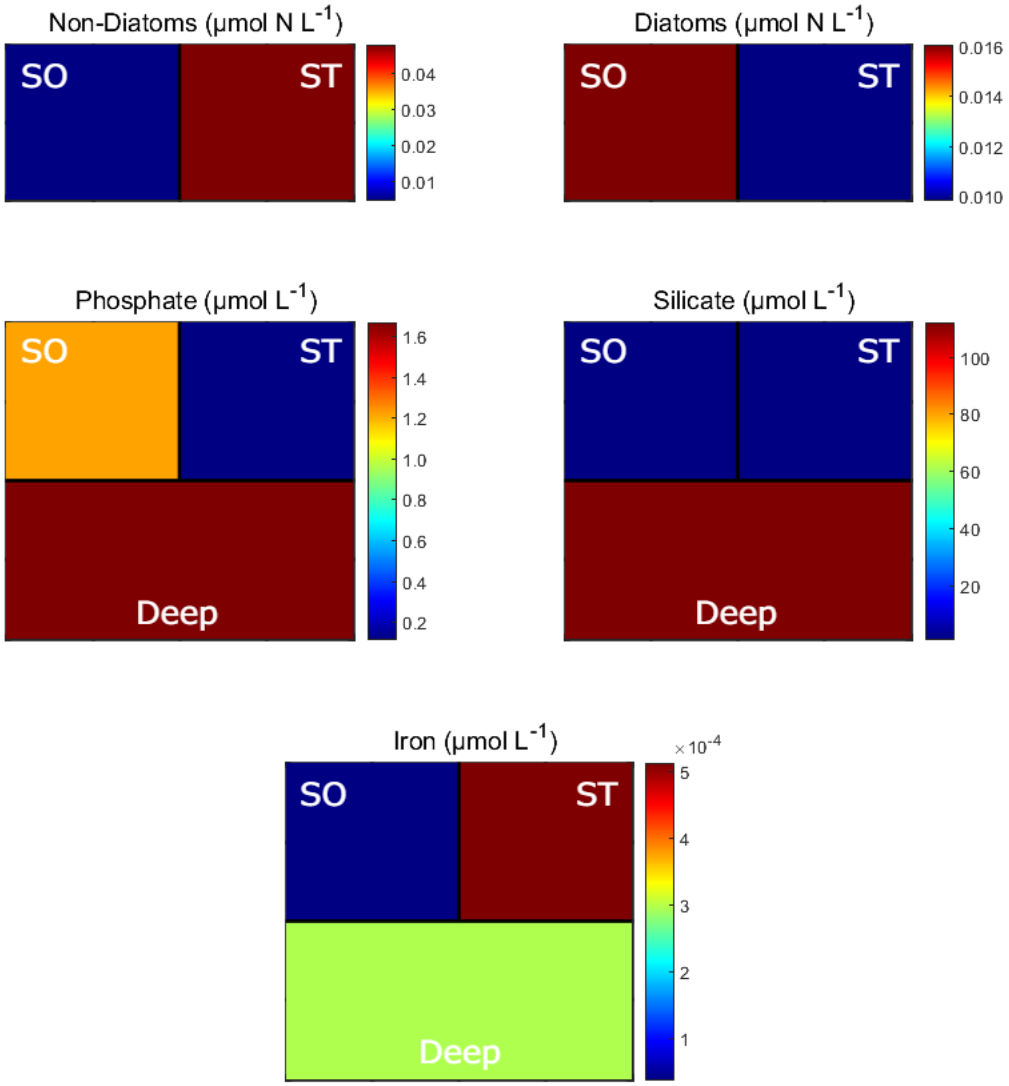


FIGURE 2.4: Distribution of state variables at steady state after the 3BOX-SIMPLE model is run with an iron dependent Si:N ratio. Phytoplankton are depicted solely for the surface boxes they are limited to, SO and ST, while nutrients are present in all 3 boxes. These diagrams do not represent the depth of the boxes to scale.

raising it above 0.7 creates a rapid increase in Si escape until there is no trapping effect. The deep box silicon concentration is initially set to 112 mmol $m^{-3}$. Removing more than 90% of this value begins to substantially remove diatoms with lack of Si. Above 179 mmol $m^{-3}$ Si escape efficiency begins to increase up to an escape efficiency of 0.12. Altering aeolian iron input yields no change within the range of -30% to +100%. Below a 40% reduction a fairly linear rise exists to complete Si leakage. Diatom $K_{Fe}$ is responsible for the steepness of the initial slope of the Michalis-Menten curve for nutrient uptake. A species with a smaller $K_{Fe}$ is better able to compete for low concentrations of Fe. The sensitivity test found that a doubling of the initial value is required to decrease Si trapping and behaved similarly to increasing $K_{sc}$. In the case where diatom maximum growth rate was altered, a 10% reduction led to complete Si

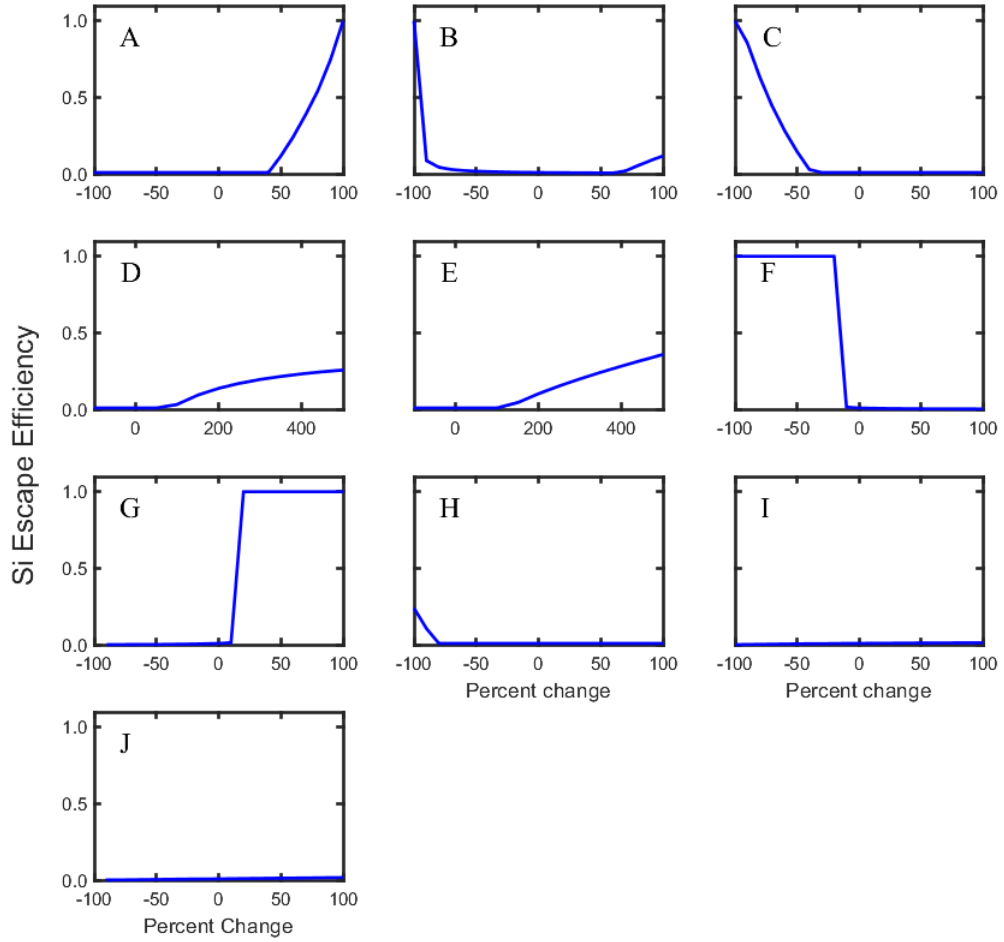


FIGURE 2.5: Sensitivity analysis of the 3BOX-SIMPLE model with a variable diatom Si:N ratio. Model parameters and initial conditions are altered to observe their effect on the efficiency of silicic acid escape from the Southern Ocean (SO). Parameters altered are (**A**) Surface dissolution fraction of silicon; (**B**) initial deep silicic acid concentration; (**C**) aeolian iron input; (**D**) iron scavenging strength; (**E**) maximum diatom growth rate; (**F**) diatom and non-diatom iron uptake half-saturation constant; (**G**) diatom mortality rate; (**H**) half-saturation constant of the silicon to nitrate ratio curve; (**I**) strength of the overturning circulation; and (**J**) silicic acid uptake half-saturation constant.

escape and this was also the case when diatom mortality is raised to 88 $yr^{-1}$ from the original value of 73 $yr^{-1}$. The degree of scavenging of iron from the deep box has no

TABLE 2.5: Phytoplankton biomass distribution in the 3BOX-SIMPLE model at steady state (nmol N $L^{-1}$).

| Phytoplankton | 1:1 | | Fe-Dependent | | EXP2 | |
|---|---|---|---|---|---|---|
| | SO | ST | SO | ST | SO | ST |
| Di | 21.8 | 17.9 | 16.1 | 9.9 | 7.5 | 7.9 |
| O | 0 | 40.3 | 5.2 | 48.1 | 13.3 | 50.0 |
| **Total** | **79.9** | | **79.2** | | **78.8** | |

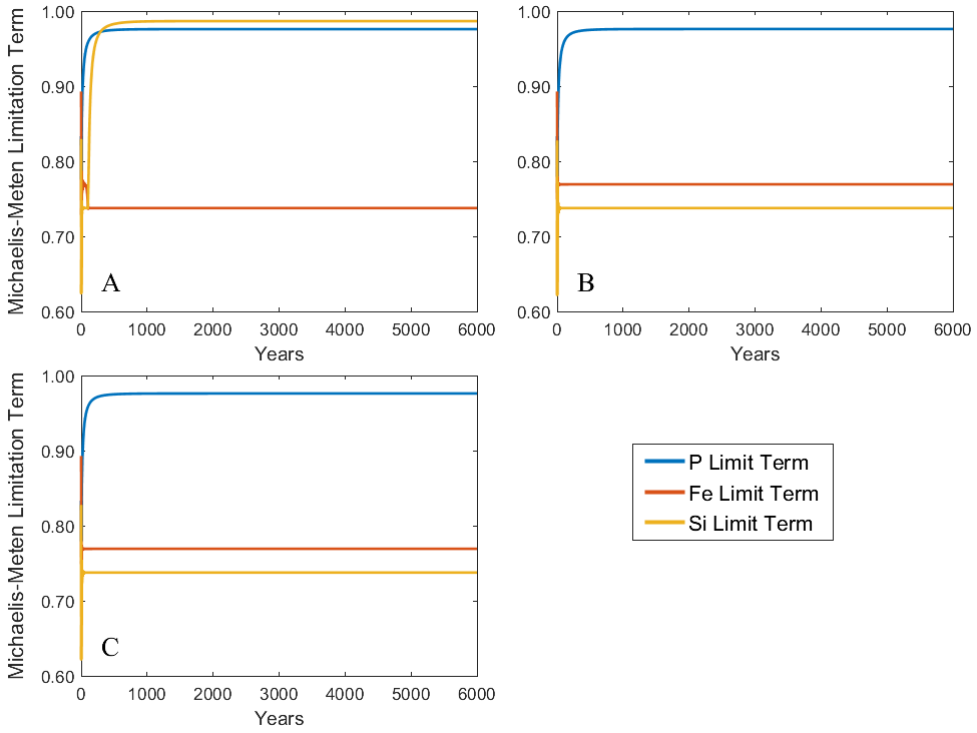


FIGURE 2.6: Michaelis-Menten limitation terms in the SO box are plotted for P, N and Si over the length of model runs using different Si:N parameterisations. These include a constant 1:1 Si:N ratio (**A**), an Fe dependent ratio (**B**) and the Fe and Si dependent EXP2 parameterisation from Holzer et al. (2019) (**C**).

appreciable effect until increased to 150% its value, above which escape efficiency rises gradually to a maximum of around 0.16. $K_{Si:N}$ represents the steepness of the increase in diatom Si:N uptake with decreasing Fe concentration. In the model, changing $K_{Si:N}$ has limited effect until reduced by 80%, below which leads to high Si:N being reached at lower Fe. Finally, diatom half saturation constant for Si uptake and strength of the overturning circulation had little to no effect on overall Si escape efficiency.

Figure 2.6 shows the Michaelis-Menten limitation terms for N, P and Si in the SO box under different Si parameterisations (Michaelis and Menten, 1913). These terms are given by the formula in Equation 2.16 where S is N, P or Si and $K_S$ is the half-saturation constant.

$$\frac{S}{S + K_S} \tag{2.16}$$

The lowest value term on the graph represents the most limiting nutrient at that point in time. It does not take long for these limitation outputs to reach a steady state. In Figure 2.6a, giving the model a constant 1:1 Si:N ratio leads to Fe limitation overall with the lowest value of 7.4 while P and Si are comparatively non-limited at around 0.98. However, in both the Fe-dependent and EXP2 parameterisations (Figure 2.6b and

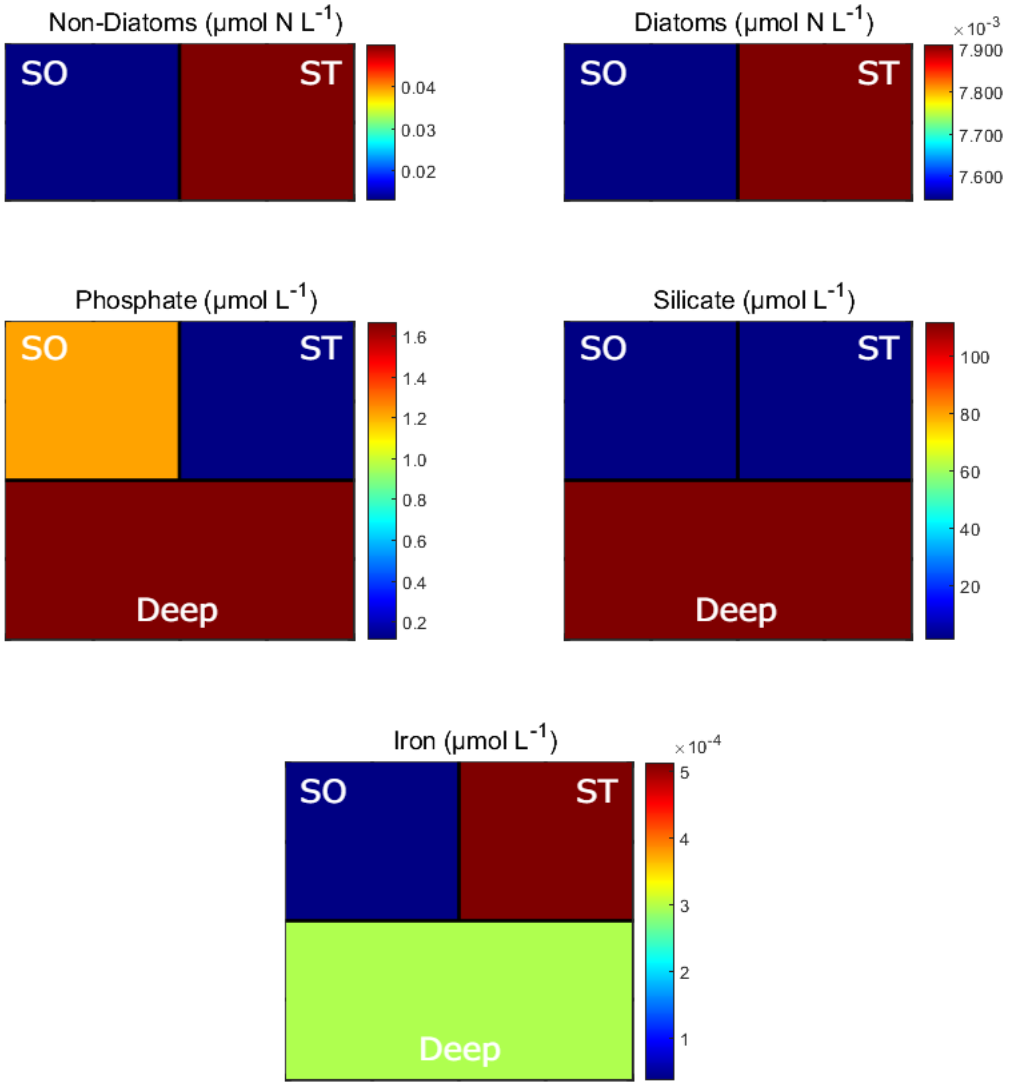


FIGURE 2.7: Distribution of state variables at steady state after 3BOX-SIMPLE is run with an Fe and Si dependent Si:N ratio (EXP2 from Holzer et al. (2019)). Phytoplankton are depicted solely for surface boxes SO and ST, while the deep box is also included for nutrients. These diagrams do not represent the depth of the boxes to scale.

c), Si limitation overtakes Fe limitation at 0.74 compared to 0.77 while P remains the same.

The results of the model paired with the EXP2 parameterisation, which characterises Si:N as Fe and Si dependent, are shown in Figure 2.7. The steady state nutrient concentrations in Table 2.4 show identical values to those of the Fe-dependent parameterisation. However, there is a large redistribution among the phytoplankton (Table 2.5) whereby SO diatoms are cut in half. The Si escape efficiency was 0.0084 as with the Fe-dependent parameterisation.

A further sensitivity analysis was performed on the response of the escape efficiency with different Si:N parameterisations to changing aeolian iron input (Figure 2.8).

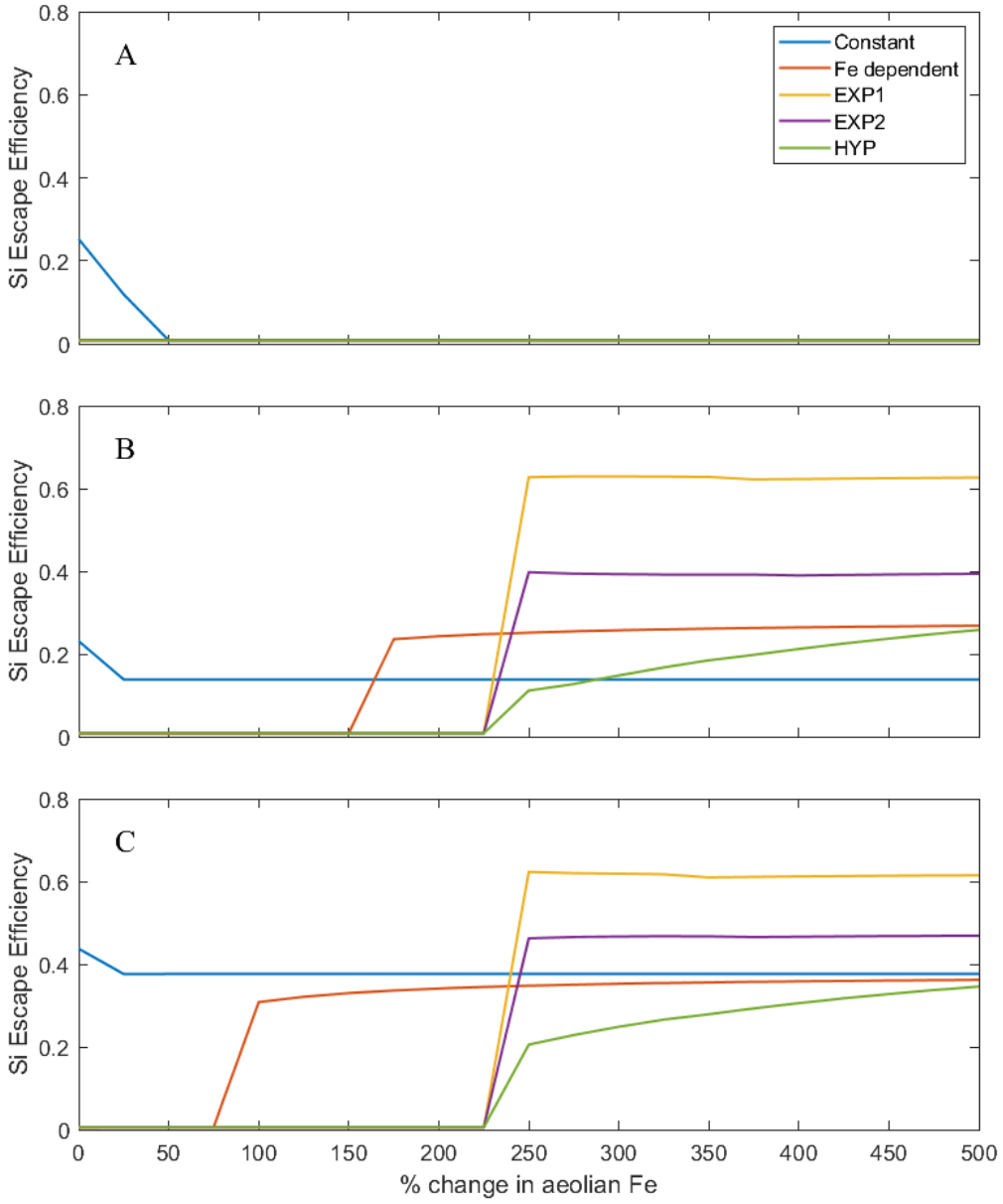


FIGURE 2.8: Si escape efficiency is plotted over changing aeolian Fe input for model simulations of different Si:N ratio parameterisations. Here, 'constant' refers to a 1:1 ratio, 'Fe dependent' is the equation constructed for this work and 'EXP1', 'EXP2', 'HYP' refer to the exponential and hyperbolic parameterisations of Holzer et al. (2019). Plot **A** shows the reaction of the model to iron addition, while **B** exhibits the same when Southern Ocean box diatoms are capped to their max population at normal iron levels. The same cap is applied to plot **C** with the addition of extra initial Si in the deep box (150%).

Initially, raising the availability of iron led to no change in Si escape efficiency for any of the Si:N parameterisations and led to a complete reduction of Si escape when a constant 1:1 Si:N was applied (Figure 2.8a). To investigate further, the response of Si:N ratios and the response of diatom growth to iron were separated. Diatom growth in the SO box was capped at its maximum value achieved for original iron levels to independently view the effect of variable Si:N ratios on Si escape efficiency (Figure 2.8b). Although artificial in the context of the current model, such a cap might be considered to represent an additional constraint not currently included within this simple formulation such as a more complex loss / grazing term and/or light limitation. Under this regime every model equipped with a variable Si:N ratio exhibits an increase in Si escape efficiency in response to increased aeolian Fe input. For the Fe-dependent parameterisation, the minimum threshold for increase is around 100% additional aeolian Fe at which point it reaches a value of 0.24 and then remains mostly static. Each of the Holzer parameterisations increase escape efficiency from a threshold of 250% extra Fe input and rise to 0.63 and 0.40 for EXP1 and EXP2 respectively while HYP shows an initial jump to 0.11 and then a gradual rise to 0.26 by 600% aeolian Fe. On the other hand, increasing aeolian Fe input still has a negative effect on escape efficiency for the model equipped with a constant 1:1 Si:N ratio, but it stabilises 0.14 Si escape efficiency. In an attempt to stimulate a response at a lower degree of Fe fertilisation, the initial deep Si concentration was raised by 50% (Figure 2.8c). This had very little effect on EXP1, but did increase the rise of Si escape efficiency observed in EXP2 and HYP at 250% extra aeolian Fe to 0.46 and 0.21 respectively with HYP reaching a new maximum escape efficiency of 0.35. The additional Si produces an earlier and greater response from the Fe-dependent parameterisation which yields an Si escape efficiency of 0.31 at 200% aeolian Fe input. The model equipped with a constant 1:1 Si:N ratio shows a higher base escape efficiency of 0.44 which descends to 0.38 at 125% of aeolian Fe input.

The changing Si:N ratio of different parameterisations in the same Fe fertilisation experiments presented above are presented with the constant 1:1 ratio from those model runs provided as reference (Figure 2.9). This shows that the EXP1 parameterisation has the highest base Si:N ratio at 7.1, followed by EXP2 and HYP at 4.4 and 4.2 respectively and finally the Fe-dependent parameterisation shows the lowest Si:N at 2.1 (Figure 2.9a). Each parameterisation begins to decline in Si:N past 225% additional aeolian Fe input. The models equipped with EXP formulas both decrease to an Si:N of 1.4 by 300% extra Fe input while HYP shows a gradual slowing decline to 1.5 at peak fertilisation. The Fe-dependent form initially descends to 1.3 at 300% extra Fe input and then gradually declines to meet the 1:1 constant. When diatom growth is capped (Figure 2.9b) a decrease in SI:N is triggered at the same threshold of fertilisation with the exception of the Fe-dependent parameterisation which now declines past 150%. Additionally, though each variable Si:N parameterisation decreases to near the same final value as the previous experiment,

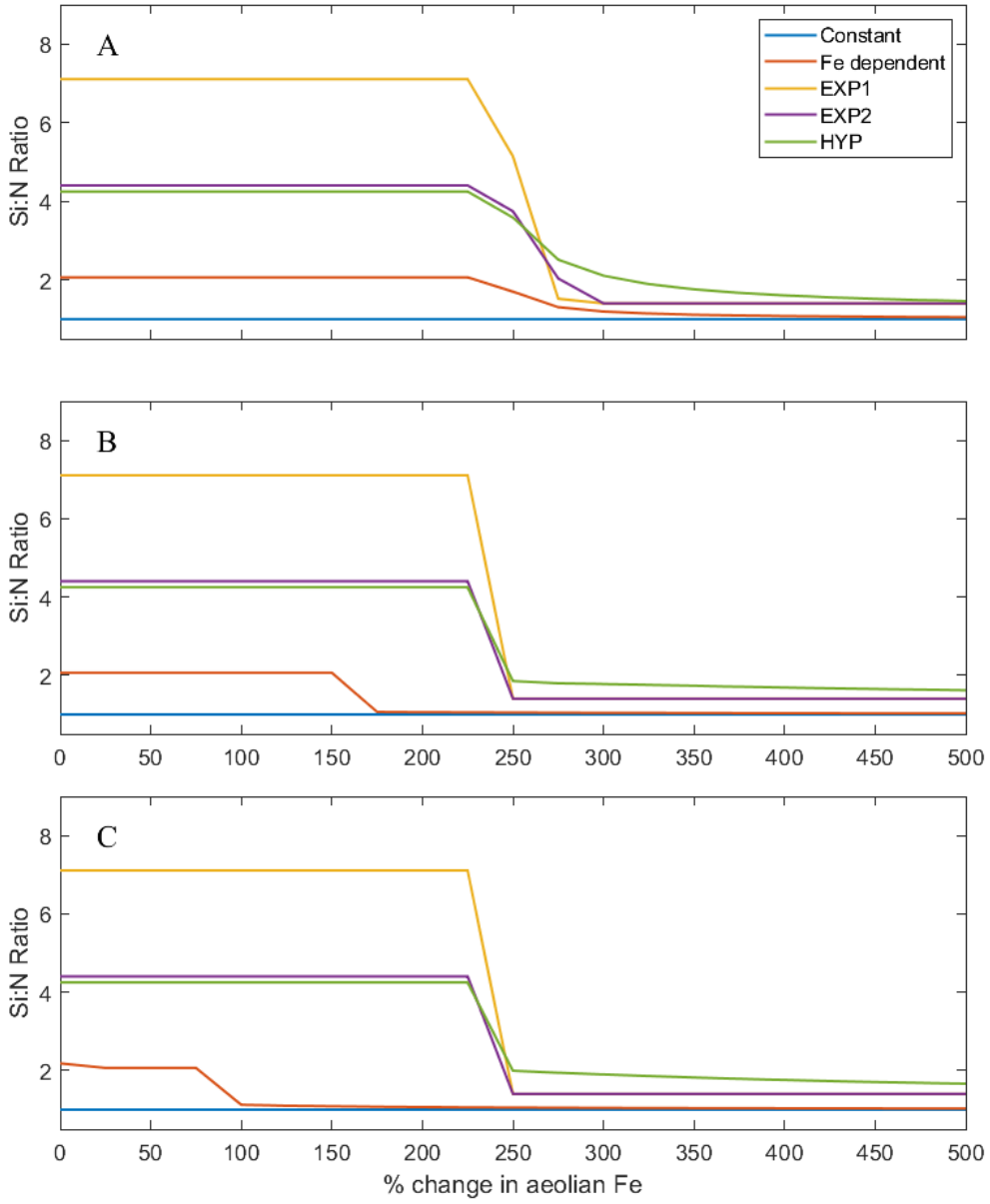


FIGURE 2.9: Diatom Si:N ratio in the SO box is plotted against changing aeolian Fe input for model simulations of different Si:N ratio parameterisations. Here, 'constant' refers to a 1:1 ratio, 'Fe dependent' is the equation constructed for this work and 'EXP1', 'EXP2', 'HYP' refer to the exponential and hyperbolic parameterisations of Holzer et al. (2019). Plot **A** shows the reaction of the model to iron addition, while **B** exhibits the same when Southern Ocean box diatoms are capped to their max population at normal iron levels. The same cap is applied to plot **C** with the addition of extra initial Si in the deep box (150%).

the decline occurs sharply within a 25% interval of aeolian Fe input (the minimum interval of the experiment). Finally, when diatom growth is capped and an additional 50% of extra initial Si is added to the deep box (Figure 2.9c), there is no change except for the further decrease in the threshold for Si:N drop-off in the Fe-dependent run which now begins at 100% additional aeolian Fe.

## 2.4 Discussion

In this chapter, a simple 3-box model approach (3BOX-SIMPLE) was used to investigate Southern Ocean Si trapping especially focusing on the effect of variable Si:N parameterisations. To the author's knowledge this is the first time variable diatom Si:N ratios have been incorporated into a box model framework. The benefits of using this tool include extremely rapid run times (4.56 s) for fast sensitivity and scenario testing. The 3-box design including a deep box and Sothern Ocean and Subtropical surface boxes (Weber and Deutsch, 2010) captures the upper limb of SO circulation: the upwelling of Circumpolar Deep Water, northward flow across the surface, and subsequent formation and subduction of mode waters (Talley, 2013). In this case, the return of nutrients from the ST box to the deep is an idealised view of the formation of North Atlantic Deep Water.

The first run of the model with a constant 1:1 Si:N ratio was performed as a baseline from which to check parameter settings and to compare against variable Si:N runs. The results of this run (Figure 2.3) agree reasonably well with observations (Table 2.4). The important divisions this model attempts to capture are the deep reservoirs of nutrients that are upwelled to the SO; the SO surface where iron availability prevents full utilisation of those nutrients (a "missed opportunity" for the biological pump (Primeau et al., 2013)); and the ST surface where sufficient iron leads to complete removal of macronutrients in the surface and N or NP co-limitation forms (Moore, Mills, Arrigo, Berman-Frank, Bopp, Boyd, Galbraith, Geider, Guieu, Jaccard, Jickells, La Roche, Lenton, Mahowald, Marañón, Marinov, Moore, Nakatsuka, Oschlies, Saito, Thingstad, Tsuda and Ulloa, 2013). This model run distributes the highest P and Si concentrations to the deep box, leaves fairly replete residual levels in the SO and leaves the ST box macro-nutrient depleted. The scarcity of Fe in the SO results from both the lower aeolian dust forcing and also the removal of Fe from deep waters by scavenging before it can upwell (Parekh et al., 2004; Moore, 2016). Deep Fe is close to that found for the deep SO and Indo-Pacific in the global iron cycle model of Parekh et al. (2004) for the same $K_{sc}$. In the SO box diatoms dominate non-diatoms completely while in the ST non-diatoms perform better. The diatoms outcompete in the SO because they have been given a competitive advantage with a higher maximum growth rate (Furnas, 1990) and a lower mortality on the assumption that their silica

tests offer enhanced grazer protection (Hamm et al., 2003). However, in the ST box diatoms become limited by Si availability and non-diatoms are able to succeed.

After the model was shown to compare reasonably with observations, a variable Si:N ratio was added to the diatoms. This raises their Si:N uptake ratio with decreasing Fe concentration from 1:1 up to a maximum of 4:1. Comparing Figure 2.3 to Figure 2.4 shows that this addition has little to no effect on P and Fe distribution in the model. However, Si in the SO box is almost fully depleted to 1.4 mmol $m^{-3}$ compared to the previous value of 30.6 mmol $m^{-3}$. This is a consequence of the Si:N ratio rising to 2.1 in the SO leading the diatoms to draw down double the Si per mol N (i.e. equivalently 2.1 x 16 = 33.6 mol Si per mol P) that they were previously. Obviously, to say the Southern Ocean surface is low in Si is counter-intuitive considering it is clearly defined as a high macronutrient region. However, the scale of this model is insufficient to capture the gradient of Si from the point of upwelling in the Antarctic Zone to the mode water formation areas of the Polar Frontal Zone (PFZ) and Subantarctic Zone (SAZ). Therefore, with the simple configuration adopted, the SO box of this model can simultaneously be considered the region of upwelling and of depletion of the Si transported from the SO to the ST box, i.e. representative of what is exported in the northward flowing intermediate and mode waters.

The low SO Si in this model run is reasonable compared to PFZ/SAZ observations of $<$10 mmol $m^{-3}$ (Garcia et al., 2018). Steady state diatom biomass is reduced in both surface boxes by a combination of increased Si requirement in the SO box and subsequent lack of transport into the ST. This benefits non-diatoms which gain the losses incurred by the diatoms. The inclusion of the variable Si:N (or effectively P) ratio only marginally lowers the total surface phytoplankton biomass. In order to measure Si trapping in the two models, the metric of Si escape efficiency is used to describe the amount of Si leaving the SO box compared to that which enters it. The introduction of variable Si:N reduces Si escape efficiency from 0.2 to 0.01. Considering an Si escape efficiency of 1 represents all Si entering the SO box escapes to the ST, the variable Si:N model run shows almost complete trapping of Si in the SO. This is unsurprising considering, as stated previously, the iron deficiency present there causes diatoms to uptake double the Si per mol of N. The Si escape efficiency measured here is on the same scale as that found by Holzer et al. (2014) who calculated that Si last utilised in the SO only had a (5±2)% chance of next being utilised outside the SO.

Changing relevant parameter values and initial conditions can effect silicon trapping in the variable Si:N model (Figure 2.5). The $SR_s$ or surface dissolution fraction of Si is the portion of Si in dead diatoms that is recycled in the surface boxes rather than the deep. Si trapping appears to be fairly stable to $SR_s$ with a 40% increase required to yield a rapid rise in Si leakage due a reduced export flux from the SO (Figure 2.5a). In an Fe limited SO, it would be predicted that any additional Si made available would be able to leak as diatoms are unable to take up more. Upon inspection, while the

constant Si:N model is Fe limited in the SO box (Figure 2.6a), the addition of variable Si:N causes Si limitation to overtake (Figure 2.6b, 2.6c). This creates a buffer, whereby any additional Si available can initially be used by diatoms before Fe then becomes limiting. Si trapping also appears to be stable to the initial deep Si concentration, deviating only at around ±60% (Figure 2.5b). Below this value, upwelling of Si becomes too low, while above, upwelling Si overcomes limitation and escapes the SO. However, these ranges produce unrealistic deep Si concentrations.

Varying aeolian iron input creates little effect above -40%. Minimising Fe this far limits diatom growth to the point of Si leakage. As Fe fertilisation is hypothesised by some to reduce Si trapping due to reduced Si:N uptake ratio (Martin, 1990; Petit et al., 1999; Brzezinski et al., 2002; Matsumoto et al., 2002), it might be expected this would appear at higher percentages in Figure 2.5c. One possibility is that the additional Si uptake caused by intensified diatom growth has outstripped the reduction in Si uptake stemming from a lower S:N ratio. This will be explored further below. Fe upwelling to the SO box responds linearly to dust input.

Fe scavenging and the Fe half-saturation constants for phytoplankton are both key controls on Fe distribution within the model, and their similar trajectories in Figures 2.5e and 2.5f show that they are well connected. Scavenging acts in the deep box model to remove Fe making it less available for upwelling to the SO box (Fig 2.5D). Eventually this reduces diatom growth to the point of overcoming the effect of increased Si:N and yields Si leakage. If altered individually, a threshold change occurs if the diatom half-saturation constant for Fe is allowed to decline to the point of complete non-diatom control of the Fe-supply. However, Figure 2.5e instead displays the outcome if the half-saturation for Fe is altered for all phytoplankton. In this case, Si leakage gradually increases from double the original value onward because their rate of uptake for low concentrations of Fe is reduced. Increasing either $K_{sc}$ or $K_{Fe}$ independently is a sure way of provoking Si leakage. However, maintaining the Fe cycle of a model requires achieving balance between Fe uptake by phytoplankton governed by phytoplankton and scavenging, with complexing by ligands and other unrepresented aspects of the Fe cycle potentially adding further complexity. In this case, Si trapping is stable to ±100% of either parameter.

It is evident in Figures 2.5f and 2.5g that both parameters react in a threshold manner to allow complete Si escape. This is because each of these parameters control diatom net growth: diatom maximum growth rate ($\mu_D$) and diatom mortality rate ($M_D$). Adjusting either to the point of making diatoms weaker than non-diatoms in the SO allows the other phytoplankton to dominate and ends Si trapping. Finally, the half-saturation constant for Si:N, overturning circulation strength, and Si half-saturation constant all yield little to no change in Si trapping. Though they might be expected to increase Fe or Si in the SO box, these parameters are likely overcome by the action of diatoms with high Si:N.

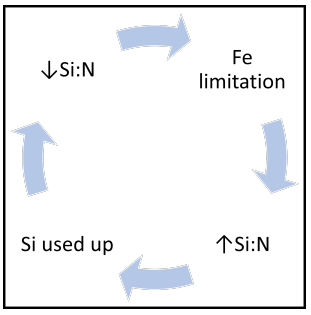


FIGURE 2.10: A diagram to describe the feedback imposed by an Si:N parameterisation that is dependent upon both Fe and Si concentration. Fe limitation causes raised Si:N uptake ratios in diatoms, which leads to enhanced Si drawdown in the mode / intermediate water formation zone. Depending on the initial availability of Si, concentrations could become low enough to become limiting or reduce the Si:N ratio. In this case, Si deficiency would be alleviated and iron would once again become limiting.

As seen in Figure 2.6b, the inclusion of an Fe-dependent Si:N parameterisation causes the SO to become Si rather than Fe limited. It proves very difficult to produce the observed Fe limited state (Moore, Mills, Arrigo, Berman-Frank, Bopp, Boyd, Galbraith, Geider, Guieu, Jaccard, Jickells, La Roche, Lenton, Mahowald, Marañón, Marinov, Moore, Nakatsuka, Oschlies, Saito, Thingstad, Tsuda and Ulloa, 2013) by limiting Fe supply via reduced aeolian input and initial deep Fe or increased scavenging. This is because lowering available Fe to promote limitation simultaneously has the effect of raising Si:N and therefore further reducing Si and driving the diatoms towards Si limitation. This is a limitation of a solely Fe-dependent parameterisation for a variable Si:N uptake ratio. In contrast, if Si:N is a balance of Si uptake rate and N uptake rate (Marchetti and Harrison, 2007) then low Si conditions should also cause Si:N to decrease per Michaelis-Menten kinetics (Leynaert et al., 2004). This can be tested by switching to an Fe and Si dependent Si:N parameterisation, in this case an exponential relationship (EXP2) proposed by Holzer et al. (2019). However, Figure 2.6c shows that this parameterisation also leads to the same state of Si limitation in the SO surface. This can also be observed in the identical steady state nutrient distribution observed in Figure 2.7. The implication of the same result being produced despite the inclusion of Si dependency in the parameterisation is that Si:N has not been sufficiently decreased to prevent diatoms from stripping the Si from the surface before it can escape to the ST. In this model, with its base parameter set, Si can barely escape the SO.

Parameterisations that decrease Si:N due to Si deficiency create a buffer at low Si concentrations because they directly relate Si concentration to diatom Si:N uptake ratio. A feedback loop could emerge whereby low Si triggers a decrease in Si:N uptake ratio which in turn forces diatoms to take up less Si thereby increasing Si concentration and raising Si:N which returns the system to Si deficiency (Figure 2.10). Therefore the parameterisation may determine the lower limit of Si achievable in the model.

After testing the model's ability to replicate present day conditions, different

parameterisations were experimented with under Fe fertilisation (Figure 2.8). During past glacial intervals Fe fertilisation may have occurred due to atmospheric dust flux to Antarctica up to 50 times greater (Angelis et al., 1987; Lambert et al., 2008). Increased aeolian Fe input has been one method by which scientists have sought to explain lower $CO_2$ concentrations during glacial periods. In addition, changes to the marine calcium carbonate budget are thought necessary to achieve this (Sigman and Boyle, 2000). The Silicic Acid Leakage Hypothesis (SALH) proposed that decreased diatom Si:N ratios in response to the extra iron could have allowed more Si to escape the SO, triggering a floristic shift to diatoms over calcifying phytoplankton (Matsumoto et al., 2002). The reduction in carbonate burial resulting from decreased export raised ocean alkalinity allowing greater $CO_2$ uptake by the oceans. Competing theories exist as to the extent diatom Si:N was involved in increased Si supply to lower latitudes (Harrison, 2000; Hendry and Brzezinski, 2014; Matsumoto et al., 2014), and therefore, modelling is an important tool to investigate the effects of Fe fertilisation on the SO.

The effect of fertilisation on the current model acts to either maintain or create the highest possible Si trapping (Figure 2.8a). Where it would be expected that increased Fe availability would lead to lower a Si:N and therefore allow Si to escape, no increase in escape efficiency is observed whatsoever. Figure 2.9a shows that every parameterisation exhibits a decrease in Si:N after just over a doubling of Fe input, but this yields no increase in Si leakage. One explanation for this could be that increased diatom productivity and nutrient utilisation due to fertilisation exceeds the gain of Si from lower Si:N. In Figure 2.8b this hypothesis is tested by capping diatom growth in the SO box to that which existed at the original aeolian Fe level. A rise in Si escape efficiency is seen that corresponds exactly to the decrease in Si:N in each variable Si:N parameterisation (Figure 2.9b), while the 1:1 Si:N ratio exhibits a slight decline before stabilising presumably due to the uncapped diatoms in the ST box. This shows increased diatom uptake due to relief of Fe limitation has indeed overcome the effect of a lower Si:N. Figure 2.8c shows the effect of rising Fe input when SO diatoms are capped and initial deep Si is raised by 50%. Although the parameterisations from (Holzer et al., 2019) are dependent on both Fe and Si concentrations, the addition of extra Si upwelling in the SO box does not lead to a further decrease in Si:N at high Fe fertilisation. Therefore, the higher Si escape efficiency observed for some parameterisations is purely a function of more Si upwelling equalling more Si leakage. It should be noted that the thresholds of aeolian Fe that these changes occur at are arbitrary due to the capping of diatom growth.

## 2.5 Conclusions

A simple 3-box model (3BOX-SIMPLE) to represent Southern Hemisphere meridional circulation was constructed and was able to reasonably replicate observed nutrient concentrations for P, Fe and Si and recreate expected distributions of diatoms versus non-diatoms. The addition of an Fe-dependent diatom Si:N ratio created near complete Si trapping, drawing down Si to the extent of establishing Si limitation in the SO box. In general, many parameters and initial conditions needed to be pushed to extremes in order to generate Si leakage. Alternatively, removing the competitiveness of diatoms against non-diatoms allowed a complete floristic shift and total Si escape from the SO. Si limitation in the SO box was difficult to alleviate as removing Fe to make it limiting raised Si:N which further removed Si. The use of an Fe and Si dependent parameterisation, EXP2 (Holzer et al., 2019) allowed adjustment of the Si:N ratio based on Si deficiency but yielded no increase in Si escape efficiency and retained Si as the limiting nutrient in the SO box. However, Si dependent parameterisations place a lower limit on the Si concentration of the system.

An Fe fertilisation experiment was conducted by increasing the aeolian iron input to the model by up to 500%. This yielded no change or an increase in Si trapping, which was due to the added Fe enhancing diatom growth and therefore Si uptake to the point of surpassing the Si gain from a reduced Si:N ratio. Consequently, the currently configured model using any of the Si:N parameterisations disagrees with the SALH, which posits reduced Si:N due to fertilisation should yield Si leakage (Matsumoto et al., 2002). However, the work reinforces how different parameterisations of the Fe and Si dependencies of Si:N uptake can lead to different levels of Si trapping and, in the absence of increased diatom growth, for example due to other constraining factors, would result in different responses to Fe fertilisation (Holzer et al., 2019).

The simplicity of this approach makes these results faster and easier to interpret but does yield limitations in exploring the whole SO system. The SO is characterised as one homogenous box within the model, but in reality is divided by the decreasing gradient of Si from the Antarctic Zone to the Polar Frontal Zone, as well as by the species composition and growth strategies of diatoms (Assmy et al., 2013) and other ecosystem processes. As the silicifying phytoplankton, diatom dominance establishes the degree to which enhanced Si:N is applied. It is possible that a more complex model might have more flexibility in responding to perturbations under different Si:N parameterisations. Nevertheless, this investigation shows the far reaching and perhaps unexpected consequences of Si:N parameterisation choice that can be caused by the feedback mechanisms inherent in tying Fe availability and Si uptake by diatoms together.

# Chapter 3

# A physiological approach to parameterising Diatom Si upregulation using a quota model to reproduce nutrient addition experiments in the Southern Ocean

This chapter contains data collected by colleagues on the DY111 cruise of the RRS Discovery. They conducted factorial nutrient addition experiments on deck which are interpreted and modelled herein. Their paper on this topic is referenced here:

*Wyatt, N.J., Birchill, A., Ussher, S., Milne, A., Bouman, H.A., Shoenfelt Troein, E., Pabortsava, K., Wright, A., Flanagan, O., Bibby, T.S. and Martin, A., 2023. Phytoplankton responses to dust addition in the Fe–Mn co-limited eastern Pacific sub-Antarctic differ by source region. Proceedings of the National Academy of Sciences, 120(28).*

## 3.1 Introduction

As discussed in Chapters 1 and 2, diatom physiology is important in understanding the distribution of nutrients in the Southern Ocean (SO) due to their impact on surface stoichiometry of macronutrients including N, P and Si, which moreover can vary under iron stress. Because this transformation occurs in a hub of mode water formation, these changes ripple outward to the rest of the ocean (Sarmiento et al.,

2004). As phytoplankton respond rapidly to environmental forcing, future changes to the Southern Ocean may thus have far reaching connotations.

A 2019 study by Holzer et al. used a data constrained model to investigate how different parameterisations of the Fe dependence of diatom Si:P respond to Fe fertilisation. Parameterisations with an exponential functional form for the Fe to Si:P relationship increased Si leakage from the Southern Ocean whereas an alternative hyperbolic form led to strengthened Si trapping as diatom Si:P did not decline sharply enough with increasing Fe availability to counteract enhanced diatom growth. Detailed understanding of the mechanisms of SO Si trapping alongside accurate predictions of the impacts of climate change for the future of our oceans thus likely require the correct formulation of the Si:N:P Fe dependence.

In December of 2019, the *RRS Discovery* ventured just west of the southerly tip of Chile (Figure 3.1) to investigate upper ocean biogeochemistry as a component of the Carbon Uptake and Seasonal Traits in Antarctic Remineralisation Depth (CUSTARD) programme. During this cruise factorial nutrient addition experiments were conducted with incubated water samples to assess how the provision of a range of nutrients including Si, Fe and Mn, both separately and in combination, influenced phytoplankton physiology, growth and nutrient uptake ratios. A smaller set of experiments where a gradient of Si was provided either with or without the addition of Fe were also undertaken. This experimental data set provides the opportunity to address Si:N parameterisation at the experimental level for future expansion to general circulation models (GCM). In this chapter, models are fit to the CUSTARD experimental data, which offers a controlled and rigorous testing environment for parameterisations, serving in contrast to previous studies that have been tested only against coarse scale ocean observations.

The first model used to fit the CUSTARD data was a simple formulation adapted from Yool and Tyrrell (2003) which represents phytoplankton growth as a function of external nutrient concentrations and in this case assumes diatoms dominate sufficiently to ignore other phytoplankton groups. Direct parameterisations are then added to this model to create an Si:N ratio that responds to Fe availability (Holzer et al., 2019) This model was named CUSTARD-SIMPLE. A quota model approach (CUSTARD-QUOTA) (Droop, 1983; Geider et al., 1998; Buitenhuis and Geider, 2010) is then employed as a more mechanistic and physiologically based consideration which represents both external and intracellular nutrient concentrations. Finally, the CUSTARD-QUOTA model is expanded to include diatoms and a non-silicified 'other' phytoplankton as two separate groups. This final novel model's ability to represent intracellular ratios makes it a more versatile tool and hence potentially a better fit for

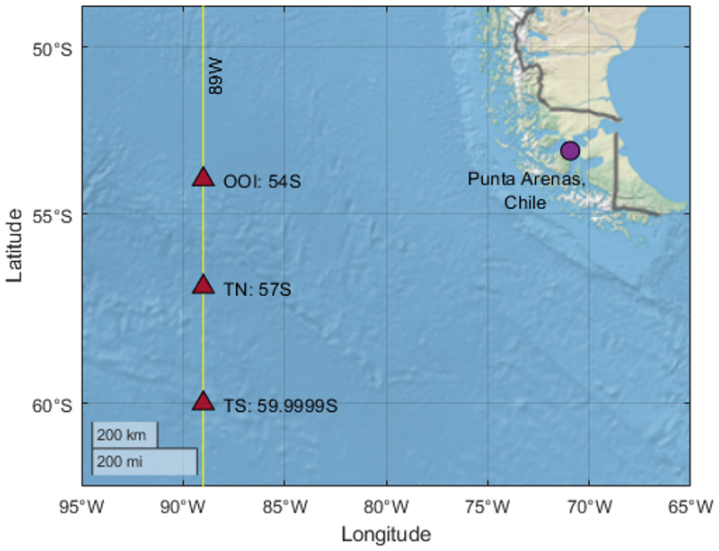


FIGURE 3.1: The cruise transect and key sampling stations including the site of the Ocean Observative Initiative (OOI) data buoy.

the SO environment where diatom Si:N ratios are a crucial part of the system (Brzezinski, 1985; Takeda, 1998; De La Rocha et al., 2000; Brzezinski et al., 2003; Timmermans et al., 2004; Hoffmann et al., 2007). Within the CUSTARD-QUOTA model, no direct parameterisation is applied but rather the Si:N ratio is left to arise implicitly from the model structure. To our knowledge, this is the first time a multi-element quota model has been developed and tuned to experimental data collected on natural phytoplankton communities.

## 3.2 Methods

### 3.2.1 CUSTARD Dataset

The data against which to fit and calibrate the models was obtained from the DY111 cruise of the CUSTARD project (Carbon Uptake and Seasonal Traits in Antarctic Remineralisation Depth) which lasted from the 2nd of December 2019 to the 9th of January 2020. This cruise sampled a latitudinal transect along 89° W comprised of three main stations: the Ocean Observative Initiative (OOI) data buoy at 54° S; 'Transect North' (TN) at 57° S; and 'Transect South' (TS) at 59.99° S (Figure 3.1).

Of interest to this study were two designs of factorial nutrient addition experiments conducted across the transect and the time period of the cruise that sought to assess changes in community physiology, elemental stoichiometry and nutrient limitation. Firstly, seven 'large-type' experiments (LTE) were performed at the locations and dates

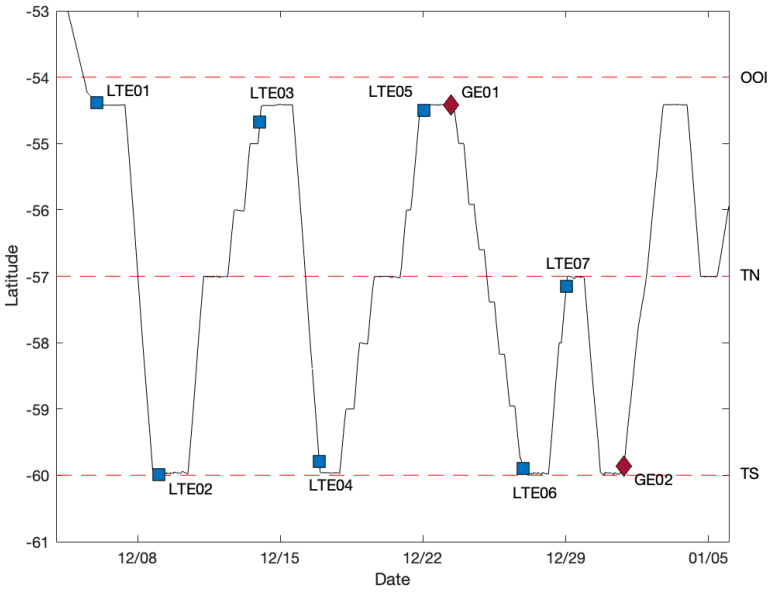


FIGURE 3.2: The distribution of factorial nutrient addition experiments during the CUSTARD cruise. This included 7 'large-type' experiments (LTE) and 2 gradient experiments (GE) distributed between 3 sampling locations: OOI, TN and TS.

shown in Figure 3.2. Surface seawater samples (2-3m) were collected with a Teflon diaphragm pump connected to a towed "Fish" sampler. For each treatment, triplicate water samples were passed unfiltered into 4 L acid-washed polycarbonate bottles in a clean air laboratory. These bottles were filled halfway in random order and then filled to to total volume again in random order. Prior to any nutrient amendment, initial measurements of chlorophyll-a, macronutrients and photophysiology were made. With the exception of three unamended controls, bottles were spiked with 2 nM Fe, 2 nM Mn and 5 µM Si in factorial combinations. The preparation of nutrient additions is further described in Wyatt et al. (2023). Following nutrient amendment, the bottles were parafilm-sealed and then placed into a temperature-controlled incubation container set to approximately local sea surface temperature (5.5 - 6.5 °C). The bottle shelves were surrounded by light banks with ∼200 µmol photons $m^{-2}$ $s^{-1}$ irradiance and set to a local day/night cycle of 6 h dark and 18 h light. After day 2 and day 6, sub-samples were taken in the clean air laboratory for the analysis of chlorophyll, macronutrients, photophysiology, biogenic silica and HPLC pigment analysis. Further detail of how these measurements were made can be found in Wyatt et al. (2023). Additionally, two gradient experiments (GE) were completed on smaller 125 ml samples using a progression of Si amendments up to 80 µM which were performed in duplicate under low and high iron availability treatments (0 and 2 nM added).

Monitoring of dissolved inorganic nitrogen (DIN: nitrate plus nitrite) and Si concentrations over time in the closed system of the experiments enabled calculation

of uptake over the course of the incubation (ΔDIN and ΔSi). ΔSi:ΔDIN was used to to compare the model against observations.

On the cruise, Fast Repetition Rate fluorimetry (FRRf) was used to measure the changing photophysiology of phytoplankton within the incubation bottles over the course of the experiments. This technique uses a a sequence of excitation flashlets to cumulatively saturate photosystem II (PSII). The fluorometer measures the curve of fluorescence produced as chlorophyll-a absorbs light at a shorter wavelength and emits it at a higher wavelength. Fluorescence continues to increase in response to the excitation flashlets until the light-harvesting antenna become saturated. From this measurement one can derive values of the minimum and maximum fluorescence ($F_o$ and $F_m$, respectively) and calculate the apparent photochemical efficiency of PSII, $F_v/F_m$ (where $F_v = F_m - F_o$) (Kolber et al., 1998). $F_v/F_m$ has been shown to relate to nutrient stress in phytoplankton and the provision of nutrients to nutrient-limited can elevate their $F_v/F_m$ measurement (Parkhill et al., 2001). On this cruise, variable chlorophyll fluorescence was measured using a Chelsea Scientific Instruments FastrackaTM Mk II Fast Repetition Rate fluorimeter integrated with a FastActTM laboratory system suplied with 125 mL samples that were dark-acclimated for 30 minutes. One again further details can be found in Wyatt et al. (2023).

### 3.2.2 CUSTARD-SIMPLE Model

The first model used in this study is a simplified version of the formulations found in Yool and Tyrrell (2003). Diatoms (D) are assumed to be the dominant phytoplankton type and therefore the only algae included to simplify the model. Their growth is determined by the availability of four nutrient variables including the main factorial additions in the CUSTARD long-term incubation experiments: nitrogen (N), iron (Fe), silicon (Si) and manganese (Mn). Phytoplankton are expressed in terms of mol N $m^{-3}$ and later converted to Chlorophyll for comparison to observations by use of chlorophyll to N ratios measured during each experiment.

$$\frac{\delta D}{\delta t} = + \left[ \mu_D \cdot min \left( \frac{N}{N + K_N}, \frac{Fe}{Fe + K_{Fe}}, \frac{Si}{Si + K_{Si}}, \frac{Mn}{Mn + K_{Mn}} \right) \cdot D \right] - [M \cdot D] \quad (3.1)$$

$$\frac{\delta X}{\delta t} = - \left[ \mu_D \cdot min \left( \frac{N}{N + K_N}, \frac{Fe}{Fe + K_{Fe}}, \frac{Si}{Si + K_{Si}}, \frac{Mn}{Mn + K_{Mn}} \right) \cdot D \right] + [M \cdot D] \quad (3.2)$$

$$\frac{\delta Si}{\delta t} = - \left[ \mu_D \cdot min \left( \frac{N}{N + K_N}, \frac{Fe}{Fe + K_{Fe}}, \frac{Si}{Si + K_{Si}}, \frac{Mn}{Mn + K_{Mn}} \right) \cdot D \cdot R^{Si:N} \right] + [M \cdot D] \quad (3.3)$$

The growth component of the diatom equation is comprised of a maximum growth rate term ($\mu_D$) and a Liebig's Law 1840 term where the minimum Michaelis-Menten term (minimisation term inside square brackets in Equations 3.1-3.3) is the growth limiting nutrient. Rather than explicitly including all possible means of diatom loss such as grazing, viruses and sinking, a single mortality term is used which depletes a constant fraction of the diatom pool at every timestep. In fact, mortality was later set to zero as it is assumed this had a minimal impact in the low volume and short time period of the experimental setup. In this model, the general nutrient equations (X) are simply the inverse of that for diatoms; nutrients are lost from their pool by diatom growth and gained by diatom mortality. Terms for mixing, riverine input and deep remineralisation considered in the box-model of Yool and Tyrrell (2003) are removed as these equations now represent the dynamics of an incubation bottle rather than the ocean. In the case of Si, an extra ratio is factored into the growth term to enact the effect of variable diatom Si:N uptake ratios explored in the introduction. The direct parameterisations tested on this model include a hyperbolic form (HYP) and an exponential form (EXP1 and EXP2):

$$R^{Si:N} = R^{Si}_{min} + \left(R^{Si}_{max} - R^{Si}_{min}\right)\left(\frac{Si}{Si + K^{Si}_{Si:N}}\right)\left(\frac{K^{Fe}_{Si:N}}{Si + K^{Fe}_{Si:N}}\right) \tag{3.4}$$

$$R^{Si:N} = max\left(R^{Si}_{max} \cdot \frac{Si}{Si + k^{Si}_{Si:N}} \cdot exp\left(-\frac{Fe}{X_0}\right), R^{Si}_{min}\right) \tag{3.5}$$

These parameterisations are taken from Holzer et al. (2019) and further details regarding these formulations are available therein. A further 'Trial' parameterisation was created as a point of comparison for this study which does not bear any specific physiological representation beyond its dependency on both Fe and Si concentrations but was purely based on adherence of its functional form to the available Si:N data (Figure 3.4):

$$R^{Si:N} = \frac{\left(\frac{Si}{Si+K_{Si}}\right)}{min\left(\frac{N}{N+K_N}, \frac{Fe}{Fe+K_{Fe}}\right)} \tag{3.6}$$

Following the results of Figure 3.8, the EXP1 parameterisation was chosen for the main model simulations of the 'large-type' experiments. The model run time is set to 6 days to mirror the length of the shipboard experiments.

The model parameters listed in Table 3.1 were hand-picked to coincide with the bounds of literature values and a reasonable model fit to observations. The initial conditions shown in Table 3.2 were taken from the mean of triplicate initial

TABLE 3.1: Model parameters and their values.

| Symbol | Parameter | Value |
|---|---|---|
| $\mu_D$ | maximum D growth rate | 130 $yr^{-1}$ |
| $K_N$ | N uptake half-saturation constant | 0.25 µmol N $L^{-1}$ |
| $K_{Fe}$ | Fe uptake half-saturation constant | 0.25 nmol Fe $L^{-1}$ |
| $K_{Si}$ | Si uptake half-saturation constant | 0.25 µmol Si $L^{-1}$ |
| $K_{Mn}$ | Mn uptake half-saturation constant | $3.38 \times 10^{-3}$ nmol Mn $L^{-1}$ |
| $M$ | Mortality rate | 0 $yr^{-1}$ |

concentration measurements from the incubation bottles for N and Si. Fe and Mn were hand-set to a reasonable starting level. These initial nutrient values were amended with 2 nM Fe, 2 nM Mn and 5 µM Si in the relevant treatments matching the factorial nutrient addition experiments. The initial diatom value was calculated by multiplying the time zero chlorophyll measurements from the bottles by the N:Chl ratio found in the data.

TABLE 3.2: Model initial conditions.

| | LTE01 | LTE02 | LTE03 | LTE04 | LTE05 | LTE06 | LTE07 | Units |
|---|---|---|---|---|---|---|---|---|
| Di | 0.42 | 1.44 | 0.46 | 2.62 | 0.63 | 0.76 | 0.86 | µmol N $L^{-1}$ |
| N | 20.22 | 24.12 | 19.62 | 21.24 | 19.13 | 23.09 | 17.14 | µmol $L^{-1}$ |
| Fe | 0.05 | 0.05 | 0.05 | 0.05 | 0.05 | 0.05 | 0.05 | nmol $L^{-1}$ |
| Si | 4.84 | 7.06 | 3.83 | 1.01 | 3.43 | 0.73 | 0.10 | µmol $L^{-1}$ |
| Mn | 0.01 | 0.01 | 0.01 | 0.01 | 0.01 | 0.01 | 0.01 | nmol $L^{-1}$ |

### 3.2.3 CUSTARD-QUOTA Model

The second model used in this study allows for phytoplankton to differentiate between the uptake of nutrients and the use of those nutrients within the cell. Additionally, the CUSTARD-QUOTA model is formulated in a manner which allows for uptake and intracellular storage of nutrients above the amount required for saturation of instantaneous growth, a process typically termed 'luxury uptake' (Buitenhuis and Geider, 2010). Although phytoplankton only have limited capacity for luxury uptake of N, this is not the case for Fe (Sunda and Huntsman, 1995; Marchetti et al., 2009), Si (Martin-Jézéquel et al., 2000) or Mn (Peers and Price, 2004). The model is based on the structure outlined by Buitenhuis and Geider (2010) as developed from (Geider et al., 1998) and Droop (1983). The base variable for phytoplankton biomass is now represented as cellular carbon (C), with cellular quotas ($Q_X$) for each modelled nutrient (X) represented by the cellular X:C ratio:

$$\frac{\delta D}{\delta t} = + \left[ \mu_D \cdot min \left( \frac{Q_N - Q_{min}^N}{Q_{opt}^N - Q_{min}^N}, \frac{Q_{Fe} - Q_{min}^{Fe}}{Q_{opt}^{Fe} - Q_{min}^{Fe}}, \frac{Q_{Si} - Q_{min}^{Si}}{Q_{opt}^{Si} - Q_{min}^{Si}}, \frac{Q_{Mn} - Q_{min}^{Mn}}{Q_{opt}^{Mn} - Q_{min}^{Mn}} \right) \cdot D \right] - [M \cdot D] \tag{3.7}$$

$$\frac{\delta O}{\delta t} = + \left[ \mu_O \cdot min \left( \frac{Q_N - Q_{min}^N}{Q_{opt}^N - Q_{min}^N}, \frac{Q_{Fe} - Q_{min}^{Fe}}{Q_{opt}^{Fe} - Q_{min}^{Fe}}, \frac{Q_{Mn} - Q_{min}^{Mn}}{Q_{opt}^{Mn} - Q_{min}^{Mn}} \right) \cdot O \right] - [M \cdot O] \tag{3.8}$$

$$\rho_{max} = \rho_{max}^{hi} - \left( \rho_{max}^{hi} - \rho_{max}^{lo} \right) \times \frac{(Q - Q_{min})}{(Q_{max} - Q_{min})} \tag{3.9}$$

$$\frac{\delta X_O}{\delta t} = + \left[ \rho_{max} \times \frac{X}{X + K_X} \times O \right] - [M \cdot X_O] \tag{3.10}$$

$$\frac{\delta X_D}{\delta t} = + \left[ \rho_{max} \times \frac{X}{X + K_X} \times D \right] - [M \cdot X_D] \tag{3.11}$$

$$\frac{\delta X}{\delta t} = - \left[ \rho_{max} \times \frac{X}{X + K_X} \times O \right] - \left[ \rho_{max} \times \frac{X}{X + K_X} \times D \right] + [M \cdot X_O] + [M \cdot X_D] \tag{3.12}$$

Here, as in Buitenhuis and Geider (2010), luxury uptake is achieved by defining an optimum nutrient to carbon ratio ($Q_{opt}$). At cellular quotas below this value, all the nutrient is utilised functionally by the cell and growth is directly related to this 'sub-optimal' quota. At cellular quotas above $Q_{opt}$, the excess nutrient is stored by the cell, which may be subsequently utilised at a later time period. Both diatoms (D) and 'other' phytoplankton (O), which lack a requirement for Si, are represented in the model with diatom starting fraction $R^{D:O}$ initially set to 0.8 as diatoms are assumed to dominate in the sampled waters. Growth terms once again involve a max growth rate ($\mu_O$ and $\mu_D$) and a minimisation function; however, this is now formulated such that growth increases linearly with actual ratio $Q$ between the minimum required ($Q_{min}$) and the optimum ratio ($Q_{opt}$) but is capped at the maximum value ($\mu_{max}$). Loss is again condensed into a single mortality term.

The maximum uptake rate term ($\rho_{max}$), expanded in Equation 3.9, is responsible for reducing the rate of nutrient uptake when the cell has accumulated excess nutrient. Nutrient-saturated maximum uptake rate $\rho_{max}^{hi}$ is reached when cellular nutrient approaches $Q_{min}$ while the maximum nutrient uptake rate decreases to the actual uptake rate at $Q_{max}$, (Morel, 1987; Buitenhuis and Geider, 2010). The same four

TABLE 3.3: CUSTARD-QUOTA model parameters and their default values.

| Symbol | Parameter | Value |
|---|---|---|
| $\mu_D$ | maximum D growth rate | 130 $yr^{-1}$ |
| $\mu_O$ | maximum O growth rate | 100 $yr^{-1}$ |
| $K_N$ | N uptake half-saturation constant | 5 umol N $L^{-1}$ |
| $K_{Fe}$ | Fe uptake half-saturation constant | 0.004 umol Fe $L^{-1}$ |
| $K_{Si}$ | Si uptake half-saturation constant | 5 umol Si $L^{-1}$ |
| $K_{Mn}$ | Mn uptake half-saturation constant | 0.004 umol Mn $L^{-1}$ |
| $M$ | mortality rate | 0 $yr^{-1}$ |
| $Q^N_{min}$ | minimum N:C ratio | 0.05 mol N : mol C |
| $Q^N_{opt}$ | optimum N:C ratio | 0.167 mol N : mol C |
| $Q^N_{max}$ | maximum N:C ratio | 0.167 mol N : mol C |
| $Q^{Fe}_{min}$ | minimum Fe:C ratio | 2×10-6 mol Fe : mol C |
| $Q^{Fe}_{opt}$ | optimum Fe:C ratio | 5×10-6 mol Fe : mol C |
| $Q^{Fe}_{max}$ | maximum Fe:C ratio | 50×10-6 mol Fe : mol C |
| $Q^{Si}_{min}$ | minimum Si:C ratio | 0.05 mol Si : mol C |
| $Q^{Si}_{opt}$ | optimum Si:C ratio | 0.167 mol Si : mol C |
| $Q^{Si}_{max}$ | maximum Si:C ratio | 0.5 mol Si : mol C |
| $Q^{Mn}_{min}$ | minimum Mn:C ratio | 0.2×10-6 mol Mn : mol C |
| $Q^{Mn}_{opt}$ | optimum Mn:C ratio | 1×10-6 mol Mn : mol C |
| $Q^{Mn}_{max}$ | maximum Mn:C ratio | 30×10-6 mol Mn : mol C |
| $N\rho^{hi}_{max}/\rho^{lo}_{max}$ | ratio of N-limited and N-saturated maximum uptake rate | 1 |
| $Fe\rho^{hi}_{max}/\rho^{lo}_{max}$ | ratio of Fe -limited and Fe-saturated maximum uptake rate | 20 |
| $Si\rho^{hi}_{max}/\rho^{lo}_{max}$ | ratio of Si -limited and Si-saturated maximum uptake rate | 1 |
| $Mn\rho^{hi}_{max}/\rho^{lo}_{max}$ | ratio of Mn-limited and Mn-saturated maximum uptake rate | 20 |
| $R^{D:O}$ | Initial diatom starting fraction | 0.8 |

TABLE 3.4: CUSTARD-QUOTA model initial conditions.

| | LTE01 | LTE02 | LTE03 | LTE04 | LTE05 | LTE06 | LTE07 | Units |
|---|---|---|---|---|---|---|---|---|
| N | 20.22 | 24.12 | 19.62 | 21.24 | 19.13 | 23.09 | 17.14 | µmol $L^{-1}$ |
| Fe | 0.05 | 0.05 | 0.05 | 0.05 | 0.05 | 0.05 | 0.05 | nmol $L^{-1}$ |
| Si | 4.84 | 7.06 | 3.83 | 1.01 | 3.43 | 0.73 | 0.10 | µmol $L^{-1}$ |
| Mn | 0.02 | 0.02 | 0.02 | 0.02 | 0.02 | 0.02 | 0.02 | nmol $L^{-1}$ |
| Di | 2.11 | 9.53 | 2.83 | 14.53 | 3.31 | 5.77 | 4.46 | µmol C $L^{-1}$ |
| O | 0.53 | 2.38 | 0.70 | 3.63 | 0.83 | 1.44 | 1.12 | µmol C $L^{-1}$ |
| Di $Q_N$ | 0.35 | 1.59 | 0.47 | 2.43 | 0.55 | 0.96 | 0.74 | mol N: mol C |
| Di $Q_{Fe}$ | 7.39e-6 | 3.34e-5 | 9.92e-6 | 5.09e-5 | 1.16e-5 | 2.02e-5 | 1.56e-5 | mol Fe: mol C |
| Di $Q_{Si}$ | 0.53 | 2.38 | 0.71 | 3.63 | 0.83 | 1.44 | 1.11 | mol Si: mol C |
| Di $Q_{Mn}$ | 2.11e-6 | 9.53e-6 | 2.83 | 1.45e-5 | 3.31e-6 | 5.77e-6 | 4.46e-6 | mol Mn: mol C |
| O $Q_N$ | 0.09 | 0.40 | 0.12 | 0.61 | 0.14 | 0.24 | 0.19 | mol N: mol C |
| O $Q_{Fe}$ | 1.85e-6 | 8.34e-6 | 2.48 | 1.27e-5 | 2.89e-6 | 5.05e-6 | 3.90e-6 | mol Fe: mol C |
| O $Q_{Mn}$ | 5.28e-7 | 2.38e-6 | 7.08 | 3.63e-6 | 8.27e-7 | 1.44e-6 | 1.11e-6 | mol Mn: mol C |

nutrient variables, nitrate (N), iron (Fe), silicon (Si) and manganese (Mn) are represented in Equation 3.12 for a generic nutrient (X) with Si uptake occurring only in the diatoms. The loss terms are uptake by diatoms and others which include a Michaelis-Menten form factored by the maximum uptake rate, while nutrients return to the extracellular pool following phytoplankton mortality. Individual uptake terms in Equation 3.10 and Equation 3.11 are set to zero if their sum exceeds the total nutrient available to both plankton groups.

### 3.2.4 Experiments

In this chapter, before any modelling is undertaken, the observations collected during the CUSTARD cruise will be considered. Firstly, a spatio-temporal picture of chlorophyll, N and Si will be provided to establish the background biogeochemistry under which the nutrient addition experiments took place. Secondly, using the data obtained from those experiments, the response of Si:N uptake ratios to Fe and Si availability will be compared to the expected dynamics discussed in Chapter 1 (Section 1.3.2).

Two models, described in detail in Sections 3.2.2 and 3.2.3, were applied to replicate the observations of the CUSTARD incubation experiments. In the first case, a model with a direct parameterisation of Si:N uptake ratio was tested against observations. A number of parameterisations were then compared by their effect on the model's fit to the data. In the second instance, a quota-type model (CUSTARD-QUOTA) was applied recreate the experiments, which rather than having nay direct

parameterisation, allowed internally flexible stoichiometric ratios by representing both nutrient uptake to the cell from the external environment and cellular usage of those nutrients. By utilising these two different methods to achieving a variable Si:N ratio, it is hoped that the approaches can be compared in addition to finding the superior fit to the observations.

## 3.3 Results

### 3.3.1 Findings from Shipboard Experiments

#### 3.3.1.1 Background Measurements

In Figure 3.3, contour plots of chlorophyll, Si and N concentration are plotted using underway data that was collected during the cruise. The chlorophyll plot shows low values in the north but a raised signature in the south from around day 7 to day 28 which peaks at 2.4 µg $L^{-1}$ suggesting a bloom in this region. N similarly shows a higher concentration in the south than the north (reaching 23.4 µM), although the lowest values appear centrally around station TN in the latter half of the cruise. Finally, Si initially appears higher in the south but quickly decreases leaving most Si remaining in the north by the end of the cruise.

#### 3.3.1.2 Si:N Response to Iron

Although direct iron (Fe) concentrations were not collected for all but the starting conditions of the experiments, Fe limitation has been shown to negatively impact the quantum efficiency of photochemistry in photosystem II (Greene et al., 1991), which can be measured using fast repetition rate fluorometry using the fluorescence parameter Fv/Fm. This technique uses pulsed high intensity flashes to saturate reaction centres, driving changes in fluorescence yield which enable determination of whether various stress factors may be influencing the cellular physiology (Greene et al., 1994; Falkowski and Kolber, 1995; Boyd and Abraham, 2001).

By using Fv/Fm as an indicator of Fe (and potentially Mn) stress, the measured Si:N uptake ratio could be compared to the relative Fe stress across both treatments and locations over the course of the experiments (Figure 3.4). The trend of higher Si:N ratios present at low Fv/Fm, indicative of greater Fe stress, is clear. Experimental treatments where no additional Fe was provided show the greatest Si:N, mainly peaking at around 2.5:1 or up to 4 in one case. A band of measurements appears

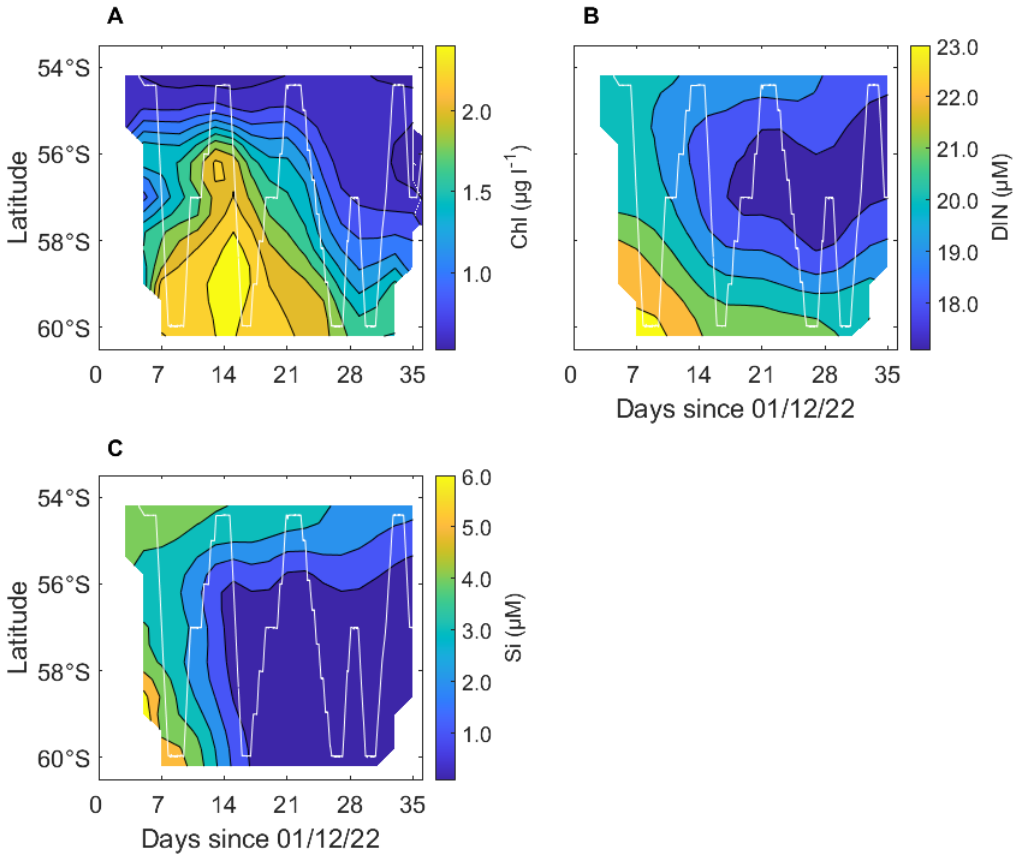


FIGURE 3.3: The concentrations of chlorophyll, N and Si across the CUSTARD cruise region plotted over time elapsed since the cruise began. The track of the cruise is overlaid in white.

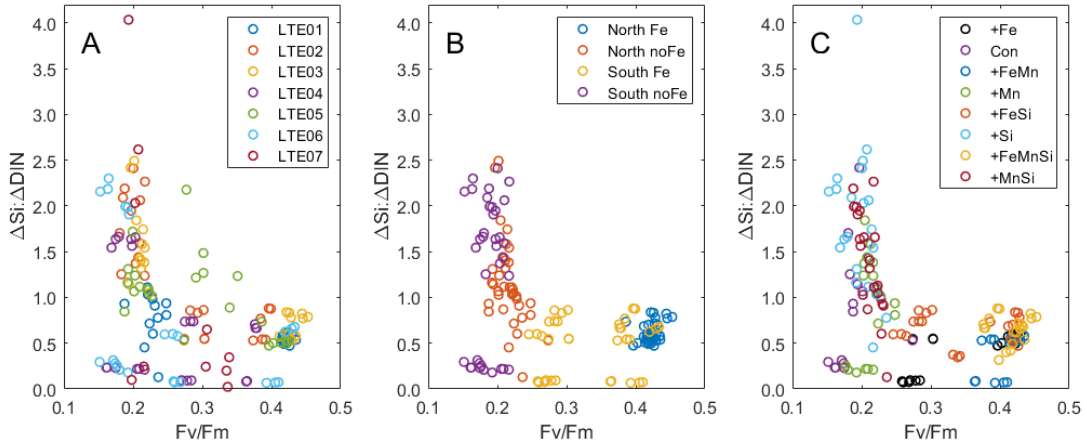


FIGURE 3.4: Phytoplankton Si:N uptake ratios across the 'large type' experiments are plotted against Fv/Fm; a measure of the quantum efficiency of photochemistry in photosystem II determined by fast repetition rate fluorometry, which provides an index of the extent of Fe limitation (Greene et al., 1991). The are separated by experiment (a); iron amendment and location (b); and treatment.

between 0.5 and 1 suggesting that Fe-replete phytoplankton in these experiments experience lower Si:N than what is considered the ocean average of 1:1 (Brzezinski, 1985). Of these Fe-replete plankton, those sampled from the south of the study region (at station TS) had a much broader range of Fv/Fm values whereas those from the north of the study region (at OOI) were very closely distributed. When broken down by individual treatment, comparing +FeMn and + FeSi clearly shows that Mn has an important secondary limitation effect in terms of the stress on the photosynthetic apparatus. The lowest Si:N values in Figure 3.4 all correspond to treatments where Si was not added. When the data are divided into the more northerly (1, 3, 5) and more southerly experiments (2, 4, 6), the iron-replete incubations from the north exhibit a far tighter grouping of high Fv/Fm values ($>$0.39) compared to their southern counterpart which spread down to 0.25 close to iron-deficient values.

#### 3.3.1.3 Gradient Experiments

The results of the two Si gradient experiments GE01 and GE02 are shown in Figure 3.5, with non-Fe amended and +Fe treatments separated. These data were fit with a non-linear regression based on a Michaelis-Menten form. While reproducing the positive effect of Fe stress on Si:N seen in Figure 3.3, Figure 3.5 demonstrates that Si concentration is also a clear driver of Si:N. The northerly OOI experiment, GE01 has an Si:Nmax of 0.95 and 1.54 for the high and low Fe conditions respectively while GE02 in the south at TS exhibited higher values of 1.45 and 3.49. The half-saturation constant, $K_{Si:N}$, rises from 0.82 with Fe to 1.59 without in GE01 whereas in GE02 it decreases from 2.57 to 1.78. In both GE01 and GE02, the curves appear to saturate at concentrations between 10 – 15 µM of Si above which iron limitation is the only factor and below which Si limitation begins to take effect.

### 3.3.2 CUSTARD-SIMPLE Model

#### 3.3.2.1 Large-Type Experiments

The observed final chlorophyll concentrations for each large-type experiment were compared against the basic model estimates in Figure 3.6. Experiments 2, 4, 5 and 7 appear to match the observed values best overall, though the model tends to underestimate the magnitude of the responses. The +Fe and +FeMn response is captured in 1, 2, 3 and 5 but notably absent elsewhere. However, all experiments produce responses for +FeSi and +FeSiMn suggesting a Si deficit may be responsible of limiting the magnitude of the positive Fe response in these cases. The addition of

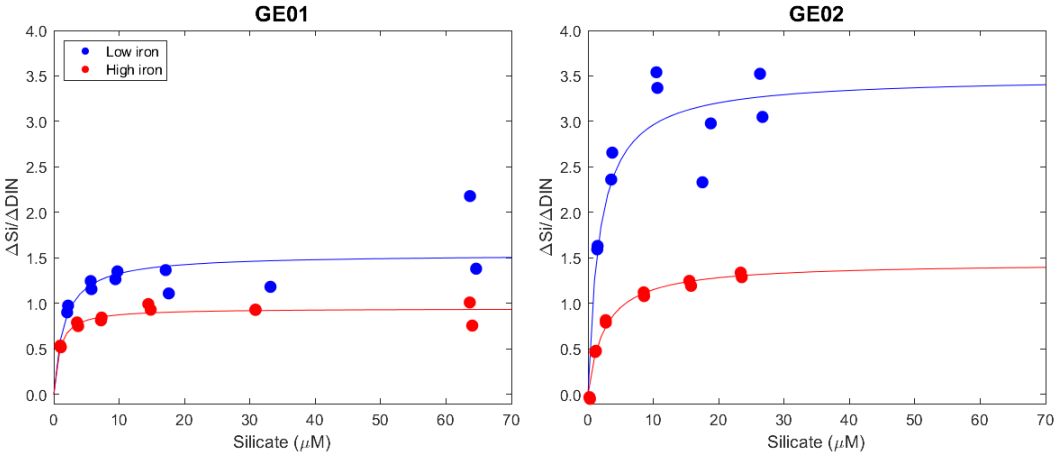


FIGURE 3.5: Si:N uptake ratios from the 2 gradient experiments are plotted against silicic acid concentration. Data are separated by whether they were iron amended and a saturating Michaelis-Menten curve is fitted.

Mn and Si alone or in combination is accurately represented as having no effect by the model.

Overall, the modelled responses appeared to overestimate the extent of Si limitation, in some cases suppressing the response to the relief of Fe limitation. Consequently, additional model runs were performed where, starting Si was increased to the starting condition of experiments 4, 6 and 7 where no Fe response was previously achieved by the model. A strong response was now produced by the model for the Fe and +FeMn treatments in these experiments, matching the observed data well, although overshooting the +FeMn response in experiment 7 (Figure 3.7).

The basic model framework was then used to test how well different parameterisations of the Si:N to Fe response fit the data (Figure 3.8). Here, a comparison is made between a fixed 1:1 ratio, a new 'trial' parameterisation, and three parameterisations used previously by Holzer et al. (2019): exponential relationships EXP1, EXP2 and hyperbolic relationship HYP. Root mean square error was used to compare each model run to the experimental results with a lower error, indicating the model run more accurately represented observations. As previously discussed, the model struggles with Si and this is clear in the much greater error for Si when compared to estimates of chlorophyll and N across the board. The 1:1 and 'trial' parameterisation are better at approaching the real chlorophyll and N, however, the main effect of these parameterisations is upon Si uptake. Here, the Holzer et al. (2019) parameterisations all produce a lower deviation for Si, at the expense of a higher deviation for N.

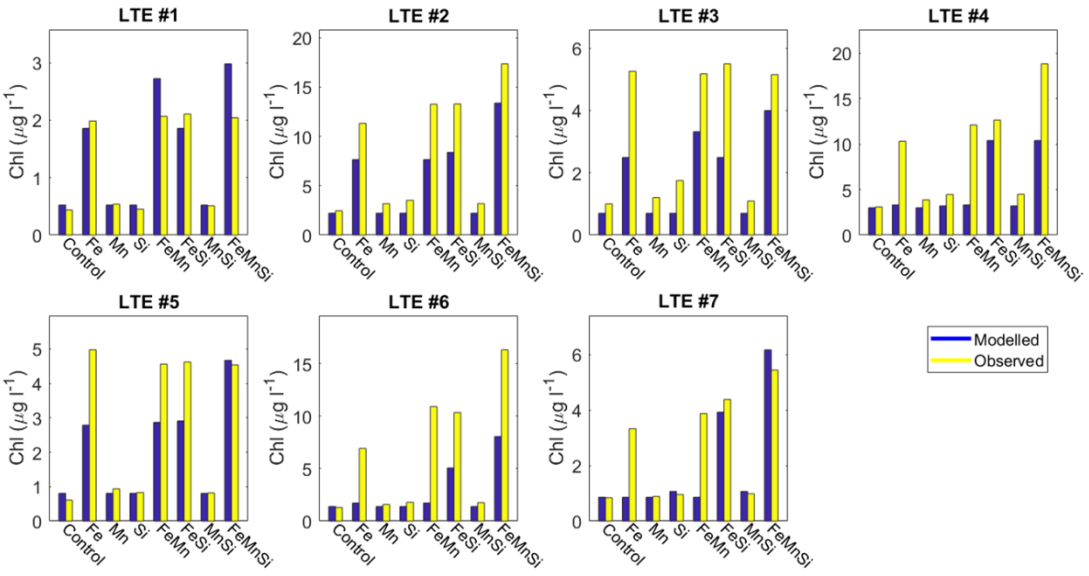


FIGURE 3.6: Average chlorophyll at the 6th day endpoint is plotted for each treatment in every 'large-type' experiment. This is compared against the results of the basic model adapted from Yool and Tyrrell (2003). The model was provided accurate starting conditions for N, Si while Fe and Mn were approximated.

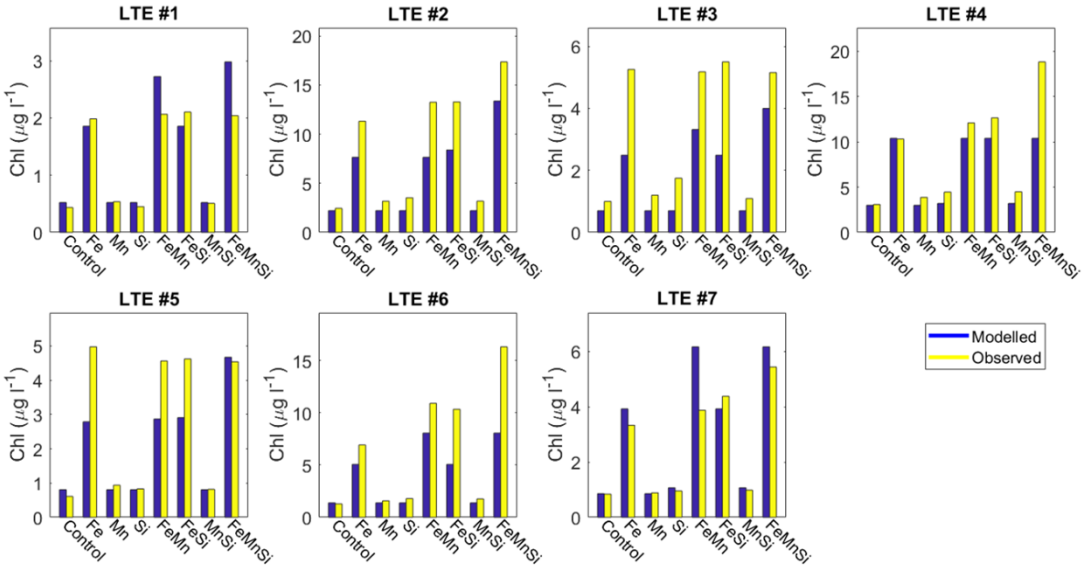


FIGURE 3.7: Average chlorophyll at the 6th day endpoint is plotted for each treatment in every 'large-type' experiment. This is compared against the results of the basic model adapted from Yool and Tyrrell (2003). An additional 10 µmol of starting Si was supplied to the starting condition of experiments 4,6 and 7 where no Fe response was previously achieved.

#### 3.3.2.2 Gradient Experiments

It is also possible to use the model to recreate experiments GE01 and GE02 where incubations were run over a gradient of Si additions paired with added iron or no

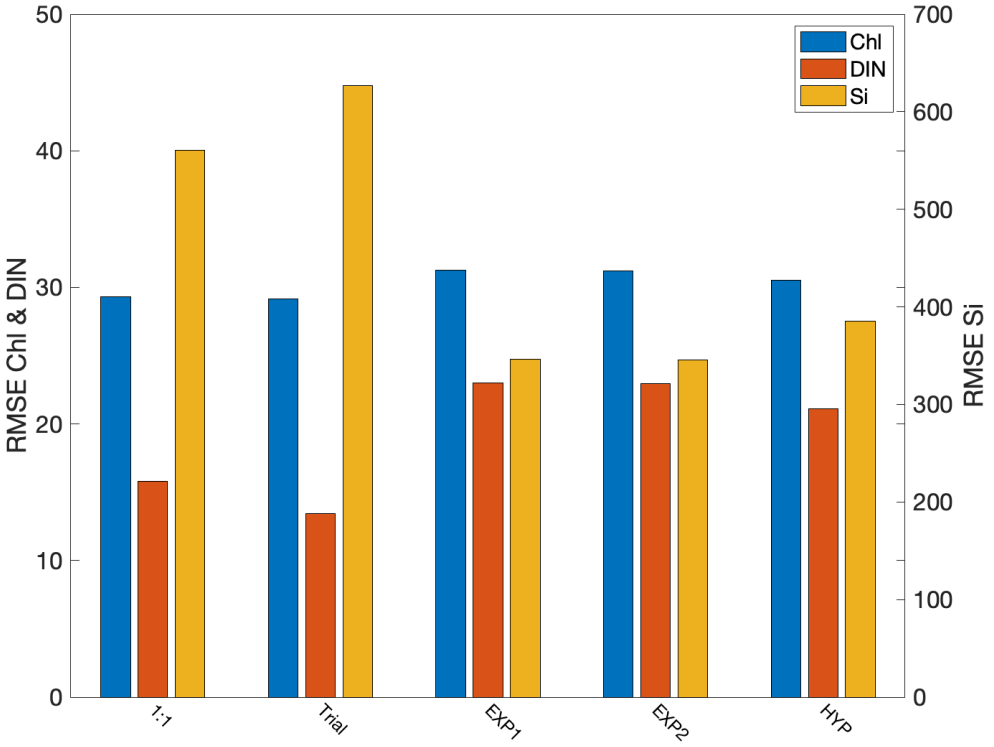


FIGURE 3.8: The results of the basic model are compared to the CUSTARD experiment observations using Root Mean Square Error. Several types of Si:N parameterisation are also compared: a 1:1 ratio; a 'trial' formula created for this study and 3 forms taken from Holzer et al. (2019).

added iron (Fig 3.9). This provides another opportunity to test the integrity of the model, particularly in regards to Si:N, or more specifically the ratio of change in Si concentration to change in N concentrations over the course of the experiment . For GE01, it is clear that all of the parameterisations overshoot the Si:N by a large amount reaching a max Si:N of 7.2, 22, 13 and 12 for the trial, EXP1, EXP2 and HYP parameterisations respectively, in the low iron treatment. However, in that treatment, they do exhibit the correct shape of a saturating curve and this is also true of the high iron treatment for the trial and HYP parameterisations. The trial parameterisation deviates least from the observations, overestimating the high iron treatment by $\sim$0.15 but still with around 6 times the maximum Si:N of the low iron treatment.

During GE02 experiment (Figure 3.5), the maximum Si:N of the low-iron non-linear regression reaches 3.4 compared to 1.5 in GE01. Correspondingly, all parameterisations increase the maximum Si:N in the low iron treatment, with the Holzer et al. (2019) equipped models showing a 0.1-0.6 increase and the trial parameterisation rising by 1 to an Si:N of 8.2 (Figure 3.10). In the high iron treatment,

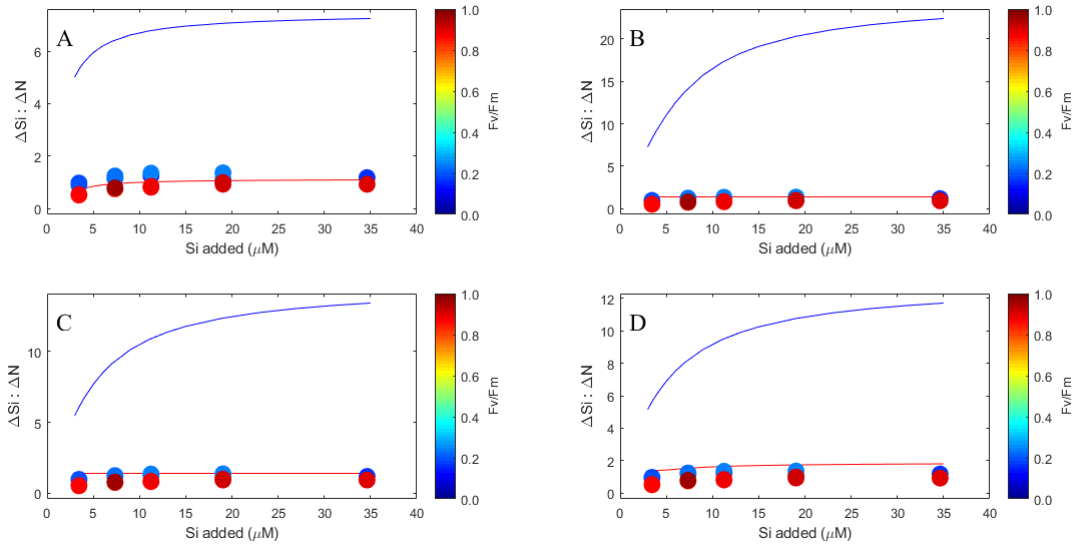


FIGURE 3.9: The results of the incubation experiment GE01 and model simulations of those experiments are shown by markers and lines respectively. The ratio of ΔSi to ΔDIN over a gradient of Si concentration and high (red) and low (blue) iron conditions is simulated using four different Si:N parameterisations: a 'trial' formula created for this study (**A**) and 3 forms taken from Holzer et al. (2019), EXP1 (**B**), EXP2 (**C**) and HYP (**D**). The markers showing the results of the incubation experiments are shaded by their Fv/Fm; a marker for stress in photosystem II. In this case, a low Fv/Fm is indicative of phytoplankton suffering from iron limitation in the treatments where none was added.

EXP1, EXP2 and HYP show almost no change but fit the higher observations better than in GE01 while the trail parameterisation exhibits an excellent fit to the data.

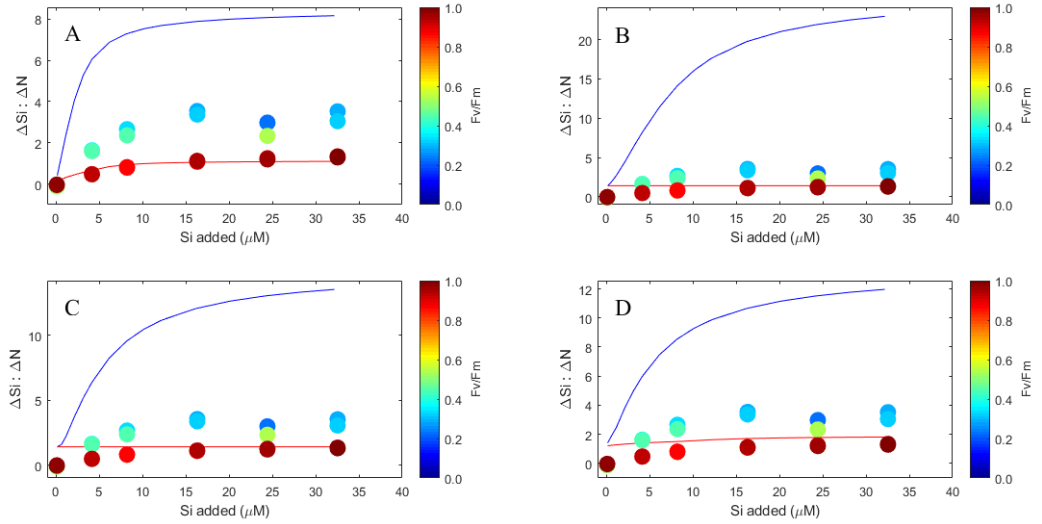


FIGURE 3.10: The results of the incubation experiment GE02 and model simulations of those experiments are shown by markers and lines respectively. The ratio of ΔSi to ΔDIN over a gradient of Si concentration and high (red) and low (blue) iron conditions is simulated using four different Si:N parameterisations: a 'trial' formula created for this study (**A**) and 3 forms taken from Holzer et al. (2019), EXP1 (**B**), EXP2 (**C**) and HYP (**D**). The markers showing the results of the incubation experiments are shaded by their Fv/Fm; a marker for stress in photosystem II. In this case, a low Fv/Fm is indicative of phytoplankton suffering from iron limitation in the treatments where none was added.

### 3.3.3 CUSTARD-QUOTA Model

#### 3.3.3.1 Large-Type Experiments

To better recreate the drawdown of Si observed in these experiments, which appeared to be a complex emergent property of both Fe amendment, location and Si availability (Figures 3.4 and 3.5) not captured well in the basic model, a model that considers the internal nutrient quota of phytoplankton cells, as well as the external nutrient concentration, was used. The results of the model are compared to the endpoint measurements of chlorophyll, dissolved inorganic nitrogen (DIN), Si and the ratio of Si to N. In Figure 3.11, the model recreates the patterns of all the +Fe treatments, also recreating some of the secondary limitation of Si and Mn in experiments 2, 4, 6 and 7 in which the +FeMnSi treatment produces the highest chlorophyll concentration. The responses of N uptake to the different experimental treatments are tightly linked to those of chlorophyll. Si uptake reproduced by the model appears to perform well except for treatments where both Fe and Si are added, where uptake typically exceeded observed values. The low uptake ratio of Si to N when Fe is added is much more closely replicated by the CUSTARD-QUOTA model than the ratio at low Fe which is too high in almost every experiment. This is created by a combination of underestimated N uptake in these treatments and sometimes overestimated Si uptake,

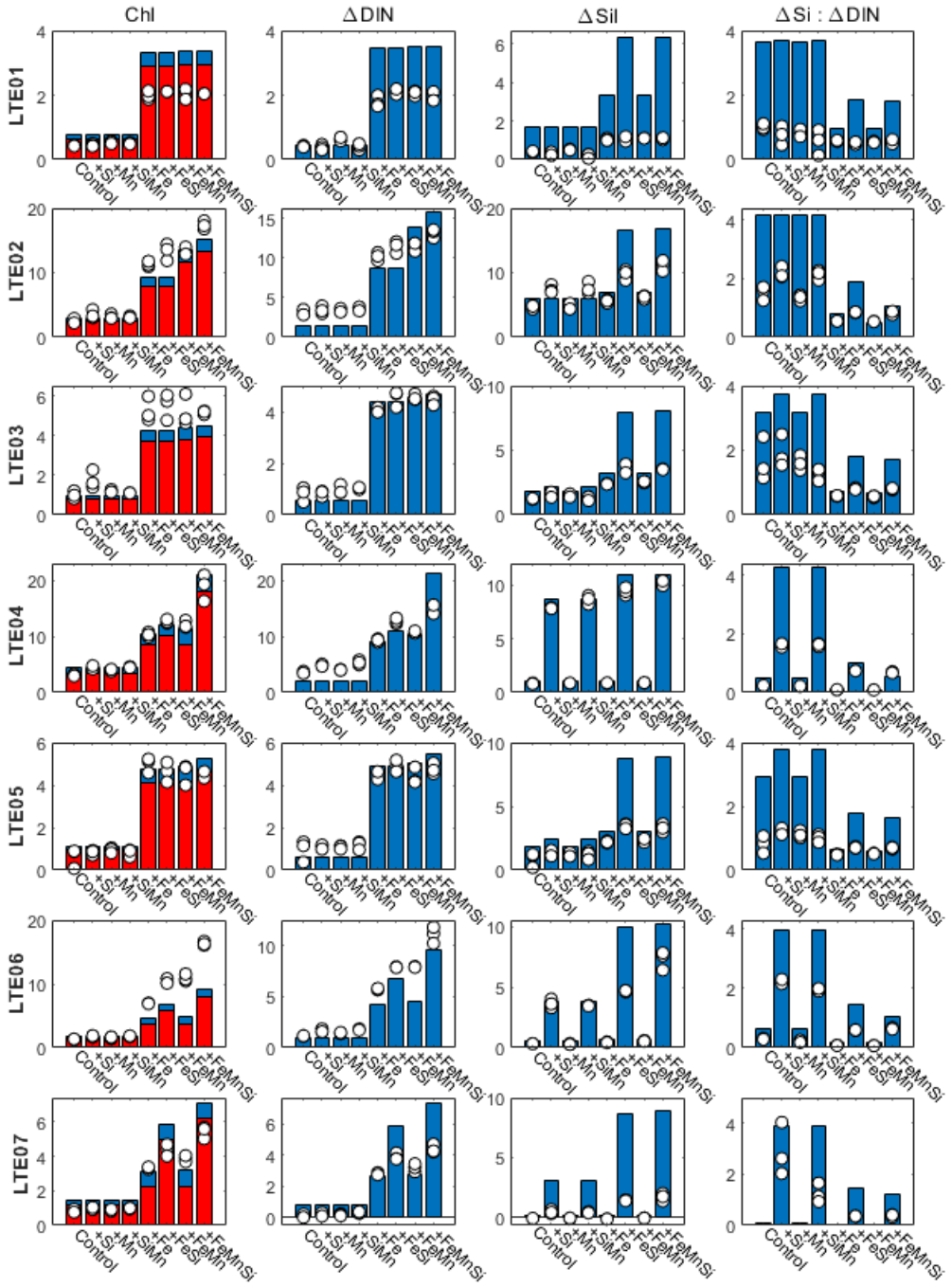


FIGURE 3.11: Comparison of data from the endpoint of each 'large-type' experiment is compared against the results of the CUSTARD-QUOTA model. Triplicate experimental observations for chlorophyll, change in dissolved inorganic nitrogen (DIN), change in silicic acid (Si) and the ratio of ΔSi to ΔN are indicated by white markers. Model results for both diatom and the 'other phytoplankton' class have blue bars while the diatom class alone are shown in red bars.

as mentioned above. Accurate measurement of Si:N in low Fe conditions is extremely important as it is these high values that affect the broader dynamics, both inside the SO and consequently the global scale implication (Sarmiento et al., 2004). However, the lower uptake of nutrients in this state makes it more difficult to measure accurately.

#### 3.3.3.2 Gradient Experiments

A similar story can be found in Figure 3.12, where the fit to gradient experiment GE01 is plotted. While reproduced chlorophyll and N appear close to the observed data, Si uptake is significantly overestimated producing a corresponding overestimate in the Si:N uptake ratio. The picture of GE02 in Figure 3.13 follows the same pattern, though a closer fit is achieved. In order to try and reduce the uptake of Si in these experiments, the $Q^{Si}_{max}$ was lowered from 0.5 to 0.2 for GE01 and to 0.4 for GE02. The results, in Figures 3.14 and 3.15, show that this approach succeeded in reducing Si uptake and subsequently led to a closer approximation of the Si:N trend in GE02, however, this effect seems to have gone too far in the case of GE02, producing a lower Si:N at lower Fe.

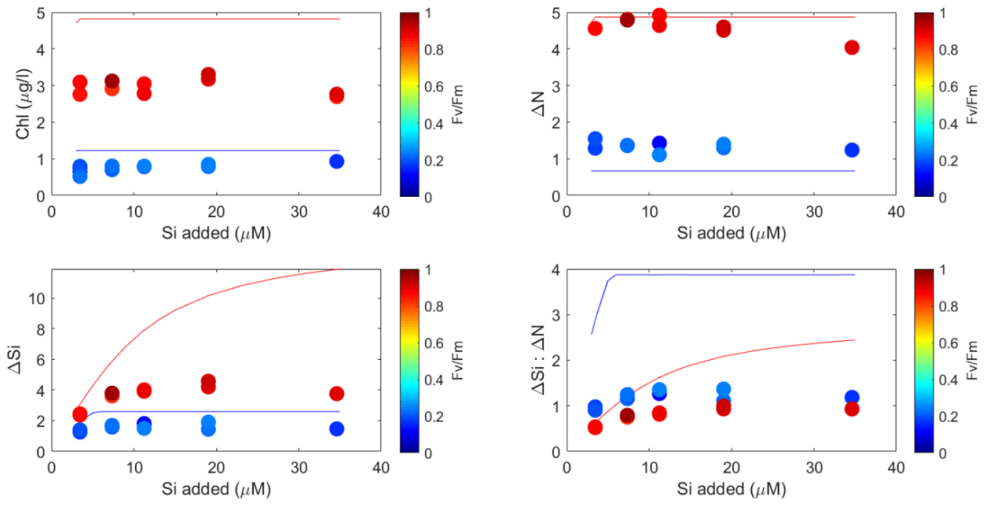


FIGURE 3.12: The results of the first gradient experiment (GE01) for chlorophyll, change in dissolved inorganic nitrogen (N), change in silicic acid (Si) and the ratio of ΔSi to ΔDIN are plotted with markers and shaded by their Fv/Fm; a marker for stress in photosystem II. In this case, a low Fv/Fm is indicative of phytoplankton suffering from iron limitation in the treatments where none was added. Results of the CUSTARD-QUOTA model simulating this experiment are shown by plotted lines; blue corresponding to the low iron treatment and red to the high iron treatment.

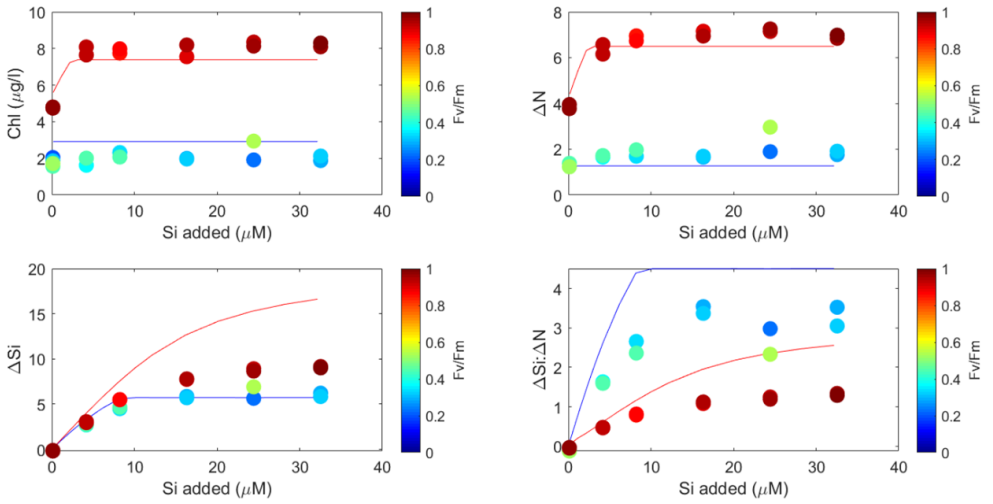


FIGURE 3.13: The results of the first gradient experiment (GE02) for chlorophyll, change in dissolved inorganic nitrogen (N), change in silicic acid (Si) and the ratio of ΔSi to ΔN are plotted with markers and shaded by their Fv/Fm; a marker for stress in photosystem II. In this case, a low Fv/Fm is indicative of phytoplankton suffering from iron limitation in the treatments where none was added. Results of the CUSTARD-QUOTA model simulating this experiment are shown by plotted lines; blue corresponding to the low iron treatment and red to the high iron treatment.

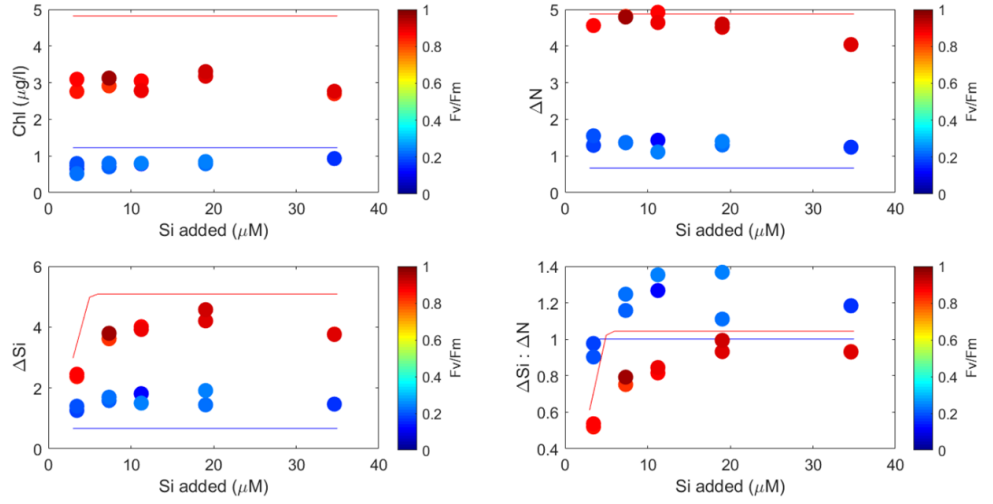


FIGURE 3.14: A repeat of the information shown in Figure 3.12 for the gradient experiment GE01 with observations shown with markers and CUSTARD-QUOTA results plotted in blue lines for the low iron treatments and red lines for the high iron treatments. However, in this case the CUSTARD-QUOTA model $Q_{max}^{Si}$ was lowered from 0.5 to 0.2.

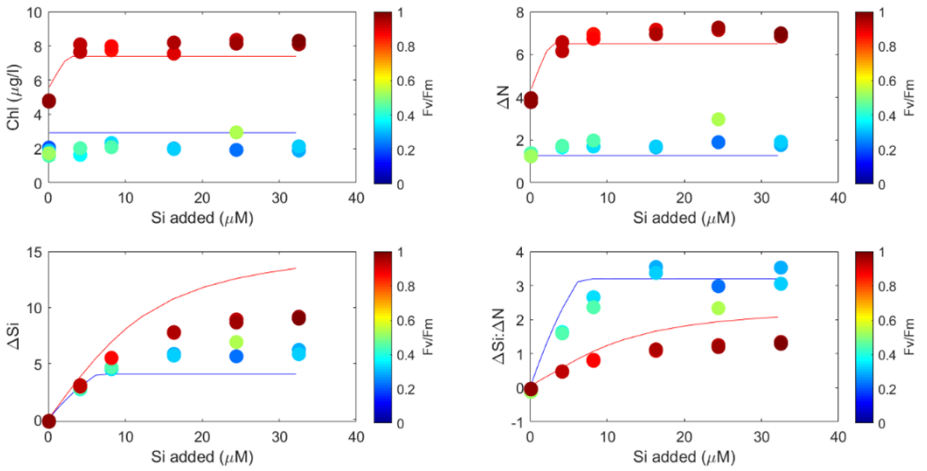


FIGURE 3.15: A repeat of the information shown in Figure 3.13 for the gradient experiment GE02 with observations shown with markers and CUSTARD-QUOTA results plotted in blue lines for the low iron treatments and red lines for the high iron treatments. However, in this case the CUSTARD-QUOTA model $Q_{max}^{Si}$ was lowered from 0.5 to 0.4.

## 3.4 Discussion

Experimental data from the sub-Antarctic South East Pacific revealed clear changes in major element stoichiometry in response to the availability of different nutrients. Comparison of the data with models of different structures and complexities enabled evaluation of the ability of these models to reproduce those observations. The Si:N with Fv/Fm data in Figure 3.4, strongly suggest that Si:N increases with Fe stress as found in many other experiments and ocean regions (Brzezinski, 1985; Takeda, 1998; De La Rocha et al., 2000; Brzezinski et al., 2003; Timmermans et al., 2004; Hoffmann et al., 2007). Moreover, considering the data across all experiments and treatments (Figure 3.12), it appears that, as might be expected, the lowest Si:N values were seen in treatments with no Si addition. The greater spread of Fv/Fm values observed in the southerly iron replete treatments (Figure 3.4b) is likely linked to the higher initial chlorophyll there (Figure 3.6), an indication of greater productivity in the area. In addition, iron amendments to the southern experiments 2, 4 and 6, in combination with other nutrients, created a maximum chlorophyll concentration of 18.8 µg $L^{-1}$ compared to 5.5 µg $L^{-1}$ in experiments 1, 3 and 5. In the southern experiments, the further addition of Mn yields a secondary chlorophyll response suggesting the alleviation of iron has pushed these phytoplankton to Mn limitation, triggering a lower Fv/Fm (Browning et al., 2014, 2021; Pausch et al., 2019; Balaguer et al., 2022). This is supported by cross-referring Figures 3.4b and 3.4c where the southern iron-replete data points with low Fv/Fm correspond to +Fe and +FeSi treatments while higher Fv/Fm values correspond to +FeMn and +FeMnSi treatments.

The independent gradient experiments (Figure 3.5) further confirmed that Si:N uptake ratios were dependent on Si availability as well as Fe. Fe availability limits N acquisition; mainly by affecting photosynthetic activity and therefore the reductive power accessible to uptake N (Morel et al., 1991); and, to a smaller extent, due to the direct role of Fe in N-reducing enzymes including nitrate reductase (Timmermans et al., 1994). Si uptake is also decreased under Fe stress, although, rather than this being a direct influence of Fe on Si uptake, it is instead thought to be linked to the cellular growth cycle (Meyerink et al., 2017). However, as might be expected, the gradient experiments show Si uptake reduction by low Si availability can produce low Si:N,. The <1:1 Si:N ratio data points observed in the 'large-type' experiments (Figure 3.4) are also present in these gradient experiments, mainly appearing in the initial slope of the curve at <10 µM Si (Figure 3.5). These low values, are therefore caused by low concentrations of Si in combination with Fe replete conditions. When Fe is available but Si is low, N acquisition is not limited by Fe but sparse Si creates low diatom uptake, possibly silicifying less or shifting to less silicified species. Although these values are below the ocean average diatom composition of 1:1 found in Brzezinski (1985), the lowest Si:N value found in that study is 0.28. However, as discussed in Chapter 1, the composition of the cell and the frustule can be disconnected from uptake.

### 3.4.1 CUSTARD-SIMPLE Model

Patterns of Fe limitation were observed across all the LTE experiments, with further indications of secondary Mn and Si limitation present in the more southerly experiments where the in situ bloom was stronger (experiments 2, 4, 6 and 7, see Figures 3.7 and 3.11), represented by the enhanced starting chlorophyll concentrations. The variation present in these results which includes primary and secondary limitation, and different levels of productivity create an ideal testing dataset for the effects of iron limitation.

While both models were able to broadly reproduce these patterns, the more basic model (Figure 3.7) struggled to reproduce a realistic response to Fe addition in experiments 4, 6 and 7 as reduced Si availability exerted too much of a restriction on the modelled response. This model deficit was clearly demonstrated when the addition of extra Si to the modelled simulation of these experiments immediately rectified the discrepancy. It was therefore hypothesised that a model able to replicate the ability of diatoms to store Si within intracellular pools (Martin-Jézéquel et al., 2000) might better reproduce the observations.

### 3.4.2 CUSTARD-QUOTA Model

The CUSTARD-QUOTA model was thus developed as an alternative framework which allowed for so-called 'luxury' uptake of multiple nutrients (Buitenhuis and Geider, 2010). This formulation was more able to capture the patterns of chlorophyll response, not only to relief of Fe limitation following Fe addition within the experiments but also to Si and Mn in those southerly experiments where secondary responses to addition of those nutrients were observed (Figure 3.9). Additionally, despite no direct relationship of Fe to Si:N being included in the model, a qualitative agreement was found between modelled and observed Si:N uptake ratios in all but the first two experiments. Within these experiments, with the parameter sets and starting conditions used, Si limitation is wrongly prescribed by the model in LTE01 while Si limitation is missed in the non-Fe treatments of LTE02. It is suggested that accounting for more of the divergent starting conditions between experiments might provide a better fit. Of the direct parameterisations trialled on the basic model in Figure 3.8, the exponential based curves from Holzer et al. (2019) best matched observations of Si, although, this seemed to come with a slight penalty in the accuracy with which N uptake was reproduced. However, across the board reproduction of Si uptake had markedly higher divergence from experimental results than N uptake. Such errors point towards Si being the hardest nutrient to model, regardless of which parameterisation is used.

While the CUSTARD-QUOTA model presents a better fit for the patterns in the CUSTARD experimental data (Figure 3.9), it bears the cost of requiring many more parameters than the simpler model (6 in the basic model vs. 23 in the CUSTARD-QUOTA model). The model requires starting conditions for cellular N, Fe, Si and Mn quotas in addition to phytoplankton biomass in carbon units for two groups of organisms, a nominal non-diatom and siliceous diatom population. When comparing the performance of the basic model with that of the CUSTARD-QUOTA model, the additional variables available in the latter make it harder to distinguish whether improved accuracy is due to a more realistic physiological representation or because of a greater ability to fine tune the model with these variables. Therefore, CUSTARD-QUOTA is first presented here without additional fine tuning for better comparison. Absence of data for starting conditions such as Fe and diatom to non-diatom ratio and the starting cellular elemental quotas must therefore all be assumed and/or tuned to match observed response. Inaccuracies in assumed parameter values may also have contributed to quantitative discrepancies between the model and the observations. An example can be seen in the improved fit produced in the quota gradient experiments (Figure 3.13) when the $Q_{max}^{Si}$ was lowered from 0.5 to

0.4. To improve the accuracy of the model and handle the large number of parameters, a genetic algorithm (Mitchell, 1996) will next be used to fine tune the model to the conditions at each individual station. Additionally, more CUSTARD data will soon become available which will provide greater constraints on the initial conditions including biogenic Si, particulate organic carbon and particulate organic nitrate (PON), allowing starting quotas for these elements to be set. Initial Fe dissolved and Mn concentrations will also be available alongside quantitative measures of the starting diatom to non-diatom ratio in the community.

Holzer et al. (2019) show how the influence of Fe on Si:N stoichiometry is interpreted in models can be important in determining modelled (de-)coupling of Si and N in the Southern Ocean and consequently in producing significant disparity in predictions of future nutrient distributions. The gradient experiments, shown in Figures 3.4 and 3.5, and both experimental LTE experiments and the CUSTARD-QUOTA based reproduction of these experiments, make it clear that the phytoplankton community Si:N ratio is dependent not only on Fe availability but also Si availability. Therefore, models that seek to represent Si:N uptake ratios in the Southern Ocean, likely need to incorporate both of these dependencies in order to fully represent system behaviour. The application of a relatively well-established quota model format (Droop, 1968, 1973; Geider et al., 1998; Buitenhuis and Geider, 2010) was able to reproduce much of the qualitative response observed in the CUSTARD data. Crucially, the Si:N ratio emerges implicitly from this model, as a response to Fe influencing growth, which determines both Si and N uptake, with Si influencing only Si uptake. Such a mechanism is supported by Brzezinski et al. (2011), who undertook similar nutrient addition experiments on diatoms in the equatorial Pacific. Si addition increased Si use and biogenic silica production but had no significant effect on the use of nitrogen. Fe addition similarly increased the rate of Si use and biogenic silica production, however, it also increased rates of organic matter production by affecting growth rate and this was what led to the removal of nitrate. In contrast to indirect links between Fe availability and Si uptake, Mock et al. (2008) found that among genes they identified that control the manipulation of Si in diatoms, a set of 75 genes were only induced under low concentrations of Si while a set of 84 genes were unexpectedly induced by both silicon and iron limitation. They suggest that Fe could be tightly coupled to Si by acting as a cofactor for silicon-specific gene products. Experimental and model results presented here suggest that such a direct linkage may not be necessary in representation of the Si:N stoichiometry. Questions thus remain relating to the importance of these genetic signals for the resulting physiological response.

## 3.5 Conclusions

Although the CUSTARD-QUOTA model described here requires more fine tuning of parameters due to its increased complexity, models that assume a direct dependence of Si:N on Fe availability could be prone to producing artificial responses as they are based on an empirical rather than a physiological mechanism. Prior to the work of Pasquier and Holzer (2017), parameterisations have not included Si and Fe concentration as duel determinants of Si:N but rather one or the other (Jin. et al., 2006; Matsumoto et al., 2013). It is worth noting that an important feature of Southern Ocean biogeochemistry is the latitudinal silicon gradient that exists from above 50 mmol $m^{-3}$ at the southern winter-ice boundary, to 10 mmol $m^{-3}$ and below at the Polar Front (Tréguer and Jacques, 1993). In the broader context, a strong dependence of Si uptake and hence Si:N stoichiometry on Si availability is likely to enhance the potential for the Southern Ocean to trap Si (Dugdale and Wilkerson, 2001; Holzer et al., 2014). Representation of these processes is thus likely important in the context of both, understanding SO Si trapping in the modern ocean and the potential for this to have changed at times in the past (Nozaki and Yamamoto, 2001; Brzezinski et al., 2002; Matsumoto et al., 2002).

# Chapter 4

# Using a genetic algorithm approach to parametrise a quota model and interrogate community structure within incubation experiments

## 4.1 Introduction

As part of the Carbon Uptake and Seasonal Traits in Antarctic Remineralisation Depth (CUSTARD) programme, a series of factorial nutrient addition experiments were conducted in the Southern Ocean to investigate how the addition of nutrients including silicic acid (Si), iron (Fe) and manganese (Mn), both separately and in combination, influenced phytoplankton physiology, growth and nutrient uptake ratios within the mixed communities present. Among these, a series of 'large-type' experiments (LTE's) observed primary limitation by Fe and secondary limitation by Si and Mn, while a separate set of gradient experiments recorded the dual effects of Si concentration and Fe limitation on the Si:N uptake ratio in the incubations.

In Chapter 3, these experiments were used as a robust test of the modelling of diatom physiology, in particular, the effect of nutrient concentrations on Si:N uptake ratios. The way that this physiology is parameterised in models can lead to dramatically different outcomes to conditions such as Fe fertilisation (Holzer et al., 2019), and so, testing the effectiveness of modelling approaches on such a dataset is an important tool for improving the modelling of coupled nutrient cycles. In the Chapter 3, a simple model (CUSTARD-SIMPLE) including diatoms and extracellular nutrients was paired

with direct parameterisations linking Fe and Si concentrations to Si:N. However, this approach had deficiencies in how Si availability limited Fe response in the LTE's and largely overestimated Si:N response to iron deficiency in the gradient experiments (GE's). A subsequent quota model approach (CUSTARD-QUOTA) that included two phytoplankton groups and internal nutrient quotas in addition to extracellular concentrations improved the simulation of both sets of experiments without the need for direct Si:N parameterisations.

The current chapter seeks to further improve the model of the CUSTARD incubation experiments and to better understand the mechanisms, on a community and cellular level, that enable a tight fit to observations. Variability in the chlorophyll to carbon ratio which was observed in the experiments is described and subsequently a dynamic cellular chlorophyll pool is introduced as an additional state variable to the model following Buitenhuis and Geider (2010). A genetic algorithm approach is then used to parameterise the model and explore how the experimental data constrains the parameter choice. Of particular interest, is the algorithm's choice of initial diatom fraction in the different LTE's which are compared to latitudinal patterns in community structure observed in the high performance liquid chromatography (HPLC) data collected on the cruise.

## 4.2 Methods

### 4.2.1 Variable Chlorophyll Model

In seeking what might be holding back the CUSTARD-QUOTA model and the ability to compare the model against observations, it was decided to explicitly model chlorophyll (Chl) as a separate state variable associated with the phytoplankton, where before it had been ascribed post-hoc at a constant ratio to carbon (C). This could be misleading to comparative and algorithmic attempts to fit the model to the incubation experiments.

Indeed, the Chl:POC ratio measured during the experiments showed considerable variance across different treatments (Figure 4.1). In general, Fe-limited treatments, characterised by the lowest values of Fv/Fm (Explained in 3.3.1.2), around 0.2, exhibited lower Chl:POC ratios compared to that within treatments that included Fe addition. Experiments 1, 4, 5 and 7 clustered around 0.1 g/mol Chl:POC while 2, 3 and 6 reached values up to 0.24. On the other hand, the Fe amended and hence higher Fv/Fm treatments (0.25-0.45) ranged from a Chl:POC of 0.14 up to 0.43 g/mol. Such reduction in Chl:C ratios under iron limitation has been well documented (Sunda and

Huntsman, 1995), but more generally, Chl:C is responsive to ambient light, temperature, and nutrient conditions (Cloern et al., 1995; Geider et al., 1997; Wang et al., 2009).

Therefore, chlorophyll is now modelled directly following the formulation of Buitenhuis and Geider (2010) allowing for a variable Chl:C ratio which prevents the fitting of chlorophyll observations being offset by unknown Chl:C. This also facilitates the inclusion of light and Chl:C in the calculation of carbon biomass. This new version of the model is referred to as CUSTARD-QUOTA-V2.

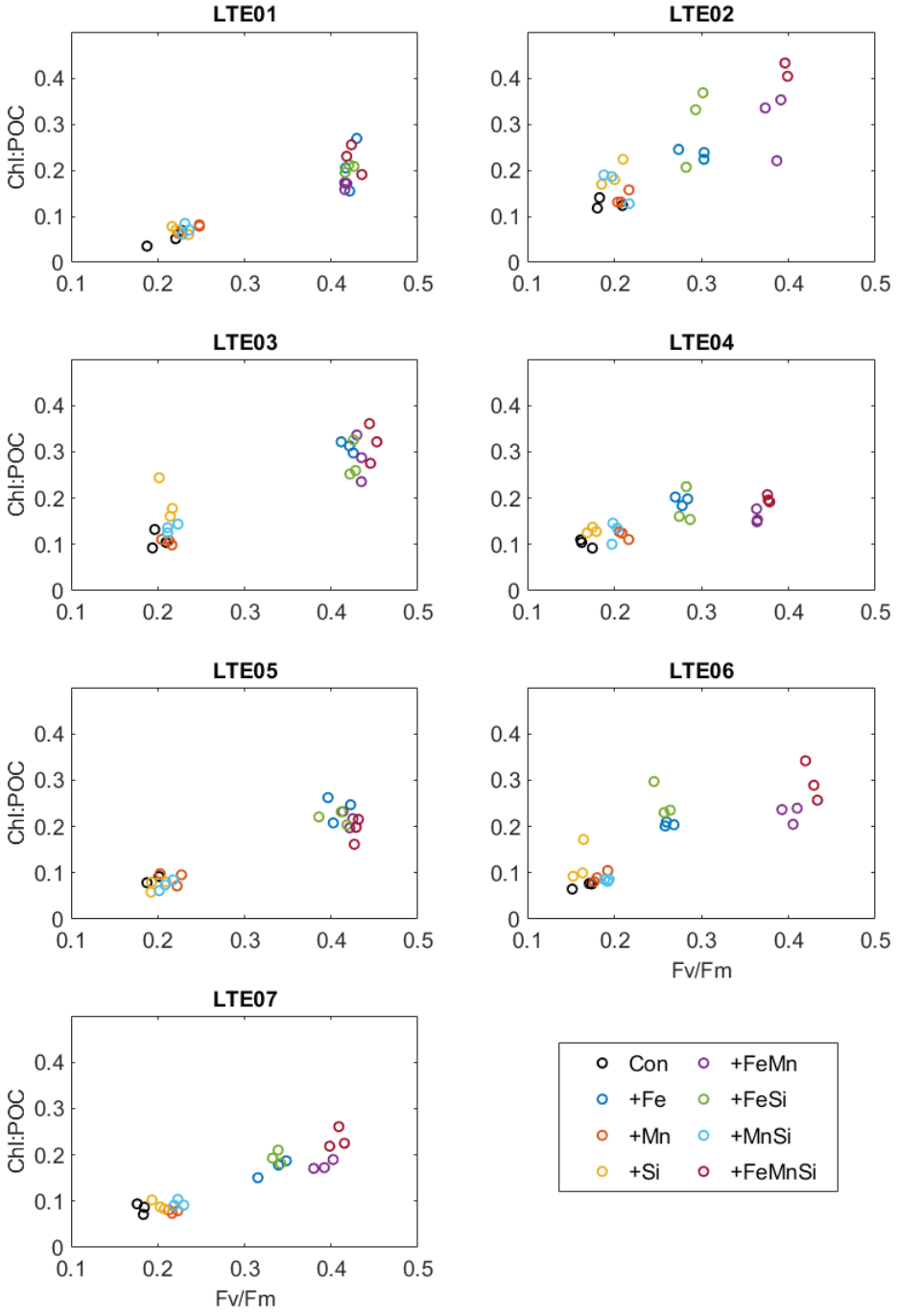


FIGURE 4.1: The ratio of chlorophyll to particulate organic carbon (µg Chl : µmol POC) is displayed against Fv/Fm; a marker for stress in photosystem II. In this case, a low Fv/Fm is indicative of phytoplankton suffering from Fe limitation in the treatments where none was added. Data points are colour-coded by treatment.

Both the formulation of Chl and C synthesis requires the calculation of $P^C_{max}$, the carbon-specific light-saturated photosynthesis rate (Equation 4.1). Maximum growth rate ($\mu_{max}$) is factored by a quota term of the limiting nutrient so that $P^C_{max}$ rises linearly between $Q_{min}$ and $Q_{opt}$ but plateaus between $Q_{opt}$ and $Q_{max}$.

$$P^C_{max} = \mu_{max} \times min\left(\frac{Q - Q_{min}}{Q_{opt} - Q_{min}}, 1\right) \tag{4.1}$$

The rate of carbon synthesis (photosynthesis) (Equation 4.2) is comprised of the carbon-specific photosynthesis rate $P^C$, defined by the first two terms in the equation, and the current C biomass. $P^C$ is a function of irradiance (E), Chl:C ratio ($\theta^C$) and $\alpha^{chl}$, the initial slope of the photosynthesis-irradiance curve. The effect of temperature and the cost of biosynthesis are ignored (Geider et al., 1998).

$$\frac{\delta C}{\delta t} = P^C_{max} \times \left(1 - exp\left(\frac{-\alpha^{chl}\theta^C E}{P^C_{max}}\right)\right) \times C \tag{4.2}$$

The rate of chlorophyll synthesis (Equation 4.3) is a product of $P^C$ and C modified by a ratio denoting the proportion of photosynthate that goes into chlorophyll biosynthesis (Geider et al., 1997). This ratio is formulated by the maximum Chl:C ratio ($\theta^C_{max}$) divided by the instantaneous light harvesting capacity ($\alpha^{chl}\theta^C E$).

$$\frac{\delta Chl}{\delta t} = \left(P^C_{max} \times \left(1 - exp\left(\frac{-\alpha^{chl}\theta^C E}{P^C_{max}}\right)\right)\right)^2 \times \frac{\theta^C_{max}}{\alpha^{chl}\theta^C E} \times C \tag{4.3}$$

The value for $\alpha^{chl}$ was taken from Buitenhuis and Geider (2010), while the value of $\theta^C_{max}$ was taken from experimental observations of Chl:POC (Figure 4.1) (Table 4.1). The mean irradiance of the incubation lighting scheme detailed in Chapter 3 was chosen for E. In later experiments, $\alpha^{chl}$ and $\theta^C_{max}$ were separated into diatom and non-diatom parameters to allow for the effect of their different physiology. Initial Chl, N, Si, Mn were provided by the mean initial conditions in the control bottles (Table 4.2). In addition, final observations of biogenic silica were used for initial cellular Si.

### 4.2.2 Genetic algorithm

In general, a genetic algorithm (GA) is a means of parameter optimisation which draws inspiration from natural selection and has been used to parameterise biogeochemical models (Ward et al., 2010; Kelly-Gerreyn et al., 2014; Wood et al., 2014; Wang et al., 2020; Falls et al., 2022). In general, GA's start with a population of randomly generated parameter sets and a cost function, which is describing the distance between the solution using a given parameter set and observations. The lowest cost parameter sets are then stochastically selected from the current and modified (mutated or mated) to form the next generation. By iteratively selecting the

TABLE 4.1: CUSTARD-QUOTA-V2 model parameters and their default values.

| Symbol | Parameter | Value | Units |
|---|---|---|---|
| $\alpha^{chl}$ | initial slopePE curve | 0.23 | g C $m^2$ (g Chl mol photons)$^{-1}$ |
| $\theta^{C}_{max}$ | maximum Chl : C ratio | 0.50 | µg Chl : µmol C |
| E | light intensity | 4730 | µmol photons $m^{-2}$ s-1 |
| $\theta^{C}$ | Chl : C ratio | | µg Chl : µmol C |
| | | | |
| $\alpha^{chl}_{D}$ | diatom $\alpha^{chl}$ | | g C $m^2$ (g Chl mol photons)$^{-1}$ |
| $\alpha^{chl}_{O}$ | non-diatom $\alpha^{chl}$ | | g C $m^2$ (g Chl mol photons)$^{-1}$ |
| $\theta^{Cmax}_{D}$ | diatom $\theta^{C}_{max}$ | | µg Chl : µmol C |
| $\theta^{Cmax}_{O}$ | non-diatom $\theta^{C}_{max}$ | | µg Chl : µmol C |

fittest parameter sets and keeping their offspring or mutants for the next generation, the model solution trends closer to the observations over generations. The combination of 'survival of the fittest' and genetic exploration by crossover or mutation within the GA creates a good balance between reaching a cost minimum and exploration which helps avoid it becoming stuck in local minima (Falls et al., 2022).

TABLE 4.2: CUSTARD-QUOTA-V2 model new or altered initial conditions.

| | LTE01 | LTE02 | LTE03 | LTE04 | LTE05 | LTE06 | LTE07 | Units |
|---|---|---|---|---|---|---|---|---|
| Mn | 0.17 | 0.09 | 0.18 | 0.04 | 0.15 | 0.22 | 0.26 | nmol $L^{-1}$ |
| Di Chl | 0.30 | 1.36 | 0.40 | 2.07 | 0.47 | 0.82 | 0.64 | µg $L^{-1}$ |
| O Chl | 0.08 | 0.34 | 0.10 | 0.52 | 0.11 | 0.21 | 0.16 | µg $L^{-1}$ |
| Di $Q_{Si}$ | 0.72 | 4.41 | 0.80 | 6.55 | 1.20 | 4.34 | 1.01 | mol Si : mol C |

In this case, the GA was given a range within which to pick the random first generation of parameter sets or 'genotypes', which was initially set to a factor of 2 either side of the original parameters described in Table 3.2, with the exception of the initial condition of starting diatom fraction which was allowed to vary between 0 and 1. The rule of thumb is that the population size or 'number of genotypes' should match the number of parameters being chosen. Each 'genotype' is used to run the model and its performance relative to the experiment incubations is returned according to a cost function. Here, the cost function is described as the total misfit of the model to observations of Chl, DIN and Si (Equation 4.4) where n is the number of observations, $M_i$ is the model output for each treatment in each experiment and $O_i$ is the corresponding observation. This was performed separately for each observation type and then summed to be able to compare their contribution to the misfit.

$$\sum_{i=1}^{n} \left( \frac{M_i - O_i}{O_i} \right)^2 \tag{4.4}$$

The fittest 'genotype' of that generation i.e. the one with the lowest cost is passed to the next without modification. The remaining genotypes are weighted by their cost and then two are randomly selected so that those with the lowest cost are more likely to be chosen. Within a genotype, the parameter set is stored as a binary number. A random point is chosen along this parameter chain, dividing it into two sets of parameters. One of these segments is then switched with the other genotype creating a new genotype with elements of both parents. Once the new population has been filled by this method, known as crossover, the genotypes are run in the model and the process repeats.

The number of generations should be determined by the point at which the cost of the parameter ceases declining and levels out. In this case, 3000 generations were sufficient. This process was repeated a minimum of 10 times per optimisation to increase the chances of avoiding local minima by allowing the random element of the algorithm to explore more of the parameter space.

In this study the GA optimisation technique was chosen over other methods to suit the parameter set at hand. Stochastic optimisation methods are superior for searching large parameter spaces and in this case as many as 42 parameters will be optimised. Compared to another popular stochastic method, the simulated annealing algorithm, the GA has been found to converge faster on an optimal solution (Athias et al., 2000). The GA technique is also less prone to falling into local minima than deterministic techniques such as variational adjoint modelling. Methods such as Latin Hypercube are better suited toward setting up model ensembles with a smaller number of parameters (Urban and Fricker, 2010).

### 4.2.3 Experiments

This section will explain the order of the experiments conducted in this chapter to provide an overview and give context for the work undertaken. Because of the variance in Chl:POC ratio observed across the experiments and the desire to provide direct modelling of chlorophyll for fitting to observations by the GA; the CUSTARD-QUOTA model used in chapter 3 was updated with a chlorophyll state variable which is allowed to vary relative to carbon (CUSTARD-QUOTA-V2). Therefore the first results shown in this chapter are runs of this new model setup to check its suitability for use with the GA.

TABLE 4.3: A description of each optimisation carried out with the genetic algorithm.

| Optimisation | Observations used | Parameters fitted | Diatom fraction condition |
|---|---|---|---|
| 1 | LTE's 1-7 | 42 | 1 |
| 2 | LTE's 1-6 | 42 | 1 north, 1 south |
| 3 - North | LTE 1, 3, 5 | 42 | 3 (one per exp.) |
| 3 - South | LTE 2, 4, 6 | 42 | 3 (one per exp.) |
| 4 | LTE's 1-7 | 42 | 7 (one per exp.) |
| Sensitivity | LTE's 1-7 | 42 | 7 (one per exp.) |
| Hybrid | LTE's 1-7 | 22 | 7 (one per exp.) |

Evaluating the work conducted with the GA on the variable chlorophyll model, the results are divided into a number of different optimisations which were undertaken to find the ideal way to fit the parameters using the observations. Table 4.3 describes the targets of each optimisation in terms of observations fitted to, number of parameters searched for and one initial condition, the proportion of diatoms to non-diatoms, was also picked by the GA.

Optimisation 1 is the simplest case scenario, where the GA is used to fit every LTE site and every model parameter. The GA is also enabled to find one diatom fraction which is used for all LTE locations.

The contextual data explored in Section X revealed a north-south gradient in chlorophyll with the bloom captured mainly by the southern stations. It was hypothesised that southern stations were likely more diatom dominated than in the north. Optimisation 2 is therefore set up to determine if allowing a separate diatom fraction between northern (LTE's 1, 3 and 5) and southern experiments (LTE's 2, 4 and 6) would improve the parameter fit and whether the GA would pick different diatom fractions for north and south based on the observations provided.

Optimisation 3 takes this idea further by conducting two separate optimisations for north and south in order to observe latitudinal variations in all parameters. Diatom fraction is further divided with one value for each LTE to observe whether they are consistent within their latitude.

Optimisation 4 is prepared similarly to number 1, fitting all sites and all parameters in one optimisation. However, in this instance, full freedom is given to the diatom fraction condition to vary between each LTE. These settings lie above optimisation 2 and below optimisation 3 in terms of degrees of freedom offered to the GA.

Providing the GA more liberty to vary parameters or diatoms fraction between experiment sites led to a decreasing cost of fit. However, at some point offering less constraints to the algorithm must hinder the usefulness and wider applicability of the parameters picked. Therefore, a sensitivity test was performed by running 120 separate optimisations. If a similar parameter value was picked in each of these runs it would show that the parameter was well constrained by the observations. On the other hand, if a parameter did not trend toward a certain value or appeared to be picked randomly within the range given to the GA, this shows it is unconstrained by the CUSTARD data. The setup chosen for this test was taken from optimisation 4 which was determined to be a good balance between freedom of community structure and only one set of parameters.

With some of the parameters determined unconstrained by the sensitivity test, the next step was to run a hybrid optimisation with the same setup. In this experiment, well-constrained parameters would be left to be chosen by the GA while all others would be left as their original hand-picked values.

The final result section of Chapter 4 compares the diatom fractions picked by the GA for each LTE with HPLC data collected on the cruise which became available after these algorithm experiments were conducted. The pigment data offers a relative comparison of diatom fraction between the experiment sites and therefore can help determine whether the observation data were sufficient to force the GA to replicate real trends in community structure between north and south when it chose its own values for diatom fraction.

## 4.3 Results

### 4.3.1 Variable Chlorophyll Model

The introduction of a new Chl state variable into the model that allowed differences in Chl:C produces new model solutions for each experiment and treatment (Figure 4.2) which can be compared to the original CUSTARD-QUOTA model presented in Figure 3.10. Despite being independently generated now, the Chl outputs of this model show very little alteration compared to the previous simpler model, remaining very well fitted to the observations. While the absolute fit of LTE 1 and 6 in particular could be improved, they adhere to the patterns of limitation found in the data. There has been a downregulation in $\Delta$DIN outputs, which has benefited the fit of some experiments (LTE 1 and 7) at the detriment of the others. $\Delta$Si has remained mostly unchanged as has the ratio of $\Delta$DIN to $\Delta$Si.

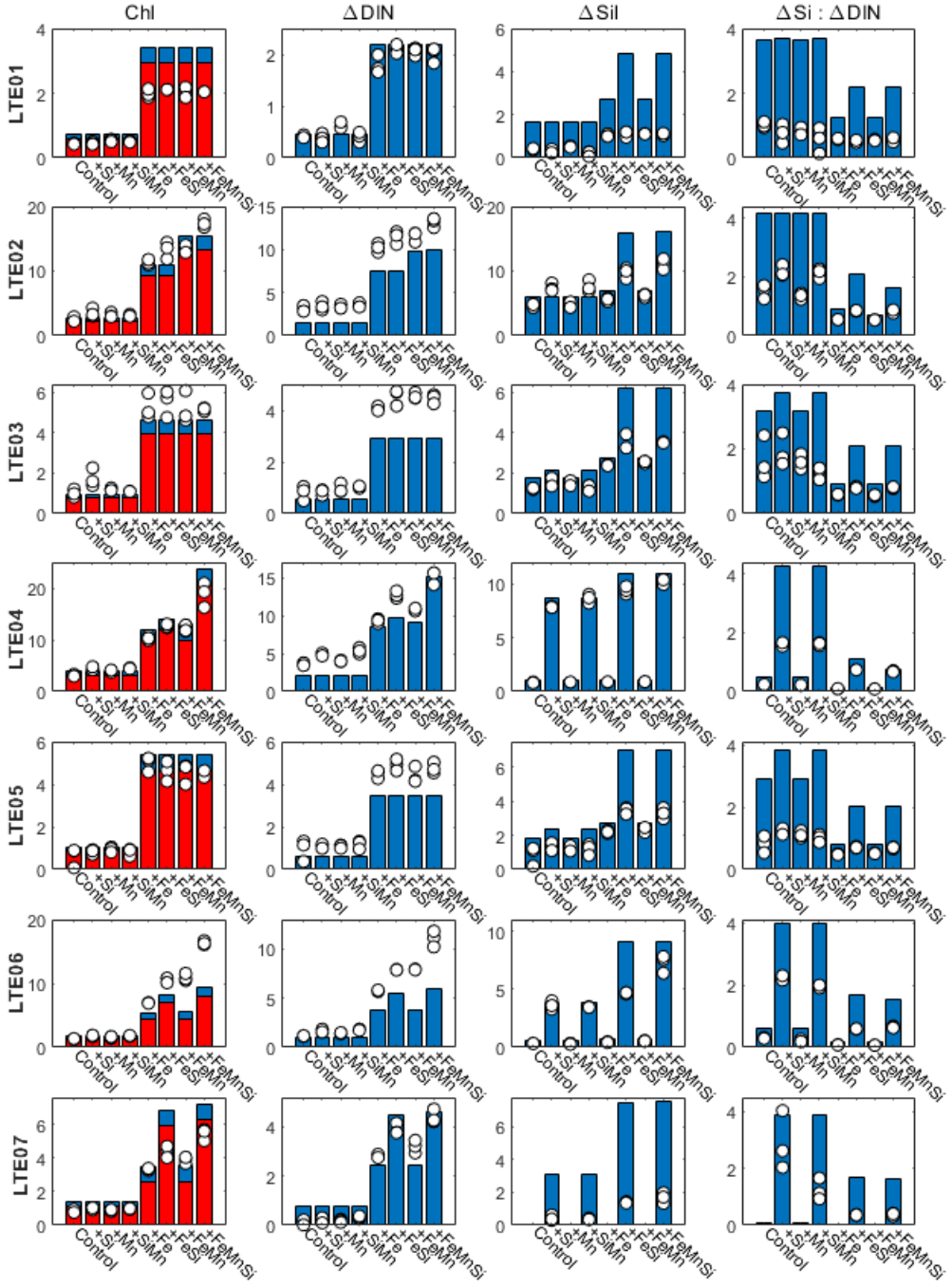


FIGURE 4.2: Comparison of data from the endpoint of each 'large-type' experiment against the results of a quota model with a variable chlorophyll to carbon ratio (CUSTARD-QUOTA-V2). Triplicate experimental observations for chlorophyll, change in dissolved inorganic nitrogen (DIN) (i.e. drawdown), change in silicic acid (Si) and the ratio of ΔSi to ΔN are indicated by white markers. Model results for the sum of both the diatom and the 'other phytoplankton' class have blue bars while the diatom class alone are shown in red bars for the chlorophyll. All nutrient concentrations are given in μmol $L^{-1}$.

The same CUSTARD-QUOTA-V2 model was run with the addition of observation based starting conditions for dissolved Mn and cellular Si (Figure 4.3). Although LTE's

2, 4 and 6 show a slightly worse fit to Chl observations, an improvement is found in ΔDIN : ΔSi for all but LTE 3 and 7 due to minor adjustments in ΔDIN and ΔSi.

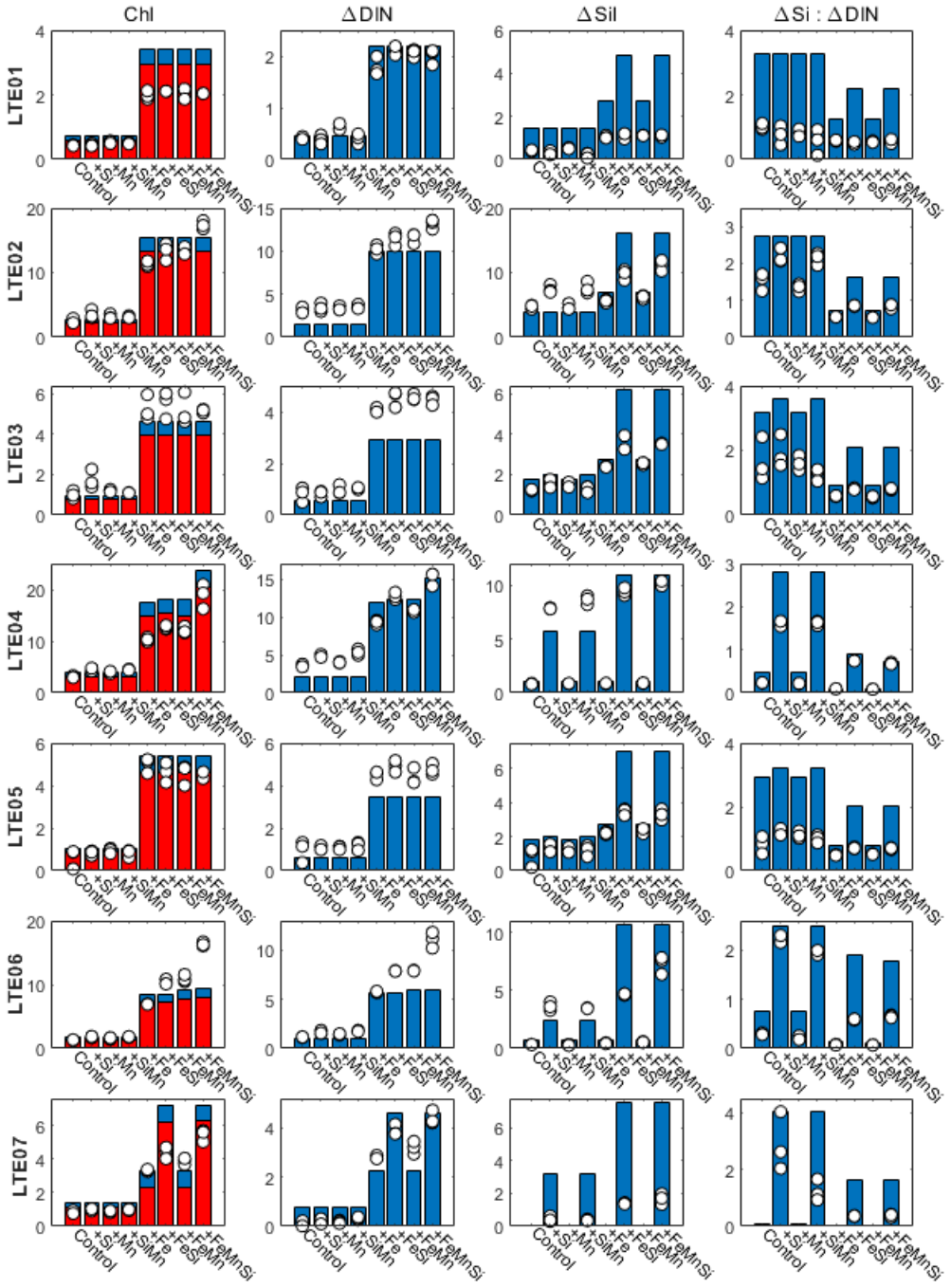


FIGURE 4.3: Comparison of data from the endpoint of each 'large-type' experiment against the results of the CUSTARD-QUOTA-V2 model with the addition of observation driven starting conditions for Mn and cellular Si. Triplicate experimental observations for chlorophyll, change in dissolved inorganic nitrogen (DIN), change in silicic acid (Si) and the ratio of ΔSi to ΔN are indicated by white markers. Model results for both the diatom and the 'other phytoplankton' class have blue bars while the diatom class alone are shown in red bars. All nutrient concentrations are given in μmol $L^{-1}$.

### 4.3.2 Genetic Algorithm

To fit the CUSTARD-QUOTA-V2 model to the observations from the incubation experiments, a GA was used to select for parameter sets that produced the lowest deviation, in a process similar to natural selection. The model chosen to run with the GA has the same number of parameters and same starting conditions as that shown in Figure 3. This includes a separate $\alpha^{chl}$ and $\theta^{C}_{max}$ for diatoms and non-diatoms, as well as using the observed initial Chl, dissolved N and Si, BSi and dissolved Mn as starting conditions while leaving the GA to select the initial fraction of diatoms versus non-diatoms. Below are recorded the cost results for the 4 different optimisation experiments that were performed (Table 4.4) in addition to a comparison of the algorithmically derived parameter sets (Figure 4.4).

TABLE 4.4: The total misfit cost of each genetic algorithm experiment and the contribution of each state variable included in the calculation. The total misfit divided by the number of LTE's parameterised is included to allow for intercomparison.

| Optimisation | Mean misfit per LTE | Total Misfit | ΔChl Misfit | ΔDIN Misfit | ΔSi Misfit |
|---|---|---|---|---|---|
| Non-GA | 135.8 | 950.67 | 642.46 | 60.00 | 248.21 |
| 1 | 8.43 | 59.00 | 21.66 | 18.22 | 19.12 |
| 2 | 3.86 | 23.17 | 14.32 | 2.47 | 6.38 |
| 3 - North | 2.93 | 8.79 | 7.36 | 0.32 | 1.11 |
| 3 - South | 0.95 | 2.86 | 1.85 | 0.50 | 0.51 |
| 3 - Combined | 1.94 | 11.66 | 9.21 | 0.82 | 1.62 |
| 4 | 4.58 | 32.07 | 12.53 | 8.32 | 11.22 |
| Sensitivity | 4.21 | 29.48 | 10.78 | 7.48 | 11.21 |
| Hybrid | 4.63 | 32.44 | 12.42 | 9.11 | 10.91 |

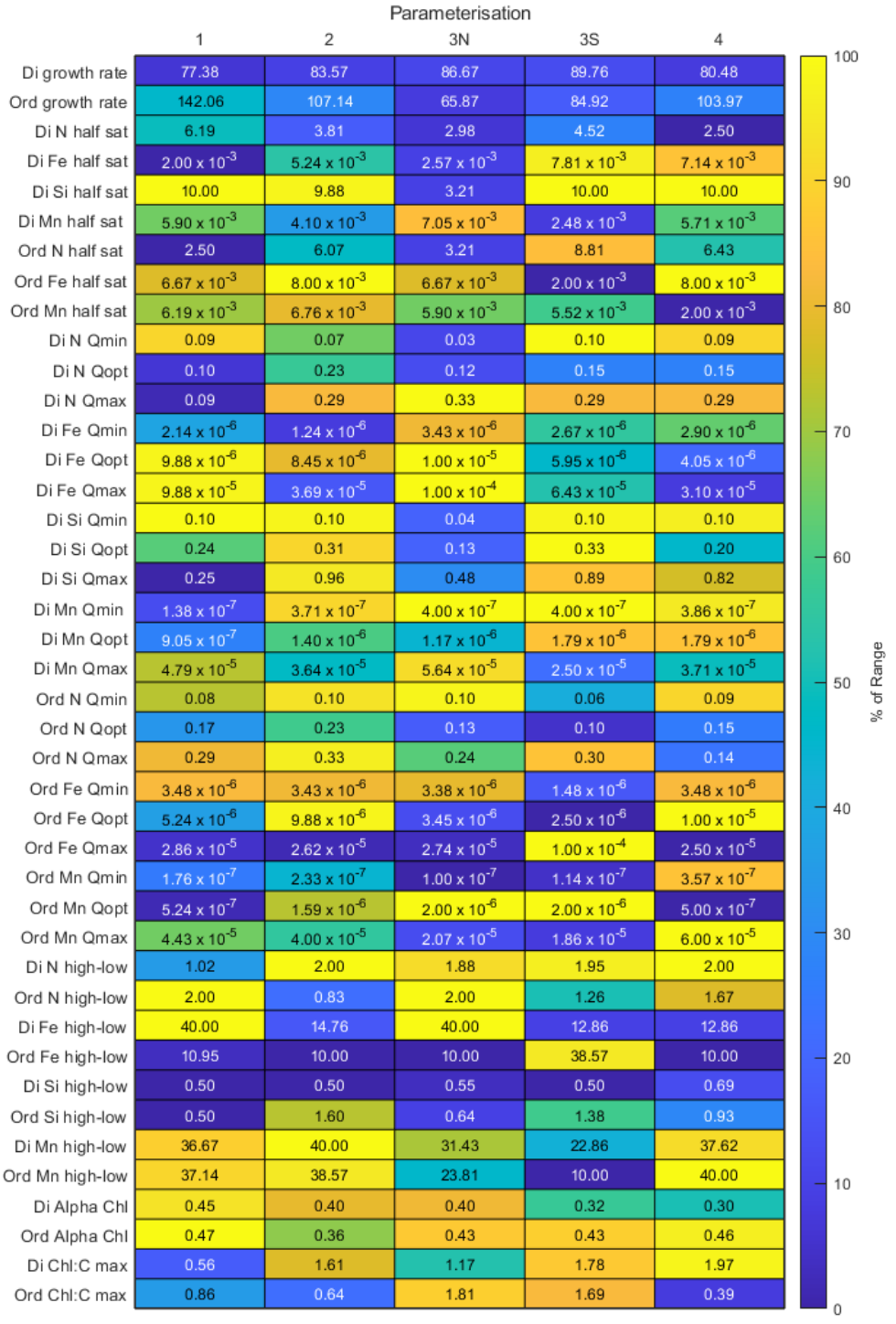


FIGURE 4.4: A table of parameter sets generated by 4 different genetic algorithm parameterisations. Each value is by the percent of the parameter range given to the algorithm it represents. Thus a row of similar colours indicates that each optimisation selected for a similar value relative to the range of possible values. Units are $yr^{-1}$ for growth rate, µmol $L^{-1}$ for half saturation constants and mol nutrient : mol C for quotas.

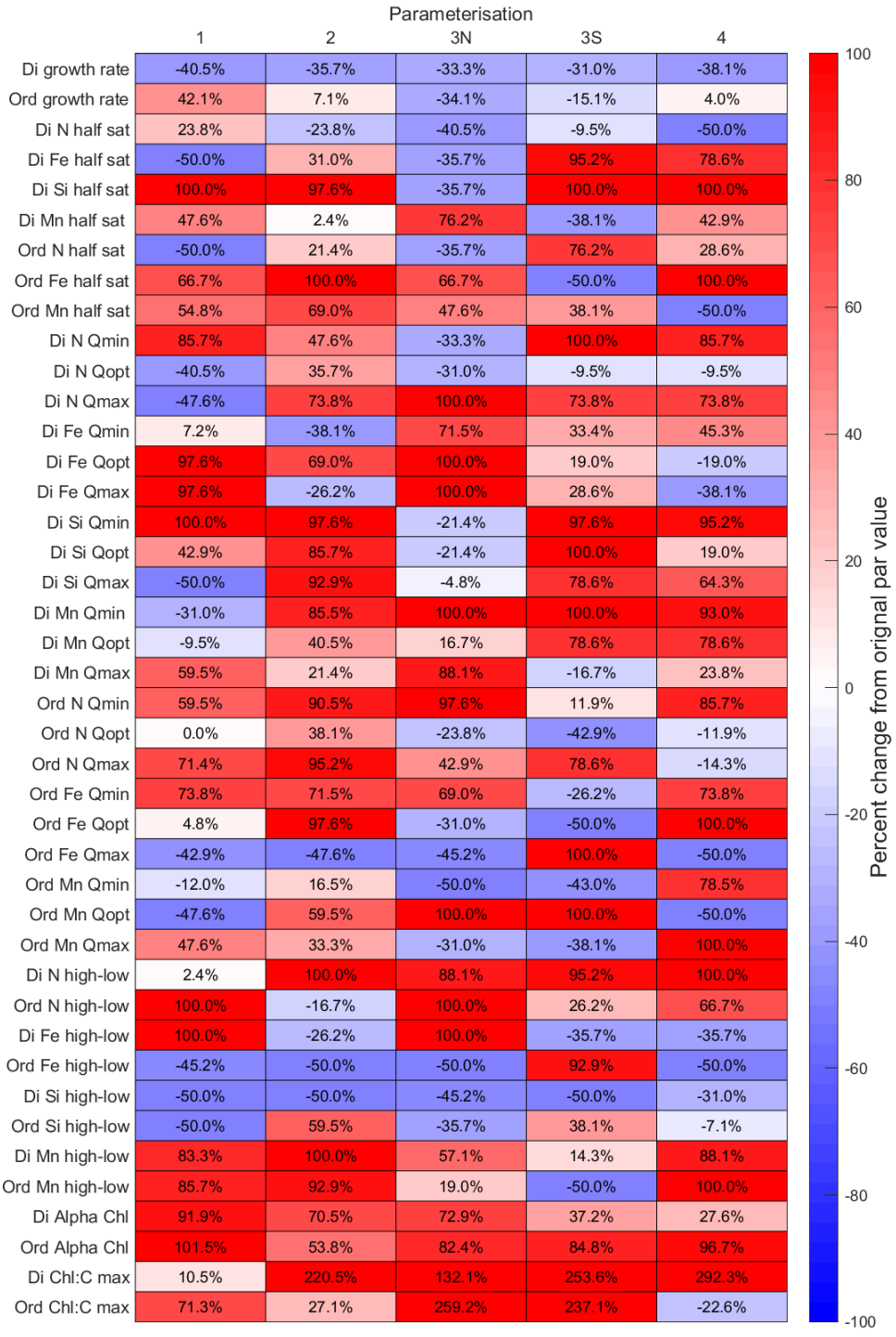


FIGURE 4.5: A table showing how parameter sets generated by 4 different genetic algorithm optimisations vary from the original hand-picked parameter set. Each value and colour represents percent change. A row of similar colours indicates that each optimisation selected for a similar value. Units are $yr^{-1}$ for growth rate, µmol $L^{-1}$ for half saturation constants and mol nutrient : mol C for quotas. Chl:C max values may eclipse 100% as they were given a wider range.

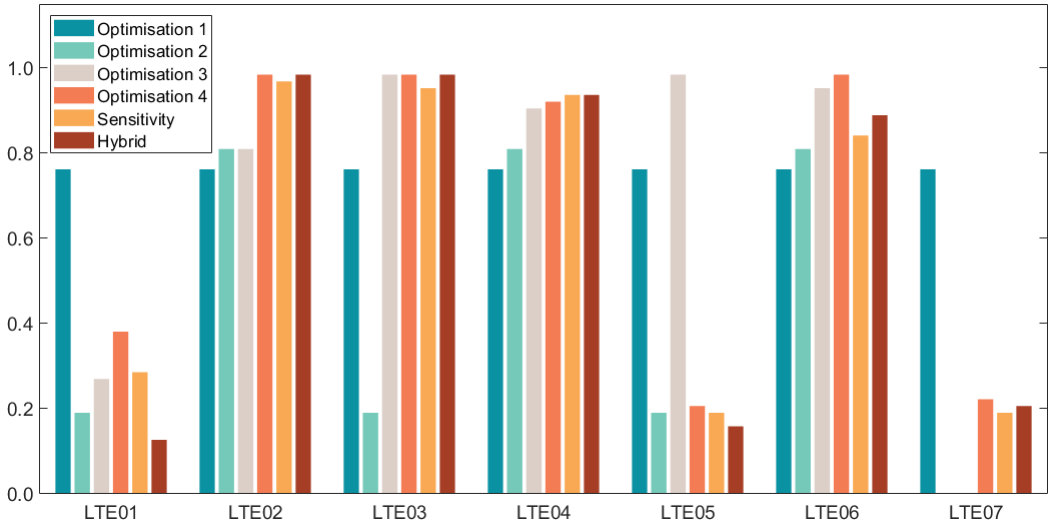


FIGURE 4.6: Initial diatom fraction picked by the genetic algorithm is shown for each optimisation run and each experiment. Optimisations 2 and 3 do not include LTE07 as they divide experiments into north and south.

#### 4.3.2.1 Optimisation 1

In the first GA optimisation, the model was run in the above manner with 42 parameters and 1 initial condition, the starting diatom fraction (here assumed the same across all experiments), selected for by the GA (Figure 4.5). The mean misfit per LTE was 8.43 which is a 93% reduction from the non-GA fitted model (Table 4.4). Chl misfit contributed the most to this value although there was a relatively even spread between the misfit of Chl, N and Si. In comparison to the non-GA fitted model (Figure 4.3), Chl outputs are generally lower and diatoms account for a lower proportion of the final value despite the starting diatom fraction chosen by the GA being 0.76 (Figure 4.6), only slightly lower than the original 0.8. ΔDIN remains relatively unchanged from the base model whereas there seems to be a poorer representation of limitation patterns in ΔSi with the exception of LTE01 (Figure 4.7). LTE's 1, 2, 3, 5 and 6 arguably show improvement in their fit, though sometimes at the cost of differentiation between treatments.

In comparing the parameters chosen to their ranges (Figure 4.4), 7 parameters approach the allowed upper limit while 5 approach lower limits. This notably includes 100% increases in $K_{Si}$, $Q^{Fe}_{opt}$, $Q^{Fe}_{max}$, $Q^{Si}_{min}$ for diatoms and $\alpha^{chl}$ values for both groups. In addition, while diatom growth rate was originally chosen to be higher than the non-diatoms, the GA has given non-diatoms double the growth rate of the other group (+65 $yr^{-1}$ from $\mu_O$ to $\mu_D$). $Q^{Si}_{max}$ was reduced by 50% as was the ratio of Si-limited and Si-saturated maximum uptake rate for both diatoms and non-diatoms.

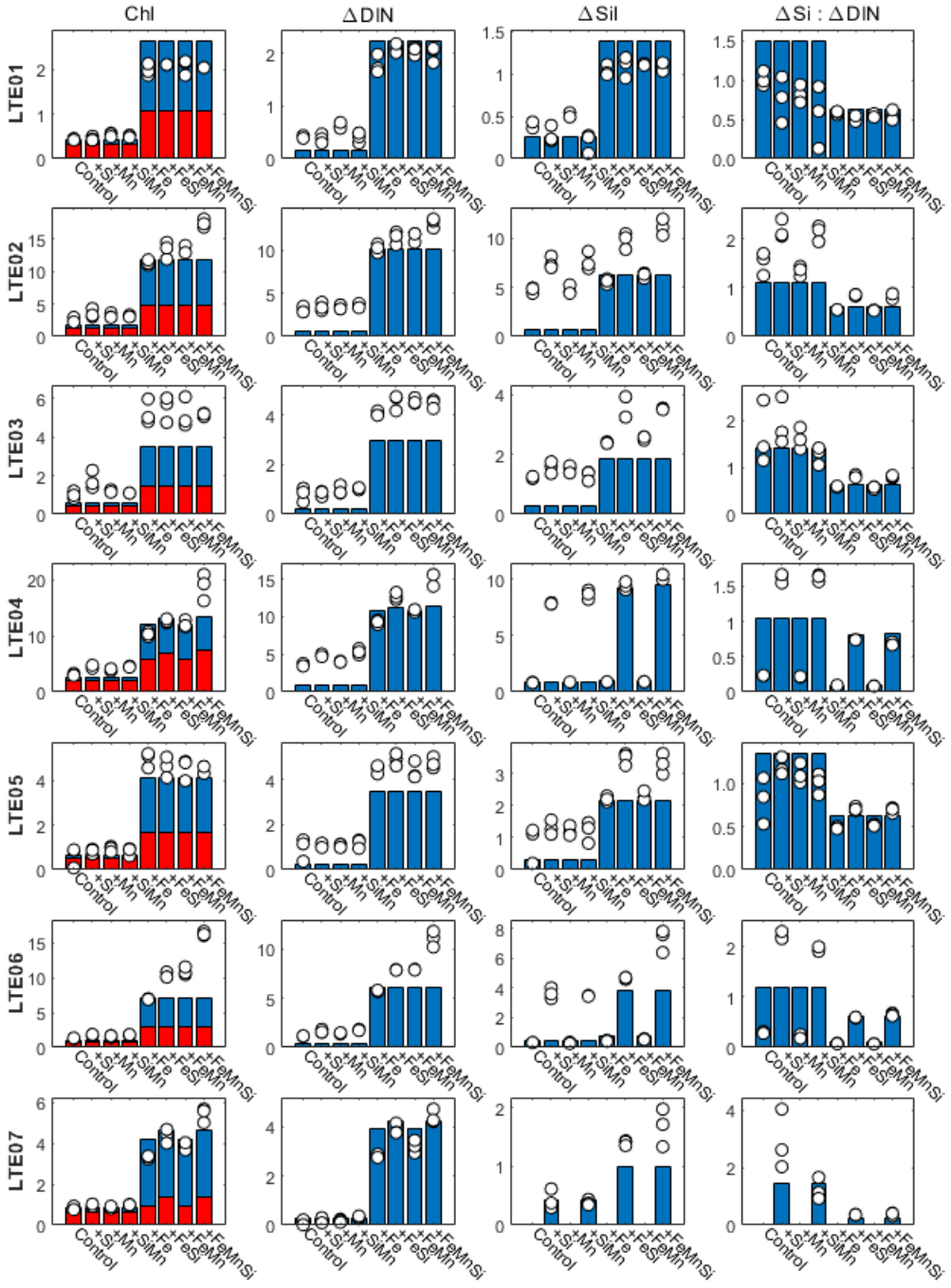


FIGURE 4.7: The results of Optimisation 1 by the genetic algorithm of the CUSTARD-QUOTA-V2 model compared with data from the endpoint of each 'large-type' experiment. Triplicate experimental observations for chlorophyll, change in dissolved inorganic nitrogen (DIN), change in silicic acid (Si) and the ratio of ΔSi to ΔN are indicated by white markers. Model results for the sum of both the diatom and the 'other phytoplankton' class have blue bars while the diatom class alone are shown in red bars. All nutrient concentrations are given in μmol $L^{-1}$.

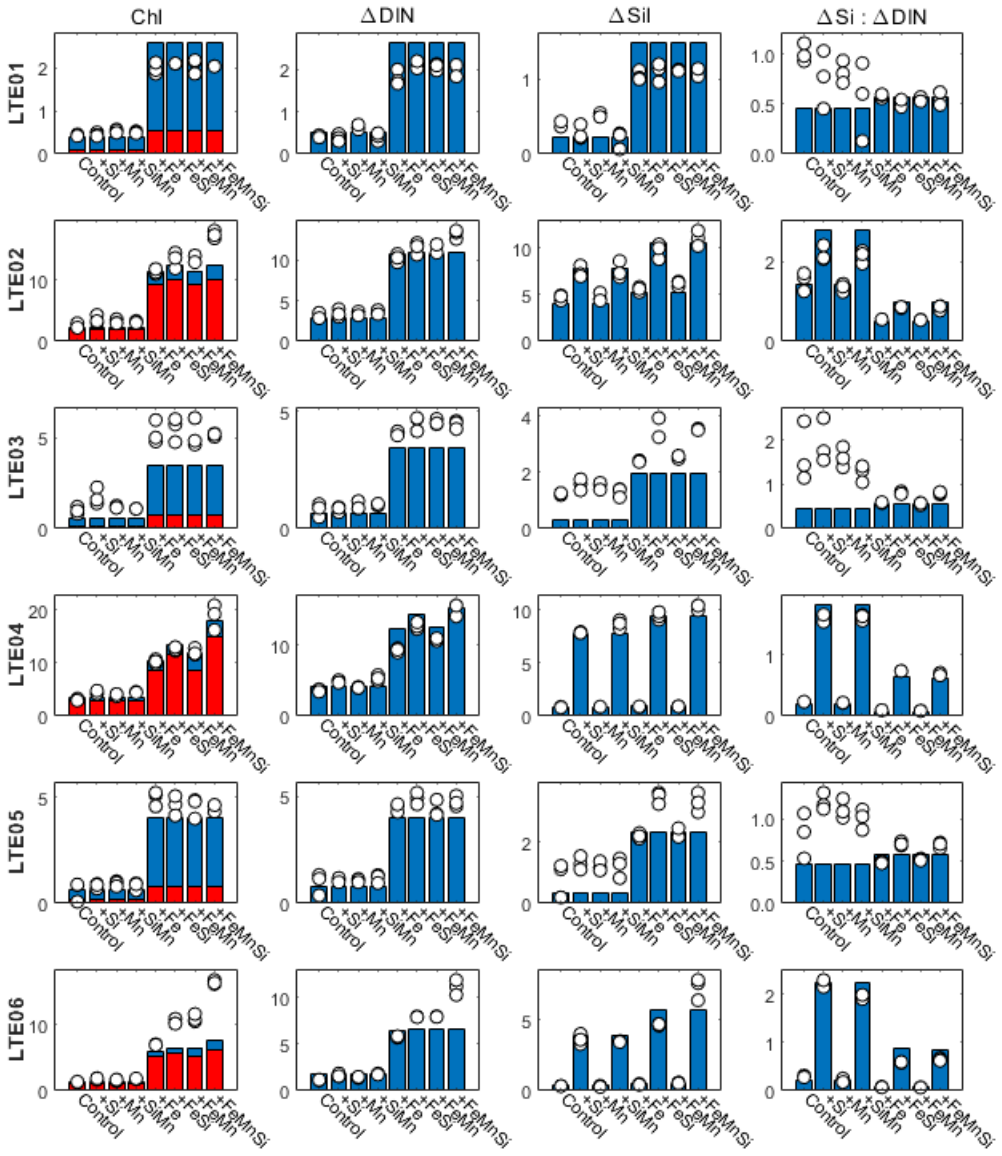


FIGURE 4.8: The results of Optimisation 2 by the genetic algorithm of the CUSTARD-QUOTA-V2 model compared with data from the endpoint of each 'large-type' experiment. A separate initial diatom fraction was fitted for the northern (1, 3, 5) and southern experiments (2 ,4, 6). Triplicate experimental observations for chlorophyll, change in dissolved inorganic nitrogen (DIN), change in silicic acid (Si) and the ratio of ΔSi to ΔN are indicated by white markers. Model results for the sum of both the diatom and the 'other phytoplankton' class have blue bars while the diatom class alone are shown in red bars. All nutrient concentrations are given in μmol $L^{-1}$.

#### 4.3.2.2 Optimisation 2

The model was then run with the same set of parameters left free to be chosen by the GA, but allowing for the selection of two separate starting diatom fractions; one for the northern experiments (LTE's 1, 3 and 5) and one for the southern experiments (LTE's 2, 4 and 6). LTE 7 was excluded from this fit as it was located at a latitude halfway between these other experiments. The lowest cost produced by this GA run

was a mean of 3.86 per LTE, an 54% improvement on optimisation 1 and a 97% improvement on the non-GA fitted model (Table 4.4). In this case, Chl dominated contribution to the total misfit making up 62% while N and Si contributed 11% and 28% respectively. Superior fits appear visually across the board in the southern experiments (Figure 4.8), producing very good reproductions of the values and patterns of ΔSi:ΔDIN. The northern experiments also produce good fits to ΔDIN but appear to underestimate Si uptake in non-Fe treatments. Diatoms have a much lower contribution to final Chl values in the northern experiments while the southern LTE's remain at a similar fraction to the non-GA fitted model.

As for optimisation 1, non-diatom growth rate was optimised as higher than that of diatoms, though in this case to a lesser extent (+24 $yr^{-1}$ from $\mu_O$ to $\mu_D$) (Figure 4.4). Starting diatom fractions were selected as 0.19 in the north compared with 0.81 in the south (Figure 4.6). The diatom parameters $K_{Si}$, $Q^{Si}_{min}$, $Q^{Si}_{max}$, and $\rho^{hi}_{max}/\rho^{lo}_{max}$ for N and Mn as well the non-diatom $K_{Fe}$ and $Q^{Fe}_{opt}$ neared or reached the upper range boundary of +100% while non-diatom $Q^{Fe}_{max}$ and Fe $\rho^{hi}_{max}/\rho^{lo}_{max}$ in addition to diatom Si $\rho^{hi}_{max}/\rho^{lo}_{max}$ have bottomed out (Figure 4.5). Only 4 parameters remain within ±20% of the hand-picked value. All diatom Si related parameters have moved to the extreme ends of their respective ranges.

#### 4.3.2.3 Optimisation 3

In this optimisation, the two separate GA fits were performed for the northern and southern experiments. Within each run, a separate initial diatom fraction was provided for each LTE to be chosen by the GA. This resulted in a mean misfit per LTE of 2.93 and 0.95 for the north and south respectively and 1.94 for both combined; a 99% improvement on the non-GA fitted model (Table 4.4). 79% of total misfit was accounted for by Chl while N and Si contributed 7% and 14% respectively. Visually comparing the data, this GA chosen parameter set shows a superior fit in almost every experiment and treatment for Chl, ΔDIN, ΔSi and ΔDIN : ΔSi (Figure 4.9). Diatoms dominate Chl production in all but LTE01.

Initial diatom fractions of 0.27, 0.98 and 0.98 were selected for LTE's 1, 3 and 5 while values of 0.81, 0.90 and 0.95 were found for LTE's 2, 4 and 6 (Figure 4.6). Uniquely, these were the only runs that yielded a higher diatom than non-diatom growth rate. Both northern and southern GA runs have chosen similarly high diatom $Q^{Mn}_{min}$ and non-diatom $Q^{Mn}_{opt}$. In addition, north places diatom $Q^{N}_{max}$, $Q^{Fe}_{opt}$, $Q^{Fe}_{max}$ and Fe $\rho^{hi}_{max}/\rho^{lo}_{max}$ as well as non-diatom $Q^{N}_{min}$ and N $\rho^{hi}_{max}/\rho^{lo}_{max}$ at the top of their ranges, while south tops out diatom $K_{Fe}$, $K_{Si}$, $Q^{N}_{min}$, $Q^{Si}_{min}$, $Q^{Si}_{opt}$ and N $\rho^{hi}_{max}/\rho^{lo}_{max}$ together with non-diatom

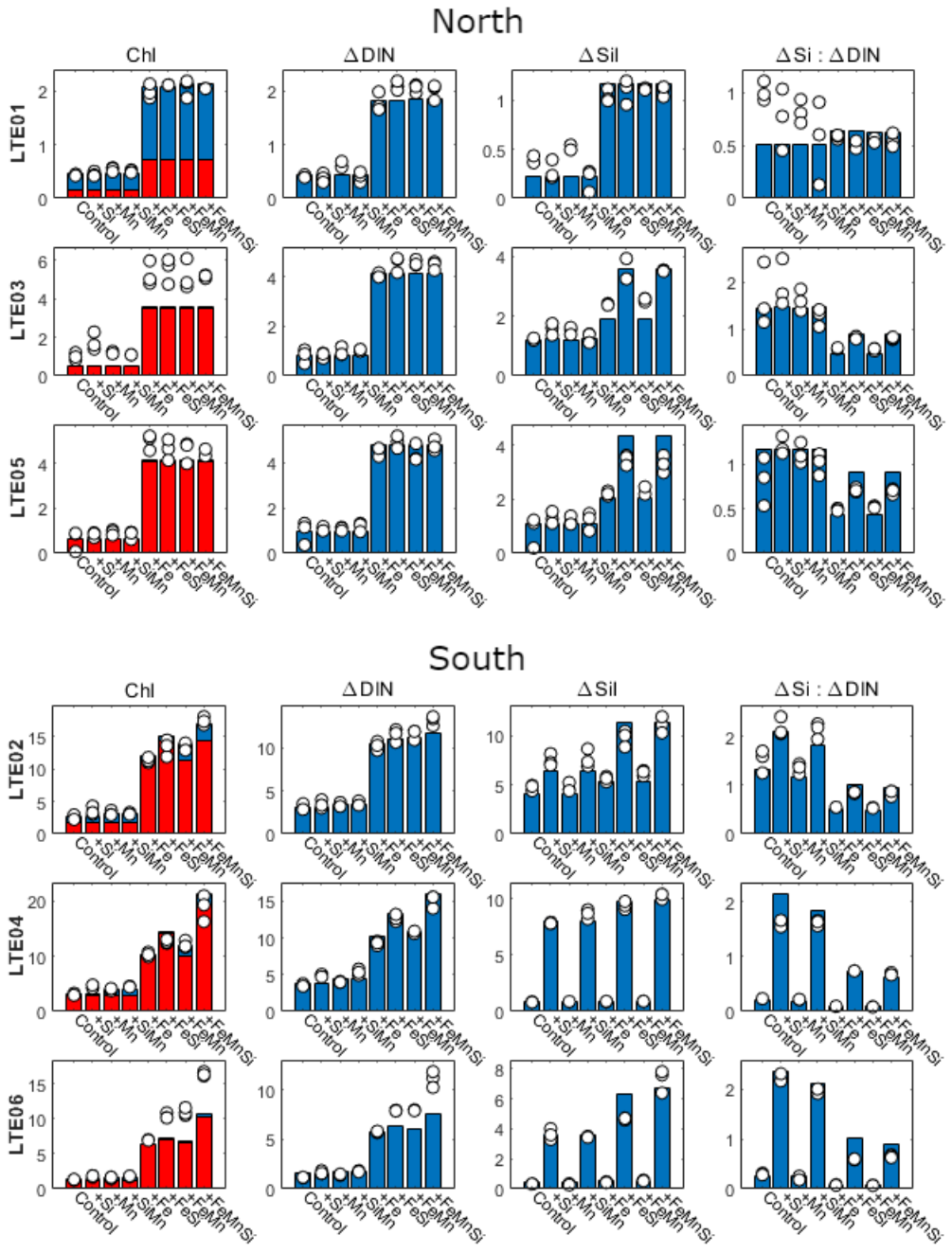


FIGURE 4.9: The results of Optimisation 3 by the genetic algorithm of the CUSTARD-QUOTA-V2 model compared with data from the endpoint of each 'large-type' experiment. A separate fit was performed for the northern (1, 3, 5) and southern experiments (2 ,4, 6) with each LTE given its own initial diatom fraction to be parameterised. Triplicate experimental observations for chlorophyll, change in dissolved inorganic nitrogen (DIN), change in silicic acid (Si) and the ratio of ΔSi to ΔN are indicated by white markers. Model results for sum of both the diatom and the 'other phytoplankton' class have blue bars while the diatom class alone are shown in red bars. All nutrient concentrations are given in μmol $L^{-1}$.

$Q^{Fe}_{max}$. Bottom of range values are incurred for non-diatom $Q^{Mn}_{min}$ and Fe $\rho^{hi}_{max}/\rho^{lo}_{max}$ in the north and non-diatom $K_{Fe}$, $Q^{Fe}_{opt}$ and diatom Si $\rho^{hi}_{max}/\rho^{lo}_{max}$ in the south. There is a clear dichotomy between higher diatom Si quota parameters in the south versus the north and higher diatom Fe quota parameters as well as Fe and Si half saturation constants in the north versus the south.

#### 4.3.2.4 Optimisation 4

In optimisation 4, all the LTE's are parameterised together but each is given its own initial diatom fraction. Given these parameters to select, the GA produces a mean misfit of 4.58 per LTE which constitutes an improvement of 97% but does not perform as well as optimisations 2 and 3 (Table 4.4). Of the total misfit, Chl once again contributed the most with 39%, though N and Si were not far away with 26% and 35% respectively. Comparing the model outputs to observations (Figure 4.10) shows good alignment though not as strong as optimisation 3 (Figure 4.7). Chl, ΔDIN and ΔSi are mostly underestimated in LTE05 though the ratio of ΔSi to ΔDIN is accurate nonetheless. In that LTE the model misses a secondary limitation effect of Si whereas in LTE01 it introduces such an effect that isn't there.

The initial diatom fractions chosen by the GA for LTE's 1-7 were 0.38, 0.98, 0.98, 0.92, 0.21, 0.98 and 0.22 respectively (Figure 4.6). As in 3 other optimisations, non-diatom growth rate is above that of diatoms at similar values to optimisation 2 (+23 $yr^{-1}$ from $\mu_O$ to $\mu_D$) (Figure 4.4). Parameters that reach near or at the top of their range include diatom $K_{Si}$, $Q^{Si}_{min}$ and N $\rho^{hi}_{max}/\rho^{lo}_{max}$ as well as non-diatom $K_{Fe}$, $Q^{Fe}_{min}$, $Q^{Mn}_{max}$ and Mn $\rho^{hi}_{max}/\rho^{lo}_{max}$ (Figure 4.5). Meanwhile, diatom $K_N$ and non-diatom $K_{Mn}$, $Q^{Fe}_{max}$, $Q^{Mn}_{opt}$ and Fe $\rho^{hi}_{max}/\rho^{lo}_{max}$.

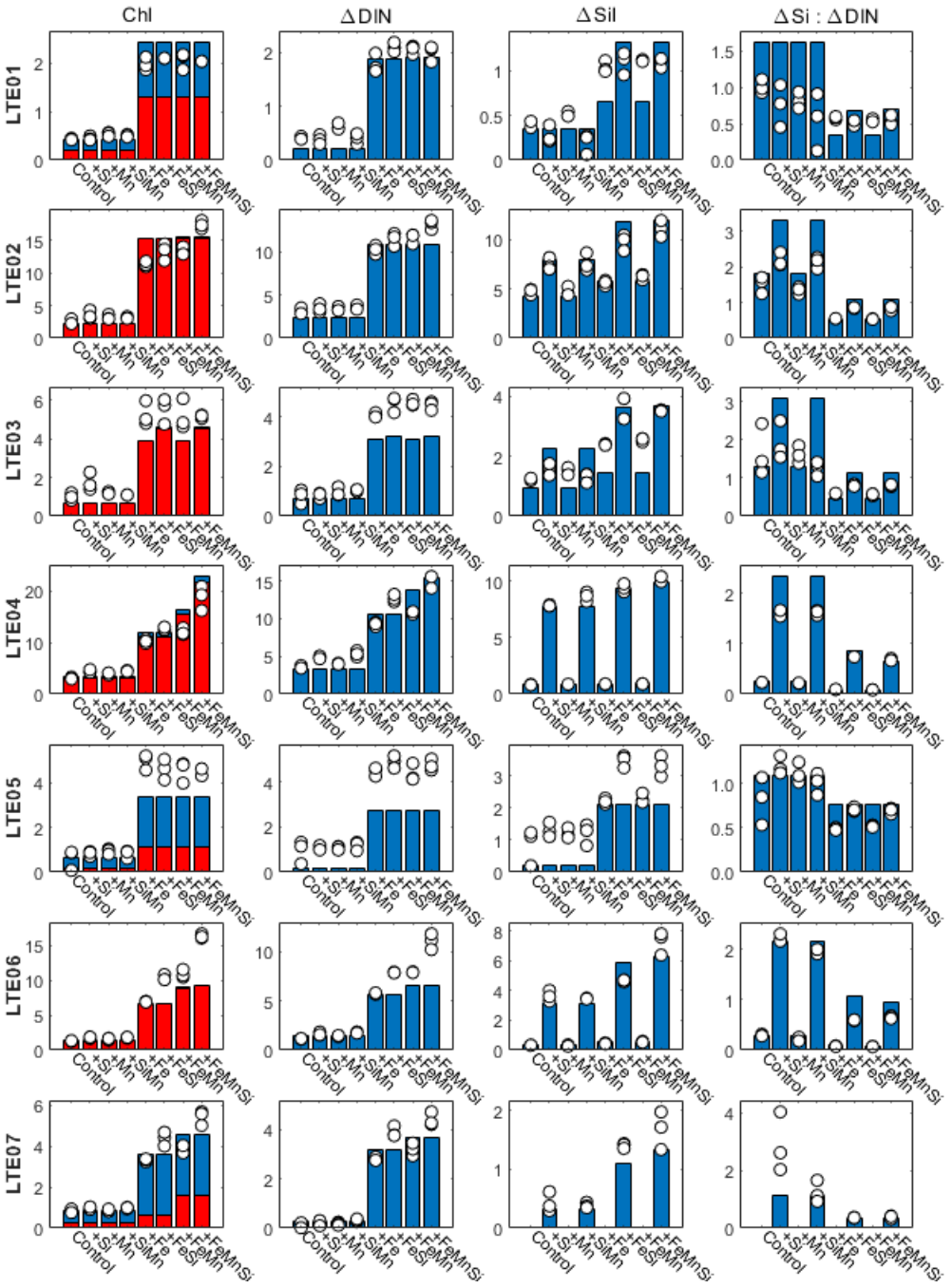


FIGURE 4.10: The results of Optimisation 4 by the genetic algorithm of the CUSTARD-QUOTA-V2 model compared with data from the endpoint of each 'large-type' experiment. Each LTE was given its own initial diatom fraction to be parameterised. Triplicate experimental observations for chlorophyll, change in dissolved inorganic nitrogen (DIN), change in silicic acid (Si) and the ratio of ΔSi to ΔN are indicated by white markers. Model results for the sum of both the diatom and the 'other phytoplankton' class have blue bars while the diatom class alone are shown in red bars. All nutrient concentrations are given in µmol $L^{-1}$.

#### 4.3.2.5 Sensitivity Optimisation

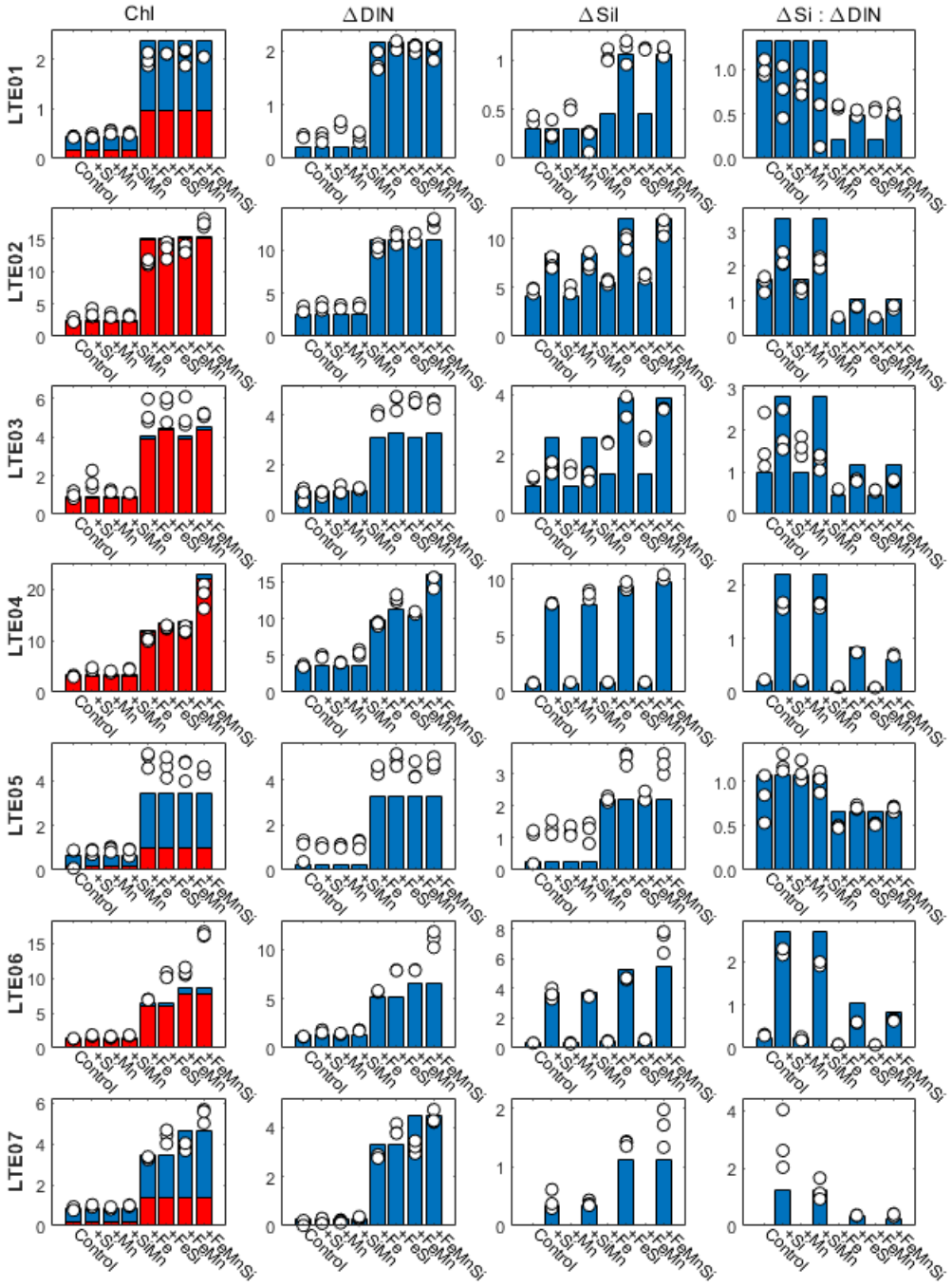


FIGURE 4.11: The results of the sensitivity optimisation by the genetic algorithm of the CUSTARD-QUOTA-V2 model compared with data from the endpoint of each 'large-type' experiment. Each LTE was given its own initial diatom fraction to be parameterised and the algorithm was run 120 times to maximise opportunity for parameter exploration and finding of the lowest cost parameter set. Triplicate experimental observations for chlorophyll, change in dissolved inorganic nitrogen (DIN), change in silicic acid (Si) and the ratio of ΔSi to ΔN are indicated by white markers. Model results for the sum of both the diatom and the 'other phytoplankton' class have blue bars while the diatom class alone are shown in red bars. All nutrient concentrations are given in µmol $L^{-1}$.

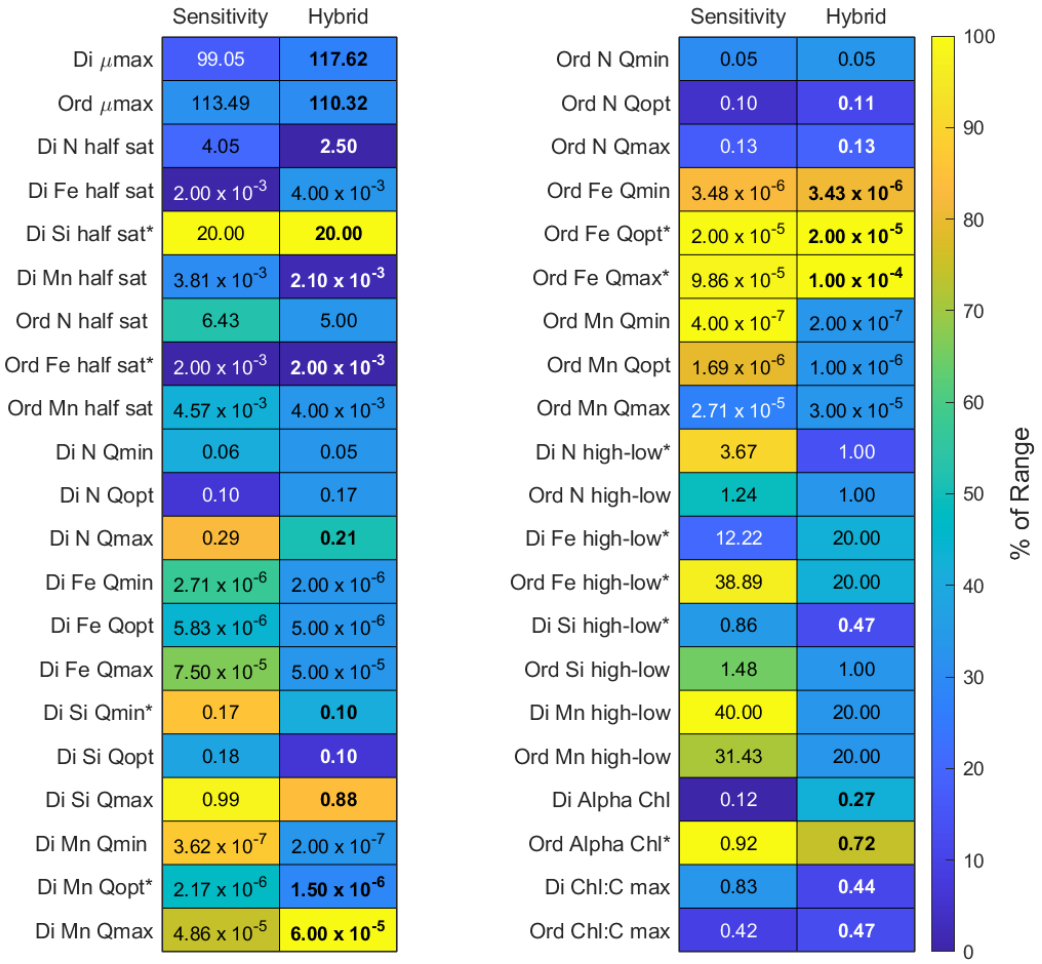


FIGURE 4.12: A table of the lowest cost parameter set generated by a sensitivity optimisation of 120 runs and the hybrid optimisation. Each value is by the percent of the parameter range given to the algorithm it represents. This optimisation features wider ranges for some parameters which are specified by asterisks. Parameters in the hybrid parameterisation picked by the genetic algorithm are in bold. Units are $yr^{-1}$ for growth rate, μmol $L^{-1}$ for half saturation constants and mol nutrient : mol C for quotas.

In the sensitivity optimisation run with the GA, 120 iterations were performed in order to increase the chance of seeking out the lowest possible misfit. The setup chosen was identical to optimisation 4, with the same parameters fit for all LTE's but a separate initial diatom fraction for each. Certain parameters that were commonly observed to reach their range boundaries in optimisation 4 type runs were given double their upper limit. These parameters were diatom $K_{Si}$, $Q^{Si}_{min}$, $Q^{Mn}_{opt}$ with N, Fe and Si $\rho^{hi}_{max}/\rho^{lo}_{max}$ in addition to non-diatom $K_{Fe}$, $Q^{Fe}_{opt}$, $Q^{Fe}_{max}$, Fe $\rho^{hi}_{max}/\rho^{lo}_{max}$ and $\alpha^{chl}$.

This optimisation leads to a mean misfit of 4.21 per LTE with a 37%, 25% and 38% contribution from Chl, N and Si respectively; the first time Si contributed the most misfit compared to Chl. Visually, the plotting of final Chl, ΔDIN, ΔSi and ΔDIN : ΔSi (Figure 4.11) show very little disparity to the results of optimisation 4.

A similar set of initial diatom fractions, 0.29, 0.97, 0.95, 0.94, 0.19, 0.84 and 0.19, are also chosen for LTE 1-7 (Figure 4.6). Once again, non-diatoms are given a higher maximum growth rate compared to diatoms (+14 $yr^{-1}$ from $\mu_O$ to $\mu_D$) (Figure 4.12). Despite being provided with wider ranges, diatom $K_{Si}$, and non-diatom $Q^{Fe}_{opt}$, $Q^{Fe}_{max}$, Fe $\rho^{hi}_{max}/\rho^{lo}_{max}$ and $\alpha^{chl}$ still approached the top of their new ranges. On the other hand, non-diatom $K_{Fe}$ bottomed out it's wider range. Diatom $\alpha^{chl}$ also sought the base of its range in contrast to the other phytoplankton group.

The 120 iterations of this optimisation provide insight into the tendencies of the GA to optimise different parameters (Figures 4.13 and 4.14). Certain parameters trend toward a narrow part of their range with decreasing cost and are therefore well-defined across iterations. These include, $\mu_D$), all initial diatom fractions, diatom $Q^{N}_{max}$, $Q^{Si}_{opt}$, $Q^{Si}_{max}$, $Q^{Mn}_{opt}$ as well as non-diatom $Q^{N}_{max}$, $Q^{Fe}_{min}$, $Q^{Fe}_{opt}$, $\alpha^{chl}$ and $\theta^{C}_{max}$. Non-diatom $K_{Fe}$ appears to trend to either extreme of its range.

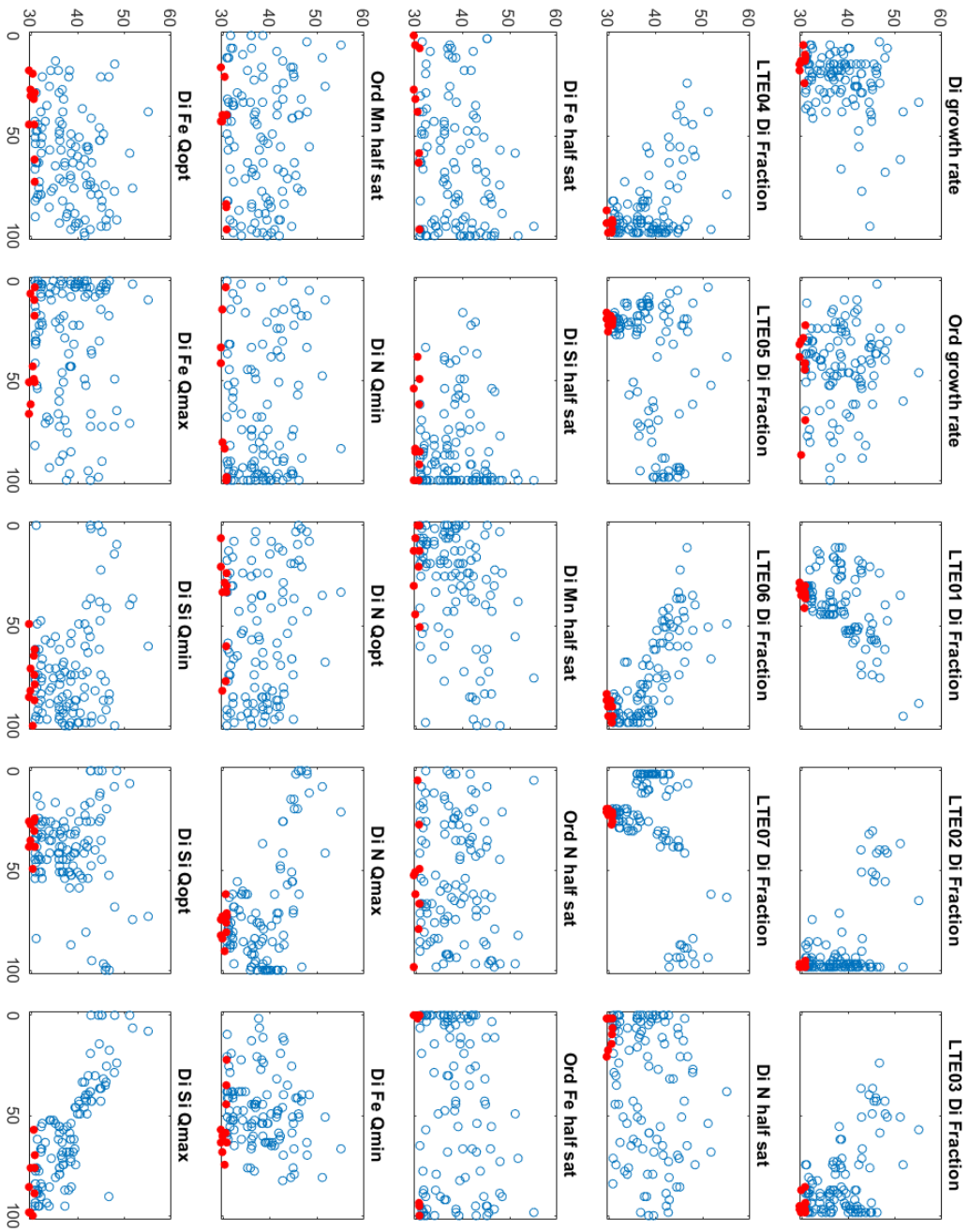


FIGURE 4.13: A summary of all 120 parameter sets generated for the sensitivity optimisation. For each parameter, the cost functions of algorithm final states are plotted against the corresponding parameter value expressed as percentage of the allowed range. The 10 lowest cost functions are shown in red. (First half of parameters)

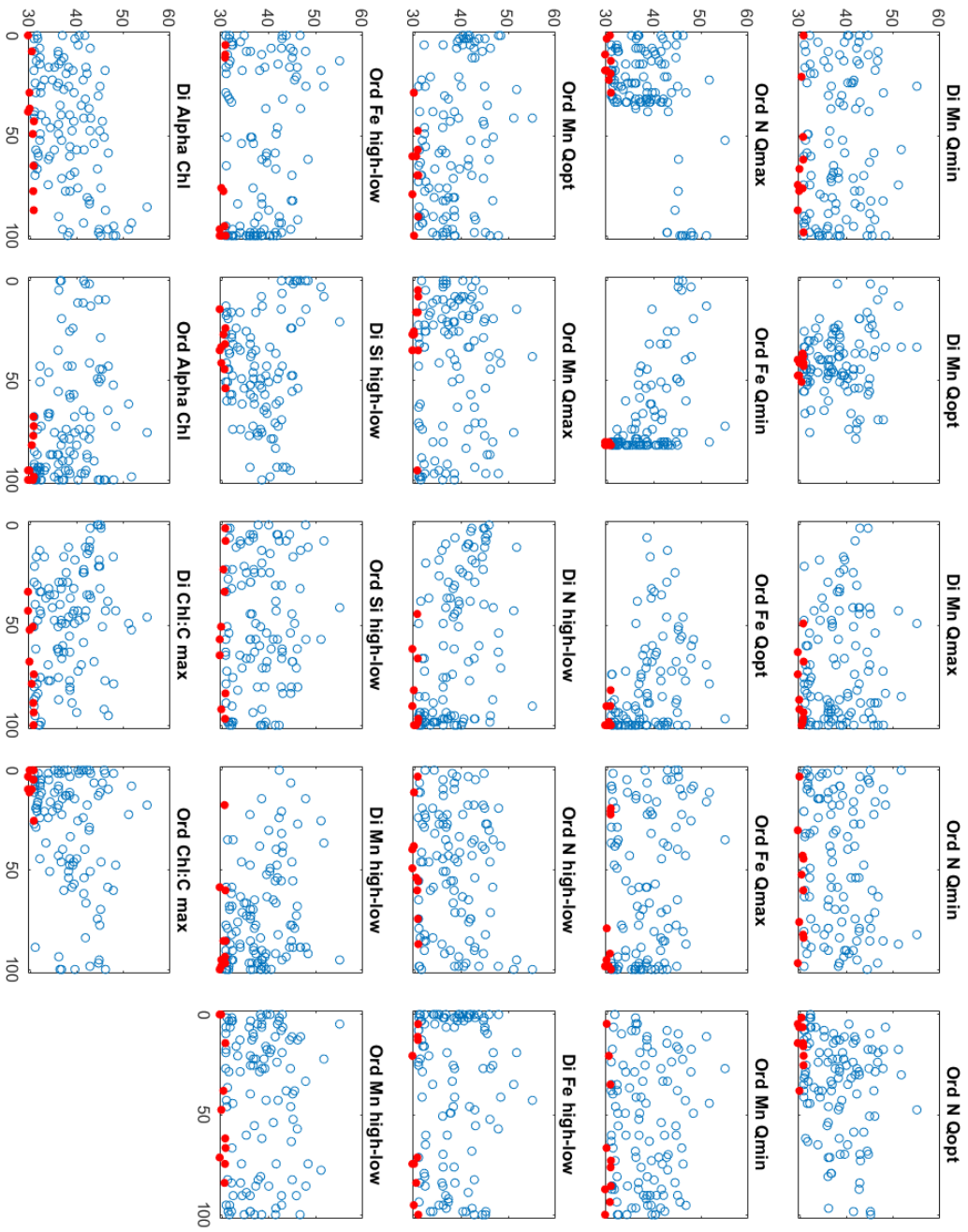


FIGURE 4.14: A summary of all 120 parameter sets generated for the sensitivity optimisation. For each parameter, the cost functions of algorithm final states are plotted against the corresponding parameter value expressed as percentage of the allowed range. The 10 lowest cost functions are shown in red. (Second half of parameters)

#### 4.3.2.6 Hybrid Optimisation

The hybrid optimisation was performed in the same way as the previous optimisation with a separate initial diatom fraction for each LTE, except for the fact that parameters which were poorly constrained within the previous optimisations have been removed from the set picked by the GA. The mean misfit per LTE was 4.63 which is similar to though above optimisation 4 and the sensitivity run and also bears a similar distribution of misfit between ΔChl, ΔN and ΔSi (Table 4.4). Chl endpoints and ΔN and ΔSi values from the hybrid optimisation remain very similar to those in the sensitivity optimisation (Figure 4.15). However, minor reductions in ΔN and increases in ΔSi in the low Fe treatments create overestimations in ΔSi:ΔN, particularly in LTE's 1 and 5. ΔSi in LTE01 does show a large improvement in the fit of the +Fe and +FeMn treatments. The initial diatom fractions chosen by the GA for LTE's 1-7 were 0.12, 0.98, 0.98, 0.94, 0.16, 0.90 and 0.21 respectively (Figure 4.6). These values are very similar to those of the sensitivity and number 4 optimisations, although the fraction diatom estimate for LTE01 is around half that in those runs. Of the parameters that were picked in the hybrid optimisation (Figure 4.12, bold values), diatom $K_{Si}$ and non-diatom $K_{Fe}$, $Q_{min}^{Fe}$, $Q_{opt}^{Fe}$, $Q_{max}^{Fe}$ and $\theta_{max}^{C}$ were the same as or very close to the values chosen in the sensitivity optimisation. In fact, when characterising chosen parameters as a percentage of their range (Figure 4.12), the mean difference in percentage from the sensitivity optimisation to the hybrid was only -7.86%. The largest deviations were diatom $Q_{min}^{Si}$ and $\alpha^{chl}$.

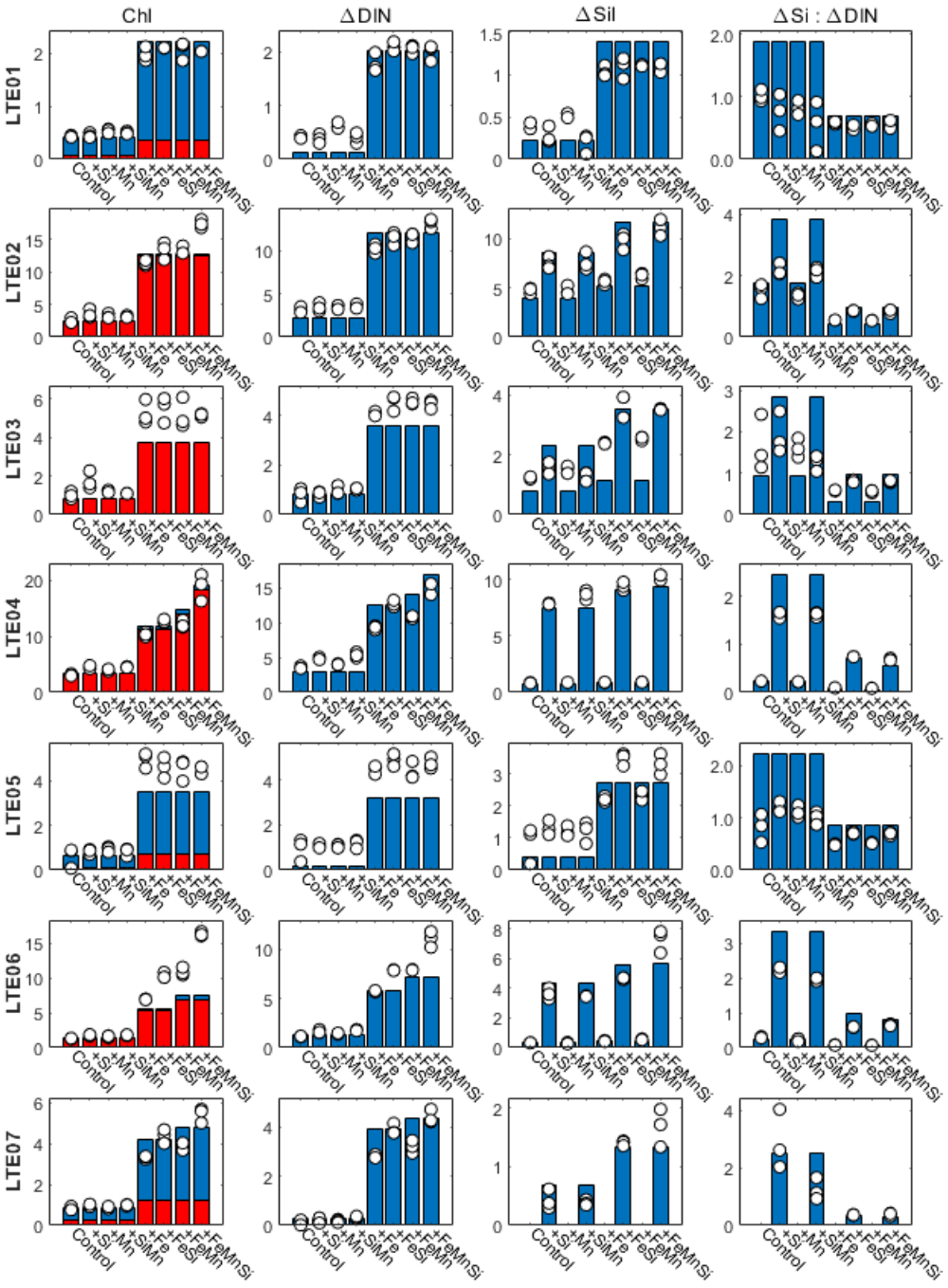


FIGURE 4.15: The results of the hybrid optimisation by the genetic algorithm of the CUSTARD-QUOTA-V2 model compared with data from the endpoint of each 'large-type' experiment. Each LTE was given its own initial diatom fraction but unconstrained parameters were replaced by the original values. Triplicate experimental observations for chlorophyll, change in dissolved inorganic nitrogen (DIN), change in silicic acid (Si) and the ratio of ΔSi to ΔN are indicated by white markers. Model results for the sum of both the diatom and the 'other phytoplankton' class have blue bars while the diatom class alone are shown in red bars. All nutrient concentrations are given in μmol $L^{-1}$.

### 4.3.3 Comparison to HPLC data

Across the different optimisations performed, the genetic algorithm has picked different initial diatom fractions for different incubation experiments (Figure 4.6). This is unsurprising as a clear latitudinal gradient in productivity is visible in the chlorophyll pigment data available for the CUSTARD cruise (Figure 4.16a) and this was found to be associated with a marked shift in community structure. Using HPLC data collected on the cruise, the ratio of fucoxanthin to total chlorophyll a, which is indicative of the proportion of phytoplankton that are diatoms at each location, was derived. It is evident that diatoms have increasing presence to the south where productivity was higher (Figure 4.16b). When the initial diatom fraction selected in the sensitivity optimisation is plotted against the ratio of fucoxanthin to total chlorophyll a, a significant fit is found (Figure 4.16, $R^2 = 0.82$, $P = 0.01$). This suggests that the GA has, just based on the experimental data available to it which will include the Si and N uptake, ascribed a difference in diatom proportion across the experiments which has some skill in predicting the actual shifts in community structure as identified within the HPLC data. Specifically, LTE's 1, 5 and 7 fall into a low diatom group and LTE's 2, 3, 4 and 6 exhibit a higher diatom proportion. However, considering the latitudinal pattern in Figure 4.16b, it is unclear why northern experiment LTE 3 falls within the higher diatom fraction group according to the GA. Although, optimisation 3 also came to the same conclusion (Figure 4.6) and there is some evidence in the HPLC data that the boundary region between relatively high (south) and low (north) diatom fractions was further to the north during that period.

The regression of initial diatom fraction and pigment ratios allows a separate prediction to be made for the starting diatom fraction for the gradient experiments on the basis of the corresponding HPLC data (Figure 4.17). The estimated diatom fractions thus derived are 0.31 and 0.94 for GE01 and GE02 respectively. Taking the final parameter set from the GA, the model can thus be used to predict the expected response within the gradient experiments which can then be independently compared to the data. Plotting the model results for GE01 (Figure 4.18) yields a reasonable fit for Chl, but the fit for ΔSi and ΔDIN were poorer. By those measures the model underestimates uptake of both nutrients, but more so ΔSi leading to overestimation of ΔSi:ΔDIN, particularly in the low iron treatment. On the other hand, the fitted diatom fraction creates an excellent fit for GE02 (Figure 4.19). This seems to continue a trend of the GA performing better for the southern experiments.

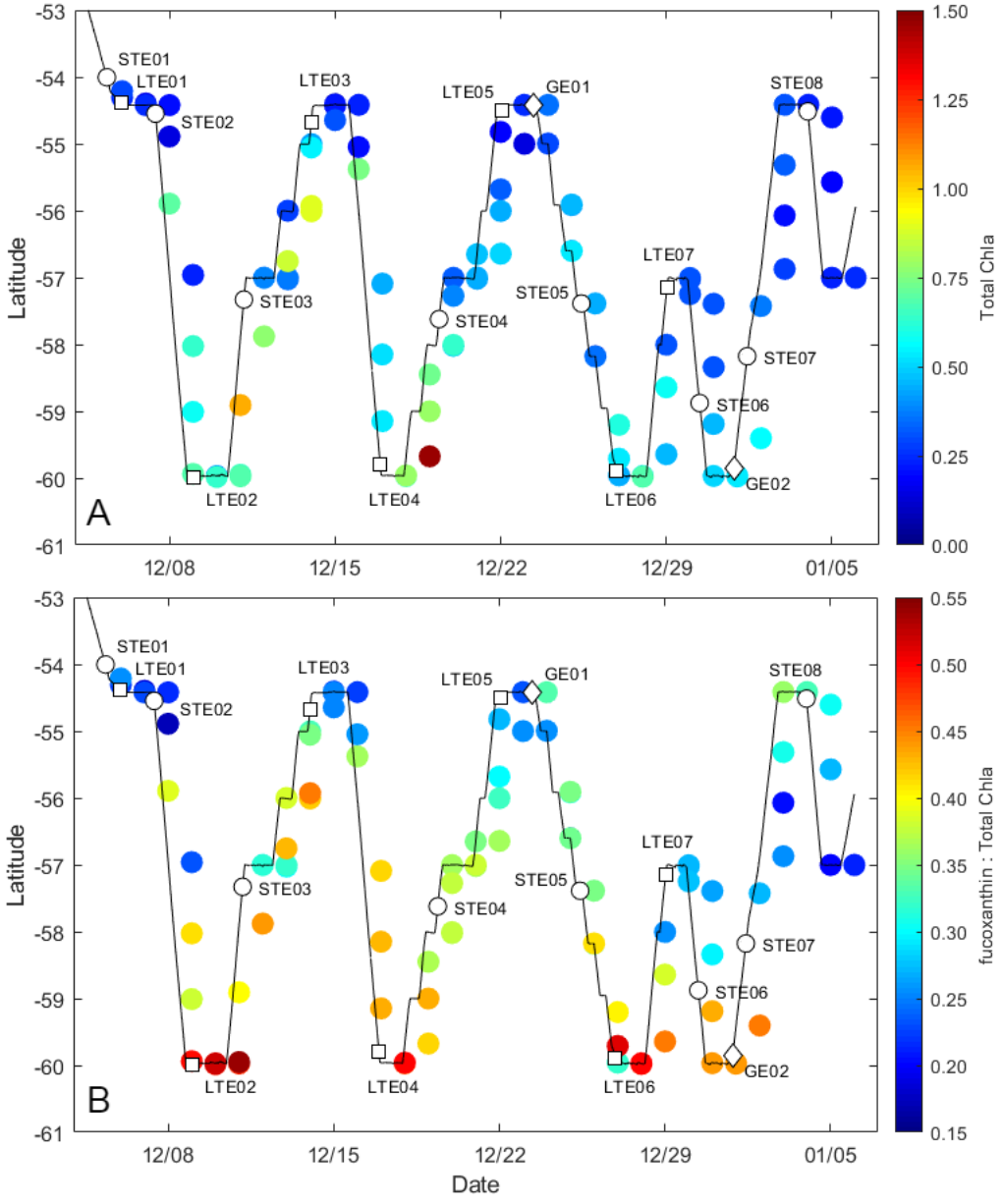


FIGURE 4.16: The distribution of total chlorophyll a (**A**) and its ratio with fucoxanthin (**B**) over the course of the CUSTARD cruise. This ratio is indicative of the proportion of diatoms in the sample. The distribution of factorial nutrient addition experiments is also displayed which includes 7 'large-type' experiments (LTE), 8 'small-type' experiments and 2 gradient experiments (GE).

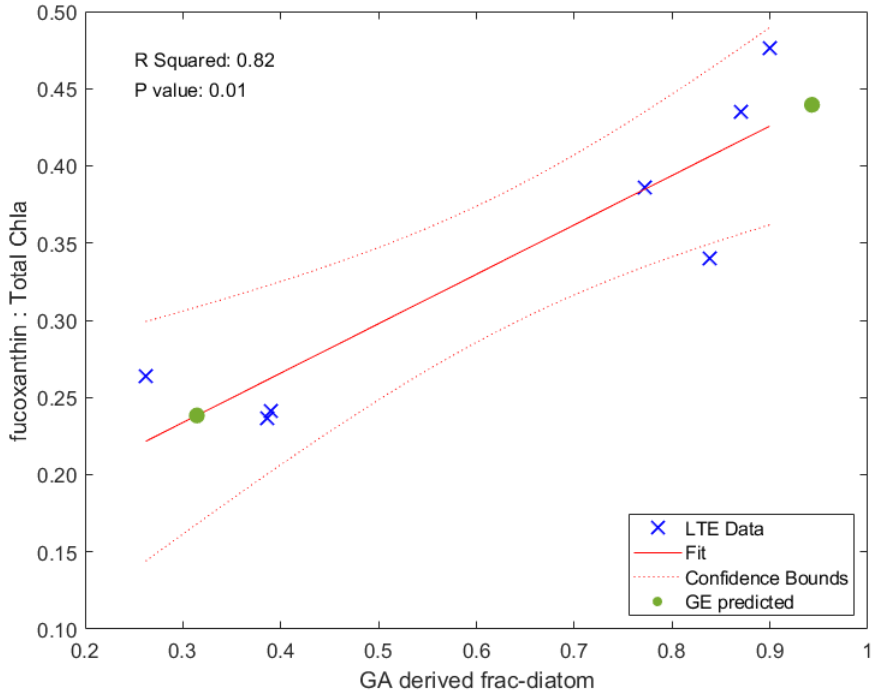


FIGURE 4.17: Initial diatom fraction determined by the final genetic algorithm optimisation is fitted against the pigment ratio of fucoxanthin to total chlorophyll a. The regression line equation is used to estimate initial diatom fraction of the gradient experiments (GE) from their pigment ratio.

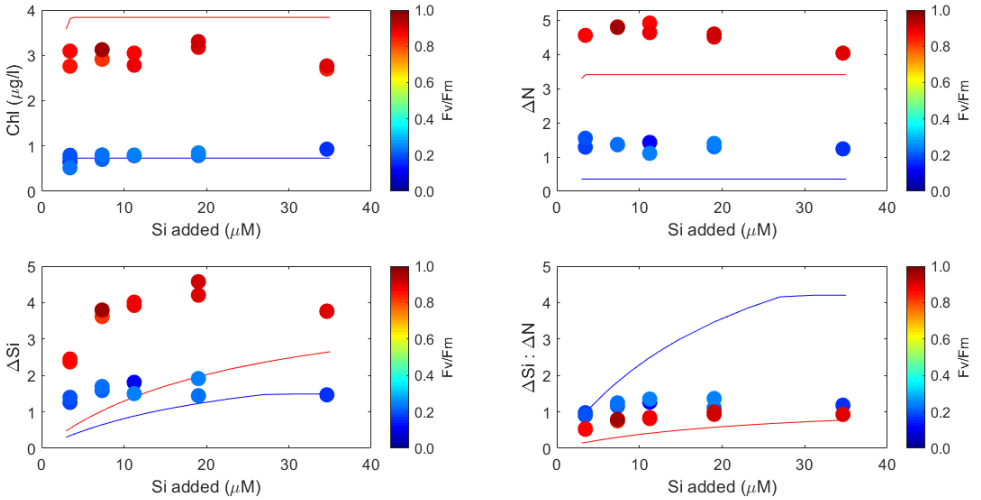


FIGURE 4.18: Results of the CUSTARD-QUOTA-V2 model using the estimated diatom fraction (Figure 4.16) are plotted against observations from the first gradient experiment (GE01). Chlorophyll, change in dissolved inorganic nitrogen (N), change in silicic acid (Si) and the ratio of ΔSi to ΔN are plotted with markers and shaded by their Fv/Fm; a marker for stress in photosystem II. In this case, a low Fv/Fm is indicative of phytoplankton suffering from iron limitation in the treatments where none was added. The CUSTARD-QUOTA-V2 results are plotted with lines; blue corresponding to the low iron treatment and red to the high iron treatment. All nutrient concentrations are given in μmol $L^{-1}$.

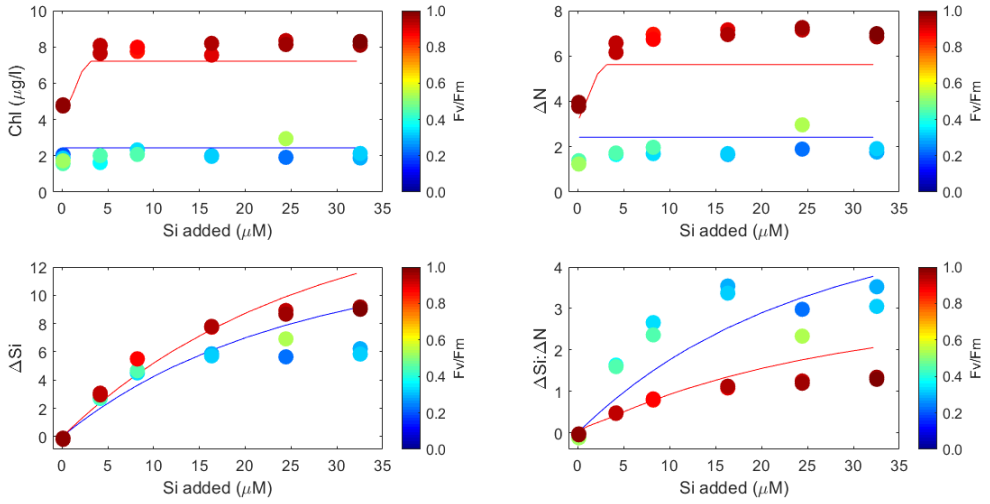


FIGURE 4.19: Results of CUSTARD-QUOTA-V2 model using the estimated diatom fraction (Figure 4.16) are plotted against observations from the second gradient experiment (GE02). Chlorophyll, change in dissolved inorganic nitrogen (N), change in silicic acid (Si) and the ratio of ΔSi to ΔN are plotted with markers and shaded by their Fv/Fm; a marker for stress in photosystem II. In this case, a low Fv/Fm is indicative of phytoplankton suffering from iron limitation in the treatments where none was added. The CUSTARD-QUOTA-V2 results are plotted with lines; blue corresponding to the low iron treatment and red to the high iron treatment. All nutrient concentrations are given in μmol $L^{-1}$.

## 4.4 Discussion

### 4.4.1 Variable Chlorophyll Model

A dynamic cellular chlorophyll pool was introduced to the model as an additional state variable due to the variable Chl:POC ratios visible in the experiments (Figure 4.1). The northern experiments (LTE's 1, 3 and 5) were all divided by which treatments had Fe additions leading to high Chl:POC and Fv/Fm group and a low group. The reduction of phytoplankton Chl:C ratios due to nutrient and light (co)limitation is well known (Geider, 1987; Greene et al., 1991; Macintyre et al., 2000) and Fe in particular is necessary for the proteins involved in chlorophyll synthesis making decreased cellular chlorophyll (chlorosis) a main symptom of Fe starvation (Geider and La Roche, 1994). The southern experiments as well as LTE07 similarly exhibit higher Chl:POC and Fv/Fm in response to Fe addition, but treatments where both Mn and Fe were added showed a higher Fv/Fm than those where solely Fe was added. Manganese also plays an important role in photosynthesis with four atoms forming the core of the water-splitting site of PSII (Dau and Haumann, 2008), however, the effects of Fe-limitation are generally more severe (Bruland et al., 1991; Schoffman et al., 2016). Using only two additional parameters, it was possible to incorporate flexibility between chlorophyll production and carbon biomass into the quota model. This enabled the chlorophyll observations of the incubation experiments to be directly compared with a mechanistic reproduction of chlorophyll from in the model, as opposed to a fixed conversion of carbon biomass.

Despite the introduction of a new state variable equation to the previously parameterised CUSTARD-QUOTA model, CUSTARD-QUOTA-V2 (Figure 4.2) retains a similar degree of improvement over the simple model's chlorophyll output (Figure 3.5), but retains the same deviations in predictions of ΔDIN, ΔSi and ΔSi:ΔDIN compared to the data. Interestingly, the maximum ΔSi : ΔDIN attained by the model in each experiment is consistently around 4 μM Si : μM N, though this does not match the observational data. A further improvement from the fit resulted from the introduction of initial dissolved Mn and BSi observations for initial dMn and cellular Si in the model. This mainly had the effect of bringing down erroneously high Si drawdown in treatments with combined Fe and Si additions. Although, initial dissolved Fe and POC observations were also available, adding these actually resulted in the model diverging further from the experiments. This may be due to the complexity of measuring which forms of Fe that are utilisable by algae and the possibility of non-phytoplankton POC present in the bottles at the start of the incubation.

### 4.4.2 Genetic Algorithm

To further refine the fit of the model to the observations from the incubation experiments, and in particular the ratio of ΔSi to ΔDIN, a genetic algorithm (GA) was used. This approach, which draws inspiration from natural selection, picks parameter values from within the ranges given to provide the lowest cost solution to the model; that is, the lowest deviation from the observations. Four different optimisations were performed using the algorithm, each with its own trade-offs, and then one of these was picked to perform a sensitivity optimisation to observe how much constraint the data places on different parameters before a final hybrid optimisation combined well constrained GA-picked parameters with hand-picked values. The algorithm was given the opportunity to pick every model parameter in addition to the initial proportion of diatoms to non-diatoms. Furthermore, the new terms added to allow for a Chl state variable, $\alpha^{chl}$ and $\theta^{C}_{max}$, were each split into a unique parameter for each phytoplankton group (Table 4.1) to allow for variation in light adaptation between communities.

### 4.4.3 Optimisation 1

In the first optimisation (Figure 4.7), one diatom fraction was fitted for the whole group of LTE experiments as in the previous quota models. Parameterisation by the algorithm resulted in a 93% reduction in mean misfit per LTE from the hand-picked parameter set (Table 4.4). A reduced diatom fraction of 0.76 was chosen by the algorithm (Figure 4.6) and this was likely the main driver of diatoms accounting for less than half of final Chl in iron additions compared to almost all in the non-GA model. Diatom productivity was also impeded by a 40% lower growth rate while non-diatom productivity was raised by the same percentage, and a higher $K_{Si}$ and $Q^{Si}_{min}$ which limits growth at lower Si concentrations and raises the Si requirement for growth (Figure 4.4 and 4.5). Therefore, Si drawdown was reduced in every experiment and in particular to +Si treatments. LTE's 4, 6 and 7 all exhibit larger Si uptake where Si is added but no Fe is added and so no additional Chl productivity is seen. This suggests that extra Si is taken up not to produce new cells but rather to either build thicker siliceous cell walls or to partly store within the cell. This luxury uptake of Si has been observed previously (Lynn et al., 2000; Domingues et al., 2011). As ΔSi values have decreased, so has ΔSi: ΔDIN, resulting in better fits, especially for +Fe treatments, but losing the Si related patterns as the others.

#### 4.4.3.1 Optimisation 2

The Chl data available for each location showed that there was greater productivity or a bloom state to the south of the cruise's range and this likely entailed a higher proportion of diatoms in the community (Brzezinski et al., 2001; Petrou et al., 2016; Deppeler and Davidson, 2017) which was later observed in the HPLC data (Figure 4.16b). The second GA optimisation (Figure 4.8) therefore only fitted the LTE's 1-6 and used two diatom fractions; one for the northern experiments (LTE's 1, 3 and 5) and one for the southern experiments (LTE's 2, 4 and 6). The leads to a 54% reduction in mean misfit per LTE from the prior optimisation (Table 4.4) and the resulting diatom fractions, 0.19 in the north and 0.81 in the south (Figure 4.6), support the latitudinal gradient in community make-up. It is most probable that the differences in the data between north and south that bring the GA to this same conclusion are found in ΔSi. It appears that lower diatom fractions may be necessary to prevent exaggerated Si drawdown in northern experiments where both Fe and Si were added. This behaviour of luxury Si uptake is necessary to recreate observed patterns in the south but only marginally in the north. In fact, with a diatom fraction chosen by the GA, the southern experiments produce an extremely tight fit. Once again, a high $K_{Si}$ is chosen which impairs growth at lower Si concentrations and all diatom Si quota parameters are maximised which produces a higher minimum Si required for growth, a higher Si required for optimum growth and a greater Si storage capacity (Figures 4.4 and 4.5). Generally, this would function to increase the Si needed for the same amount of biomass production. Furthermore, their largely increased maximum Chl:C allows for diatoms to also decouple biomass production from Chl production.

#### 4.4.3.2 Optimisation 3

To further explore the effect of the latitudinal productivity gradient on the parameter sets picked by the GA, optimisation 3 ran the algorithm separately for the northern and southern experiments. In addition, each LTE was allowed a unique initial diatom fraction. It is unsurprising that setting the GA with a lower bar of fitting only 3 similar experiments at a time resulted in the lowest cost: a mean misfit of 1.94 per LTE (Table 4.4). Visually, it is hard to distinguish whether the northern or southern set of experiments had a better fit to the observations (Figure 4.9) as they have different magnitudes of absolute nutrient drawdown, however, the northern optimisation has a mean misfit of 2.93 per LTE compared with 0.95 in the south. Superior fits for southern experiments have also been observed in the previous optimisations. This is primarily the result of Chl misfit in LTE03 and underestimated Si uptake in non-Fe treatments.

With the option of an individual initial diatom fraction for each LTE, the GA picked a high value (0.8-1) for every experiment except LTE01 (0.27) (Figure 4.6). This is an interesting divergence from optimisation 2 where a lower diatom fraction was preferred for the north. However, the higher proportion of diatoms in LTE's 3 and 5 has fixed the underestimation of Si uptake in non-Fe treatments. Optimisation 3 is the only optimisation that results in a high diatom maximum growth rate compared to non-diatoms (Figure 4.4 and 4.5) which is conventionally what would be expected (Furnas, 1990; Edwards et al., 2015). The northern experiments have selected for low diatom $K_{Si}$ and $K_{Fe}$ by the GA, while the south has top-of-range values. This suggests the optimisation is seeking to reduce Si and Fe uptake by diatoms at lower concentrations in the south. The north also maximises diatom Fe quota parameters while the south maximises diatom Si quota parameters. Although this optimisation offers the best fit to the observations, it comes at the cost of essentially doubling the parameters necessary to model them. Not having a single parameter set makes it implausible to scale this model beyond this particular use case. In a conceptual sense, it is equivalent to some aspect of any community structure differences between the northern and southern set of experiments remaining unrepresented by the model as structured, hence necessitating the different parameter set. Fitting fewer experiments at a time thus created less constraint on the model from the data as a mechanistic representation of the whole system, rather than a subcomponent of the system.

#### 4.4.3.3 Optimisation 4

As a balance between the previous approaches, optimisation 4 used one parameter set for all of the experiments but included a separate initial diatom fraction for each LTE. The mean misfit per LTE for this experiment was 4.58 (Table 4.4) which constitutes an improvement from optimisation 1 but not 2 and 3. In this case, initial diatom fraction was high (>0.9) for LTE's 2, 3, 4, 6 and low for LTE's 1, 5 and 7 (Figure 4.6). Here, LTE05 has switched from the high fraction observed in optimisation 3 back to what was seen in optimisation 2 and what is expected based on the latitudinal productivity gradient. This either implies that sharing a parameter set forces a lower diatom fraction, or that this starting condition is not very strongly constrained for LTE05. This optimisation for LTE05 certainly has a visibly worse fit than its high diatom fraction counterpart in optimisation 3 which does suggest it is only a favourable condition when parameters must apply to both bloom and non-bloom diatoms. LTE07 has a maximum final Chl below 6 µg $L^{-1}$ as do the northern experiments whereas the southern experiments exceed 15 µg $L^{-1}$, which makes it logical that this LTE was selecting for a low diatom fraction as it likely fits more with the non-bloom group. The

southern LTE's once again exhibit a superior fit with a third of the misfit of the northern experiments. As in the southern run of optimisation 3, a high $K_{Si}$ and $K_{Fe}$ yield lower Si and Fe uptake for diatoms at lower concentrations (Figure 4.4 and 4.5). This appears to be a consistent strategy of the GA to avoid the overestimation of Si uptake in combined Fe and Si additions. $Q_{min}$ for diatom Si, N, and Mn are all elevated, raising the minimum requirement for diatom growth.

#### 4.4.3.4 Sensitivity Optimisation

The methodology of optimisation 4 was chosen as the best structure with which to proceed due to its low cost with one parameter set for all LTE's and the information on community structure gained from including unique initial diatom fractions for each experiment. While optimisation 3 had the lowest deviation from observations, separate parameter sets are not scalable unless by use of, for example, allometric relationships (Ward et al., 2018) and they would also limit the constraint of the data on the GA. Some parameters that consistently reached their limits were provided wider ranges. To fully understand how well constrained each parameter is by the data and provide the GA the most opportunity to seek out alternative pathways to low-cost solutions, this optimisation was performed 120 times. Of these runs, the lowest cost parameter set yielded a mean misfit of 4.21 per LTE, an 8% improvement from optimisation 4 (Table 4.4). Within the best parameter set, the initial diatom fraction chosen by the GA maintained the same profile as optimisation 4 showing that this was indeed the optimum configuration for this setup (Figure 4.6). The fit is visually almost indistinguishable from optimisation 4 and no misfit reduction occurs in ΔSi. However, despite this relatively minimal change in cost, many parameters have been altered, which suggests that these are not strongly constrained. This optimisation picks the highest diatom maximum growth rate of any so far (99 $yr^{-1}$, Figure 4.12) and maintains a higher maximum growth rate for non- diatoms (114 $yr^{-1}$). When given a wider range diatom $K_{Si}$ reached the upper limit of this as well (20 µmol $L^{-1}$. Setting this parameter higher further limits the ability of diatoms to take up Si, which is potentially why maximum growth rate can be raised without overestimating Si drawdown. But while this parameter adopts a similar part of its range, $K_{Fe}$ in both groups travels from the top 80-100% of their range to the lower limit, reducing Fe uptake. This may be responsible for the increase in non-diatom Fe $\rho^{hi}_{max}/\rho^{lo}_{max}$ from optimisation 4 although this does not change in the diatoms. Diatom $Q^{Si}_{min}$ was provided a wider range in this optimisation as it stayed at its maximum value in all prior optimisations with the exception of 3-north. The GA utilised this wider parameter space by further raising $Q^{Si}_{min}$, though not to the new max. Given that this

parameter controls the minimum Si required for growth and appears to be well constrained, it is likely that the GA is attempting to firmly delineate the responses of ΔSi between the +Si and non-Si treatments. Diatom $Q_{max}^{Si}$ also remained high as in 3 of the previous optimisations. Alpha chlorophyll is set to the bottom of the range for diatoms but the top of the range for non-diatoms. This parameter determines the rate of chlorophyll production for a given light intensity below saturation and so increasing it reduces ΔChl.

Performing 120 iterations in this optimisation allowed the observation of how well constrained parameters were by the experimental data used to fit the model in the GA. When the range of a parameter decreases as cost is reduced it shows that the parameter is well constrained, whereas when the value of the parameter has no relationship to cost, the parameter is less well constrained. The top 10 lowest GA iterations in this optimisation (Figure 4.13 and 4.14, red markers) produced very tight clusters for the initial diatom fraction in each LTE. Given that other differences between diatoms and non-diatoms can be altered by the algorithm (e.g. $\mu_{max}$), the variation in Si drawdown between LTE's must be responsible for constraining diatom fraction. This may explain why LTE03 does not fit with the other northern, non-bloom experiments and why LTE07 does, as the first has the highest ΔSi values of these experiments while the latter has some of the lowest. As has also been observed in previous optimisations, diatom $\mu_{max}$ is well constrained around 90 $yr^{-1}$ (mean of top 10 iterations). The non-diatoms avoid taking a lower $\mu_{max}$ value than the diatoms but otherwise are less well constrained with a slight tendency toward around 120 $yr^{-1}$. If non-diatom $\mu_{max}$ is too low, Chl production and N drawdown is insufficient to match that found in observations. However, values near the top of the range promote too much growth unless another parameter is altered. The low trending $\alpha_O^{chl}$ also bolsters Chl production in non-diatoms. Diatom $K_N$ was exclusively in the lower quarter of its range for the top 10 lowest cost iterations while diatom $K_{Si}$ and $K_{Mn}$ skewed to their upper and lower halves respectively. Non-diatom $K_{Fe}$ was more likely to be chosen at the extremes of its range. Diatom $Q_{max}^{N}$, $Q_{max}^{Si}$, $Q_{min}^{Si}$, $Q_{opt}^{Si}$, $Q_{max}^{Mn}$ and $Q_{opt}^{Mn}$ are all also better constrained as well as all non-diatom $Q_{opt}^{N}$, $Q_{max}^{N}$, $Q_{min}^{Fe}$, $Q_{opt}^{Fe}$ and $Q_{max}^{Fe}$. For each nutrient $Q_{max}$ places an upper limit on cellular uptake, and so a larger value increases uptake. On the other hand, decreasing $Q_{min}$ increases uptake because $Q_{min}$ becomes closer to Q.

#### 4.4.3.5 Hybrid Optimisation

While feeding all of the model parameters to the GA produces the best results, the reality is that if those parameters are largely unconstrained then the values chosen for

them are essentially random. While unconstrained parameters will, by definition, have little effect on the model being fitted against the observations used for the fit, they have been shown to decrease performance when running larger scale models (Ward et al., 2010). Furthermore, providing the GA with so much flexibility may mean that many parameters of low consequence to the output can be tuned to overcome the signal of more sensitive parameters. Therefore, the results of the sensitivity optimisation were used to further select a subset of well-constrained parameters to pick via the algorithm while retaining the original hand-picked values for unconstrained parameters. This was one of the approaches suggested by Ward et al. (2010). The parameters that were fitted by the GA are highlighted in bold in Figure 4.12. In some cases, relatively unconstrained parameters were still included due to their association to other parameters, such as non-diatom $\mu_{max}$ and diatom $\alpha^{chl}$ and $\theta^{C}_{max}$. The fact that the mean misfit per LTE only increases slightly from the sensitivity and number 4 optimisations indicates just how non-influential the unconstrained parameters were (Table 4.4 and Figure 4.15). This methodology retains a 97% decrease in cost per LTE over the original non-optimised model. The distribution of starting diatom fraction found among the two previous optimisations is maintained here (Figure 4.6), providing further confidence in this distribution. As previously mentioned, LTE03 consistently deviates from the other northern experiments with the GA consistently selecting for a relatively high diatom fraction. If the fraction for LTE03 is set low instead, as is the case for the other northern experiments, Chl endpoints, ΔDIN and ΔSi are all underestimated, confirming the necessity of greater diatom presence in that LTE. ΔSi misfit has actually decreased in this optimisation compared to the sensitivity run, though ΔChl and ΔDIN misfit have grown. Many GA picked parameters remained close or identical to their previous optimisation values, once again implying the lack of influence of the other parameters. The largest deviations from this were diatom $Q^{Si}_{min}$ and $\alpha^{chl}$. Diatom $\alpha^{chl}$ was included due to its possible relationship to non-diatom $\alpha^{chl}$, but was itself relatively unconstrained; observing a large shift in its range here suggests that this remains the case and could probably be left hand-picked in future runs. Diatom $Q^{Si}_{min}$ previously sought the higher end of its range, but here has been capped by the lower value of diatom $Q^{Si}_{opt}$.

### 4.4.4 Comparison to HPLC data

While optimising the model with the GA, it has become clear that assigning initial diatom fractions to each LTE is well constrained by the observations (Figure 4.13 and 4.14). With the notable exception of LTE03, these fractions appeared to match the

north-south gradient of Chl found across the data (Figure 4.16a) if it is assumed that diatoms dominate in Southern Ocean bloom conditions. Fortunately, HPLC data also became available for the cruise data which offers quantification of different phytoplankton pigments. Because fucoxanthin, a carotenoid pigment, is only found in diatoms (Peng et al., 2011) but chlorophyll a is present in all; the ratio of fucoxanthin:chlorophyll can be used as a proxy for the proportion of diatoms present near the incubation locations. When mapped out (Figure 4.16b), these values show a similar latitudinal gradient to that of chlorophyll, suggesting that there is indeed a greater proportion of diatoms present in the bloom conditions to the south. Plotting the GA derived diatom fractions against the HPLC data leads to a significant correlation showing that the data is leading the GA to rightly vary the diatom fraction between north and south. The pigment ratio backs up the assertion that LTE07 fits with the northern experiments. However, while the line of best fit would place LTE03 somewhere between north and south, the GA picks at the higher end placing this point outside of the confidence bands. Nonetheless, these results make clear the importance of correctly modelling community structure in order to accurately simulate Si and N uptake and thus the Si:N ratio. A model must balance the influences of Fe, Si and community structure in order to estimate Si:N.

Using the correlation of the pigment ratio to diatom fraction, it was possible to estimate the proportion of diatoms for the GE01 and GE02 where a gradient of silicon additions was made crossed with a +Fe and non-Fe treatment. Based on their location in the north and south respectively (Figure 4.16), it would be expected that GE01 would have a low fraction while GE02 would be high. This is indeed what the pigment data suggests (Figure 4.16b), estimating a diatom fraction of 0.31 for GE01 and 0.94 for GE02. Using this estimation to simulate GE02 works very well (Figure 4.19), reproducing Chl, $\Delta$DIN, $\Delta$Si and even $\Delta$Si:$\Delta$DIN accurately. However, for GE01 (Figure 4.18), $\Delta$DIN and $\Delta$Si in particular are underestimated and $\Delta$Si:$\Delta$DIN in the low iron treatment is severely raised above observations. This continues the trend of finding superior fits to observations when working with the southern experiments within the bloom. This is perhaps unsurprising as bloom conditions are likely to be dominated by only a limited diversity of phytoplankton groups, in this case diatoms. Whereas, in non-bloom or low-nutrient conditions a wider diversity of phytoplankton are able to exploit the available niches (Ignatiades, 1969; Tilman et al., 1982). Thus, it might be expected that it is easier to model or even measure one group producing large responses in Chl, Si and N than it is to model multiple groups having a smaller effect on their environment.

## 4.5 Conclusions

This chapter sought to take the CUSTARD-QUOTA model that was successful at modelling the incubation experiments from the CUSTARD cruise in Chapter 3 and improve it further through the addition of a dynamic cellular Chl pool as an additional state variable and through fitting the parameters using a genetic algorithm. In achieving this, it was also possible to explore how sensitive parameters were to the data constraining the model and how to best apply the power of a genetic algorithm without unnecessary and detrimental tuning.

The additional Chl state variable was introduced to the model with little change in model fit from the previous format, while gaining the ability to directly simulate the available Chl observation data. Furthermore, this allowed a variable Chl:C ratio to exist within the model which was observed to exist in the data, where the ratio increased when iron limitation was alleviated.

When a genetic algorithm was used to fit the model parameters, allowing the algorithm to fit different initial diatom fractions for LTE's in the north and south proved to improve the results of the optimisations. This was corroborated by a latitudinal gradient of Chl which indicated bloom conditions in the south which were likely dominated by diatoms. Increasing the specificity of the optimisation, when the northern and southern experiments were each given their own entire parameter set was found to provide the best fit to the observations. However, increasing specificity leads to a degree of overtuning and limits any broader applicability of the model. In general, the southern bloom experiments (LTE's 2, 4 and 6) produced stronger fits, likely because it was easier to model large responses driven by a community dominated by a single phytoplankton group. A sensitivity optimisation, which included 120 iterations and produced a range of misfit values, showed that a large number of parameters were in fact poorly constrained by the data available. This result warns against a one-step process of feeding parameters to an algorithm without knowing if they will be well constrained by the data. This could potentially be achieved by a pre-algorithm sensitivity-test of the model's parameters or a sensitivity analysis using the algorithm itself, as is performed here. Based on these findings, optimisation proceeded with a hybrid approach that left unconstrained parameters hand-picked and only used the algorithm to find parameters that were well defined by the observations. The well constrained parameters included $\mu_D$, all initial diatom fractions, diatom $Q^N_{max}$, $Q^{Si}_{opt}$, $Q^{Si}_{max}$, $Q^{Mn}_{opt}$ as well as non-diatom $Q^N_{max}$, $Q^{Fe}_{min}$, $Q^{Fe}_{opt}$, $\alpha^{chl}$ and $\theta^C_{max}$. This approach produced little decrease in the fit of the model compared to the previous method while avoiding the effectively random tuning of unconstrained parameters.

Community composition in the model, represented by starting diatom fraction, was very well-constrained and appeared to match assumed diatom dominance the south. This suggested that these fractions might correlate well to the real proportion of diatoms at the location of the incubations. Performing a regression between the estimations of the GA and the fucoxanthin to total Chl a ratio, which is indicative of the representation of diatoms within the total community, resulted in a significant positive correlation. The fact that the algorithm was able to mostly predict the correct gradient in diatom fraction between the north and south shows that community composition is another key factor to consider when modelling the Si:N drawdown at different locations in the ocean alongside Si and Fe availability as mentioned in Chapter 3. Overall, the attempt to fit the model to the multi-factorial experimental data thus indicated that representation of a two component (diatom and non-diatom) community was important in addition to allowing flexible quotas and associated luxury uptake.

# Chapter 5

# Synthesis and Concluding Remarks

## 5.1 Summary

Diatoms are eukaryotic phytoplankton known for their two-part intersecting silica cell wall and the fact that they contribute  20% of global primary productivity (Nelson et al., 1995; Falkowski et al., 1998; Field et al., 1998). Since their rise to dominance in the Cretaceous, diatoms have depleted the world's oceans of silicic acid (Si), reducing concentrations by more than 90% from around 1000 µM to <100 µM (Conley et al., 2017; Sims et al., 2019). Today, the Southern Ocean (SO) is the largest region of carbon export by diatoms (Schlitzer, 2002; Arteaga et al., 2018). As a key junction of the Meridional Overturning Circulation, the SO upwells old nutrient rich water masses via the Circumpolar Deep Water (CDW). However, primary productivity at the surface is limited by light and iron (Fe) availability (Gran, 1931; Martin et al., 1989; Martin, 1990; Boyd et al., 2007) and so these nutrients are able to escape to the lower latitudes where they are estimated to support about three-quarters of the biological production north of 30° S (Sarmiento et al., 2004). Silicic acid (Si), on the other hand, exhibits a diminishing gradient as surface waters move northward across the SO and so remains trapped relative to other macronutrients. This decoupling of Si in the surface is caused by the upregulation of diatom Si:N uptake ratios under Fe stress (Brzezinski, 1985; Takeda, 1998; De La Rocha et al., 2000; Brzezinski et al., 2003; Timmermans et al., 2004; Hoffmann et al., 2007) in combination with the decreased dissolution of silica in cold polar waters (Sarmiento and Gruber, 2006). At depth, Si is attenuated much less than phosphate and a portion re-enters the CDW to form a continuous loop of SO utilisation and regeneration with little escaping to lower latitudes (Whitney et al., 2005; Holzer et al., 2014). SO Si trapping influences global productivity by limiting the growth of diatoms beyond the SO, although this may have been relieved during some

glacial – interglacial periods (Harrison, 2000; Nozaki and Yamamoto, 2001; Brzezinski et al., 2002; Matsumoto et al., 2002; Hendry and Brzezinski, 2014). Therefore, modelling the global ocean in the past, present and future requires an understanding of silicon trapping and diatom stoichiometry in the SO. Holzer et al. (2019) have shown that how diatom Si:N is parameterised in relation to Fe deficiency can lead to contrary results under a regime of Fe fertilisation. The ultimate aim of this study was to evaluate the drivers of Si trapping in the SO using models of different scales. In particular, the specific methodology used to model variable diatom uptake stoichiometry is interrogated using a powerful set of observations.

Chapter 2 aimed to build a simple 3-box model (3BOX-SIMPLE) representation of the overturning pathway between the SO upwelling zone, the subtropical (ST) ocean surface layer and the deep ocean in order to observe how key mechanisms keep Si from leaving the SO to the ST. These mechanisms included the upwelling of nutrients in the SO, the attenuation of Si dissolution and the parameterisation of diatom Si:N stoichiometry by different methods. Sensitivity testing allowed comparison of how each factor mediates the proportion of Si that leaves the SO surface northwards after being upwelled.

In December 2019 a cruise of the *RRS Discovery*, as part of the Carbon Uptake and Seasonal Traits in Antarctic Remineralisation Depth (CUSTARD) programme, conducted multifactorial nutrient addition experiments in the SO that revealed the response of Si:N uptake ratios to the availability of Fe, Si and Mn. Chapter 3 aimed to use this data as a rigorous test for two modelling approaches: a simple model which calculates growth via Michaelis-Menten type uptake of external nutrients (CUSTARD-SIMPLE) (Tyrrell, 1999; Yool and Tyrrell, 2003); and a quota model which represents cellular nutrient pools and can modulate uptake based upon cellular accumulation approach (CUSTARD-QUOTA) (Droop, 1983; Geider et al., 1998; Buitenhuis and Geider, 2010).

Chapter 4 sets out to further the quota model work of chapter 3 to create a closer simulation of the cruise experiments and explore the influence of parameterisation and community structure in fitting the model. The chapter introduces an additional state variable to represent a dynamic cellular chlorophyll pool and uses a genetic algorithm (GA) approach to fit the resulting CUSTARD-QUOTA-V2 model to observations and infer community composition from a latitudinal gradient in experimental responses.

## 5.2 Key Results

In Chapter 2, a 3-box model representation of Southern Hemisphere meridional circulation (3BOX-SIMPLE) was able to reasonably replicate observed nutrient concentrations for P, Fe and Si and recreate expected distributions of diatoms versus non-diatoms. However, the addition of an Fe-dependent diatom Si:N ratio led to near complete Si trapping and their elevated removal of Si was sufficient to replace Fe limitation with Si limitation in the SO surface box. A sensitivity test determined that parameters and initial conditions required dramatic alteration to allow Si to escape to the subtropics. Although, allowing non-diatoms to outcompete diatoms allowed a complete floristic shift and total Si escape from the SO. The SO box was somewhat trapped in a state of Si limitation for diatoms as lowering Fe to produce Fe limitation yielded an increased Si:N and so reinforced Si depletion. Introducing Si:N parameterisations that were both Si and Fe dependent could also not alleviate Si trapping. A model Fe fertilisation experiment was performed to observe the response of Si trapping and Si:N ratios to rising aeolian Fe input. For all parameterisations this did not produce an increase in Si escape efficiency as additional Si uptake due to greater productivity surpasses reduction of Si uptake via decreased Si:N ratio. This was confirmed by the expected reduction in Si trapping appearing when diatom growth was capped. Overall, this chapter emphasises the strength of Si trapping that can be implemented by direct parameterisations of diatom Si:N uptake ratios. The nature of these mechanisms can lead to feedback in both Fe and Fe/Si dependent parameterisations which stabilise concentrations of Fe and Si.

In Chapter 3, the data from the nutrient addition experiments conducted on a SO research cruise showed a clear increase in Si:N uptake ratio by the phytoplankton community in Fe deficient conditions up to $\sim$2.5 or 4 in one extreme. Incubations conducted with a gradient of Si determined that the Si:N uptake ratio was reliant on both Fe and Si concentrations due to the downregulation of Si uptake at low concentrations. Attempting to fit a simple model (CUSTARD-SIMPLE) to the data with a direct Si:N parameterisation, that took Fe and Si concentrations into account, yielded many of the same responses to nutrient additions observed in the experiments. However, in some experiments, CUSTARD-SIMPLE did not reproduce responses to Fe addition, due to depleting the available Si. Experimenting with alternative Si:N parameterisations from Holzer et al. (2019) did not yield a better root mean square error to the observations. Furthermore, all parameterisations resulted in a poor fit to the Si gradient experiments, where Si:N uptake ratios were largely overestimated in the low Fe treatment. A quota model (CUSTARD-QUOTA) that represented internal cellular nutrients and allowed for luxury uptake of nutrients was able to reproduce all

of the chlorophyll responses to different nutrient additions, also producing endpoints very close to those of the observations. This model also performed significantly better at fitting the Si gradient experiments than any of the CUSTARD-SIMPLE parameterisations, though ΔSi, and therefore ΔSi:ΔDIN, was still overestimated.

In Chapter 4, an additional Chl state variable was introduced to the CUSTARD-QUOTA model to account for the variable Chl:C ratios observed in the data, while maintaining an equally good fit to the observations. This new model was designated CUSTARD-QUOTA-V2. The fit was further improved by using experiment BSi and Mn data to set the initial cellular Si and external Mn concentrations. When a GA was used to fit the model parameters and initial fraction of diatoms to non-diatoms, the distance of the simulation from the observations was reduced dramatically. The algorithm also set diatom fractions which mostly appeared to match expected community structure differences in diatom abundance according to the latitudinal chlorophyll gradient across the cruise area. Increasing the number of parameters and the specificity of the experiments led to an exceptionally close fit of the model to the data. However, this likely resulted in over-tuning which may have led to very low likelihood of this model being applicable outside of this specific circumstance. Furthermore, a sensitivity test that performed 120 tuning runs of the GA found that many of the parameters were in fact completely unconstrained by the data. This led to the adoption of a hybrid approach where poorly constrained parameters were left at values informed by the literature, while well-constrained parameters were fitted by the algorithm. The hybrid approach resulted in only a small reduction in the fit of the model to the observations while hopefully avoiding over-tuning and retaining a higher degree of scalability to wider problems. Finally, diatom fractions picked by the GA for each experiment were found to significantly correlate to a pigment indicator of diatom proportion in the community. Using this regression to estimate diatom fraction for the gradient experiments yielded a very strong fit to GE02 but overestimated ΔSi:ΔDIN in GE01.

## 5.3 Discussion

Chapter 2 attempted to model the present day SO Si trap in the simplest manner possible by reducing the system to a three-box model. This model was based on the two-box biogeochemical model of Yool and Tyrrell (2003) which successfully used two functional groups, diatoms and non-diatoms to simulate the broad cycles of Si and P in the global ocean. The 3-box approach used here contains an SO box, Subtropical (ST) box and a deep box connected by an overturning circulation which represent the

upwelling of the CDW into the surface SO, export from the SO to the ST via intermediate waters and the return path of nutrients to the deep ocean via the North Atlantic Deep Water (NADW) (Talley, 2013). A basic Fe cycle was also added to the model as a key limitation of biological productivity in the SO and was made responsible for the variable diatom Si:N stoichiometry that plays a role in the Si trap. Basic mechanisms of Fe input to the surface box via aeolian dust and Fe scavenging from the deep box were included in this cycle which allowed the study of scenarios such as Fe fertilisation which have been hypothesised by some to reduce SO Si trapping during past glacial maxima (Brzezinski et al., 2002; Matsumoto et al., 2002). Without any direct parameterisation of Si:N, the model reaches steady state solutions conforming to sensible nutrient distributions and establishes a diatom dominance in the SO but sets up dominance of ordinary phytoplankton in the ST due to the limited availability of Si (Table 2.5). In this scenario, 25% of the Si that enters the SO box through upwelling and mixing is transported to the ST box.

When an Fe-dependent Si:N parameterisation is introduced, diatoms deplete all of the Si in the SO box before it can be transported out and therefore less than 1% of Si imported to the SO box is carried to the ST, compared to 65% of P. This compares to a 5% chance for Si and 45% chance for P to be next utilised outside of the SO according to global modelling by Holzer et al. (2014). Consequently, diatom biomass in the ST box is reduced by 45% and, due to the Si limitation created by the high Si:N in the SO, other phytoplankton make up 24% of SO production. This SO ratio of diatoms to non-diatoms is consistent with Assmy et al. (2013) who found that non diatoms generally made up $<$30% of phytoplankton carbon, although this was in a single patch over 5 weeks in austral summer and diatom proportion maybe lower in non-bloom periods (Hirata et al., 2011; Hashioka et al., 2013). Assuming a N:P ratio 16:1 (Redfield, 1934), the SO box measures an Si* ($[Si(OH)_4]$ - $[NO_3{}^-]$) of -18 mmol $m^{-3}$ which is lower than the range of -10 to -15 mmol $m^{-3}$ found by Sarmiento et al. (2004). This could be the result of over-trapping of Si in the box-model. Another suggestion that trapping may be overly vigorous is the Si-limitation generated by the model in the SO box, while the SO is thought to be predominantly Fe-limited (Moore, Mills, Arrigo, Berman-Frank, Bopp, Boyd, Galbraith, Geider, Guieu, Jaccard, Jickells, La Roche, Lenton, Mahowald, Marañón, Marinov, Moore, Nakatsuka, Oschlies, Saito, Thingstad, Tsuda and Ulloa, 2013). Using an Fe-dependent Si:N ratio creates an SO box Si:N of 2:1 which is relatively low compared to some findings (Table 1.1. However, using one of the three parameterisations employed by Holzer et al. (2019) results in Si:N ratios from 4:1 to just over 7:1. In these scenarios, Si supply to the SO would need to be higher or diatom growth would need to be otherwise limited to result in anything other than total Si trapping. Of these options, it seems that the latter would

be more likely as sensitivity testing showed that Si escape efficiency was mostly insensitive to at least ±50% changes in the surface dissolution fraction of Si, the initial deep Si concentration, the aeolian iron input or the strength of iron scavenging.

Increasing Fe fertilisation in the model was shown to produce no rise in the escape of Si from the SO box despite the negative effect this had on Si:N ratios under all parameterisations. This was because the extra Fe available stimulated diatom productivity to the degree that Si was still fully removed before it could be transported north. The solution achieved here appears to run contrary to the Silicic Acid Leakage Hypothesis (SALH) (Brzezinski et al., 2002; Matsumoto et al., 2002) which proposes that increased Fe deposition in glacial times decreased diatom Si:N uptake ratios and this let Si escape the SO to fuel diatom production in the rest of the world's oceans and drawdown more atmospheric $CO_2$. However, the model of Matsumoto et al. (2002) does not measure the escape of Si from the SO but rather the accumulation of excess Si in the subantarctic, the point of mode water formation. They point out that one possible fate of the excess Si created in the subantarctic could be consumption by diatoms if productivity was enhanced, which is an expected response to increased Fe availability (Martin and Fitzwater, 1988; Coale et al., 1996; Boyd et al., 2000). A later study (Crosta et al., 2007) suggested that Si isotope records do not imply an increase in diatom productivity outside the SO when the potential for Si leakage was greatest, which may support the results of this model, although the paper instead offers a lower rate of intermediate water formation at the time as an explanation. Matsumoto and Sarmiento (2008) also later argued that the decrease in atmospheric $CO_2$ could be achieved simply by the dominance of diatoms over coccolithophorids brought about by Si leakage not necessarily by the magnitude of diatom production.

In Chapter 3, shipboard nutrient addition experiments from the CUSTARD cruise were used as a basis to constrain different types of model to try to achieve an optimum solution to the representation of variable diatom stoichiometry. Treatments with no Fe enrichment displayed Si:N uptake ratios up to ∼2.5:1 with one data point reaching 4:1. However, in general, the highest Si:N values came in experiments with added Si while only one data point in the control treatment eclipsed 1.7:1. In comparison, other shipboard incubation experiments have observed Si:N uptake ratios of 3:1 in the California coastal upwelling (Hutchins and Bruland, 1998); 2.3:1 in the Southern Ocean, 2.6:1 in the Subarctic North Pacific and 1.3:1 in the Equatorial Pacific (Takeda, 1998). The higher Si:N in +Si treatments suggest that while Si was not the main limiting nutrient, availability was low enough for diatoms not to have reached maximum uptake rates prior to the addition of Si.

To the author's knowledge, this is the first time models have been applied to recreating the results of an incubation experiment such as this. When using CUSTARD-SIMPLE to simulate these experiments, diatoms did not have sufficient Si to yield chlorophyll increases in response to Fe that were observed in the experiments for LTE's 4, 6 and 7. Of the initial Si available before additions were made in each experiment, these LTE's had the lowest Si concentration of $\leq$1 µmol $L^{-1}$ compared to $\geq$3.4 in the other experiments. This result is observed regardless of Si:N parameterisation. It was therefore hypothesised that there could be Si available within the cell to prompt growth upon the relief of Fe limitation. It is debatable whether intracellular pools of Si stored by diatoms would have any dramatic effect on the ability of diatoms to respond to Fe addition. Kumar et al. (2020) estimated the cells they measured held roughly enough Si to form half of a new cell wall. Alternatively, flexibility in diatom community composition may play a role in varying the Si:C ratio between experiments. The CUSTARD-SIMPLE model overestimated Si:N in the low iron treatments of the gradient experiments, however, this in part may be explained by the sole use of a diatom group within the model. Use of N by other phytoplankton could lower the community Si:N uptake ratio.

To enable the modelling of cellular nutrient concentrations, a quota model (CUSTARD-QUOTA) was employed to simulate the CUSTARD experiments. In the past, quota models have been used to provide the option for luxury uptake of P and Fe (Droop, 1973; Buitenhuis and Geider, 2010; Aumont et al., 2015). Here, the maximum nutrient quota $Q_{max}$ to carbon is set above the optimum quota $Q_{opt}$ for Si, Fe and Mn. With this model setup, an improved fit was seen to the patterns of Chl in the observations, suggesting more appropriate levels of Si utilisation were observed in the experiments that had previously been difficult to replicate. Furthermore, the gradient experiments were far more closely replicated by the CUSTARD-QUOTA model compared to CUSTARD-SIMPLE, although, there was still substantial overshoot in the ΔSi:ΔDIN of GE01. In general, ΔSi:ΔDIN was commonly overestimated for experiments where no Fe was added, though this was much more extreme in the CUSTARD-SIMPLE model. Removing 'other' phytoplankton from the model only minorly increases ΔSi:ΔDIN in CUSTARD-QUOTA which suggests the higher values found in CUSTARD-SIMPLE are not solely the fault of having only diatoms.

In Chapter 4, using a GA approach to pick parameters improved the fit of the CUSTARD-QUOTA-V2 model to the observations. However, the dataset was shown to poorly constrain many parameters. Ward et al. (2010) show that using poorly constrained parameters to fit a model means that the model performs badly when applied to other scenarios. For the hybrid approach settled upon in this study, Ward et al. (2010) point out that this comes at the risk of reintroducing any uncertainty

found in literature-based values. However, in this case, the hybrid approach is likely the best compromise between these two risks. Both in the initial fit of the CUSTARD-QUOTA-V2 model and the subsequent GA optimisations, it is the high ΔSi:ΔDIN values that are hardest for the model to fit. This is likely because high Si:N values occur in the absence of Fe and therefore tend to coincide with the lowest values of ΔDIN and ΔSi. This inherently makes high Si:N harder to measure as is evidenced by a mean standard deviation of 0.02 for ΔSi:ΔDIN in +Fe treatments compared to 0.38 in the non-Fe treatments. Although the cost function does not view low values of ΔSi:ΔDIN any differently than large values in terms of fitting the model, more uncertainty in the measurements potentially makes it harder for the model to reconcile them.

In the sensitivity optimisation, $Q_{max}^{Si}$ and $Q_{min}^{Si}$ were shown to be consistently chosen high in their potential range of values as well as higher than their original hand-picked values. The fact that values of $Q_{max}^{Si}$ from the model fits did not trend toward $Q_{opt}^{Si}$, supports the idea that a degree of luxury uptake is necessary to simulate these observations. Maximum diatom growth rate ($\mu_{max}$) is predicted by almost all GA optimisations to be smaller than that of other algae. This contradicts the general idea that diatoms tend to have higher growth rates (Furnas, 1990; Edwards et al., 2015). However, it has been shown that larger diatoms have slower growth rates than smaller or intermediately sized diatoms (Timmermans et al., 2004; Marañón et al., 2013). Assmy et al. (2013) also report a progression from small, fast-growing cells with low iron requirements to large, slow-growing cells with stronger Si armour during the course of an iron-stimulated bloom. The results from the GA suggest that it is these larger cells that may be more present, particularly in +Fe treatments or in the southern experiments which exhibited bloom conditions.

The initial diatom fraction set by the fits to each LTE was strongly constrained by the GA and correlated to a pigment indicator of the proportion of diatoms in the starting communities. This shows that community structure played a key role in defining the responses to the nutrient addition experiments. Just among diatoms, size, growth rate, silicification and tendency for aggregation result in different contributions to carbon and Si export and different Si:N uptake ratios (Assmy et al., 2013; Tréguer et al., 2018). Warming temperatures are also expected to benefit some diatoms more than others (Jabre et al., 2021). At the community scale, changes in community composition are predicted as a response to climate change including the colonisation of the Southern Ocean by small dinoflagellates (Henson et al., 2021). It will be important to combine predictions of future species and composition with knowledge of their specific uptake stoichiometries and silicification strategies. Models currently include different size

classes of diatoms and this could be paired with different levels of silicification and Si:N uptake ratios to observe emergent classes.

## 5.4 Limitations

In Chapter 2 a 3-box model (3BOX-SIMPLE) is used to study the mechanics of the SO Si trap. This simplistic view was chosen in order to reduce the Si trap to its most important key features and to easily interpret the effects of changing parameters and starting conditions. However, this necessarily comes with large assumptions. In reducing the phytoplankton community down to two groups, this model misses the potential effects of a more diverse phytoplankton assembly on Si:N ratios in the SO. For instance, the slow growing, thick shelled diatom species like *Fragilariopsis* compared to fast-growing, less silicified species like *Chaetoceros*. The assumption of diatoms having a faster growth rate than non-diatoms was also called into question by some optimisations in Chapter 4. Furthermore, seasonality and light-limitation play an important role in the biology of SO (Thomalla et al., 2011) and therefore, the transport of Si to the ST and the export of Si to depth. While it is useful to create large scale steady state estimates, precisely because we cannot directly measure such values, it can be difficult to translate data taken from a very specific place and time to the parameterisation of large-scale models. This is why Chapter's 3 and 4 aim to bridge the gap between small scale experiments on diatom physiology and such models. A very simple Fe cycle is used in this model to allow for the limitation of SO production and enhancement of diatom Si:N ratios in response to Fe deficiency as well as the reduction of Si:N when fertilisation occurs. Because of the several forms that exist in seawater and therefore different bioavailability, Fe in the ocean is very difficult to model (Parekh et al., 2004). From this standpoint, this model likely does not suffer much compared to much more complex models that still are not able to place great faith in the realism of their Fe cycles.

In Chapters 3 and 4, two quota model approaches (CUSTARD-QUOTA and CUSTARD-QUOTA-V2) were used to fit nutrient addition experiments conducted in the SO. These experiments showed a range of responses to the provision of Si, Fe and Mn which provided a good target to improve the modelling of diatom physiology. However, these experiments took place at one time of the year (austral summer) in one portion (Eastern Pacific) of the SO and therefore do not necessarily represent the average SO diatom responses, although the latitudinal gradient in productivity and diatom representation seen in Figure 4.16 do provide some heterogeneity. As discussed in Chapter 4, utilising a genetic algorithm to fit CUSTARD-QUOTA-V2 to

the observations carries the risk of over-tuning the model and mistaking this for model performance. It is hoped that, by using the algorithm to identify and exclude poorly constrained parameters and making the algorithm pick parameter values from within ranges based on the literature, a balance between tuning and versatility has been struck. However, until the model is tested on more data it is not possible to know this for certain.

## 5.5 Future Work

In Chapter 3 and 4, quota models were developed and optimised to provide a strong fit to the observations of the nutrient addition experiments. By exposing SO diatoms to a range of nutrient conditions these experiments provided a good basis of diatom physiology on which to target the model. The next step in this research is to apply the resulting model and parameter set in larger scale models to test how broadly they may be applied. In Demuynck et al. (2020), a model consisting of a chain of boxes representing the mixed and subsurface layer of the SO was used to study the latitudinal Si gradient in the region. In the southern section of the model, upwelling was introduced from deep layer forced by prior observations while nutrients in the mixed layer were advected northwards toward the point of mode water formation. Three classes of diatoms uptake nutrients and interact with two classes of zooplankton over a seasonal cycle. The variable chlorophyll model from this thesis has been placed within the structure of the Demuynck et al. model as ongoing work with the aim of using water column data from the CUSTARD cruise as deep forcing and trying to replicate the surface observations made there. Furthermore, work has begun to introduce the parameter set created here to a version of EcoGEnIE (Ward et al., 2018), a marine ecology enabled Earth system model. This will enable the testing of the response of the whole ocean to the quota model and parameters developed in this thesis.

Chapter 2 shows how important parameterisations of diatom Si:N are in determining Si trapping and therefore diatom productivity in the rest of the world (Sarmiento et al., 2004). Given the key role Si trapping plays, an intercomparison should be conducted between earth system models specifically focusing on how much Si they estimate to leak from the SO based on their particular parameterisation of diatom physiology and sinking, remineralisation depth and circulation. This research could potentially use the data from existing runs of the models.

Overall the work presented in this thesis has improved understanding of the coupling and decoupling of Si:N:P:Fe stoichiometry through community structure and diatom

physiology over different scales. Further application of this new knowledge in other model frameworks has the potential to generate an improved understanding of Southern Ocean Si trapping over multiple time and space scales.

# References

Anderson, T. R., Gentleman, W. C. and Yool, A. (2015), 'EMPOWER-1.0: An Efficient Model of Planktonic ecOsystems WrittEn in R', *Geoscientific Model Development* **8**(7), 2231–2262.

Angelis, M. D., Barkov, N. I. and Petrov, V. N. (1987), 'Aerosol concentrations over the last climatic cycle (160 kyr) from an Antarctic ice core', *Nature 1987 325:6102* **325**(6102), 318–321.
**URL:** *https://www.nature.com/articles/325318a0*

Armstrong, R. A., Lee, C., Hedges, J. I., Honjo, S. and Wakeham, S. G. (2002), 'A new, mechanistic model for organic carbon fluxes in the ocean based on the quantitative association of POC with ballast minerals', *Deep Sea Research Part II: Topical Studies in Oceanography* **49**(1-3), 219–236.
**URL:** *https://www.sciencedirect.com/science/article/pii/S096706450100101 1bBIB32*

Arrigo, K. R., Robinson, D. H., Worthen, D. L., Dunbar, R. B., DiTullio, G. R., VanWoert, M. and Lizotte, M. P. (1999), 'Phytoplankton community structure and the drawdown of nutrients and CO2 in the southern ocean', *Science* **283**(5400), 365–7.
**URL:** *http://www.ncbi.nlm.nih.gov/pubmed/9888847*

Arteaga, L., Haëntjens, N., Boss, E., Johnson, K. S. and Sarmiento, J. L. (2018), 'Assessment of Export Efficiency Equations in the Southern Ocean Applied to Satellite-Based Net Primary Production', *Journal of Geophysical Research: Oceans* **123**(4), 2945–2964.
**URL:** *https://onlinelibrary.wiley.com/doi/full/10.1002/2018JC013787*

Assmy, P., Smetacek, V., Montresor, M., Klaas, C., Henjes, J., Strass, V. H., Arrieta, J. M., Bathmann, U., Berg, G. M., Breitbarth, E., Cisewski, B., Friedrichs, L., Fuchs, N., Herndl, G. J., Jansen, S., Kragefsky, S., Latasa, M., Peeken, I., Rottgers, R., Scharek, R., Schuller, S. E., Steigenberger, S., Webb, A. and Wolf-Gladrow, D. (2013), 'Thick-shelled, grazer-protected diatoms decouple ocean carbon and silicon cycles in the iron-limited Antarctic Circumpolar Current', *Proceedings of the National*

*Academy of Sciences* **110**(51), 20633–20638.
**URL:** *http://www.pnas.org/cgi/doi/10.1073/pnas.1309345110*

Athias, V., Mazzega, P. and Jeandel, C. (2000), 'Selecting a global optimization method to estimate the oceanic particle cycling rate constants', *Journal of Marine Research* **58**(5), 675–707.
**URL:** *https://elischolar.library.yale.edu/.*

Aumont, O., Ethé, C., Tagliabue, A., Bopp, L. and Gehlen, M. (2015), 'PISCES-v2: An ocean biogeochemical model for carbon and ecosystem studies', *Geoscientific Model Development* **8**(8), 2465–2513.

Azam, F., Hemmingsen, B. B. and Volcani, E. (1974), 'Role of Silicon in Diatom Metabolism', *Archives of Microbiology* **97**, 103–114.

Balaguer, J., Koch, F., Hassler, C. and Trimborn, S. (2022), 'Iron and manganese co-limit the growth of two phytoplankton groups dominant at two locations of the Drake Passage', *Communications Biology* **5**(1), 1–12.

Banse, K. (1995), 'Zooplankton: Pivotal role in the control of ocean production', *ICES Journal of Marine Science* **52**(3-4), 265–277.
**URL:** *https://academic.oup.com/icesjms/article-lookup/doi/10.1016/1054-3139(95)80043-3*

Barnola, J. M., Raynaud, D., Korotkevich, Y. S. and Lorius, C. (1987), 'Vostok ice core provides 160,000-year record of atmospheric CO2', *Nature* **329**(6138), 408–414.
**URL:** *https://www.nature.com/articles/329408a0*

Bidle, K. D. and Azam, F. (1999), 'Accelerated dissolution of diatom silica by marine bacterial assemblages', *Nature 1999 397:6719* **397**(6719), 508–512.
**URL:** *https://www.nature.com/articles/17351*

Blackman, F. F. (1905), 'Optima and limiting factors', *Annals of Botany* **os-19**(2).

Boyd, P. and Law, C. (2001), 'The Southern Ocean Iron RElease Experiment (SOIREE)—introduction and summary', *Deep Sea Research Part II: Topical Studies in Oceanography* **48**(11-12), 2425–2438.
**URL:** *https://www.sciencedirect.com/science/article/pii/S0967064501000029BIB42*

Boyd, P. W. (2015), 'Toward quantifying the response of the oceans' biological pump to climate change', *Frontiers in Marine Science* **2**(OCT), 77.

Boyd, P. W. and Abraham, E. R. (2001), 'Iron-mediated changes in phytoplankton photosynthetic competence during SOIREE', *Deep-Sea Research Part II: Topical Studies in Oceanography* **48**(11-12), 2529–2550.

Boyd, P. W., Claustre, H., Levy, M., Siegel, D. A. and Weber, T. (2019), 'Multi-faceted particle pumps drive carbon sequestration in the ocean', *Nature* **568**(7752), 327–335.
**URL:** *http://dx.doi.org/10.1038/s41586-019-1098-2*

Boyd, P. W., Dillingham, P. W., Mcgraw, C. M., Armstrong, E. A., Cornwall, C. E., Feng, Y. Y., Hurd, C. L., Gault-Ringold, M., Roleda, M. Y., Timmins-Schiffman, E. and Nunn, B. L. (2015), 'Physiological responses of a Southern Ocean diatom to complex future ocean conditions', *Nature Climate Change* **6**(2), 207–213.
**URL:** *www.nature.com/natureclimatechange*

Boyd, P. W. and Ellwood, M. J. (2010), 'The biogeochemical cycle of iron in the ocean', *Nature Geoscience 2010 3:10* **3**(10), 675–682.
**URL:** *https://www.nature.com/articles/ngeo964*

Boyd, P. W., Jickells, T., Law, C. S., Blain, S., Boyle, E. A., Buesseler, K. O., Coale, K. H., Cullen, J. J., De Baar, H. J., Follows, M., Harvey, M., Lancelot, C., Levasseur, M., Owens, N. P., Pollard, R., Rivkin, R. B., Sarmiento, J., Schoemann, V., Smetacek, V., Takeda, S., Tsuda, A., Turner, S. and Watson, A. J. (2007), 'Mesoscale iron enrichment experiments 1993-2005: Synthesis and future directions', *Science* **315**(5812), 612–617.
**URL:** *http://science.sciencemag.org/*

Boyd, P. W., Watson, A. J., Law, C. S., Abraham, E. R., Trull, T., Murdoch, R., Bakker, D. C. E., Bowie, A. R., Buesseler, K. O., Chang, H., Charette, M., Croot, P., Downing, K., Frew, R., Gall, M., Hadfield, M., Hall, J., Harvey, M., Jameson, G., LaRoche, J., Liddicoat, M., Ling, R., Maldonado, M. T., McKay, R. M., Nodder, S., Pickmere, S., Pridmore, R., Rintoul, S., Safi, K., Sutton, P., Strzepek, R., Tanneberger, K., Turner, S., Waite, A. and Zeldis, J. (2000), 'A mesoscale phytoplankton bloom in the polar Southern Ocean stimulated by iron fertilization', *Nature* **407**(6805), 695–702.
**URL:** *http://www.nature.com/articles/35037500*

Broeker, W. S. (1991), 'The Great Ocean Conveyor', *Oceanography* **4**(2), 79–89.

Browning, T. J., Achterberg, E. P., Engel, A. and Mawji, E. (2021), 'Manganese co-limitation of phytoplankton growth and major nutrient drawdown in the Southern Ocean', *Nature Communications* **12**(1), 1–9.
**URL:** *http://dx.doi.org/10.1038/s41467-021-21122-6*

Browning, T. J., Bouman, H. A., Henderson, G. M., Mather, T. A., Pyle, D. M., Schlosser, C., Woodward, E. M. S. and Moore, C. M. (2014), 'Strong responses of Southern Ocean phytoplankton communities to volcanic ash', *Geophysical Research Letters* **41**(8), 2851–2857.
**URL:** *http://doi.wiley.com/10.1002/2014GL059364*

Bruland, K. W., Donat, J. R. and Hutchins, D. A. (1991), 'Interactive influences of bioactive trace metals on biological production in oceanic waters', *Limnology and Oceanography* **36**(8), 1555–1577.

Brzezinski, M. A. (1985), 'The Si:C:N ratio of marine diatoms: interspecific variability and the effect of some environmental variables', *Journal of Phycology* **21**(3), 347–357.
**URL:** *http://doi.wiley.com/10.1111/j.0022-3646.1985.00347.x*

Brzezinski, M. A., Baines, S. B., Balch, W. M., Beucher, C. P., Chai, F., Dugdale, R. C., Krause, J. W., Landry, M. R., Marchi, A., Measures, C. I., Nelson, D. M., Parker, A. E., Poulton, A. J., Selph, K. E., Strutton, P. G., Taylor, A. G. and Twining, B. S. (2011), 'Co-limitation of diatoms by iron and silicic acid in the equatorial Pacific', *Deep-Sea Research Part II: Topical Studies in Oceanography* **58**(3-4), 493–511.

Brzezinski, M. A. and Conley, D. J. (1994), 'Silicon deposition during the cell cycle of Thalassiosira weissflogii (Bacillariophyceae) determined using dual rhodamine 123 and propidium iodide staining.', *Journal of Phycology* **30**(1), 45–55.
**URL:** *https://onlinelibrary.wiley.com/doi/full/10.1111/j.0022-3646.1994.00045.x*

Brzezinski, M. A., Dickson, M.-L., Nelson, D. M. and Sambrotto, R. (2003), 'Ratios of Si, C and N uptake by microplankton in the Southern Ocean', *Deep Sea Research Part II: Topical Studies in Oceanography* **50**(3-4), 619–633.
**URL:** *https://www.sciencedirect.com/science/article/pii/S0967064502005878*

Brzezinski, M. A., Krause, J. W., Bundy, R. M., Barbeau, K. A., Franks, P., Goericke, R., Landry, M. R. and Stukel, M. R. (2015), 'Enhanced silica ballasting from iron stress sustains carbon export in a frontal zone within the California Current', *Journal of Geophysical Research: Ocseans* **120**(7), 4654–4669.
**URL:** *http://doi.wiley.com/10.1002/2015JC010829*

Brzezinski, M. A., Nelson, D. M., Franck, V. M. and Sigmon, D. E. (2001), 'Silicon dynamics within an intense open-ocean diatom bloom in the Pacific sector of the Southern Ocean', *Deep-Sea Research Part II: Topical Studies in Oceanography* **48**(19-20), 3997–4018.

Brzezinski, M. A., Pride, C. J., Franck, V. M., Sigman, D. M., Gruber, N., Rau, G. H. and Coale, K. H. (2002), 'A switch from Si(OH)4 to NO3 depletion in the glacial Southern Ocean', *Geophysical Research Letters* **29**(12), 3–6.

Brzezinski, M., Olson, R. and Chisholm, S. (1990), 'Silicon availability and cell-cycle progression in marine diatoms', *Marine Ecology Progress Series* **67**(1), 83–96.

Buitenhuis, E. T. and Geider, R. J. (2010), 'A model of phytoplankton acclimation to iron-light colimitation', *Limnology and Oceanography* **55**(2), 714–724.

Burmaster, D. E. (1979), 'The Continuous Culture of Phytoplankton: Mathematical Equivalence Among Three Steady-State Models', *The American Naturalist* **113**(1), 123–134.
**URL:** *https://www.journals.uchicago.edu/doi/10.1086/283368*

Caperon, J. (1967), 'Population Growth in Micro-Organisms Limited by Food Supply', *Ecology* **48**(5), 715–722.

Chepurnov, V. A., Mann, D. G., Sabbe, K. and Vyverman, W. (2004), 'Experimental Studies on Sexual Reproduction in Diatoms', *International Review of Cytology* **237**, 91–154.

Chisholm, S. W., Azam, F. and Eppley, R. W. (1978), 'Silicic acid incorporation in marine diatoms on light:dark cycles: Use as an assay for phased cell division', *Limnology and Oceanography* **23**(3).

Claquin, P., Martin-Jezequel, V., Kromkamp, J. C., Veldhuis, M. J. W. and Kraay, G. W. (2002), 'Uncoupling Of Silicon Compared With Carbon And Nitrogen Metabolisms And The Role Of The Cell Cycle In Continuous Cultures Of Thalassiosira Pseudonana (Bacillariophyceae) Under Light, Nitrogen, And Phosphorus Control', *Journal of Phycology* **38**(5), 922–930.
**URL:** *http://doi.wiley.com/10.1046/j.1529-8817.2002.t01-1-01220.x*

Cloern, J. E., Grenz, C. and Vidergar-Lucas, L. (1995), 'An empirical model of the phytoplankton chlorophyll : carbon ratio-the conversion factor between productivity and growth rate'.

Coale, K. H., Johnson, K. S., Chavez, F. P., Buesseler, K. O., Barber, R. T., Brzezinski, M. A., Cochlan, W. P., Millero, F. J., Falkowski, P. G., Bauer, J. E., Wanninkhof, R. H., Kudela, R. M., Altabet, M. A., Hales, B. E., Takahashi, T., Landry, M. R., Bidigare, R. R., Wang, X., Chase, Z., Strutton, P. G., Friederich, G. E., Gorbunov, M. Y., Lance, V. P., Hilting, A. K., Hiscock, M. R., Demarest, M., Hiscock, W. T., Sullivan, K. F., Tanner, S. J., Gordon, R. M., Hunter, C. N., Elrod, V. A., Fitzwater, S. E., Jones, J. L., Tozzi, S., Koblizek, M., Roberts, A. E., Herndon, J., Brewster, J., Ladizinsky, N., Smith, G., Cooper, D., Timothy, D., Brown, S. L., Selph, K. E., Sheridan, C. C., Twining, B. S. and Johnson, Z. I. (2004), 'Southern Ocean Iron Enrichment Experiment: Carbon Cycling in High- and Low-Si Waters', *Science* **304**(5669), 408–414.

Coale, K. H., Johnson, K. S., Fitzwater, S. E., Gordon, R. M., Tanner, S., Chavez, F. P., Ferioli, L., Sakamoto, C., Rogers, P., Millero, F., Steinberg, P., Nightingale, P., Cooper, D., Cochlan, W. P., Landry, M. R., Constantinou, J., Rollwagen, G., Trasvina, A. and

Kudela, R. (1996), 'A massive phytoplankton bloom induced by an ecosystem-scale iron fertilization experiment in the equatorial Pacific Ocean', *Nature* **383**(6600), 495.
**URL:** *http://www.nature.com/articles/383495a0*

Collins, W. J., Bellouin, N., Doutriaux-Boucher, M., Gedney, N., Halloran, P., Hinton, T., Hughes, J., Jones, C. D., Joshi, M., Liddicoat, S., Martin, G., O'Connor, F., Rae, J., Senior, C., Sitch, S., Totterdell, I., Wiltshire, A. and Woodward, S. (2011), 'Development and evaluation of an Earth-System model - HadGEM2', *Geoscientific Model Development* **4**(4), 1051–1075.

Conley, D. J., Frings, P. J., Fontorbe, G., Clymans, W., Stadmark, J., Hendry, K. R., Marron, A. O. and De La Rocha, C. L. (2017), 'Biosilicification drives a decline of dissolved si in the oceans through geologic time', *Frontiers in Marine Science* **4**(DEC), 397.

Corzo, A., Morillo, J. and Rodríguez, S. (2000), 'Production of transparent exopolymer particles (TEP) in cultures of Chaetoceros calcitrans under nitrogen limitation', *Aquatic Microbial Ecology* **23**(1), 63–72.
**URL:** *http://www.int-res.com/abstracts/ame/v23/n1/p63-72/*

Crosta, X., Beucher, C., Pahnke, K. and Brzezinski, M. A. (2007), 'Silicic acid leakage from the Southern Ocean: Opposing effects of nutrient uptake and oceanic circulation', *Geophysical Research Letters* **34**(13).
**URL:** *https://onlinelibrary.wiley.com/doi/full/10.1029/2006GL029083*

Cullen, J. J. (1991), 'Hypotheses to explain high-nutrient conditions in the open sea', *Limnology and Oceanography* **36**(8), 1578–1599.
**URL:** *http://doi.wiley.com/10.4319/lo.1991.36.8.1578*

Dafner, E. V. and Mordasova, N. V. (1994), 'Influence of biotic factors on the hydrochemical structure of surface water in the Polar Frontal Zone of the Atlantic Antarctic', *Marine Chemistry* **45**(1-2), 137–148.

Dau, H. and Haumann, M. (2008), 'The manganese complex of photosystem II in its reaction cycle—Basic framework and possible realization at the atomic level', *Coordination Chemistry Reviews* **252**(3-4), 273–295.

de Baar, H. J. (1994), 'von Liebig's law of the minimum and plankton ecology (1899-1991)', *Progress in Oceanography* **33**(4), 347–386.

de Baar, H. J. W., de Jong, J. T. M., Bakker, D. C. E., Löscher, B. M., Veth, C., Bathmann, U. and Smetacek, V. (1995), 'Importance of iron for plankton blooms and carbon dioxide drawdown in the Southern Ocean', *Nature* **373**(6513), 412–415.
**URL:** *http://www.nature.com/articles/373412a0*

De La Rocha, C. (2006), The Biological Pump, *in* H. Elderfield, ed., 'Treatise on Geochemistry', 1st edn, Elsevier, Oxford, chapter 6.04, pp. 83–112.

De La Rocha, C., Hutchins, D., Brzezinski, M. and Zhang, Y. (2000), 'Effects of iron and zinc deficiency on elemental composition and silica production by diatoms', *Marine Ecology Progress Series* **195**, 71–79.
**URL:** *http://www.int-res.com/abstracts/meps/v195/p71-79/*

Demuynck, P., Tyrrell, T., Naveira Garabato, A., Moore, M. C. and Martin, A. P. (2020), 'Spatial variations in silicate-to-nitrate ratios in Southern Ocean surface waters are controlled in the short term by physics rather than biology', *Biogeosciences* **17**(8), 2289–2314.
**URL:** *https://bg.copernicus.org/articles/17/2289/2020/*

Deppeler, S. L. and Davidson, A. T. (2017), 'Southern Ocean phytoplankton in a changing climate', *Frontiers in Marine Science* **4**(FEB), 40.

Devries, T. (2014), 'The oceanic anthropogenic CO2 sink: Storage, air-sea fluxes, and transports over the industrial era', *Global Biogeochemical Cycles* **28**(7), 631–647.
**URL:** *http://doi.wiley.com/10.1002/2013GB004739*

*Dive and Discover : Antarctica : Circulation* (2005).
**URL:** *https://divediscover.whoi.edu/archives/ecosystem/circulation-en.html*

Domingues, R. B., Anselmo, T. P., Barbosa, A. B., Sommer, U. and Galvão, H. M. (2011), 'Nutrient limitation of phytoplankton growth in the freshwater tidal zone of a turbid, Mediterranean estuary', *Estuarine, Coastal and Shelf Science* **91**(2), 282–297.

Drapeau, D. T., Dam, H. G. and Grenie, G. (1994), 'An improved flocculator design for use in particle aggregation experiments', *Limnology and Oceanography* **39**(3), 723–729.
**URL:** *http://doi.wiley.com/10.4319/lo.1994.39.3.0723*

Droop, M. R. (1968), 'Vitamin B12 and Marine Ecology. IV. The Kinetics of Uptake, Growth and Inhibition in Monochrysis Lutheri', *Journal of the Marine Biological Association of the United Kingdom* **48**(3), 689–733.

Droop, M. R. (1973), 'Some thoughts on nutrient limitation in algae', *Journal of Phycology* **9**(3), 264–272.
**URL:** *https://onlinelibrary.wiley.com/doi/full/10.1111/j.1529-8817.1973.tb04092.x*

Droop, M. R. (1983), '25 Years of Algal Growth Kinetics: A Personal View', *Botanica Marina* **26**(3), 99–112.
**URL:** *https://www.degruyter.com/view/journals/botm/26/3/article-p99.xml*

Dugdale, R. C. (1967), 'Nutrient limitation in the sea: dynamics, identification, and significance.', *Limnology and Oceanography* **12**(4), 685–695.

Dugdale, R. C. and Wilkerson, F. P. (2001), 'Sources and fates of silicon in the ocean: The role of diatoms in the climate and glacial cycles', *Scientia Marina* **65**(SUPPLEMENT 2), 141–152.

Edwards, K. F., Thomas, M. K., Klausmeier, C. A. and Litchman, E. (2015), 'Light and growth in marine phytoplankton: Allometric, taxonomic, and environmental variation', *Limnology and Oceanography* **60**(2), 540–552.
**URL:** *https://onlinelibrary.wiley.com/doi/full/10.1002/lno.10033*

Evans, G. T. and Parslow, J. S. (1985), 'A model of annual plankton cycles', *Biological Oceanography* **3**(3), 327–347.
**URL:** *https://www.tandfonline.com/action/journalInformation?journalCode=tboc20*

Falkowski, P. G., Barber, R. T. and Smetacek, V. (1998), 'Biogeochemical Controls and Feedbacks on Ocean Primary Production', *Science (New York, N.Y.)* **281**(5374), 200–7.
**URL:** *http://www.ncbi.nlm.nih.gov/pubmed/9660741*

Falkowski, P. G. and Kolber, Z. (1995), 'Variations in chlorophyll fluorescence yields in phytoplankton in the world oceans', *Australian Journal of Plant Physiology* **22**(2), 341–355.
**URL:** *https://www.publish.csiro.au/fp/pp9950341*

Falls, M., Bernardello, R., Castrillo, M., Acosta, M., Llort, J. and Galí, M. (2022), 'Use of genetic algorithms for ocean model parameter optimisation: a case study using PISCES-v2_RC for North Atlantic particulate organic carbon', *Geoscientific Model Development* **15**(14), 5713–5737.

Fasham, M. J. (1995), 'Variations in the seasonal cycle of biological production in subarctic oceans: A model sensitivity analysis', *Deep-Sea Research Part I* **42**(7), 1111–1149.

Fasham, M. J., Ducklow, H. W. and McKelvie, S. M. (1990), 'A nitrogen-based model of plankton dynamics in the oceanic mixed layer', *Journal of Marine Research* **48**(3), 591–639.

Field, C. B., Behrenfeld, M. J., Randerson, J. T. and Falkowski, P. (1998), 'Primary production of the biosphere: Integrating terrestrial and oceanic components', *Science* **281**(5374), 237–240.
**URL:** *https://www.science.org/doi/10.1126/science.281.5374.237*

Franck, V., Bruland, K., Hutchins, D. and Brzezinski, M. (2003), 'Iron and zinc effects on silicic acid and nitrate uptake kinetics in three high-nutrient, low-chlorophyll (HNLC) regions', *Marine Ecology Progress Series* **252**, 15–33.
**URL:** *http://www.int-res.com/abstracts/meps/v252/p15-33/*

François, R., Altabett, M. A., Yu, E. F., Sigman, D. M., Bacon, M. P., Frank, M., Bohrmann, G., Bareille, G. and Labeyrie, L. D. (1997), 'Contribution of Southern Ocean surface-water stratification to low atmospheric CO2 concentrations during the last glacial period', *Nature* **389**(6654), 929–935.
**URL:** *https://www.nature.com/articles/40073*

Friedrichs, L., Hörnig, M., Schulze, L., Bertram, A., Jansen, S. and Hamm, C. (2013), 'Size and biomechanic properties of diatom frustules influence food uptake by copepods', *Marine Ecology Progress Series* **481**, 41–51.

Frölicher, T. L., Sarmiento, J. L., Paynter, D. J., Dunne, J. P., Krasting, J. P. and Winton, M. (2015), 'Dominance of the Southern Ocean in anthropogenic carbon and heat uptake in CMIP5 models', *Journal of Climate* **28**(2), 862–886.
**URL:** *https://journals.ametsoc.org/view/journals/clim/28/2/jcli-d-14-00117.1.xml*

Frost, B. W. (1991), 'The role of grazing in nutrient-rich areas of the open sea', *Limnology and Oceanography* **36**(8), 1616–1630.
**URL:** *https://onlinelibrary.wiley.com/doi/full/10.4319/lo.1991.36.8.1616*

Furnas, M. J. (1990), 'In situ growth rates of marine phytoplankton: Approaches to measurement, community and species growth rates', *Journal of Plankton Research* **12**(6), 1117–1151.

Gall, M. P., Boyd, P. W., Hall, J., Safi, K. A. and Chang, H. (2001), 'Phytoplankton processes. Part 1: Community structure during the Southern Ocean Iron RElease Experiment (SOIREE)', *Deep-Sea Research Part II: Topical Studies in Oceanography* **48**(11-12), 2551–2570.
**URL:** *https://www.sciencedirect.com/science/article/pii/S096706450100008X*

Garcia, H., Weathers, K., Paver, C., Smolyar, I., Boyer, T., Locarnini, R., Zweng, M., Mishonov, A., Baranova, O., Seidov, D. and Reagan, J. (2018), 'World Ocean Atlas 2018. Volume 4: Dissolved Inorganic Nutrients (phosphate, nitrate and nitrate+nitrite, silicate)', *NOAA Atlas NESDIS 84* **84**(July).

Geider, R. J. (1987), 'Light and temperature dependence of the carbon to chlorophyll ratio in microalgae an cyanobacteria: Implications for physiology and growth of phytoplankton', *New Phytologist* **106**(1), 1–34.

Geider, R. J. and La Roche, J. (1994), 'The role of iron in phytoplankton photosynthesis, and the potential for iron-limitation of primary productivity in the sea', *Photosynthesis Research* **39**(3), 275–301.

Geider, R. J., MacIntyre, H. L. and Kana, T. M. (1997), 'Dynamic model of phytoplankton growth and acclimation: responses of the balanced growth rate and the chlorophyll a:carbon ratio to light, nutrient-limitation and temperature', *Marine Ecology Progress Series* **148**(1-3), 187–200.
**URL:** *https://www.int-res.com/abstracts/meps/v148/p187-200/*

Geider, R. J., MacIntyre, H. L. and Kana, T. M. (1998), 'A dynamic regulatory model of phytoplanktonic acclimation to light, nutrients, and temperature', *Limnology and Oceanography* **43**(4), 679–694.
**URL:** *https://aslopubs.onlinelibrary.wiley.com/doi/full/10.4319/lo.1998.43.4.0679*

Gentleman, W. (2002), 'A chronology of plankton dynamics in silico: How computer models have been used to study marine ecosystems', *Hydrobiologia* **480**(1), 69–85.
**URL:** *https://link.springer.com/article/10.1023/A:1021289119442*

Gervais, F., Riebesell, U. and Gorbunov, M. Y. (2002), 'Changes in primary productivity and chlorophyll a in response to iron fertilization in the Southern Polar Frontal Zone', *Limnology and Oceanography* **47**(5), 1324–1335.
**URL:** *http://doi.wiley.com/10.4319/lo.2002.47.5.1324*

Gran, H. H. (1931), 'II. On the Conditions for the Production of Plankton in the Sea', *Rapports et procès-verbaux des réunions, ICES Journal* **75**, 37–46.

Greene, R. M., Geider, R. J. and Falkowski, P. G. (1991), 'Effect of iron limitation on photosynthesis in a marine diatom', *Limnology and Oceanography* **36**(8), 1772–1782.
**URL:** *https://aslopubs.onlinelibrary.wiley.com/doi/full/10.4319/lo.1991.36.8.1772*

Greene, R. M., Kolber, Z. S., Swift, D. G., Tindale, N. W. and Falkowski, P. G. (1994), 'Physiological limitation of phytoplankton photosynthesis in the eastern equatorial Pacific determined from variability in the quantum yield of fluorescence', *Limnology and Oceanography* **39**(5), 1061–1074.
**URL:** *http://doi.wiley.com/10.4319/lo.1994.39.5.1061*

Gröger, C., Sumper, M. and Brunner, E. (2008), 'Silicon uptake and metabolism of the marine diatom Thalassiosira pseudonana: Solid-state 29Si NMR and fluorescence microscopic studies', *Journal of Structural Biology* **161**(1), 55–63.

Guildford, S. J. and Hecky, R. E. (2000), 'Total nitrogen, total phosphorus, and nutrient limitation in lakes and oceans: Is there a common relationship?', *Limnology and Oceanography* **45**(6), 1213–1223.

Gurvan, M. and The NEMO Team (2022), 'NEMO ocean engine'.
**URL:** *https://zenodo.org/record/6334656*

Hamm, C. (2000), 'Architecture, ecology and biogeochemistry of Phaeocystis colonies', *Journal of Sea Research* **43**(3-4), 307–315.
**URL:** *https://www.sciencedirect.com/science/article/pii/S1385110100000149*

Hamm, C. E., Merkel, R., Springer, O., Jurkojc, P., Maier, C., Prechtel, K. and Smetacek, V. (2003), 'Architecture and material properties of diatom shells provide effective mechanical protection', *Nature* **421**(6925), 841–843.
**URL:** *http://www.nature.com/articles/nature01416*

Hanawa, K. and Talley, L. D. (2001), Chapter 5.4 Mode waters, *in* G. Siedler, J. Church and J. Gould, eds, 'Ocean Circulation and Climate', Vol. 77 of *International Geophysics*, Academic Press, pp. 373–386.
**URL:** *https://www.sciencedirect.com/science/article/pii/S0074614201801297*

Haney, J. D. and Jackson, G. A. (1996), 'Modeling phytoplankton growth rates', *Journal of Plankton Research* **18**(1), 63–85.
**URL:** *https://academic.oup.com/plankt/article/18/1/63/1468938*

Harrison, K. G. (2000), 'Role of increased marine silica input on paleo-pCO2 levels', *Paleoceanography* **15**(3), 292–298.

Hashioka, T., Vogt, M., Yamanaka, Y., Le Quéré, C., Buitenhuis, E. T., Aita, M. N., Alvain, S., Bopp, L., Hirata, T., Lima, I., Sailley, S. and Doney, S. C. (2013), 'Phytoplankton competition during the spring bloom in four plankton functional type models', *Biogeosciences* **10**(11), 6833–6850.

Hauck, J., Lenton, A., Langlais, C. and Matear, R. (2018), 'The Fate of Carbon and Nutrients Exported Out of the Southern Ocean', *Global Biogeochemical Cycles* **32**(10), 1556–1573.
**URL:** *https://onlinelibrary.wiley.com/doi/full/10.1029/2018GB005977*

Hein, M., Pedersen, M., Sand-Jensen, K. and Sand-Jensen (1995), 'Size-dependent nitrogen uptake in micro- and macroalgae', *Marine Ecology Progress Series* **118**, 247–253.
**URL:** *http://www.int-res.com/abstracts/meps/v118/p247-253/*

Hendry, K. R. and Brzezinski, M. A. (2014), 'Using silicon isotopes to understand the role of the Southern Ocean in modern and ancient biogeochemistry and climate', *Quaternary Science Reviews* **89**, 13–26.

Henson, S. A., Cael, B. B., Allen, S. R. and Dutkiewicz, S. (2021), 'Future phytoplankton diversity in a changing climate', *Nature Communications 2021 12:1* **12**(1), 1–8.
**URL:** *https://www.nature.com/articles/s41467-021-25699-w*

Hildebrand, M. (2000), Silicic Acid Transport and Its Control During Cell Wall Silicification in Diatoms, *in* 'Biomineralization', Wiley-VCH, Weinheim, chapter 10, pp. 171–188.
**URL:** *https://onlinelibrary.wiley.com/doi/abs/10.1002/3527604138.ch10*

Hildebrand, M. (2008), 'Diatoms, biomineralization processes, and genomics', *Chemical Reviews* **108**(11), 4855–4874.
**URL:** *https://pubs.acs.org/doi/full/10.1021/cr078253z*

Hirata, T., Hardman-Mountford, N. J., Brewin, R. J. W., Aiken, J., Barlow, R., Suzuki, K., Isada, T., Howell, E., Hashioka, T., Noguchi-Aita, M. and Yamanaka, Y. (2011), 'Synoptic relationships between surface Chlorophyll-a and diagnostic pigments specific to phytoplankton functional types', *Biogeosciences* **8**, 311–327.
**URL:** *www.biogeosciences.net/8/311/2011/*

Hoffmann, L. J., Peeken, I. and Lochte, K. (2007), 'Effects of iron on the elemental stoichiometry during EIFEX and in the diatoms Fragilariopsis kerguelensis and Chaetoceros dichaeta', *Biogeosciences* **4**(4), 569–579.
**URL:** *www.biogeosciences.net/4/569/2007/*

Holm-Hansen, O. (1985), Nutrient Cycles in Antarctic Marine Ecosystems, *in* 'Antarctic Nutrient Cycles and Food Webs', Springer Berlin Heidelberg, Berlin, Heidelberg, pp. 6–10.
**URL:** *http://link.springer.com/10.1007/978-3-642-82275-9*$_2$

Holzer, M., Pasquier, B., DeVries, T. and Brzezinski, M. (2019), 'Diatom Physiology Controls Silicic Acid Leakage in Response to Iron Fertilization', *Global Biogeochemical Cycles* **33**(12), 1631–1653.

Holzer, M., Primeau, F. W., DeVries, T. and Matear, R. (2014), 'The Southern Ocean silicon trap: Data-constrained estimates of regenerated silicic acid, trapping efficiencies, and global transport paths', *Journal of Geophysical Research: Oceans* **119**(1), 313–331.
**URL:** *https://agupubs.onlinelibrary.wiley.com/doi/full/10.1002/2013JC009356*

Honda, M. C. and Watanabe, S. (2010), 'Importance of biogenic opal as ballast of particulate organic carbon (POC) transport and existence of mineral ballast-associated and residual POC in the Western Pacific Subarctic Gyre',

*Geophysical Research Letters* **37**(2), L02605.
**URL:** *http://doi.wiley.com/10.1029/2009GL041521*

Hutchins, D. A. and Bruland, K. W. (1998), 'Iron-limited diatom growth and Si:N uptake ratios in a coastal upwelling regime', *Nature* **393**(6685), 561–564.
**URL:** *http://www.nature.com/articles/31203*

Hutchins, D. A., Franck, V. M., Brzezinski, M. A. and Bruland, K. W. (1999), 'Inducing phytoplankton iron limitation in iron-replete coastal waters with a strong chelating ligand', *Limnology and Oceanography* **44**(4), 1009–1018.
**URL:** *http://doi.wiley.com/10.4319/lo.1999.44.4.1009*

Huysman, M. J., Vyverman, W. and De Veylder, L. (2014), 'Molecular regulation of the diatom cell cycle', *Journal of Experimental Botany* **65**(10), 2573–2584.
**URL:** *https://academic.oup.com/jxb/article/65/10/2573/572304*

Ignatiades, L. (1969), 'Annual cycle, species diversity and succession of phytoplankton in lower Saronicos Bay, Aegean Sea', *Marine Biology* **3**(3), 196–200.
**URL:** *https://link.springer.com/article/10.1007/BF00360951*

Iler, R. (1979), *The Chemistry of Silica: Solubility, Polymerization, Colloid and Surface Properties, and Biochemistry.*, John Wiley & Sons, Ltd, New York.

Ilyina, T., Six, K. D., Segschneider, J., Maier-Reimer, E., Li, H. and Núñez-Riboni, I. (2013), 'Global ocean biogeochemistry model HAMOCC: Model architecture and performance as component of the MPI-Earth system model in different CMIP5 experimental realizations', *Journal of Advances in Modeling Earth Systems* **5**(2), 287–315.
**URL:** *https://onlinelibrary.wiley.com/doi/full/10.1029/2012MS000178*

Jabre, L. J., Allen, A. E., McCain, S. J., McCrow, J. P., Tenenbaum, N., Spackeen, J. L., Sipler, R. E., Green, B. R., Bronk, D. A., Hutchins, D. A. and Bertrand, E. M. (2021), 'Molecular underpinnings and biogeochemical consequences of enhanced diatom growth in a warming Southern Ocean', *Proceedings of the National Academy of Sciences of the United States of America* **118**(30), e2107238118.
**URL:** *https://www.pnas.org/doi/abs/10.1073/pnas.2107238118*

Jackson, G. A. (1990), 'A model of the formation of marine algal flocs by physical coagulation processes', *Deep Sea Research Part A. Oceanographic Research Papers* **37**(8), 1197–1211.
**URL:** *https://www.sciencedirect.com/science/article/pii/019801499090038W*

Jickells, T. D., An, Z. S., Andersen, K. K., Baker, A. R., Bergametti, G., Brooks, N., Cao, J. J., Boyd, P. W., Duce, R. A., Hunter, K. A., Kawahata, H., Kubilay, N., laRoche, J.,

Liss, P. S., Mahowald, N., Prospero, J. M., Ridgwell, A. J., Tegen, I. and Torres, R. (2005), 'Global iron connections between desert dust, ocean biogeochemistry, and climate.', *Science (New York, N.Y.)* **308**(5718), 67–71.
**URL:** *http://www.ncbi.nlm.nih.gov/pubmed/15802595*

Jin., X., Gruber, N., Dune, J. P., Sarmiento, J. L. and Armstrong, R. A. (2006), 'Diagnosing the contributions of phytoplankton functional groups to the production and export of particulate organic carbon, CaCO3, and opal from global nutrient and alkalinity distributions', *Global Biogeochemical Cycles* **20**(2).

Kelly-Gerreyn, B. A., Martin, A. P., Bett, B. J., Anderson, T. R., Kaariainen, J. I., Main, C. E., Marcinko, C. J. and Yool, A. (2014), 'Benthic biomass size spectra in shelf and deep-sea sediments', *Biogeosciences* **11**(22), 6401–6416.

Khatiwala, S., Primeau, F. and Hall, T. (2009), 'Reconstruction of the history of anthropogenic CO2 concentrations in the ocean', *Nature* **462**(7271), 346–349.
**URL:** *https://www.nature.com/articles/nature08526*

Klaas, C. and Archer, D. E. (2002), 'Association of sinking organic matter with various types of mineral ballast in the deep sea: Implications for the rain ratio', *Global Biogeochemical Cycles* **16**(4), 63–1.
**URL:** *http://doi.wiley.com/10.1029/2001GB001765*

Kolber, Z. S., Prášil, O. and Falkowski, P. G. (1998), 'Measurements of variable chlorophyll fluorescence using fast repetition rate techniques: Defining methodology and experimental protocols', *Biochimica et Biophysica Acta - Bioenergetics* **1367**(1-3).

Kraemer, S. M. (2004), 'Iron oxide dissolution and solubility in the presence of siderophores', *Aquatic Sciences - Research Across Boundaries* **66**(1), 3–18.
**URL:** *http://link.springer.com/10.1007/s00027-003-0690-5*

Kumar, N., Anderson, R. F., Mortlock, R. A., Froelich, P. N., Kubik, P., Dittrich-Hannen, B. and Suter, M. (1995), 'Increased biological productivity and export production in the glacial Southern Ocean', *Nature* **378**(6558), 675–680.
**URL:** *http://www.nature.com/doifinder/10.1038/378675a0*

Kumar, S., Rechav, K., Kaplan-Ashiri, I. and Gal, A. (2020), 'Imaging and quantifying homeostatic levels of intracellular silicon in diatoms', *Science Advances* **6**(42), 7554–7570.
**URL:** *https://www.science.org/doi/abs/10.1126/sciadv.aaz7554*

Lambert, F., Delmonte, B., Petit, J. R., Bigler, M., Kaufmann, P. R., Hutterli, M. A., Stocker, T. F., Ruth, U., Steffensen, J. P. and Maggi, V. (2008), 'Dust - Climate

couplings over the past 800,000 years from the EPICA Dome C ice core', *Nature* **452**(7187), 616–619.

Landry, M. R., Constantinou, J., Latasa, M., Brown, S. L., Bidigare, R. R. and Ondrusek, M. E. (2000), 'Biological response to iron fertilization in the eastern equatorial Pacific (IronEx II). III. Dynamics of phytoplankton growth and microzooplankton grazing', *Marine Ecology Progress Series* **201**, 57–72.
**URL:** *http://www.int-res.com/abstracts/meps/v201/p57-72/*

Le Quéré, C., Harrison, S. P., Prentice, I. C., Buitenhuis, E. T., Aumont, O., Bopp, L., Claustre, H., Cotrim Da Cunha, L., Geider, R., Giraud, X., Klaas, C., Kohfeld, K. E., Legendre, L., Manizza, M., Platt, T., Rivkin, R. B., Sathyendranath, S., Uitz, J., Watson, A. J. and Wolf-Gladrow, D. (2005), 'Ecosystem dynamics based on plankton functional types for global ocean biogeochemistry models', *Global Change Biology* **11**(11), 2016–2040.
**URL:** *https://research-portal.uea.ac.uk/en/publications/ecosystem-dynamics-based-on-plankton-functional-types-for-global-*

Lerman, A. and Lal, D. (1977), 'Regeneration Rates in the Ocean.', *American Journal of Science* **277**(3), 238–258.

Levitus, S., Conkright, M. E., Reid, J. L., Najjar, R. G. and Mantyla, A. (1993), 'Distribution of nitrate, phosphate and silicate in the world oceans', *Progress in Oceanography* **31**(3), 245–273.
**URL:** *https://www.sciencedirect.com/science/article/pii/007966119390003V*

Leynaert, A., Bucciarelli, E., Claquin, P., Dugdale, R. C., Martin-Jézéquel, V., Pondaven, P. and Ragueneau, O. (2004), 'Effect of iron deficiency on diatom cell size and silicic acid uptake kinetics', *Limnology and Oceanography* **49**(4), 1134–1143.
**URL:** *http://doi.wiley.com/10.4319/lo.2004.49.4.1134*

Li, F., Ginoux, P. and Ramaswamy, V. (2008), 'Distribution, transport, and deposition of mineral dust in the Southern Ocean and Antarctica: Contribution of major sources', *Journal of Geophysical Research: Atmospheres* **113**(D10).
**URL:** *https://onlinelibrary.wiley.com/doi/full/10.1029/2007JD009190*

Liebig, J. v. (1840), *Chemistry and its Application to Agriculture and Physiology*, Taylor and Walton, London.

Long, M. C., Moore, J. K., Lindsay, K., Levy, M., Doney, S. C., Luo, J. Y., Krumhardt, K. M., Letscher, R. T., Grover, M. and Sylvester, Z. T. (2021), 'Simulations With the Marine Biogeochemistry Library (MARBL)', *Journal of Advances in Modeling Earth*

*Systems* **13**(12), e2021MS002647.
**URL:** *https://onlinelibrary.wiley.com/doi/full/10.1029/2021MS002647*

Longhurst, A., Sathyendranath, S., Platt, T. and Caverhill, C. (1995), 'An estimate of global primary production in the ocean from satellite radiometer data', *Journal of Plankton Research* **17**(6), 1245–1271.
**URL:** *https://academic.oup.com/plankt/article/17/6/1245/1441236*

Lüthi, D., Le Floch, M., Bereiter, B., Blunier, T., Barnola, J. M., Siegenthaler, U., Raynaud, D., Jouzel, J., Fischer, H., Kawamura, K. and Stocker, T. F. (2008), 'High-resolution carbon dioxide concentration record 650,000–800,000years before present', *Nature 2008 453:7193* **453**(7193), 379–382.
**URL:** *https://www.nature.com/articles/nature06949*

Lynn, S. G., Kilham, S. S., Kreeger, D. A. and Interlandi, S. J. (2000), 'Effect of nutrient availability on the biochemical and elemental stoichiometry in the freshwater diatom Stephanodiscus minutulus (Bacillariophyceae)', *Journal of Phycology* **36**(3), 510–522.
**URL:** *https://onlinelibrary.wiley.com/doi/full/10.1046/j.1529-8817.2000.98251.x*

M. Franck, V., Brzezinski, M. A., Coale, K. H. and Nelson, D. M. (2000), 'Iron and silicic acid concentrations regulate Si uptake north and south of the Polar Frontal Zone in the Pacific Sector of the Southern Ocean', *Deep Sea Research Part II: Topical Studies in Oceanography* **47**(15-16), 3315–3338.
**URL:** *https://www.sciencedirect.com/science/article/pii/S0967064500000709*

Macintyre, H. L., Kana, T. M. and Geider, R. J. (2000), 'The effect of water motion on short-term rates of photosynthesis by marine phytoplankton', *Trends in Plant Science* **5**(1), 12–17.

Mahowald, N. M., Baker, A. R., Bergametti, G., Brooks, N., Duce, R. A., Jickells, T. D., Kubilay, N., Prospero, J. M. and Tegen, I. (2005), 'Atmospheric global dust cycle and iron inputs to the ocean'.

Marañón, E., Cermeño, P., López-Sandoval, D. C., Rodríguez-Ramos, T., Sobrino, C., Huete-Ortega, M., Blanco, J. M. and Rodríguez, J. (2013), 'Unimodal size scaling of phytoplankton growth and the size dependence of nutrient uptake and use', *Ecology Letters* **16**(3).

Marchetti, A. and Cassar, N. (2009), 'Diatom elemental and morphological changes in response to iron limitation: A brief review with potential paleoceanographic applications', *Geobiology* **7**(4), 419–431.

Marchetti, A. and Harrison, P. J. (2007), 'Coupled changes in the cell morphology and elemental (C, N, and Si) composition of the pennate diatom Pseudo-nitzschia due to iron deficiency', *Limnology and Oceanography* **52**(5), 2270–2284.
**URL:** *http://doi.wiley.com/10.4319/lo.2007.52.5.2270*

Marchetti, A., Parker, M. S., Moccia, L. P., Lin, E. O., Arrieta, A. L., Ribalet, F., Murphy, M. E., Maldonado, M. T. and Armbrust, E. V. (2009), 'Ferritin is used for iron storage in bloom-forming marine pennate diatoms', *Nature* **457**(7228), 467–470.
**URL:** *https://www.nature.com/articles/nature07539*

Marshall, J. and Speer, K. (2012), 'Closure of the meridional overturning circulation through Southern Ocean upwelling', *Nature Geoscience 2012 5:3* **5**(3), 171–180.
**URL:** *https://www.nature.com/articles/ngeo1391*

Martin, A. P., Richards, K. J., Bracco, A. and Provenzale, A. (2002), 'Patchy productivity in the open ocean', *Global Biogeochemical Cycles* **16**(2), 9–1.
**URL:** *https://onlinelibrary.wiley.com/doi/full/10.1029/2001GB001449*

Martin, J. H. (1990), 'Glacial-interglacial CO2 change: The Iron Hypothesis', *Paleoceanography* **5**(1), 1–13.
**URL:** *https://onlinelibrary.wiley.com/doi/full/10.1029/PA005i001p00001*

Martin, J. H. and Fitzwater, S. E. (1988), 'Iron deficiency limits phytoplankton growth in the north-east Pacific subarctic', *Nature* **331**(6154), 341–343.
**URL:** *http://www.nature.com/articles/331341a0*

Martin, J. H., Gordon, M. and Fitzwater, S. E. (1991), 'The case for iron', *Limnology and Oceanography* **36**(8), 1793–1802.
**URL:** *https://onlinelibrary.wiley.com/doi/full/10.4319/lo.1991.36.8.1793*

Martin, J. H., Gordon, R. M., Fitzwater, S. and Broenkow, W. W. (1989), 'Vertex: phytoplankton/iron studies in the Gulf of Alaska', *Deep Sea Research Part A, Oceanographic Research Papers* **36**(5), 649–680.

Martin, J. H., Gordon, R. M. and Fitzwater, S. E. (1990), 'Iron in Antarctic waters', *Nature* **345**(6271), 156–158.
**URL:** *http://www.nature.com/articles/345156a0*

Martin, J. H., Knauer, G. A., Karl, D. M. and Broenkow, W. W. (1987), 'VERTEX: carbon cycling in the northeast Pacific', *Deep Sea Research Part A. Oceanographic Research Papers* **34**(2), 267–285.
**URL:** *https://www.sciencedirect.com/science/article/pii/0198014987900860*

Martin-Jézéquel, V., Hildebrand, M. and Brzezinski, M. A. (2000), 'Silicon metabolism in diatoms: Implications for growth', *Journal of Phycology* **36**(5), 821–840.

Matsumoto, K., Chase, Z. and Kohfeld, K. (2014), 'Different mechanisms of silicic acid leakage and their biogeochemical consequences', *Paleoceanography* **29**(3), 238–254.
**URL:** *https://onlinelibrary.wiley.com/doi/full/10.1002/2013PA002588*

Matsumoto, K. and Sarmiento, J. L. (2008), 'A corollary to the silicic acid leakage hypothesis', *Paleoceanography* **23**(2).
**URL:** *https://onlinelibrary.wiley.com/doi/full/10.1029/2007PA001515*

Matsumoto, K., Sarmiento, J. L. and Brzezinski, M. A. (2002), 'Silicic acid leakage from the Southern Ocean: A possible explanation for glacial atmospheric pCO2', *Global Biogeochemical Cycles* **16**(3).

Matsumoto, K., Tokos, K., Huston, A. and Joy-Warren, H. (2013), 'MESMO 2: a mechanistic marine silica cycle and coupling to a simple terrestrial scheme', *Geoscientific Model Development* **6**(2), 477–494.
**URL:** *https://gmd.copernicus.org/articles/6/477/2013/*

McNeil, B. I. and Matear, R. J. (2008), 'Southern Ocean acidification: A tipping point at 450-ppm atmospheric CO2', *Proceedings of the National Academy of Sciences of the United States of America* **105**(48), 18860–18864.

Meyerink, S., Ellwood, M. J., Maher, W. A. and Strzepek, R. (2017), 'Iron Availability Influences Silicon Isotope Fractionation in Two Southern Ocean Diatoms (Proboscia inermis and Eucampia antarctica) and a Coastal Diatom (Thalassiosira pseudonana)', *Frontiers in Marine Science* **4**(JUL), 217.
**URL:** *http://journal.frontiersin.org/article/10.3389/fmars.2017.00217/full*

Michaelis, L. and Menten, M. L. (1913), 'Die Kinetik der Invertinwirkung.', *Biochemische Zeitschrift* **49**, 333–369.

Milligan, A. J. and Morel, F. M. (2002), 'A proton buffering role for silica in diatoms', *Science* **297**(5588), 1848–1850.
**URL:** *https://www.science.org/doi/10.1126/science.1074958*

Mitchell, M. (1996), *An introduction to genetic algorithms.*, MIT Press, Cambridge, MA.

Mock, T., Samanta, M. P., Iverson, V., Berthiaume, C., Robison, M., Holtermann, K., Durkin, C., BonDurant, S. S., Richmond, K., Rodesch, M., Kallas, T., Huttlin, E. L., Cerrina, F., Sussman, M. R. and Armbrust, E. V. (2008), 'Whole-genome expression profiling of the marine diatom Thalassiosira pseudonana identifies genes involved in silicon bioprocesses', *Proceedings of the National Academy of Sciences of the United*

*States of America* **105**(5), 1579–1584.
**URL:** *www.pnas.orgcgidoi10.1073pnas.0707946105*

Moore, C. (2016), 'Diagnosing oceanic nutrient defciency', *Philosophical Transactions of the Royal Society A: Mathematical, Physical and Engineering Sciences* **374**(2081).

Moore, C. M., Mills, M. M., Arrigo, K. R., Berman-Frank, I., Bopp, L., Boyd, P. W., Galbraith, E. D., Geider, R. J., Guieu, C., Jaccard, S. L., Jickells, T. D., La Roche, J., Lenton, T. M., Mahowald, N. M., Marañón, E., Marinov, I., Moore, J. K., Nakatsuka, T., Oschlies, A., Saito, M. A., Thingstad, T. F., Tsuda, A. and Ulloa, O. (2013), 'Processes and patterns of oceanic nutrient limitation'.
**URL:** *www.nature.com/naturegeoscience*

Moore, J. K., Fu, W., Primeau, F., Britten, G. L., Lindsay, K., Long, M., Doney, S. C., Mahowald, N., Hoffman, F. and Randerson, J. T. (2018), 'Sustained climate warming drives declining marine biological productivity', *Science* **359**(6380), 1139–1143.
**URL:** *http://science.sciencemag.org/content/359/6380/1139*

Moore, J. K., Lindsay, K., Doney, S. C., Long, M. C. and Misumi, K. (2013), 'Marine Ecosystem Dynamics and Biogeochemical Cycling in the Community Earth System Model [CESM1(BGC)]: Comparison of the 1990s with the 2090s under the RCP4.5 and RCP8.5 Scenarios', *Journal of Climate* **26**(23), 9291–9312.
**URL:** *https://journals.ametsoc.org/view/journals/clim/26/23/jcli-d-12-00566.1.xml*

Morel, F. M. (1987), 'Kinetics of uptake and growth in phytoplankton.', *Journal of Phycology* **23**(1), 137–150.
**URL:** *http://doi.wiley.com/10.1111/j.0022-3646.1987.00137.x*

Morel, F. M., Hudson, R. J. and Price, N. M. (1991), 'Limitation of productivity by trace metals in the sea', *Limnology and Oceanography* **36**(8), 1742–1755.
**URL:** *https://aslopubs.onlinelibrary.wiley.com/doi/full/10.4319/lo.1991.36.8.1742*

Morrison, A. K., Frölicher, T. L. and Sarmiento, J. L. (2015), 'Upwelling in the Southern Ocean', *Physics Today* **68**(1), 27–32.
**URL:** *http://physicstoday.scitation.org/doi/10.1063/PT.3.2654*

Muggli, D., Lecourt, M. and Harrison, P. (1996), 'Effects of iron and nitrogen source on the sinking rate, physiology and metal composition of an oceanic diatom from the subarctic Pacific', *Marine Ecology Progress Series* **132**, 215–227.
**URL:** *http://www.int-res.com/abstracts/meps/v132/p215-227/*

Munk, W. H. (1966), 'Abyssal recipes', *Deep-Sea Research and Oceanographic Abstracts* **13**(4), 707–730.

Nelson, D. M., Tréguer, P., Brzezinski, M. A., Leynaert, A. and Quéguiner, B. (1995), 'Production and dissolution of biogenic silica in the ocean: Revised global estimates, comparison with regional data and relationship to biogenic sedimentation', *Global Biogeochemical Cycles* **9**(3), 359–372.
**URL:** *http://doi.wiley.com/10.1029/95GB01070*

Nodder, S. D. and Waite, A. M. (2001), 'Is Southern Ocean organic carbon and biogenic silica export enhanced by iron-stimulated increases in biological production? Sediment trap results from SOIREE', *Deep-Sea Research Part II: Topical Studies in Oceanography* **48**(11-12), 2681–2701.

Nowlin, W. D. and Klinck, J. M. (1986), 'The physics of the Antarctic Circumpolar Current', *Reviews of Geophysics* **24**(3), 469–491.
**URL:** *https://onlinelibrary.wiley.com/doi/full/10.1029/RG024i003p00469*

Nozaki, Y. and Yamamoto, Y. (2001), 'Radium 228 based nitrate fluxes in the eastern Indian Ocean and the South China Sea and a silicon-induced "alkalinity pump" hypothesis', *Global Biogeochemical Cycles* **15**(3), 555–567.
**URL:** *http://doi.wiley.com/10.1029/2000GB001309*

O'Neill, R. V., DeAngelis, D. L., Pastor, J. J., Jackson, B. J. and Post, W. M. (1989), 'Multiple nutrient limitations in ecological models', *Ecological Modelling* **46**(3-4), 147–163.

Paasche, E. (1973*a*), 'Silicon and the ecology of marine plankton diatoms. I. Thalassiosira pseudonana (Cyclotella nana) grown in a chemostat with silicate as limiting nutrient', *Marine Biology* **19**(2), 117–126.

Paasche, E. (1973*b*), 'Silicon and the ecology of marine plankton diatoms. II. Silicate-uptake kinetics in five diatom species', *Marine Biology* **19**(3), 262–269.

Pančić, M., Torres, R. R., Almeda, R. and Kiørboe, T. (2019), 'Silicified cell walls as a defensive trait in diatoms', *Proceedings of the Royal Society B: Biological Sciences* **286**(1901), 20190184.
**URL:** *http://www.royalsocietypublishing.org/doi/10.1098/rspb.2019.0184*

Parekh, P., Dutkiewicz, S., Follows, M. J. and Ito, T. (2006), 'Atmospheric carbon dioxide in a less duty world', *Geophysical Research Letters* **33**(3).

Parekh, P., Follows, M. J. and Boyle, E. (2004), 'Modeling the global ocean iron cycle', *Global Biogeochemical Cycles* **18**(1), 1002.
**URL:** *https://onlinelibrary.wiley.com/doi/full/10.1029/2003GB002061*

Parkhill, J. P., Maillet, G. and Cullen, J. J. (2001), 'Fluorescence-based maximal quantum yield for PSII as a diagnostic of nutrient stress', *Journal of Phycology* **37**(4).

Pasquier, B. and Holzer, M. (2017), 'Inverse-model estimates of the ocean's coupled phosphorus, silicon, and iron cycles', *Biogeosciences* **14**(18), 4125–4159.
**URL:** *https://bg.copernicus.org/articles/14/4125/2017/*

Passow, U. and De La Rocha, C. L. (2006), 'Accumulation of mineral ballast on organic aggregates', *Global Biogeochemical Cycles* **20**(1), GB1013.
**URL:** *http://doi.wiley.com/10.1029/2005GB002579*

Pausch, F., Bischof, K. and Trimborn, S. (2019), 'Iron and manganese co-limit growth of the Southern Ocean diatom Chaetoceros debilis', *PLoS ONE* **14**(9), 1–16.

Peers, G. and Price, N. M. (2004), 'A role for manganese in superoxide dismutases and growth of iron-deficient diatoms', *Limnology and Oceanography* **49**(5), 1774–1783.
**URL:** *http://doi.wiley.com/10.4319/lo.2004.49.5.1774*

Pellichero, V., Sallée, J. B., Chapman, C. C. and Downes, S. M. (2018), 'The southern ocean meridional overturning in the sea-ice sector is driven by freshwater fluxes', *Nature Communications* **9**(1), 1789.
**URL:** *http://www.nature.com/articles/s41467-018-04101-2*

Peng, J., Yuan, J. P., Wu, C. F. and Wang, J. H. (2011), 'Fucoxanthin, a Marine Carotenoid Present in Brown Seaweeds and Diatoms: Metabolism and Bioactivities Relevant to Human Health', *Marine Drugs 2011, Vol. 9, Pages 1806-1828* **9**(10), 1806–1828.
**URL:** *https://www.mdpi.com/1660-3397/9/10/1806/htm*

Petit, J. R., Jouzel, J., Raynaud, D., Barkov, N. I., Barnola, J. M., Basile, I., Bender, M., Chappellaz, J., Davis, M., Delaygue, G., Delmotte, M., Kotiyakov, V. M., Legrand, M., Lipenkov, V. Y., Lorius, C., Pépin, L., Ritz, C., Saltzman, E. and Stievenard, M. (1999), 'Climate and atmospheric history of the past 420,000 years from the Vostok ice core, Antarctica'.
**URL:** *https://www.nature.com/articles/20859*

Petrou, K., Kranz, S. A., Trimborn, S., Hassler, C. S., Blanco Ameijeiras, S., Sackett, O., Ralph, P. J. and Davidson, A. T. (2016), 'Southern Ocean phytoplankton physiology in a changing climate', *Journal of Plant Physiology* .
**URL:** *http://dx.doi.org/10.1016/j.jplph.2016.05.004*

Pondaven, P., Ragueneau, O., Tréguer, P., Hauvespre, A., Dezileau, L. and Reyss, J. L. (2000), 'Resolving the 'opal paradox' in the Southern Ocean', *Nature*

**405**(6783), 168–172.
**URL:** *http://www.nature.com/articles/35012046*

Post, A., L., Meijers, A., Fraser, A., Meiners, K., Ayers, J., Bindoff, N., Griffiths, H., Van de Putte, A., O'Brien, P., Swadling, K. and Raymond, B. (2014), Environmental setting, *in* 'Biogeographic Atlas of the Southern Ocean', number August, pp. 46–64.

Poulton, S. W. and Raiswell, R. (2002), 'The low-temperature geochemical cycle of iron: From continental fluxes to marine sediment deposition', *American Journal of Science* **302**(9), 774–805.
**URL:** *http://www.ajsonline.org/cgi/doi/10.2475/ajs.302.9.774*

Primeau, F. W., Holzer, M. and Devries, T. (2013), 'Southern Ocean nutrient trapping and the efficiency of the biological pump', *J. Geophys. Res. Oceans* **118**, 2547–2564.
**URL:** *https://agupubs.onlinelibrary.wiley.com/doi/pdf/10.1002/jgrc.20181*

Ragueneau, O., Tréguer, P., Leynaert, A., Anderson, R. F., Brzezinski, M. A., DeMaster, D. J., Dugdale, R. C., Dymond, J., Fischer, G., François, R., Heinze, C., Maier-Reimer, E., Martin-Jézéquel, V., Nelson, D. M. and Quéguiner, B. (2000), 'A review of the Si cycle in the modern ocean: Recent progress and missing gaps in the application of biogenic opal as a paleoproductivity proxy', *Global and Planetary Change* **26**(4), 317–365.
**URL:** *https://www.sciencedirect.com/science/article/pii/S0921818100000527*

Raven, J. A. (1983), 'The transport and function of silicon in plants', *Biological Reviews* **58**(2), 179–207.
**URL:** *https://onlinelibrary.wiley.com/doi/full/10.1111/j.1469-185X.1983.tb00385.x*

Redfield, A. C. (1934), 'On the proportions of organic derivatives in sea water and their relation to the composition of plankton', *James Johnstone Memorial Volume* pp. 176–192.

Round, F. E., Crawford, R. M. and Mann, D. G. (1990), *Diatoms: Biology and Morphology of the Genera.*, Cambridge University Press, Cambridge.

Ruud, J. T. (1930), 'Nitrates and phosphates in the southern seas', *ICES Journal of Marine Science* **5**(3), 347–360.

Sabine, C. L., Feely, R. A., Gruber, N., Key, R. M., Lee, K., Bullister, J. L., Wanninkhof, R., Wong, C. S., Wallace, D. W., Tilbrook, B., Millero, F. J., Peng, T. H., Kozyr, A., Ono, T. and Rios, A. F. (2004), 'The oceanic sink for anthropogenic CO2', *Science* **305**(5682), 367–371.
**URL:** *https://www.science.org/doi/10.1126/science.1097403*

Salter, I., Lampitt, R. S., Poulton, A., Kemp, A. E., Boorman, B., Saw, K. and Pearce, R. (2007), 'Estimating carbon, silica and diatom export from a naturally fertilised phytoplankton bloom in the Southern Ocean using PELAGRA: A novel drifting sediment trap', *Deep Sea Research Part II: Topical Studies in Oceanography* **54**(18-20), 2233–2259.
**URL:** *https://www.sciencedirect.com/science/article/pii/S0967064507001622*

Sarmiento, J. L. and Gruber, N. (2002), 'Sinks for anthropogenic carbon', *Physics Today* **55**(8), 30.
**URL:** *http://dx.doi.org/10.1063/1.1510279*

Sarmiento, J. L. and Gruber, N. (2006), *Ocean Biogeochemical Dynamics*, Princeton University Press, Princeton.

Sarmiento, J. L., Gruber, N., Brzezinski, M. A. and Dunne, J. P. (2004), 'High-latitude controls of thermocline nutrients and low latitude biological productivity', *Nature* **427**(6969), 56–60.
**URL:** *http://www.nature.com/articles/nature02127*

Sarthou, G., Timmermans, K. R., Blain, S. and Tréguer, P. (2005), 'Growth physiology and fate of diatoms in the ocean: a review', *Journal of Sea Research* **53**(1-2), 25–42.
**URL:** *https://www.sciencedirect.com/science/article/pii/S1385110104000644*

Schlitzer, R. (2002), 'Carbon export fluxes in the Southern Ocean: results from inverse modeling and comparison with satellite-based estimates', *Deep Sea Research Part II: Topical Studies in Oceanography* **49**(9-10), 1623–1644.

Schlitzer, R., Anderson, R. F., Dodas, E. M., Lohan, M., Geibert, W., Tagliabue, A., Bowie, A., Jeandel, C., Maldonado, M. T., Landing, W. M., Cockwell, D., Abadie, C., Abouchami, W., Achterberg, E. P., Agather, A., Aguliar-Islas, A., van Aken, H. M., Andersen, M., Archer, C., Auro, M., de Baar, H. J., Baars, O., Baker, A. R., Bakker, K., Basak, C., Baskaran, M., Bates, N. R., Bauch, D., van Beek, P., Behrens, M. K., Black, E., Bluhm, K., Bopp, L., Bouman, H., Bowman, K., Bown, J., Boyd, P., Boye, M., Boyle, E. A., Branellec, P., Bridgestock, L., Brissebrat, G., Browning, T., Bruland, K. W., Brumsack, H. J., Brzezinski, M., Buck, C. S., Buck, K. N., Buesseler, K., Bull, A., Butler, E., Cai, P., Mor, P. C., Cardinal, D., Carlson, C., Carrasco, G., Casacuberta, N., Casciotti, K. L., Castrillejo, M., Chamizo, E., Chance, R., Charette, M. A., Chaves, J. E., Cheng, H., Chever, F., Christl, M., Church, T. M., Closset, I., Colman, A., Conway, T. M., Cossa, D., Croot, P., Cullen, J. T., Cutter, G. A., Daniels, C., Dehairs, F., Deng, F., Dieu, H. T., Duggan, B., Dulaquais, G., Dumousseaud, C., Echegoyen-Sanz, Y., Edwards, R. L., Ellwood, M., Fahrbach, E., Fitzsimmons, J. N., Russell Flegal, A., Fleisher, M. Q., van de Flierdt, T., Frank, M., Friedrich, J., Fripiat,

F., Fröllje, H., Galer, S. J., Gamo, T., Ganeshram, R. S., Garcia-Orellana, J., Garcia-Solsona, E., Gault-Ringold, M., George, E., Gerringa, L. J., Gilbert, M., Godoy, J. M., Goldstein, S. L., Gonzalez, S. R., Grissom, K., Hammerschmidt, C., Hartman, A., Hassler, C. S., Hathorne, E. C., Hatta, M., Hawco, N., Hayes, C. T., Heimbürger, L. E., Helgoe, J., Heller, M., Henderson, G. M., Henderson, P. B., van Heuven, S., Ho, P., Horner, T. J., Hsieh, Y. T., Huang, K. F., Humphreys, M. P., Isshiki, K., Jacquot, J. E., Janssen, D. J., Jenkins, W. J., John, S., Jones, E. M., Jones, J. L., Kadko, D. C., Kayser, R., Kenna, T. C., Khondoker, R., Kim, T., Kipp, L., Klar, J. K., Klunder, M., Kretschmer, S., Kumamoto, Y., Laan, P., Labatut, M., Lacan, F., Lam, P. J., Lambelet, M., Lamborg, C. H., Le Moigne, F. A., Le Roy, E., Lechtenfeld, O. J., Lee, J. M., Lherminier, P., Little, S., López-Lora, M., Lu, Y., Masque, P., Mawji, E., Mcclain, C. R., Measures, C., Mehic, S., Barraqueta, J. L. M., van der Merwe, P., Middag, R., Mieruch, S., Milne, A., Minami, T., Moffett, J. W., Moncoiffe, G., Moore, W. S., Morris, P. J., Morton, P. L., Nakaguchi, Y., Nakayama, N., Niedermiller, J., Nishioka, J., Nishiuchi, A., Noble, A., Obata, H., Ober, S., Ohnemus, D. C., van Ooijen, J., O'Sullivan, J., Owens, S., Pahnke, K., Paul, M., Pavia, F., Pena, L. D., Peters, B., Planchon, F., Planquette, H., Pradoux, C., Puigcorbé, V., Quay, P., Queroue, F., Radic, A., Rauschenberg, S., Rehkämper, M., Rember, R., Remenyi, T., Resing, J. A., Rickli, J., Rigaud, S., Rijkenberg, M. J., Rintoul, S., Robinson, L. F., Roca-Martí, M., Rodellas, V., Roeske, T., Rolison, J. M., Rosenberg, M., Roshan, S., Rutgers van der Loeff, M. M., Ryabenko, E., Saito, M. A., Salt, L. A., Sanial, V., Sarthou, G., Schallenberg, C., Schauer, U., Scher, H., Schlosser, C., Schnetger, B., Scott, P., Sedwick, P. N., Semiletov, I., Shelley, R., Sherrell, R. M., Shiller, A. M., Sigman, D. M., Singh, S. K., Slagter, H. A., Slater, E., Smethie, W. M., Snaith, H., Sohrin, Y., Sohst, B., Sonke, J. E., Speich, S., Steinfeldt, R., Stewart, G., Stichel, T., Stirling, C. H., Stutsman, J., Swarr, G. J., Swift, J. H., Thomas, A., Thorne, K., Till, C. P., Till, R., Townsend, A. T., Townsend, E., Tuerena, R., Twining, B. S., Vance, D., Velazquez, S., Venchiarutti, C., Villa-Alfageme, M., Vivancos, S. M., Voelker, A. H., Wake, B., Warner, M. J., Watson, R., van Weerlee, E., Alexandra Weigand, M., Weinstein, Y., Weiss, D., Wisotzki, A., Woodward, E. M. S., Wu, J., Wu, Y., Wuttig, K., Wyatt, N., Xiang, Y., Xie, R. C., Xue, Z., Yoshikawa, H., Zhang, J., Zhang, P., Zhao, Y., Zheng, L., Zheng, X. Y., Zieringer, M., Zimmer, L. A., Ziveri, P., Zunino, P. and Zurbrick, C. (2018), 'The GEOTRACES Intermediate Data Product 2017', *Chemical Geology* **493**, 210–223.

Schoemann, V., Wollast, R., Chou, L. and Lancelot, C. (2001), 'Effects of photosynthesis on the accumulation of Mn and Fe by Phaeocystis colonies', *Limnology and Oceanography* **46**(5), 1065–1076.
**URL:** *http://doi.wiley.com/10.4319/lo.2001.46.5.1065*

Schoffman, H., Lis, H., Shaked, Y. and Keren, N. (2016), 'Iron-nutrient interactions within phytoplankton', *Frontiers in Plant Science* **7**(AUG2016).

Séférian, R., Berthet, S., Yool, A., Palmiéri, J., Bopp, L., Tagliabue, A., Kwiatkowski, L., Aumont, O., Christian, J., Dunne, J., Gehlen, M., Ilyina, T., John, J. G., Li, H., Long, M. C., Luo, J. Y., Nakano, H., Romanou, A., Schwinger, J., Stock, C., Santana-Falcón, Y., Takano, Y., Tjiputra, J., Tsujino, H., Watanabe, M., Wu, T., Wu, F. and Yamamoto, A. (2020), 'Tracking Improvement in Simulated Marine Biogeochemistry Between CMIP5 and CMIP6', *Current Climate Change Reports* **6**(3), 95–119.
**URL:** *https://doi.org/10.1007/s40641-020-00160-0*

Seland, , Bentsen, M., Olivié, D., Toniazzo, T., Gjermundsen, A., Graff, L. S., Debernard, J. B., Gupta, A. K., He, Y. C., Kirkeväg, A., Schwinger, J., Tjiputra, J., Schanke Aas, K., Bethke, I., Fan, Y., Griesfeller, J., Grini, A., Guo, C., Ilicak, M., Karset, I. H. H., Landgren, O., Liakka, J., Moseid, K. O., Nummelin, A., Spensberger, C., Tang, H., Zhang, Z., Heinze, C., Iversen, T. and Schulz, M. (2020), 'Overview of the Norwegian Earth System Model (NorESM2) and key climate response of CMIP6 DECK, historical, and scenario simulations', *Geoscientific Model Development* **13**(12), 6165–6200.

Shemesh, A., Burckle, L. H. and Froelich, P. N. (1989), 'Dissolution and Preservation of Antarctic Diatoms and the Effect on Sediment Thanatocoenoses', *Qaternary Research* **31**(2), 288–308.
**URL:** *https://ac.els-cdn.com/0033589489900100/1-s2.0-0033589489900100-main.pdf?*$_t id = 7221f543 - ca90 - 479c - 922a - a252e57841c7acdnat = 1551362892_a 2fa8ffbfe8e51b6e902f44596267cfc$

Sigman, D. M. and Boyle, E. A. (2000), 'Glacial/interglacial variations in atmospheric carbon dioxide'.
**URL:** *https://www.nature.com/articles/35038000*

Sigman, D. M., Hain, M. P. and Haug, G. H. (2010), 'The polar ocean and glacial cycles in atmospheric CO2 concentration', *Nature* **466**(7302), 47–55.

Sims, P. A., Mann, D. G., Medlin, L. K., Sims, P. A., Mann, D. G. and Medlin, L. K. . (2019), 'Evolution of the diatoms: insights from fossil, biological and molecular data', *https://doi.org/10.2216/05-22.1* **45**(4), 361–402.
**URL:** *https://www.tandfonline.com/doi/abs/10.2216/05-22.1*

Singh, A., Lomas, M. W. and Bates, N. R. (2013), 'Revisiting N2 fixation in the North Atlantic Ocean: Significance of deviations from the Redfield Ratio, atmospheric deposition and climate variability', *Deep-Sea Research Part II: Topical Studies in Oceanography* **93**, 148–158.

Sloyan, B. M. and Rintoul, S. R. (2001), 'The Southern Ocean limb of the global deep overtuning circulation', *Journal of Physical Oceanography* **31**(1), 143–173.

Smetacek, V., Assmy, P. and Henjes, J. (2004), 'The role of grazing in structuring Southern Ocean pelagic ecosystems and biogeochemical cycles'.
**URL:**
*https://www.cambridge.org/core/product/identifier/S0954102004002317/type/journal$_a$rticle*

Smith, W. O., Anderson, R. F., Moore, J. K., Codispoti, L. A. and Morrison, J. M. (2000), 'The US Southern Ocean Joint Global Ocean Flux Study: An introduction to AESOPS', *Deep-Sea Research Part II: Topical Studies in Oceanography* **47**(15-16), 3073–3093.

Steele, J. H. (1958), 'Plant Production in the Northern North Sea', *Marine Research* **7**, 1–36.

Stock, C. A., Dunne, J. P., Fan, S., Ginoux, P., John, J., Krasting, J. P., Laufkötter, C., Paulot, F. and Zadeh, N. (2020), 'Ocean Biogeochemistry in GFDL's Earth System Model 4.1 and Its Response to Increasing Atmospheric CO2', *Journal of Advances in Modeling Earth Systems* **12**(10).

Sugie, K., Kuma, K., Fujita, S. and Ikeda, T. (2010), 'Increase in Si:N drawdown ratio due to resting spore formation by spring bloom-forming diatoms under Fe- and N-limited conditions in the Oyashio region', *Journal of Experimental Marine Biology and Ecology* **382**(2), 108–116.

Sullivan, C. W. (1977), 'Diatom mineralization of silicic acid. II. Regulation of Si(OH)4 transport rates during the cell cycle of Navicula pelliculosa.', *Journal of Phycology* **13**(1), 86–91.
**URL:** *https://onlinelibrary.wiley.com/doi/full/10.1111/j.1529-8817.1977.tb02892.x*

Sunda, W. G. and Huntsman, S. A. (1995), 'Iron uptake and growth limitation in oceanic and coastal phytoplankton', *Marine Chemistry* **50**(1-4), 189–206.
**URL:** *https://www.sciencedirect.com/science/article/pii/030442039500035P*

Sunda, W. G. and Huntsman, S. A. (1997), 'Interrelated influence of iron, light and cell size on marine phytoplankton growth', *Nature* **390**(6658), 389–392.
**URL:** *http://www.nature.com/articles/37093*

Tagliabue, A., Bopp, L., Dutay, J.-C., Bowie, A. R., Chever, F., Jean-Baptiste, P., Bucciarelli, E., Lannuzel, D., Remenyi, T., Sarthou, G., Aumont, O., Gehlen, M. and Jeandel, C. (2010), 'Hydrothermal contribution to the oceanic dissolved iron inventory', *Nature Geoscience* **3**(4), 252–256.
**URL:** *http://www.nature.com/articles/ngeo818*

Tagliabue, A., Mtshali, T., Aumont, O., Bowie, A. R., Klunder, M. B., Roychoudhury, A. N. and Swart, S. (2012), 'A global compilation of dissolved iron measurements: Focus on distributions and processes in the Southern Ocean', *Biogeosciences* **9**(6), 2333–2349.

Tagliabue, A., Sallée, J. B., Bowie, A. R., Lévy, M., Swart, S. and Boyd, P. W. (2014), 'Surface-water iron supplies in the Southern Ocean sustained by deep winter mixing', *Nature Geoscience 2014 7:4* **7**(4), 314–320.
**URL:** *https://www.nature.com/articles/ngeo2101*

Takeda, S. (1998), 'Influence of iron availability on nutrient consumption ratio of diatoms in oceanic waters', *Nature* **393**(6687), 774–777.
**URL:** *http://www.nature.com/articles/31674*

Talley, L. D. (2013), 'Closure of the global overturning circulation through the Indian, Pacific, and southern oceans', *Oceanography* **26**(1), 80–97.

Thomalla, S. J., Fauchereau, N., Swart, S. and Monteiro, P. M. (2011), 'Regional scale characteristics of the seasonal cycle of chlorophyll in the Southern Ocean', *Biogeosciences* **8**(10), 2849–2866.

Thornton, D. C. O. (2002), 'Diatom aggregation in the sea: mechanisms and ecological implications', *European Journal of Phycology* **37**(2), 149–161.
**URL:** *http://www.tandfonline.com/action/journalInformation?journalCode=tejp20*

Tilman, D., Kilham, S. S. and Kilham, P. (1982), 'Phytoplankton community ecology: the role of limiting nutrients.', *Annual review of ecology and systematics. Volume 13* pp. 349–372.
**URL:** *www.annualreviews.org*

Timmermans, K. R., Gerringa, L. J., De Baar, H. J., Van der Wagt, B., Veldhuis, M. J., De Jong, J. T. and Croot, P. L. (2001), 'Growth rates of large and small Southern Ocean diatoms in relation to availability of iron in natural seawater', *Limnology and Oceanography* **46**(2), 260–266.
**URL:** *http://doi.wiley.com/10.4319/lo.2001.46.2.0260*

Timmermans, K. R., Stolte, W. and de Baar, H. J. (1994), 'Iron-mediated effects on nitrate reductase in marine phytoplankton', *Marine Biology* **121**(2), 389–396.
**URL:** *https://link.springer.com/article/10.1007/BF00346749*

Timmermans, K. R., van der Wagt, B. and de Baar, H. J. W. (2004), 'Growth rates, half-saturation constants, and silicate, nitrate, and phosphate depletion in relation to iron availability of four large, open-ocean diatoms from the Southern Ocean',

*Limnology and Oceanography* **49**(6), 2141–2151.
**URL:** *http://doi.wiley.com/10.4319/lo.2004.49.6.2141*

Toggweiler, J. R. and Samuels, B. (1993), New Radiocarbon Constraints on the Upwelling of Abyssal Water to the Ocean's Surface, *in* 'The Global Carbon Cycle', Springer Berlin Heidelberg, Berlin, Heidelberg, pp. 333–366.
**URL:** *http://www.springerlink.com/index/10.1007/978-3-642-84608-*$3_1$4

Toggweiler, J. R. and Samuels, B. (1995), 'Effect of drake passage on the global thermohaline circulation', *Deep Sea Research Part I: Oceanographic Research Papers* **42**(4), 477–500.

Toggweiler, J. R. and Samuels, B. (1998), 'On the ocean's large-scale circulation near the limit of no vertical mixing', *Journal of Physical Oceanography* **28**(9), 1832–1852.

Tréguer, P., Bowler, C., Moriceau, B., Dutkiewicz, S., Gehlen, M., Aumont, O., Bittner, L., Dugdale, R., Finkel, Z., Iudicone, D., Jahn, O., Guidi, L., Lasbleiz, M., Leblanc, K., Levy, M. and Pondaven, P. (2018), 'Influence of diatom diversity on the ocean biological carbon pump'.

Tréguer, P. J. and De La Rocha, C. L. (2013), 'The world ocean silica cycle', *Annual Review of Marine Science* **5**, 477–501.
**URL:** *https://doi.org/10.1146/annurev-marine-121211-172346*

Tréguer, P. and Jacques, G. (1993), Review Dynamics of nutrients and phytoplankton, and fluxes of carbon, nitrogen and silicon in the Antarctic Ocean BT - Weddell Sea Ecology: Results of EPOS European "Polarstern" Study, *in* 'Weddell Sea Ecology', Springer Berlin Heidelberg, Berlin, Heidelberg, pp. 149–162.
**URL:** *http://www.springerlink.com/index/10.1007/978-3-642-77595-*$6_1 7 http://dx.doi.org/10.1007/978-3-642-77595-6_1 7$

Tungaraza, C., Rousseau, V., Brion, N., Lancelot, C., Gichuki, J., Baeyens, W. and Goeyens, L. (2003), 'Contrasting nitrogen uptake by diatom and Phaeocystis-dominated phytoplankton assemblages in the North Sea', *Journal of Experimental Marine Biology and Ecology* **292**(1), 19–41.
**URL:** *https://www.sciencedirect.com/science/article/pii/S002209810300145X*

Tyrrell, T. (1999), 'The relative influences of nitrogen and phosphorus on oceanic primary production.', *Nature* **400**(-), 525–531.

Urban, N. M. and Fricker, T. E. (2010), 'A comparison of Latin hypercube and grid ensemble designs for the multivariate emulation of an Earth system model', *Computers and Geosciences* **36**(6).

Volk, T. and Hoffert, M. I. (1985), 'Ocean carbon pumps: analysis of relative strengths and efficiencies in ocean-driven atmospheric CO2 changes.', *The carbon cycle and atmospheric CO* pp. 99–110.
**URL:** *https://onlinelibrary.wiley.com/doi/full/10.1029/GM032p0099*

Waite, A. M. and Nodder, S. D. (2001), 'The effect of in situ iron addition on the sinking rates and export flux of Southern Ocean diatoms', *Deep Sea Research Part II: Topical Studies in Oceanography* **48**(11-12), 2635–2654.
**URL:** *https://www.sciencedirect.com/science/article/pii/S0967064501000121*

Waite, A. M., Thompson, P. A. and Harrison, P. J. (1992), 'Does energy control the sinking rates of marine diatoms?', *Limnology and Oceanography* **37**(3), 468–477.
**URL:** *http://doi.wiley.com/10.4319/lo.1992.37.3.0468*

Wang, B., Fennel, K., Yu, L. and Gordon, C. (2020), 'Assessing the value of biogeochemical Argo profiles versus ocean color observations for biogeochemical model optimization in the Gulf of Mexico', *Biogeosciences* **17**(15), 4059–4074.

Wang, X. J., Behrenfeld, M., Le Borgne, R., Murtugudde, R. and Boss, E. (2009), 'Regulation of phytoplankton carbon to chlorophyll ratio by light, nutrients and temperature in the equatorial pacific ocean: A basin-scale model', *Biogeosciences* **6**(3), 391–404.

Ward, B. A., Friedrichs, M. A., Anderson, T. R. and Oschlies, A. (2010), 'Parameter optimisation techniques and the problem of underdetermination in marine biogeochemical models', *Journal of Marine Systems* **81**(1-2), 34–43.

Ward, B. A., Wilson, J. D., Death, R. M., Monteiro, F. M., Yool, A. and Ridgwell, A. (2018), 'EcoGEnIE 1.0: plankton ecology in the cGEnIE Earth system model', *Geoscientific Model Development* **11**, 4241–4267.

Wassmann, P. (1997), 'Retention versus export food chains: processes controlling sinking loss from marine pelagic systems', *Hydrobiologia* **363**(1/3), 29–57.
**URL:** *http://link.springer.com/10.1023/A:1003113403096*

Watson, A. J., Bakker, D. C. E., Ridgwell, A. J., Boyd, P. W. and Law, C. S. (2000), 'Effect of iron supply on Southern Ocean CO2 uptake and implications for glacial atmospheric CO2', *Nature* **407**(6805), 730–733.
**URL:** *http://www.nature.com/articles/35037561*

Waugh, D. W., Primeau, F., DeVries, T. and Holzer, M. (2013), 'Recent changes in the ventilation of the southern oceans', *Science* **339**(6119), 568–570.

Weber, T. and Deutsch, C. (2012), 'Oceanic nitrogen reservoir regulated by plankton diversity and ocean circulation', *Nature* **489**(7416), 419–422.
**URL:** *http://www.nature.com/articles/nature11357*

Weber, T. S. and Deutsch, C. (2010), 'Ocean nutrient ratios governed by plankton biogeography', *Nature* **467**(7315), 550–554.
**URL:** *https://www.nature.com/articles/nature09403*

Weier, J. (2001), 'John Martin'.
**URL:** *https://earthobservatory.nasa.gov/features/Martin*

Whitney, F. A., Crawford, D. W. and Yoshimura, T. (2005), 'The uptake and export of silicon and nitrogen in HNLC waters of the NE Pacific Ocean', *Deep-Sea Research Part II: Topical Studies in Oceanography* **52**(7-8), 1055–1067.

Wilken, S., Hoffmann, B., Hersch, N., Kirchgessner, N., Dieluweit, S., Rubner, W., Hoffmann, L. J., Merkel, R. and Peeken, I. (2011), 'Wilken, Susanne, et al. Diatom frustules show increased mechanical strength and altered valve morphology under iron limitation. Limnol. Oceanogr., 56(4), 2011, 1399–1410', *Limnology and Oceanography* **56**(4), 1399–1410.
**URL:** *https://aslopubs.onlinelibrary.wiley.com/doi/pdf/10.4319/lo.2011.56.4.1399*

Wood, C. C., Statham, P. J., Kelly-Gerreyn, B. A. and Martin, A. P. (2014), 'Modelling macronutrients in shelf sea sediments: Fitting model output to experimental data using a genetic algorithm', *Journal of Soils and Sediments* **14**(1), 218–229.
**URL:** *https://link.springer.com/article/10.1007/s11368-013-0793-0*

Wyatt, N. J., Birchill, A., Ussher, S., Milne, A., Bouman, H. A., Shoenfelt Troein, E., Pabortsava, K., Wright, A., Flanagan, O., Bibby, T. S., Martin, A. and Moore, C. M. (2023), 'Phytoplankton responses to dust addition in the Fe–Mn co-limited eastern Pacific sub-Antarctic differ by source region', *Proceedings of the National Academy of Sciences* **120**(28).
**URL:** *https://pnas.org/doi/10.1073/pnas.2220111120*

Yool, A., Popova, E. E. and Anderson, T. R. (2013), 'MEDUSA-2.0: An intermediate complexity biogeochemical model of the marine carbon cycle for climate change and ocean acidification studies', *Geoscientific Model Development* **6**(5), 1767–1811.

Yool, A. and Tyrrell, T. (2003), 'Role of diatoms in regulating the ocean's silicon cycle', *Global Biogeochemical Cycles* **17**(4), 1103.
**URL:** *http://doi.wiley.com/10.1029/2002GB002018*

Zurzolo, C. and Bowler, C. (2001), 'Exploring bioinorganic pattern formation in diatoms. A story of polarized trafficking', *Plant Physiology* **127**(4), 1339–1345. **URL:** *https://academic.oup.com/plphys/article/127/4/1339/6103649*